4-20-2010

# The Optical and Radio Properties of a Low-Redshift Sample of Broad-lined Active Galactic Nuclei

Stephen E. Rafter
*Georgia State University*

# The Optical and Radio Properties of a Low-Redshift Sample of Broad-lined Active Galactic Nuclei

by

Stephen E. Rafter

Under the Direction of D. Michael Crenshaw

## Abstract

The question as to whether the distribution of radio loudness in active galactic nuclei (AGN) is actually bimodal has been discussed extensively in the literature. Furthermore, there have been claims that radio loudness depends on black hole mass ($M_{BH}$) and Eddington ratio ($L_{bol}/L_{Edd}$). We investigate these claims using the low redshift broad line AGN sample of Greene & Ho (2007), which consists of 8434 objects at $z < 0.35$ from the Sloan Digital Sky Survey (SDSS) Fourth Data Release. We obtained radio fluxes from the Very Large Array Faint Images of the Radio Sky at Twenty-Centimeters (FIRST) survey for the SDSS AGN. Out of the 8434 SDSS AGN, 846 have radio emission within $4''$ of the optical counterpart and are considered to be core emission. We also perform a systematic search for extended emission in FIRST that can be positively associated with the optical counterparts and find 51 out of the 846 previously detected core sources have extended emission that must be taken into account when calculating the total radio luminosity. Further, we find

an additional 12 objects that have extended radio emission but no detectable radio core and have classic FR II type morphologies. Using these data, the question of radio bimodality and the dependence of radio-loudness on physical parameters are investigated for different subsets of the total sample. We find modest trends in the radio-loud fraction as a function of $M_{BH}$ and $L_{bol}/L_{Edd}$, where the fraction of RL AGN increases for the largest $M_{BH}$ group and decreases with increasing $L_{bol}/L_{Edd}$. With extended emission taken into account, we find strong evidence for a bimodal distribution in $\mathcal{R}$, where the lower radio luminosity core-only sources appear as a population separate from the extended sources with a dividing line at $\log(\mathcal{R}) \approx 1.75$. This dividing line is interesting in that it requires the radio luminosity to be 50 times the optical luminosity, ensuring that these are indeed the most RL AGN, which may have different or extreme physical conditions in their central engines when compared to the more numerous radio quiet AGN in this sample.

INDEX WORDS: Active galaxies, Radio galaxies

# The Optical and Radio Properties of a Low-Redshift Sample of Broad-lined Active Galactic Nuclei

by

Stephen E. Rafter

A Dissertation Presented in Partial Fulfillment of Requirements for the Degree of

Doctor of Philosophy

in the College of Arts and Sciences

Georgia State University

2010

# The Optical and Radio Properties of a Low-Redshift Sample of Broad-lined Active Galactic Nuclei

by

Stephen E. Rafter

| | |
|---|---|
| Committee Chair: | D. Michael Crenshaw |
| Committee: | Paul J. Wiita |
| | H. Richard Miller |
| | Harold A. McAlister |
| | Brian Thoms |

Electronic Version Approved:

Office of Graduate Studies

College of Arts & Sciences

Georgia State University

May 2010

# Dedication

My teachers are my friends, my friends are my family, and my family is both. It is to all my experience in life, and to all the wonderful people in mine that I would like to dedicate this work.

# Acknowledgments

I would like to thank my parents for encouraging me to be my own person and do my own thing, and for allowing my to find my own way. I would like to thank all of my friends who have always been there for me and taught me what it is to be dedicated though not blood related. I would also like to thank all of the faculty and staff in the Georgia State University Department of Physics & Astronomy who have helped me along with my academic career. And most especially, I would like to thank my advisor, Mike Crenshaw, for taking on one more graduate student even though he did not have to, and giving me a chance.

# Table of Contents

# List of Tables

# List of Figures

# List of Abbreviations

| | |
|---|---|
| **2MASS** | 2-micron All Sky Survey |
| **3C** | 3rd Cambridge Catalogue of Radio Sources |
| **4C** | 4th Cambridge Catalogue of Radio Sources |
| **87GB** | 87 Green Bank Catalogue of Radio Sources |
| **8C** | 8th Cambridge Catalogue of Radio Sources |
| **Å** | Angström |
| **AGN** | Active Galactic Nuclei |
| **BH** | black hole |
| **BL** | broad-line |
| **BLR** | broad-line region |
| **BLRG** | broad-line radio galaxy |
| **DDRG** | double-double radio galaxy |
| **DR4** | Data Release 4 |
| **FBQS** | First Bright Quasar Survey |
| **FR I** | Fanaroff-Riley class I |
| **FR II** | Fanaroff-Riley class II |
| **FIRST** | Faint Images of the Radio Sky at Twenty-centimeters |
| **FWHM** | full-width at half-maximum |
| **GB6** | Green Bank 6th Catalogue of Radio Sources |

| | |
|---|---|
| **GRG** | Giant radio galaxy |
| **H$\alpha$** | H$\alpha$ balmer line |
| **HYMORS** | HYbrid MOrphology Radio Source |
| **IGM** | inter-galactic medium |
| **ISM** | inter-stellar medium |
| **kpc** | kiloparsecs |
| **$L_{bol}$** | bolometric luminosity |
| **$L_{Edd}$** | Eddington luminosity |
| **LINERs** | low ionization emission-line regions |
| **$M_{BH}$** | black hole mass |
| **Mpc** | Megaparsecs |
| **mJy** | millijansky |
| **$n_e$** | electron density |
| **NL** | narrow-line |
| **NLR** | narrow-line region |
| **NLS1** | Narrow-line Seyfert 1 |
| **NRAO** | National Radio Astronomy Observatory |
| **PKS** | Parkes Radio Survey |
| **pc** | parsecs |
| **PG** | Palomar-Green |
| **PMN** | Parkes-MIT-NRAO radio survey |

| | |
|---|---|
| **QSO** | quasi-stellar object |
| **quasar** | quasi-stellar radio source |
| $\mathbf{R_{BLR}}$ | radius of the BLR |
| **ROSAT** | RÖntgenSATellit |
| **RL** | Radio loud |
| **RLF** | Radio loud fraction |
| **RM** | Reverberation Mapping |
| **RQ** | Radio quiet |
| **SDSS** | Sloan Digital Sky Survey |
| **SED** | spectral energy distribution |
| **SMBH** | supermassive black hole |
| **U** | ionization parameter |
| **UV** | ultraviolet |
| **VLA** | Very Large Array |
| **3CR** | Third Cambridge Revised Catalog |
| **3C** | Third Cambridge Catalog |

– 1 –

# Introduction to Active Galactic Nuclei

## 1.1 History of AGN Identification

It is thought that at the center of nearly every galaxy, including the Milky Way, there is a super massive black hole (SMBH) whose mass can exceed $10^6$ solar masses ($M_\odot$). In most normal galaxies they are quiescent and show little sign of activity, meaning that they do not give off any measurable radiation. There is however another class of objects called Active Galactic Nuclei (AGN) whose SMBHs are thought to be gaining mass by accreting some of the surrounding matter in an accretion disk. As material in the disk loses angular momentum and gravitational potential energy, it falls farther into the disk and gives off substantial amounts of electromagnetic radiation. The total sum of this radiation in an AGN is sometimes enough to outshine all the other billions of stars in the host galaxy. For example the integrated luminosity of the Milky Way is $L_{MW} \approx 10^{44}$ ergs $s^{-1}$ versus a typical AGN luminosity of $L_{AGN} \approx 10^{45}$ ergs $s^{-1}$. These objects are the most continuously luminous class of all astronomical objects and therefore can be found at the farthest reaches of the universe.

The discovery of AGN cannot be attributed to a single person. Since AGN emit radiation across the entire electromagnetic spectrum, i.e. from radio to X-rays and beyond, the earliest observations in these different wavebands took a while to reconcile. Edward Fath first took optical spectra of 'spiral nebulae' in 1909 in an attempt

to prove that they were, in fact, distant conglomerations of billions of stars, with composite spectra made up of stellar type absorption spectra. While this result proved generally true, he did find one object, NGC 1068, that had both absorption and emission lines (Fath 1909).

With the advent of radio astronomy in the 1940's, a few extragalactic radio sources were being resolved into discrete sources in the MHz regime. An optical counterpart to one of these discrete radio sources was M87, an elliptical galaxy with an optical jet, and was first reported by Bolton et al. (1949). Once the nature of these objects was confirmed, meaning that they are extragalactic in nature and extremely luminous in all wavebands, the investigation into the physical mechanism responsible for this phenomenon was begun.

## 1.2 Optical Properties of AGN

### 1.2.1 Type 1 Versus Type 2 AGN

In 1943 Carl Seyfert first identified several spiral galaxies whose cores had similar emission features as those found by Fath in 1909, two of which are the well known NGC 1068 and NGC 4151 (Seyfert 1943). Objects such as these, which are now referred to as Seyfert galaxies, were further subdivided into two distinct classes based on the emission line features seen in their optical spectra by Khachikian & Weedman (1974). Type 1 Seyfert galaxies have narrow (hundreds of km $s^{-1}$) forbidden and permitted emission lines, as well as broad (thousands of km $s^{-1}$) permitted lines. Type

2 Seyfert galaxies have only the narrow-lines (NLs) present. The NLs originate from the narrow-line region (NLR), a lower density ($n_H = 10^{2-6}$ cm$^{-3}$) region typically located hundreds of pc from the central engine (Peterson 1997). The broad lines (BLs) originate from the broad-line region (BLR), a higher density ($n_H \geq 10^8$ cm$^{-3}$) region much closer to the central engine (Ferland et al. 1992). Seyfert galaxies have moderate luminosities ($10^{43-45}$ ergs s$^{-1}$) and are found in relatively nearby, resolvable spiral galaxies.

There is another class of AGNs, quasars, that are much more luminous (typically $\geq 10^{45}$ ergs s$^{-1}$). Generally, quasar host galaxies are found at cosmological distances and are often unresolved. While their optical spectra have emission line features similar to Seyfert galaxies, their extreme luminosities and high continuum levels usually mask any strong absorption features that could be attributed to stars in the host galaxy. Quasars also follow the type 1 and type 2 differentiation used with Seyfert galaxies.

In order to explain the differences between type 1 and type 2 AGN, a unification scheme employing an obscuring toroidal structure composed of gas and dust surrounding the AGN continuum source has been postulated (Antonucci 1984). The toroidal obscuring structure, usually referred to as the 'torus', can hide the BLR and non-stellar continuum source when viewed edge-on (hence the disappearance of the BLs in type 2 AGN), so that only the NLs from the more distant NLR are visible. When an AGN is viewed pole-on, a clear view of the BLR will produce BLs in the spectra, as well as NLs. It is the inclination of the obscuring toroidal structure with

respect to the observers line of sight that determines which type of AGN will be seen. This dissertation is concerned with the properties of BL AGN.

### 1.2.2 BL AGN Fundamental Properties

The BLR is thought to be made up of clouds in gravitational motion about the central object (Peterson 1997). It is the bulk motion of these clouds that Doppler broadens the lines to typical widths of $\sim$ 5000 km s$^{-1}$. The high densities ($n_H \geq 10^8$ cm$^{-3}$) found in the BLR serve to collisionally de-excite atomic metastable levels, hence the forbidden NLs do not originate from there.

All AGN are intrinsically variable on all timescales (hours, days, years) and in all wavebands, where a primary source of the variation is the continuum emission from the accretion disk itself. The ultraviolet (UV) and X-ray continuum emission photoionizes the BLR clouds after some time lag, and the response can be seen by variations in the BL integrated luminosity. The technique of Reverberation Mapping (RM) uses the time lag between the continuum and the BL features to measure the radius of the BLR ($R_{BLR}$). The virial masses of SMBHs can then be calculated using

$$M_{BH} = \frac{f R_{BLR} \Delta V^2}{G}, \tag{1.1}$$

where $f$ is a scaling factor that depends on the geometry and kinematics of the BLR and $\Delta V$ is the velocity dispersion (Peterson 1997; Peterson et al. 2004; Kaspi et al. 2000, 2005). Empirical relations have been found to relate $R_{BLR}$ to the optical luminosity at 5100 Å ($L_\lambda$[5100 Å]), allowing one simple measurement to be used as a

proxy for $R_{BLR}$ (Peterson et al. 2004; Kaspi et al. 2005). There is some debate over the empirical power law that governs this relation, and a few different scalings are used, but recent studies have $R_{BLR} \propto (L_\lambda[5100\ \text{Å}])^\gamma$ where $\gamma \approx 0.5$ (Vestergaard & Peterson 2006). This is the (zeroth order) theoretical expectation obtained by assuming a constant ionization parameter (U) and constant electron density ($n_e$) for the BLR in all AGN (Peterson 1997). The FWHM of the BLs gives a measure of the velocity dispersion of the BLR clouds due to their assumed Keplerian orbits around the BH. These two combined measurements ($L_\lambda$[5100 Å], FWHM) from a single spectrum can give a relatively reliable virial estimate of $M_{BH}$ (Vestergaard & Peterson 2006).

Another important parameter, the Eddington ratio, is the ratio of the bolometric luminosity ($L_{bol}$) to the Eddington luminosity ($L_{Edd} = 1.26 \times 10^{38}\ M_{BH}/M_\odot$ erg $s^{-1}$). Determination of the true $L_{bol}$ gives a measure of the accretion rate since $L_{bol} = \eta \dot{M} c^2$, where $\eta$ is the efficiency factor for the conversion of matter into energy during accretion, and $\eta \approx 0.1$. Determining the true $L_{bol}$ requires a full spectral energy distribution (SED) that spans from radio to X-ray emission and beyond for most AGN. AGN that have an observed SED that spans the entire spectrum provide normalization relations so that one can use a single continuum measurement in the optical or X-ray bands to stand in as a reasonable proxy for $L_{bol}$ (e.g., Elvis et al. 1994, 2002; McLure & Dunlop 2004).

## 1.3 Radio Properties of AGN

### 1.3.1 Physical Source of Radio Emission

The primary component of radio emission in AGN is synchrotron radiation. It was first discovered in 1946 by Frank Elder, Anatole Gurewitsch, Robert Langmuir, and Herb Pollock while working at General Electric (Elder et al. 1947). Synchrotron emission is a form of non-thermal radiation (as opposed to black body radiation) caused by the spiraling of relativistically accelerated electrons around magnetic field lines. This spiraling motion causes a change in the velocity of the electron, which produces a non-thermal power law spectrum and the high degree of polarization at radio frequencies as seen in AGN. In 1956, M87 became the first astrophysical object confirmed as a source of synchrotron emission by Geoffery Burbidge (Burbidge 1956).

### 1.3.2 Radio Morphology

A natural consequence of matter accreting onto a compact astrophysical object is the formation of highly collimated jets (Blandford & Payne 1982 and references therein). In AGN, these jets can be extremely powerful and span distances on multi-kpc to nearly Mpc scales from the central source. In general, sources that are edge darkened and have strong, usually symmetric, jets are classified as Fanaroff & Riley Type I (FR I) sources, and a typical FR I is shown in Figure 1.1 (Fanaroff & Riley 1974).

As these jets pass through the host galaxy's interstellar medium (ISM), and then into the intergalactic medium (IGM), the plasma passing through the jets diffuses and creates lobes. These show hot spots of emission due to shock fronts produced where the bulk flow of the jets is dramatically slowed where there are strong interactions of the lobe with the jet that is feeding it. In this case, the lobes tend to be edge brightened and are classified as Fanaroff & Riley Type II (FR II) sources (Fanaroff & Riley 1974), and a typical example is shown in Figure 1.2. Note that each of these images has a point like source at the center of their radio structures that align with the optical AGN and are considered to be core radio emission. AGN radio emission can range from a few kpcs to more than a Mpc for giant radio galaxies (GRG) whose total projected linear extent exceeds 750 kpc (Saripalli & Subrahmanyan 2009 and references therein).

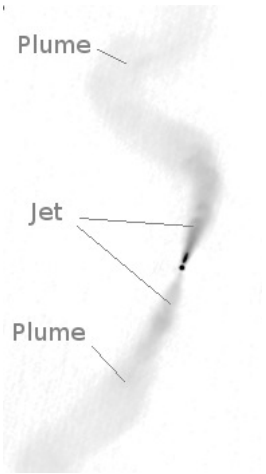


FIGURE 1.1: The highly collimated, symmetric jets in 3C31 are labeled, showing that this is a classic FR I radio galaxy.

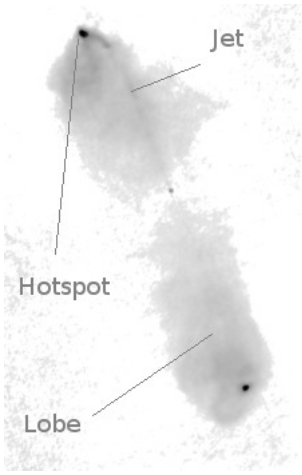


FIGURE 1.2: The edge-brightened lobes are labeled as hot spots in this radio image of 3C98. This double lobe symmetry is typical of most FR II radio galaxies.

While a majority of radio sources tend to be either symmetric FR Is or FR IIs, it has been shown by Gopal-Krishna & Wiita (2000) that an asymmetric class of radio galaxies known as 'HYbrid MOrphology Radio Sources' (HYMORS) exist. These sources show asymmetries possibly due to the different deceleration rates as the jets interact with a different IGM on either side of the host galaxy. This can cause a hybrid morphology where on side has an FR II-like lobe and the other side has an FR I-like jet.

Two of the other common radio morphologies are double-double radio galaxies (DDRGs) and X-shaped sources. As shown in Figure 1.3, taken from Saikia et al. (2006), DDRGs have two sets of symmetric lobes, usually aligned about the central source, and are caused by the disruption, and later restarting, of the jets in the AGN. This results in a younger pair of lobes closer to the AGN than an older, more distant pair (see e.g., Jamrozy et al. 2009). The appearance of an X-shaped radio morphology,

as shown in Figure 1.4 from Capetti et al. (2002), is not as well understood and has two main explanations. The first is that a merger event between two SMBHs has caused a spin reorientation and hence a realignment of the jet, which produces an X-shaped radio morphology (Merritt & Ekers 2002). The other leading explanation proposed by Capetti et al. (2002) is that the plasma in the lobes backflows and creates an overpressured cocoon that ejects new outflows along the minor axis of the galaxy.

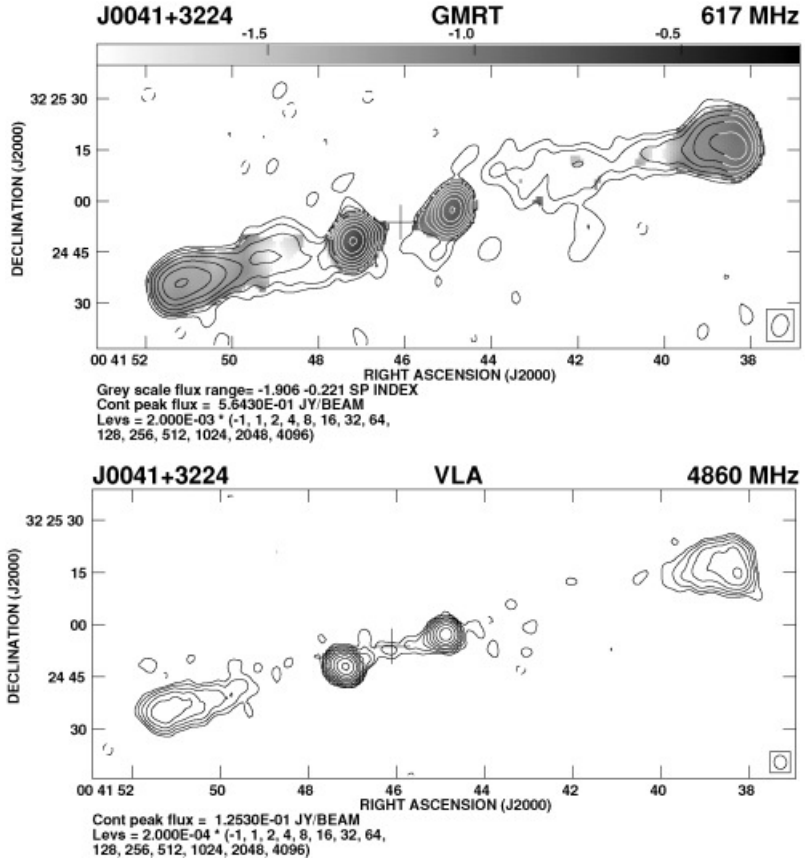


FIGURE 1.3: The Giant Metrewave Radio Telescope (GMRT) image of J0041+3224 at 617 MHz with an angular resolution of 5.6′ (upper panel) and the VLA C-array image at 4860 MHz with an angular resolution of 3.8′ (lower panel). The spectral index image obtained by smoothing the 4860-MHz image to that of the 617-MHz one is shown superimposed on the 617-MHz image in grey-scale. Image and text taken from Saikia et al. (2006).

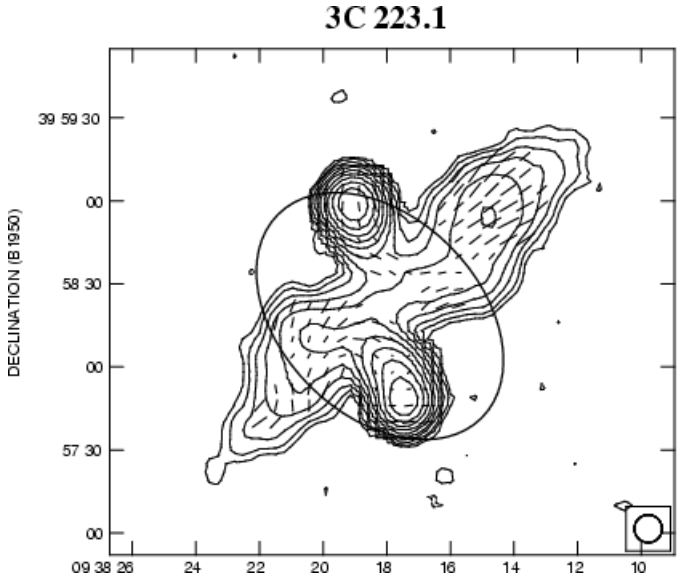


FIGURE 1.4: Ryle Telescope observations of 3C 223.1 at 15.2 GHz. The lowest contour is at 3; the 10 contours are equally spaced in logarithmic intervals to peak flux density (77 mJy beam$^{-1}$). (Contours: 1.03, 1.03, 1.59, 2.44, 3.76, 5.79, 8.92, 13.73, 21.14, 32.54, 50.10 mJy beam$^{-1}$). The superposition of the host galaxy shape (not in scale) onto the radio maps was added by Capetti et al. (2002). Original image and text taken from Dennett-Thorpe et al. (2002).

### 1.3.3 Radio Loudness in AGN

The degree of radio-loudness is a means by which to classify AGN, and is based on the amount of radio emission in the form of core emission, jets and/or lobes that can be positively associated with the central engine. There are two main characterizations of the radio-loudness of AGN. The first is to set a dividing line between radio-loud (RL) and radio-quiet (RQ) based on the $\mathcal{R}$ parameter defined as the ratio of the monochromatic 5 GHz (6 cm) radio luminosity to the 4400 Å (B band) optical luminosity ($\mathcal{R} \equiv \nu_{5\mathrm{GHz}} \mathrm{L}_{5\mathrm{GHz}} / \nu_{4400} \mathrm{L}_{4400}$). By convention, RL AGNs have $\mathcal{R} > 10$ and RQ AGNs have $\mathcal{R} < 10$ (Kellermann et al. 1989). The second way to characterize the degree of radio-loudness is by using the radio luminosity alone. Fanaroff & Riley

(1974) originally found a transition from the FR I type radio morphology to the FR II type at a luminosity of $10^{24.5}$ Watts Hz$^{-1}$ at 1.4 GHz (e.g., Kawakatu et al. 2009). While this luminosity is not a RL/RQ dividing line, the distribution in the radio luminosity plane shows that most FR Is have luminosities below this dividing line and FR IIs have luminosities above. However it is well established that many FR Is are RL when following the classic $\mathcal{R}$ convention, and therefore a lower luminosity dividing line has occasionally been used as an alternate way to classify AGN as either RL or RQ; e.g., Best et al. (2005) specify $10^{23}$ Watts Hz$^{-1}$ as a dividing line for the Very Large Array's (VLA) Faint Images of the Radio Sky at Twenty-centimeters (FIRST) survey which operates at 1.4 GHz.

A quasar radio dichotomy has been postulated because only 5% – 10% of all AGNs are RL according to the $\mathcal{R} > 10$ criterion (Kellermann et al. 1989; Urry & Padovani 1995; Ivezić et al. 2002; White et al. 2007). This has led to claims that there is a bimodal distribution in the $\mathcal{R}$ parameter for high optical luminosity, high redshift sources (Laor 2003; Ivezić et al. 2004 and references therein), where usually only the core radio emission is taken into account. While the RL AGNs are usually thought to be powered by the same phenomenon of matter accreting onto a SMBH, it has been suggested that they may have a different accretion mode (e.g., advection dominated accretion flow vs a standard thin disk), or that their BH's are more massive or spinning faster, or some combination of both (Sikora et al. 2007 and references therein). Other models propose that powerful jets tap the spin energy of the BH (e.g., Blandford &

Znajek 1977) so that accretion rate is nearly irrelevant. Either case suggests that $\mathcal{R}$, although not a fundamental quantity, may be linked to one.

Very often the most extreme RL AGNs are FR II types that have giant radio lobes that grow and extend from the host galaxy out to Mpc scales while being fed by highly collimated jets. Statistically, these AGN are associated most often with giant elliptical galaxies that tend to have optical spectra with very broad Balmer line (H$\alpha$, H$\beta$) profiles with a large full width at half maximum (FWHM), typically $>$ 8000 km s$^{-1}$ (Osterbrock & Ferland 2006). In studies of high redshift, high luminosity AGN, it has generally been thought that most RL AGN have $M_{BH} > 10^8$ $M_\odot$ (e.g., Laor 2000; McLure & Jarvis 2004). This clearly manifests itself for most FR IIs when determining $M_{BH}$ from single epoch measurements, since empirically, $M_{BH} \propto FWHM^2_{H\alpha} L^{0.5}$ (Bentz et al. 2009).

It has been shown in studies by Ho (2002) and Sikora et al. (2007) that there is a strong correlation between radio-loudness and Eddington ratio, where AGNs with very low accretion rates (corresponding to $\sim 10^{-5}$ $L_{bol}/L_{Edd}$) are almost exclusively all RL based on the $\mathcal{R}$ parameter. A clear trend can be seen of decreasing radio-loudness with increasing $L_{bol}/L_{Edd}$ as shown in Figure 1.5 from Sikora et al. (2007) (note that in this plot $L_{bol}/L_{Edd} = \lambda$). Further, Sikora et al. (2007) find two separate populations of AGN in the $\mathcal{R}$ vs $L_{bol}/L_{Edd}$ plane, where the upper population consists of FR I, BLRG and RL quasars (shown in Figure 1.5 as triangles, filled circles and open circles respectively) hosted by giant elliptical galaxies. The lower population are

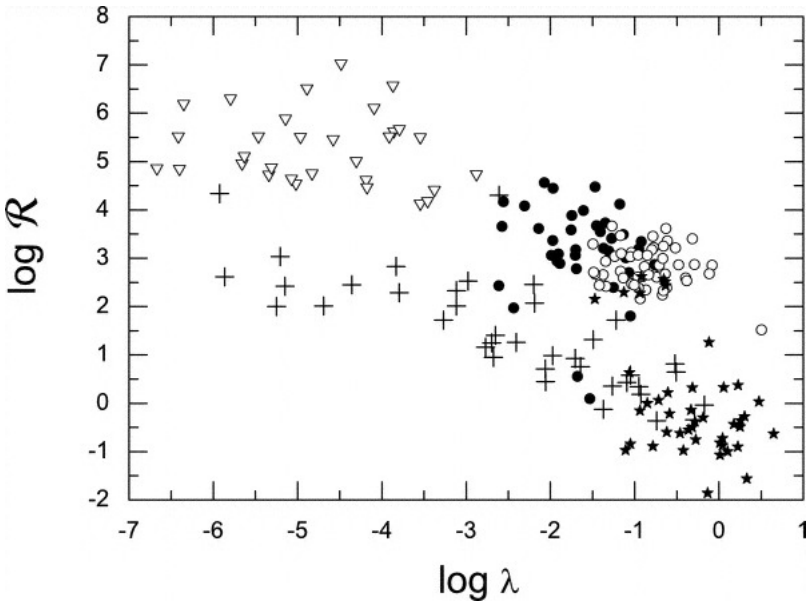


FIGURE 1.5: Sikora et al. (2007) Figure 3: log($\mathcal{R}$) vs log($L_{bol}/L_{Edd}$). Note that $L_{bol}/L_{Edd} = \lambda$. The BLRGs are marked by filled circles, RL quasars by open circles, Seyfert galaxies and LINERs by crosses, FR I radio galaxies by open triangles, and PG quasars by filled stars. There is a clear trend of decreasing $\mathcal{R}$ with increasing $L_{bol}/L_{Edd}$. Note that this plot covers 8 decades in Eddington ratio and 10 decades in $\mathcal{R}$

mostly Seyfert and Low Ionization Nuclear Emission-line Region (LINER) galaxies, shown in Figure 1.5 as crosses and are usually hosted by spiral galaxies, and the Palomar-Green (PG) quasars, shown as filled stars (for further information on PG quasars see Schmidt & Green 1983; Green et al. 1986). While these studies do show a dependence of radio-loudness on accretion rate, they do not exclude the possibility that there may be other factors that contribute to the generation of strong radio emission, such as accretion mode, which is directly related to the amount of matter in the accretion disk, or the spin of the SMBH.

## 1.4 Motivation for the Current Study

The classification of AGN can depend on many factors and it is not uncommon to find a particularly radio luminous AGN classified as a broad line radio galaxy (BLRG), a quasar, *and* a FR I. Generally, an AGN's classification can depend on many factors such as when and in what part of the spectrum it was first discovered, which particular study it is being used in, and the source of the data. Moving beyond an often blurred and overlapping system of identification into one based on more quantitative parameters could allow a more continuous classification scheme that is easier to apply to the large samples that continue to become available with large area surveys in the radio (VLA's FIRST survey), infrared (2MASS), optical (SDSS), and X-ray (ROSAT) bands. The AGN in these large samples can now be classified based on measured quantities in a statistical fashion that is inherently more continuous than the discrete nomenclature generally used (e.g., Kewley et al. 2006). In this way we can move away from a 'by eye' classification scheme to one based on physical parameters like $M_{BH}$, $L_{bol}/L_{Edd}$, or $\mathcal{R}$, which is likely related to a physical parameter like accretion rate or BH spin. Adopting this philosophy, we will examine the interdependence of these parameters in a large sample of AGN.

We will also use this sample to examine the relative numbers of RL and RQ AGN. Several investigations into this claim of bimodality between the RL and RQ sources have yielded results that differ, in that some studies support this claim and others do not, based on the AGN sample, the selection criteria, and inclusion or exclusion of

extended radio emission (White et al. 2000; Ivezić et al. 2002, 2004; Cirasuolo et al. 2003, 2004; Laor 2003; White et al. 2007). Also higher redshift studies imply that the properties of RL AGN may be different than in the local universe, indicating an evolution of the radio luminosity function and possibly $\mathcal{R}$ (Jiang et al. 2007).

The motivation behind this study is to determine how the radio properties of AGN in the local universe may differ from those at higher redshift, and what physical characteristics cause them to be so much different from the remaining, generally RQ, AGN population. In other words, why are only 5% - 10% of all AGN RL, and how can the measurable physical quantities be related to radio loudness? Do they actually have different physical conditions in their central engines that make them behave as a truly separate class of AGN, or is there a continuous set of physical conditions responsible for this phenomenon, where the more numerous RQ AGNs reside on one end, and the RL AGNs are at the other extreme? Using this optical sample (described in Chapter 2) is ideal as it provides us with a perfect unbiased sample in that it was not chosen based on radio properties, and further, we can determine $M_{BH}$ and $L_{bol}/L_{Edd}$ for every source.

– 2 –

# Sloan Digital Sky Survey and the BL AGN Sample

## 2.1 SDSS Survey

The optical data discussed in this dissertation comes from the Sloan Digital Sky Survey (SDSS) Data Release 4 (DR4) (Adelman-McCarthy et al. 2006). The SDSS is designed to map nearly 25% of the entire sky using a dedicated 2.5 m wide-angle optical telescope located at Apache Point Observatory in New Mexico. The telescope is capable of multi-filter photometry (the u, g, r, i, z bands are specific to SDSS) and has taken images of 180 million unique astronomical objects over 6670 $\deg^2$ of the sky, with an astrometric accuracy of $< 0.1''$. The photometric data are then used to select specific objects for spectrographic follow-up observations. The spectrograph is fiber fed through holes drilled into an aluminum plate, where each hole is positioned on a target in the field of view. In this way the SDSS spectrograph can take over 600 spectra simultaneously in any field of view. The wavelength coverage is from 3800-9200 Å and has a modest resolving power of 1800. The spectroscopic catalogue for DR4 has 67,382 AGN/quasars out to a redshift of $\sim 2.3$ (Adelman-McCarthy et al. 2006). This dissertation is concerned with the quasar spectra at redshifts less than 0.35.

## 2.2 SDSS Optical Sample and Properties

The BL AGN sample and all optical data come from Greene & Ho (2007) and consists of 8434 AGN, all with $z < 0.35$ to ensure the observation of the H$\alpha$ Balmer

line, taken from the SDSS DR4. Greene & Ho subtract the stellar continuum from all spectra following their prescription (Greene & Ho 2004) to ensure that the AGN broad-lines are not masked or suppressed by host galaxy features. For this study the relevant data taken from the spectra consist of the full width at half maximum of H$\alpha$ (FWHM$_{\mathrm{H}\alpha}$) and the luminosity of H$\alpha$ (L$_{\mathrm{H}\alpha}$). With the 35 or so reverberation-mapped AGN, empirical relations between the continuum luminosity and broad H$\beta$ FWHM have been calibrated to derive black hole masses of AGN central engines (Peterson et al. 2004). Other recent empirical relations have allowed the use of H$\alpha$ to derive M$_{\mathrm{BH}}$, because H$\beta$ is usually about 3 times weaker and H$\alpha$ has lower signal-to-noise requirements (Greene & Ho 2005). The following relations from Greene & Ho (2007) were used to calculate M$_{\mathrm{BH}}$ and L$_{\mathrm{Edd}}$ for all 8434 AGN in the sample:

$$\mathrm{M_{BH}} = (2 \times 10^6) \left( \frac{\mathrm{L_{H\alpha}}}{10^{42}\ \mathrm{erg\ s^{-1}}} \right)^{0.55} \left( \frac{\mathrm{FWHM_{H\alpha}}}{10^3\ \mathrm{km\ s^{-1}}} \right)^{2.06} \mathrm{M_\odot} \tag{2.1}$$

$$\mathrm{L_{Edd}} = (1.26 \times 10^{38}) \left( \frac{\mathrm{M_{BH}}}{\mathrm{M_\odot}} \right)\ \mathrm{erg\ s^{-1}}. \tag{2.2}$$

Equation 2.1 is an empirical relation based on the virial M$_{\mathrm{BH}}$ relation shown in equation 1.1. Equation 2.2 is based on the proportionality between M$_{\mathrm{BH}}$ and L$_{\mathrm{Edd}}$ as shown in section 1.2.2. To find L$_{\mathrm{bol}}$/L$_{\mathrm{Edd}}$, the bolometric luminosity (L$_{\mathrm{bol}}$) is required. Greene & Ho (2005) find that L$_{\mathrm{H}\alpha}$ scales with L$_{\mathrm{bol}}$, which is then calculated using the following relation:

$$L_{bol} = (2.34 \times 10^{44}) \left(\frac{L_{H\alpha}}{10^{42}}\right)^{0.86} \text{ erg s}^{-1}. \quad (2.3)$$

The monochromatic continuum luminosity at 5100 Å ($\lambda L_\lambda$[5100 Å]) is found to scale with $L_{bol}$ (McLure & Dunlop 2004; Greene & Ho 2005), but because the typical $\mathcal{R}$ value is based on $L_\lambda$(4400 Å), it is necessary to scale $L_\lambda$(5100 Å) using a typical optical spectral index of 0.5 (Sikora et al. 2007) so that:

$$L_\lambda(4400\text{Å}) = (L_\lambda[5100\text{Å}]) \left(\frac{4400\text{Å}}{5100\text{Å}}\right)^{-0.5} = (2.59 \times 10^{43}) \left(\frac{L_{H\alpha}}{10^{42}}\right)^{0.86} \text{ erg s}^{-1}. \quad (2.4)$$

The sample in general (as shown later in Figure 3.3) has roughly equal numbers of objects at redshifts between ∼0.05 and 0.35 and spans about 2 decades in luminosity at a given redshift. One advantage of using this sample is that it is a spectroscopic sample of BL AGN from which $M_{BH}$ and $L_{bol}/L_{Edd}$ can be calculated as shown above. Our final optical data set consists of redshifts, $FWHM_{H\alpha}$, $L_{H\alpha}$, $L_\lambda$(5100 Å), and $L_\lambda$(4400 Å), along with calculated $M_{BH}$ and $L_{bol}/L_{Edd}$ for all objects in the sample. The full optical sample has 7576 AGN with $M_{BH} < 10^8$ $M_\odot$, and 858 AGN with $M_{BH} > 10^8$ $M_\odot$. In Figure 2.1 we show the distribution of $M_{BH}$ for the full sample normalized by the total number of sources (8434) which spans nearly 4 decades in magnitude and peaks at $\sim 10^{7.5}$ $M_\odot$.

In Figure 2.2 we show the distribution of $L_{bol}/L_{Edd}$ for the full optical sample. While this sample spans a over 3 decades in $L_{bol}/L_{Edd}$, we do not get lower than $10^{-3}$

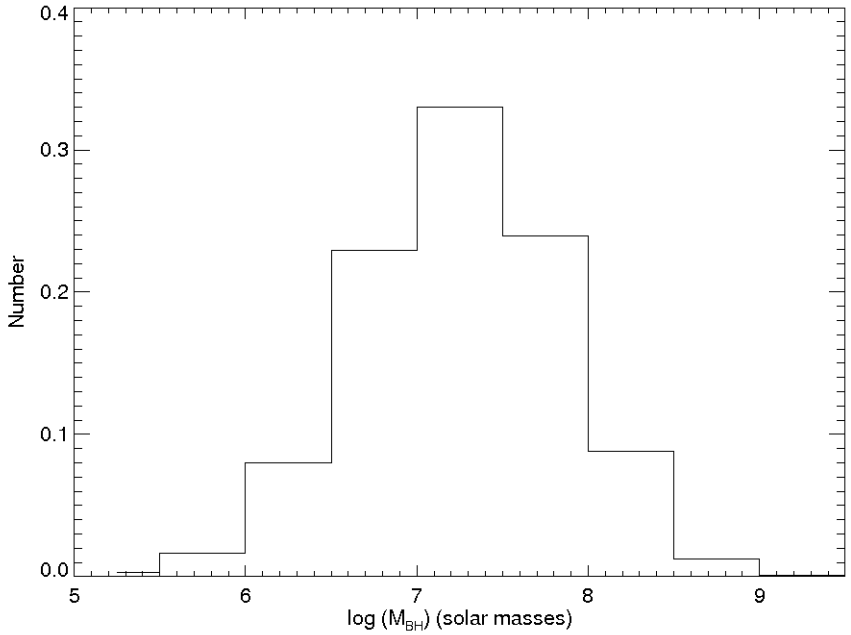


FIGURE 2.1: The $M_{BH}$ histogram spans 4 decades and peaks at $10^{7.5}$ $M_{\odot}$ for the full optical sample.

due to the flux limits of the SDSS spectrograph. While super-Eddington accretion is theoretically impossible when derived for a spherical geometry, it still is possible for AGN since the accretion disk is not spherically symmetric (e.g., Paczyńsky & Wiita 1980), and we find that 0.03% of our sample has $L_{bol}/L_{Edd} > 1$. Of course this fraction may come arise from errors in the $M_{BH}$ or $L_{bol}$ determinations.

Based on the radio data introduced in Chapter 3 the full data sets will be broken into subsamples based on optical flux limits. The advantage of using a flux limited sample is that it is complete to a given limiting magnitude and therefore suffers less from Malmquist bias and approximates a volume limited sample. Finally, the AGN

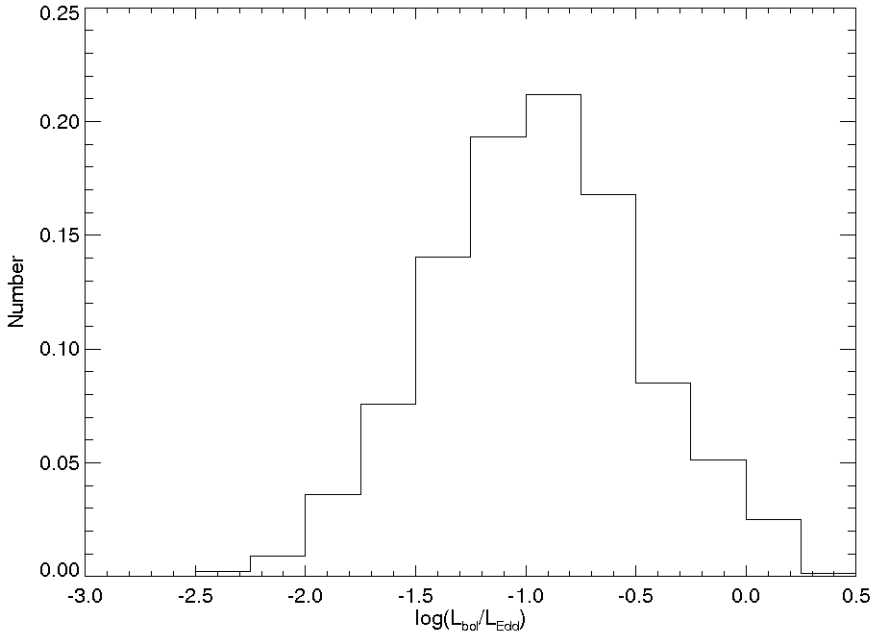


FIGURE 2.2: The $L_{bol}/L_{Edd}$ histogram spans over 3 decades and peaks at $\sim 0.1$ $L_{bol}/L_{Edd}$ for the full optical sample.

in this sample were not, in general, selected on the basis of their radio properties, and thus we can determine the true fraction of AGN at low redshift that are RL.

– 3 –

# Radio Sample

## 3.1 Faint Images of the Radio Sky at Twenty-centimeters (FIRST) Survey

The FIRST survey utilizes the National Radio Astronomy Observatory's (NRAO) Very Large Array (VLA) in the B-configuration to map 9,055 deg$^2$ of the North Galactic Cap. The coverage area was chosen to coincide with that of the SDSS. The survey operates at 1.4 GHz, has a 1 mJy source detection threshold and a resolution of 5″. The current version of the FIRST catalog (released July 16, 2008) has over 816,000 sources with detectable radio emission (Becker et al. 1995). Figure 3.1 shows a SDSS image and a FIRST image of an AGN in this sample.

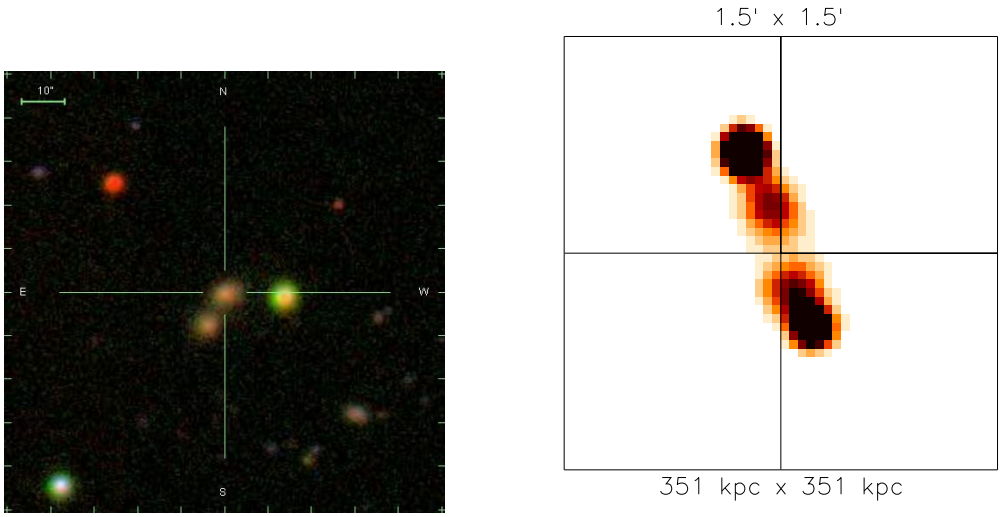


Figure 3.1: The SDSS image (left) is nearly 1.5′ and the FIRST image (right) is 1.5′. In both images north is up and east is to the left. The SDSS image shows two galaxies that may have interacted sometime in the past, possibly triggering the AGN seen at the center of the image (for optical spectra see Figure B.30). The FIRST image shows that this is a FR II type radio galaxy, and possibly a double-double radio source (see end of Chapter 3.3).

### 3.2 Core-only Sample Using a 4″ Search Radius

We obtained radio fluxes based on correspondence in position with the optical data. This was done by cross-correlating the positions of all the AGNs in the optical sample with the positions of all sources in the FIRST catalogue using an Interactive Data Language code which we wrote specifically for this project. The search radius was only 4″ from the optical counterpart to ensure that the radio emission at the sample redshift limit was still within the host galaxy. The 4″ search radius may, however, exclude objects with weak or no core emission and extended radio stuctures such as lobes or jets. Figure 3.2 shows a histogram of the position offsets (indicating the accurate astrometry in both SDSS and FIRST databases). Only 3% of the FIRST sources are off by more than 2″ from the SDSS optical counterpart (which corresponds to ∼14 kpc at the $z = 0.35$ sample limit) and shows that most core sources are well within the optical host galaxy. For each object the integrated flux ($F_{int}$) given in mJy was taken. Out of the 8434 AGN, there were 846 sources with radio flux above the FIRST limit. Table B.1 gives the SDSS object name, the FIRST field, integrated flux, and calculated $\log(\mathcal{R})$ for these 846 AGN. All objects that did not have a FIRST counterpart were given a flux upper limit of 1 mJy. For consistency, we converted $F_{int}$ into a luminosity using the usual flux-luminosity relation with the same cosmology and redshifts used by Greene & Ho (2007) from Spergel et al. (2003) ($H_0 = 71$ km s$^{-1}$ Mpc$^{-1}$, $\Omega_m = 0.27$, and $\Omega_\Lambda = 0.73$, where $H_0$ is Hubble's constant, $\Omega_m$ is the fraction of baryonic and dark matter, and $\Omega_\Lambda$ is the fraction of dark energy). We conform to

the standard definition of $\mathcal{R}$ so that comparisons could be made with previous work, where $L_{radio}$ is at 5 GHz. Since the radio flux in AGN is generally characterized by a power law where $F_\nu \propto \nu^{-\alpha}$, the luminosity was scaled by $(\nu_{5\mathrm{GHz}}/\nu_{1.4\mathrm{GHz}})^{-\alpha_\mathrm{R}} = 0.361$, where the most common radio spectral index, $\alpha_\mathrm{R} = 0.8$, was used (Sikora et al. 2007). So the assumed upper limit of 1 mJy at 1.4 GHz assigned to undetected objects corresponds to 0.361 mJy at 5 GHz.

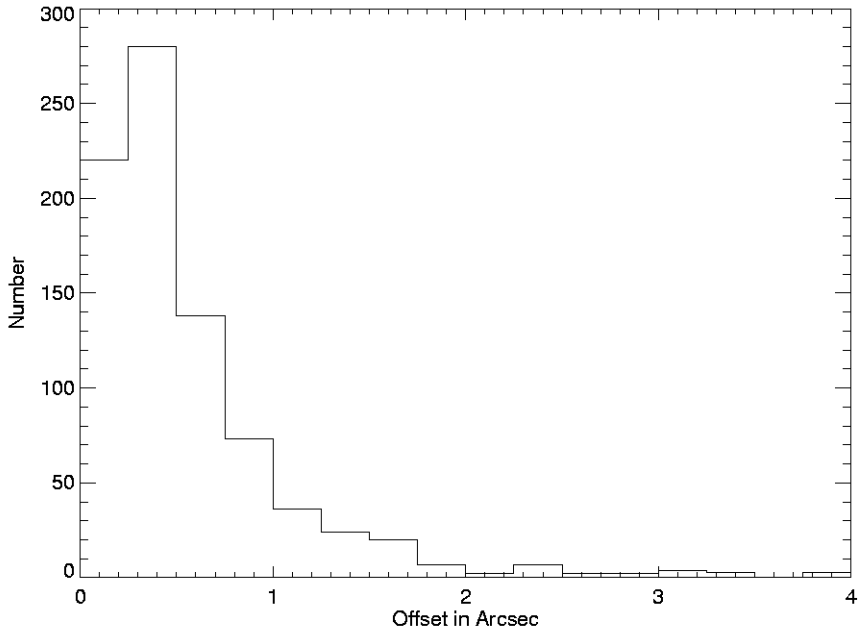


FIGURE 3.2: Core-only source position offset in arcseconds. Only 3% are off by more than $2'$.

### 3.2.1 Sample Subsets Using the Core-only Sources

The total sample can be broken into subsets and analyzed separately based on detections and flux limits. The first subset is the 846 objects that have measured FIRST fluxes. This subset will be referred to as the 'detected' sample. The detected

sample is advantageous in that all $\mathcal{R}$ values will be uniquely determined for each object. In this subsample, $\log(\mathcal{R})$ ranges from $-0.68$ to 4.47, spaning over 5 orders of magnitude, and has 707 AGN with $M_{BH} < 10^8$ $M_\odot$, and 139 AGN with $M_{BH} > 10^8$ $M_\odot$.

The next subset is found by setting an optical flux limit of $F_\lambda(4400\ \text{Å}) = 5.6\times10^{-17}$ ergs $s^{-1}$ $cm^{-2}$ $Å^{-1}$ ($F_\nu[4400\ Å] = 0.0361$ mJy). The practical reason for the optical flux limited sample is that for an object not detected by FIRST, we can not uniquely determine if it is RL or RQ if $F_\nu(4400\ Å) < 0.0361$ mJy. All AGN designated RL with an $\mathcal{R}$ upper limit (1 mJy at 1.4 GHz = 0.361 mJy at 5GHz) are cut when this optical flux limit is set. Some of these may be true RL AGN, but since they lack a FIRST counterpart (i.e., too faint for FIRST detection and have a $F_\nu[5\ \text{GHz}] < 0.361$ mJy) they do not make the cut. Some objects from the detected subsample, and some that are designated RQ with an $\mathcal{R}$ upper limit are cut as well. This subset will be referred to as the 'flux limited' sample and consists of 5485 objects. The dashed line in Figure 3.3 shows the optical flux limit used to make this cut, and the solid line approximates the SDSS magnitude limit.

The last subset is from the flux limited sample and is found by imposing even more stringent flux limits following Ivezić et al. (2002). This last flux imposition takes into account that a large number of objects in a radio vs optical flux plot will tend to overpopulate the region of the plot just above each respective flux limit. Ivezić et al. (2002) claim that to get a true representation of the $\mathcal{R}$ distribution this must be taken

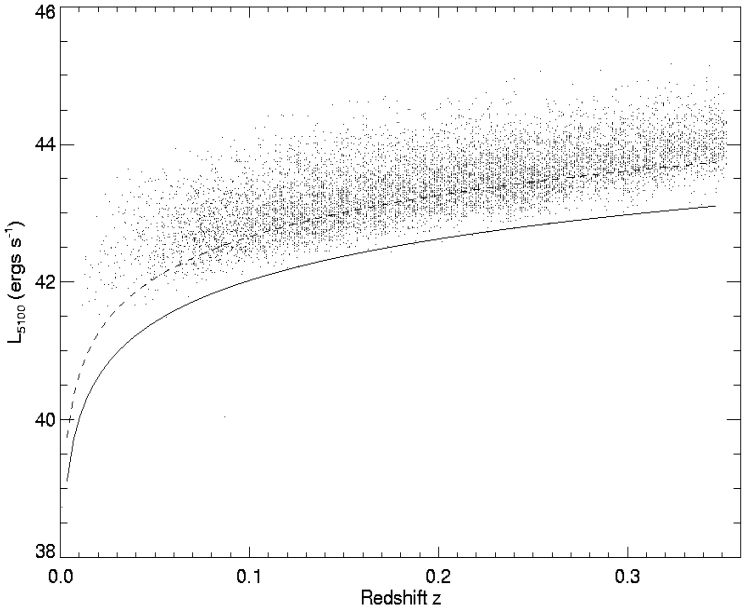


FIGURE 3.3: $\lambda L_\lambda(5100\ \text{Å})$ vs z for all SDSS AGN. The solid line is an approximate SDSS flux limit ($F_\lambda(5100\ \text{Å}) = 1{\times}10^{-17}$ ergs s$^{-1}$ cm$^{-2}$ Å$^{-1}$). The dashed line indicates the flux limit of the flux limited sample ($F_\lambda(5100\ \text{Å}) = 3.9{\times}10^{-17}$ ergs s$^{-1}$ cm$^{-2}$ Å$^{-1}$)

into account. Figure 3.4 is a plot of the radio flux (at 5 GHz) as a function of the optical flux (at 4400 Å), both given in mJy. The horizontal and vertical lines indicate the FIRST and SDSS flux limits respectively. The region just above both of these limits is the most populated, as shown by the dots. The positively sloped dot-dashed lines are lines of constant $\log(\mathcal{R}) = 2, 1, 0$ from the top down, respectively. According to Ivezić et al. (2002), it is necessary to take samples in regions that are perpendicular to these lines and well away from the flux limits. The square symbols are the ones that are in the region of interest. This 'stringently flux limited' sample has only 234 objects. We use the core-only sources and the different subsets to compare with higher redshift, higher luminosity studies.

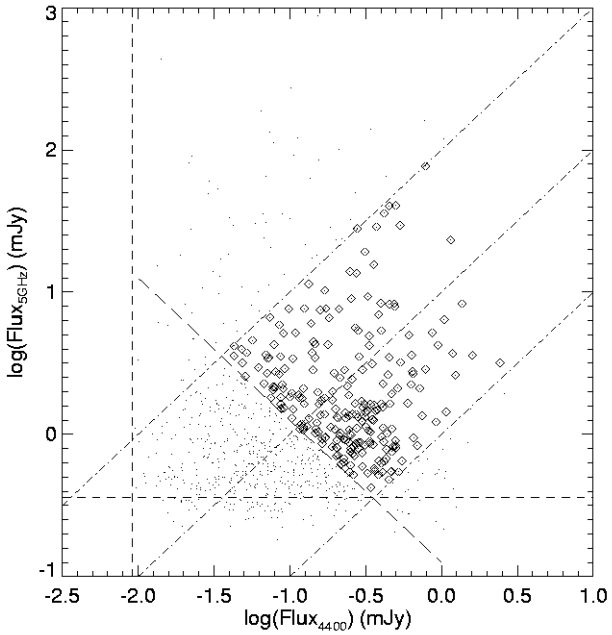


FIGURE 3.4: 5 GHz radio flux vs 4400 Å optical flux. The horizontal and vertical dashed lines indicate the FIRST and (approximate) SDSS flux limits respectively. The positively sloped dot-dashed lines are the lines of constant $\log(\mathcal{R}) = 2, 1, 0$ (from the top line down). Objects above the line perpendicular to the $\log(\mathcal{R})$ lines defines a boundary for the stringently flux limited sample. The dots are objects that are outside the region of interest and do not make this sample; the squares are objects that do satisfy these flux cuts.

## 3.3 Extended Sample Using a 60″ Search Radius

We next took the radio core emission AGN described in Chapter 3.2 as the detected sample and performed a search around a much wider, 60″ radius, to identify any extended emission (at positions $> 4''$ from the optical AGN) that may be associated with them. The 60″ search radius was chosen due to the fact that the largest known FR IIs are on the scale of a Mpc (Saripalli & Subrahmanyan 2009 and references therein), and at the sample redshift limit of $z = 0.35$, a 60″ search radius corresponds to nearly 1 Mpc in diameter. All extended sources were visually inspected in the SDSS and FIRST images to give us confidence that the radio emission is associated. This

does not mean that any clearly associated emission out past 60″ was not included, but that any associated emission out past 60″ was added to the total by hand after visual inspection of the FIRST images.

In order to confirm the association of extended emission with the optical counterpart, it is first necessary to make sure that the extended emission is not associated with another optical source in the field. The majority of cases where this takes place is when there is a core source within 4″ and a second source within 60″, where the second source is at the same position as another galaxy in the SDSS image. Therefore, any FIRST sources found in the extended search with obvious optical counterparts in the SDSS images were eliminated as possible extended source matches (e.g., SDSS J094603.94+013923.6 is a BL AGN misclassified as a star in SDSS DR7 with a resolved spiral galaxy to the north that is more likely the source of the extended radio emission). The criteria used to confirm the association of the extended emission to the central optical source are illustrated in Figure 3.5, where the center of each image is the SDSS optical AGN position and the linear scale is given below each image. In Figure 3.5 the sources a−e were all found to have core emission in the original 4″ search described in Chapter 3.2. In Figure 3.5a (top left) we show the radio map of SDSS J170013.70+400855.6, which shows the core-source with a nearby ($\sim$ 35 kpc projected distance) knot of radio emission. There is also a possible lobe to the south−west that is below the flux limit of FIRST. The association is based on the fact that the second emission region is close to the host galaxy and there is no optical

source at or in the vicinity of the extended emission. The sources that had only two emission regions turned out to be the most numerous, and most were associated in this fashion. In Figure 3.5b we show the radio map of SDSS J122011.89+020342.2. Here the association is based on the physical connection of several emission knots in the eastern jet to the core-source, and to a somewhat distant ($\sim$ 275 kpc projected distance) faint lobe to the west. In Figure 3.5c we show the radio map of SDSS J132834.14-012917.6. The association is based on the alignment of the very distant lobes (both are $\sim$ 500 kpc projected distance) with the radio core emission along with clear trails of radio emission back to the core. There are several variations of this type, such as those having small bending angles (usually less than $\sim 15^{\circ}$) between the distant lobes, as shown in Figure 3.5d. In Figure 3.5e we show the radio map of SDSS J091401.76+050750.6. The association is based on the distant southern lobe ($\sim$ 400 kpc projected distance) having a hot spot and lobe emission structure that points back to the core radio emission. This object may in fact have an additional lobe source to the north that is just outside of the image. However, this was not added to the total radio emission due to the fact that association at that distance is not guaranteed without the other criteria being met. In this case, the exclusion of this 'could-be lobe' has very little effect on the conclusions due to the fact that it is very dim and the added emission would have been only 4% of the total. After visual inspection of all possible matches, we find that all AGNs with 3 or more radio sources

outside 4″, but inside 60″, are all positively associated when the search is done using the original radio core sources.

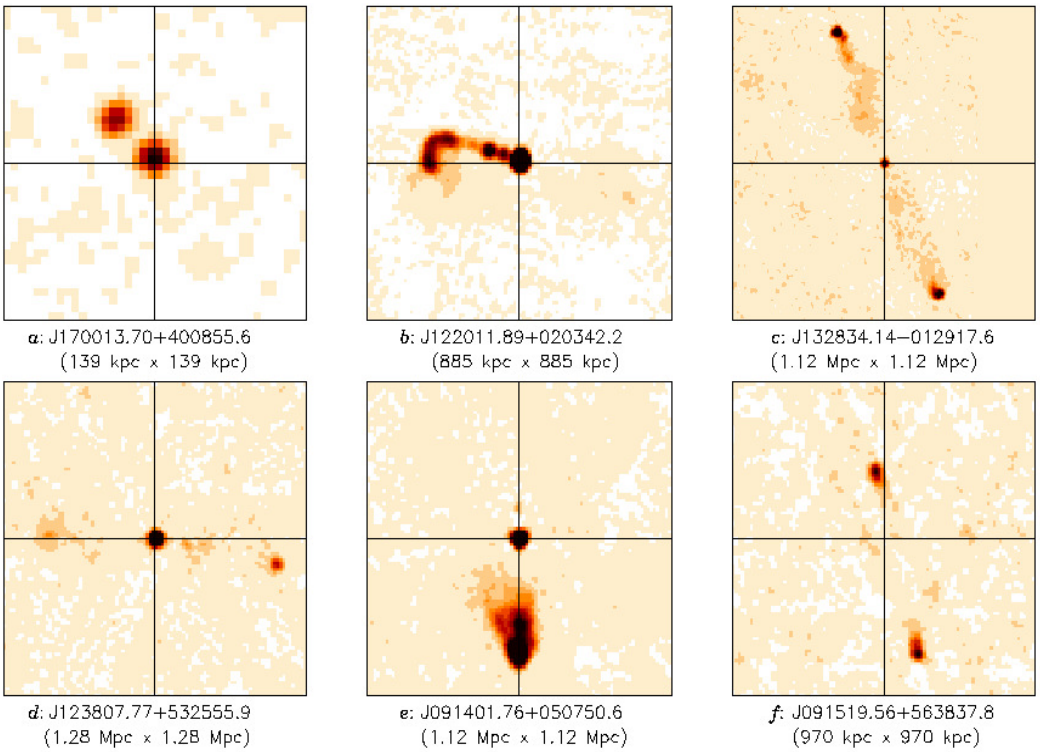


FIGURE 3.5: Images of FIRST extended sources with the optical source at the center of each frame, north is up and east is to the left. The SDSS name and projected physical size is given beneath each image. **a:** The 1.2′× 1.2′ image shows a double source with one component on the optical core and one offset from it. **b:** The 3.0′× 3.0′ image has a strong jet and lobe to the east and a weaker lobe to the west. **c:** The 6.0′× 6.0′ image shows a giant FR II where the lobe to the NE is aligned with the radio core and lobe to the SW. **d:** The 3.0′× 3.0′ image shows a distant lobe to the east, a radio core, and a lobe to the west slightly misaligned. **e:** The 3.0′× 3.0′ image shows a giant radio lobe with multiple sources to the south that all point back to the radio core. Not shown in this image is a more distant and slightly misaligned source to the north that may be an associated lobe, but with very low flux. **f:** The 3.0′× 3.0′ image shows two lobes that are roughly aligned with the optical center, but with no detected radio core.

We find 51 (6% of the original radio core emission sample and 0.6% of the total sample) AGN with extended emission that must be taken into account when calcu-

lating the total AGN radio luminosity. Of these 51, we find varying ranges in the amount of extra emission that is picked up. Some objects have a brighter core and one dimmer lobe ($\sim$10%-50% in added radio emission), but we also find huge, bright FR IIs that have total integrated fluxes in the 1000 mJy range (100%-6000% in added radio emission). In order to characterize the amount of flux added due to extended emission, we show in Figure 3.6 the fraction of extended flux added with respect to the initial core emission. About half of the sources lie in the 0.01 – 2 range, showing that nearly half of the sources add only a small fraction to twice of the core flux to the total, while the other half of the sample at least doubles the amount of flux added to the core, and the brightest source adds nearly 70 times more emission when compared to the core.

A second search was done using the entire optical sample to find possible FR II types in which radio emission is only seen from lobes but there is weak (below the 1 mJy flux limit of FIRST) or no core radio emission. The largest group found in this search has just one single radio source that is within 60″. After visual inspection, usually there was another optical sources at the extended radio source. Even when there is no such alternative optical identification it is not possible to claim an association since there is no discernible jet to lobe connection or double lobe symmetry that would be excellent indications of association. Most of these were rejected outright. We do however find an additional 12 objects (these are not included in the 51 AGN discussed above) that have significant flux inside the 60″ search radius but no core

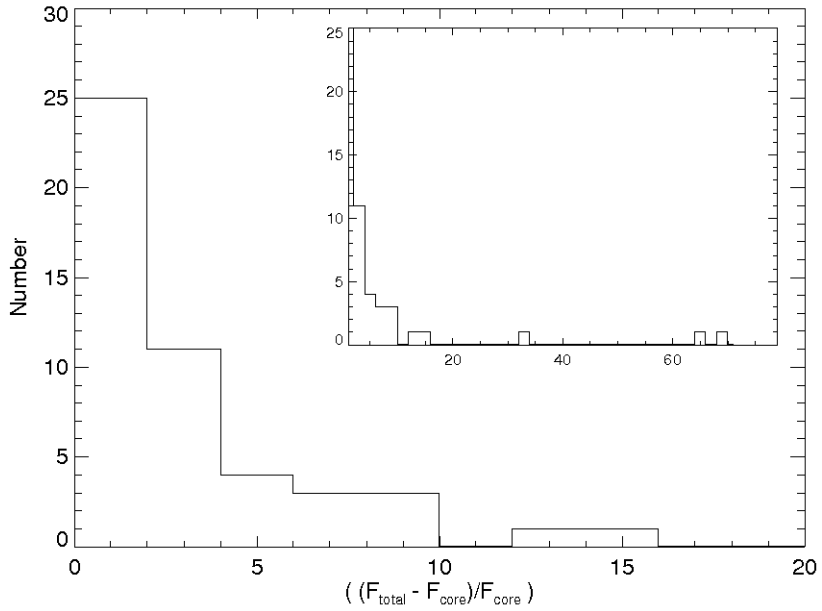


FIGURE 3.6: Histogram characterizing the amount of extended radio flux detected for the 51 multi-components sources with core emission. Nearly half (25) of the sources add only a fraction and up to two times the core flux. The inset shows that the largest increase in total flux due to extended emission is nearly 70 times the core flux.

emission inside 4″ that can be positively associated with the optical source. All of these were visually inspected to ensure that the radio emission was not associated with another optical source in the field and that any emission out past 60″ was taken into account and added by hand to the total radio flux. The criteria for establishing association for these objects is the alignment of emission out past 4″ with the optical source (having no radio core), as shown in Figure 3.5f for SDSS J091519.56+563837.8. We do note that any sources with radio lobes that have significant bending angles would not satisfy our alignment criteria, and some sources may be excluded due to this effect.

Table B.2 lists the SDSS name of all 63 AGN with extended radio emission along with their redshifts, projected physical extent and a 'by eye' classification of the radio morphology based on FIRST images. There are 22 sources with no previous radio identification in the NASA extragalactic database (NED) from other radio surveys and they therefore have no radio catalogue source name in Table 1. The radio classification column makes use of the 'giant radio galaxy' (GRG) classification, where the total projected linear extent exceeds 750 kpc (Saripalli & Subrahmanyan 2009 and references therein), and the hybrid morphology radio sources (HYMORS) classification, where an FR II lobe is seen on one side and an FR I jet is seen on the other side of the central source (Gopal-Krishna & Wiita 2000). We also classify X-shaped radio sources (e.g., Gopal-Krishna et al. 2003), where a possible reorientation of the jets has taken place to feed two individual sets of lobes, and the double-double morphology where interruption of the jets can cause two distinct sets of lobes to form throughout the lifetime of the AGN, where the first and older set is at a larger distance than the second, younger pair (e.g., Schoenmakers et al. 2000). We summarize these results here in Table 3.1.

Table 3.1: Summary of Morphologies for the Extended Radio Sample

| **Radio Morphology** | **Number** |
|---|---|
| FR I | 10 |
| FR II | 25 |
| FR II/GRG | 6 |
| DDRG | 2 |
| X−shaped | 1 |
| HYMORS | 2 |
| Indeterminate | 17 |

We use the usual flux-luminosity relation with the same cosmology used by Greene & Ho (2007) from Spergel et al. (2003) ($H_0 = 71$ km s$^{-1}$ Mpc$^{-1}$, $\Omega_m = 0.27$, and $\Omega_\Lambda = 0.73$) to calculate the total radio luminosity for each source. From these new data, we update the $\mathcal{R}$ values of the radio detected sample of Chapter 3.2, including all associated extended emission.

### 3.3.1 Sample Subsets Using the Extended and Core-only Sources

We again break this sample into subsamples as described in Chapter 3.2. We make use of the 'detected sample' which consists of all the AGN with radio emission and contains the core-only sources and the extended sources. The 63 extended sources are all RL (i.e., all have $\mathcal{R} > 10$) with the exception of one ($\mathcal{R} = 2.39$) that is a face-on spiral galaxy (SDSS J220233.84-073225.0) with a modest $L_{H\alpha} = 10^{42.01}$ ergs s$^{-1}$, but a very low flux radio core ($F_{int} = 2.36$ mJy) and an even fainter 'lobe' ($F_{int} = 0.97$ mJy) offset by $10.5''$. We find that of the 793 remaining core-only sources, 383 are RL and 410 are RQ based on $\mathcal{R}$. We also use the 'flux limited sample' which is explicitly defined in Chapter 3.2 and has 5485 total objects, using an upper limit of 1 mJy at 1.4 GHz for all AGN without radio detections as an optical flux cutoff. With extended emission taken into account for the flux limited sample we find that 4.9% (270/5485) of the AGN are RL, compared to the 4.7% (259/5485) found when extended emission was not taken into account.

– 4 –

# Analysis of the Core-only Sample

In this chapter we show our analysis based on different subsamples. The detected sample is useful when plotting $\mathcal{R}$ as a function of $M_{BH}$ and $L_{bol}/L_{Edd}$, since $\mathcal{R}$ is uniquely determined for all AGN in this subsample. It is however highly biased when calculating the radio-loud fraction (RLF), in that the number of RQ AGN is significantly underestimated due to the FIRST flux limit. The flux limited sample is not as affected by this bias since many of the RQ AGN still make the optical flux cut and remain in the subsample, and is therefore used to determine the RLF. The statistical errors in the RLF plots are calculated from Poisson statistics.

## 4.1 Radio Loudness Results

Figure 4.1 shows a histogram of the radio-loudness, $\mathcal{R}$. The solid line is for all 846 AGN detected with the FIRST survey. The dashed line in Figure 4.1 shows the total sample with upper limits on $\mathcal{R}$ calculated for all AGN undetected by FIRST. The insert shows the peak of the total sample. In both histograms there is a smooth distribution about $\log(\mathcal{R}) \approx 0.9$ and no clear evidence for two distinct populations. The dashed line histogram is an upper limit and could always move farther to the left in Figure 4 as indicated by the arrows, since all these objects have an upper limit of 1 mJy for their radio fluxes. However, to actually see a bimodal distribution, the upper limit histogram peak would have to shift very far to the left, with the peak moving at least an order of magnitude or more. Neither the detected nor upper limit

histogram shows a double peak profile, indicating a continuous distribution from RL to RQ in this sample. We note that 51% of the AGN in the detected sample are RL, using the $\mathcal{R} = 10$ boundary, but this number is extremely biased, in that $\sim 90\%$ of our total sample was below the FIRST detection limit and therefore were mostly RQ.

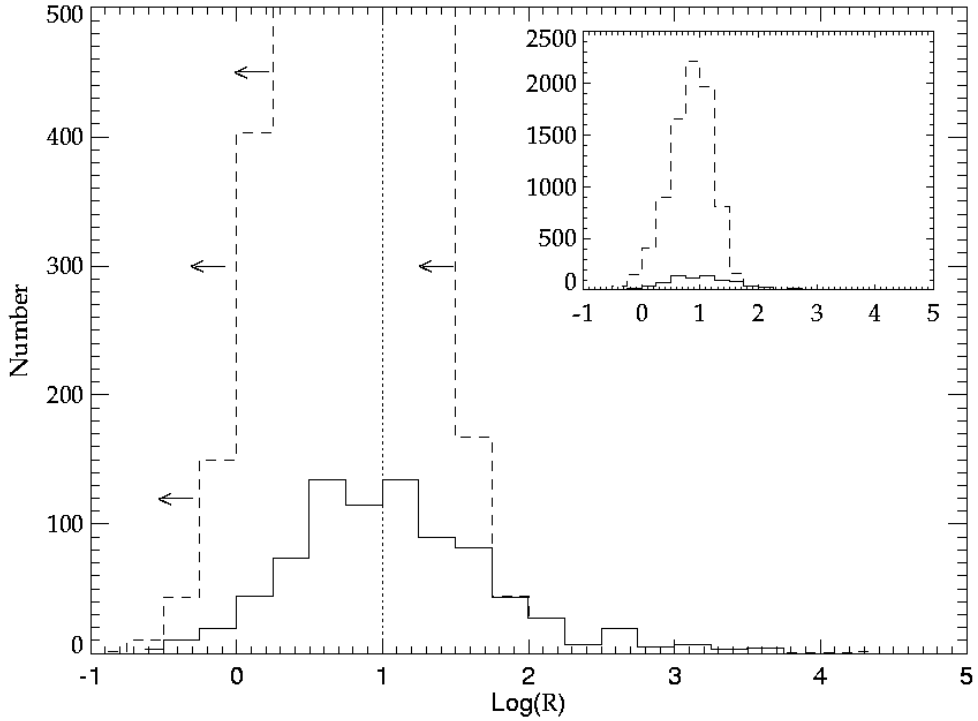


FIGURE 4.1: Radio-loudness ($\mathcal{R}$) histogram: the solid line is for the 846 objects in the detected subsample and the dashed line is a cumulative upper limit for the entire sample using a FIRST flux limit of 1 mJy at 5 GHz. The insert shows the peak of the upper limit histogram. Both peak at $\log(\mathcal{R}) \approx 0.9$.

The $\mathcal{R}$ histogram is shown in Figure 4.2 for the optically flux limited sample. The solid line is for all AGN above the optical flux limit and detected by the FIRST survey. The dashed line is for the total sample (undetected FIRST sources included) after

the optical flux limit is imposed, with the insert showing the peak. The sharp cut off at $\log(\mathcal{R}) = 1$ for the total sample is due to the flux limits imposed. In both cases there is still no evidence for bimodality in this sample. The peak for the flux limited histogram is at $\log(\mathcal{R}) \approx 0.75$. We find that 4.7% of the AGN in this subsample are RL. This percentage is similar to the roughly 5% - 10% that have been found in other studies based primarily on higher-redshift AGN (Kellermann et al. 1989; Urry & Padovani 1995).

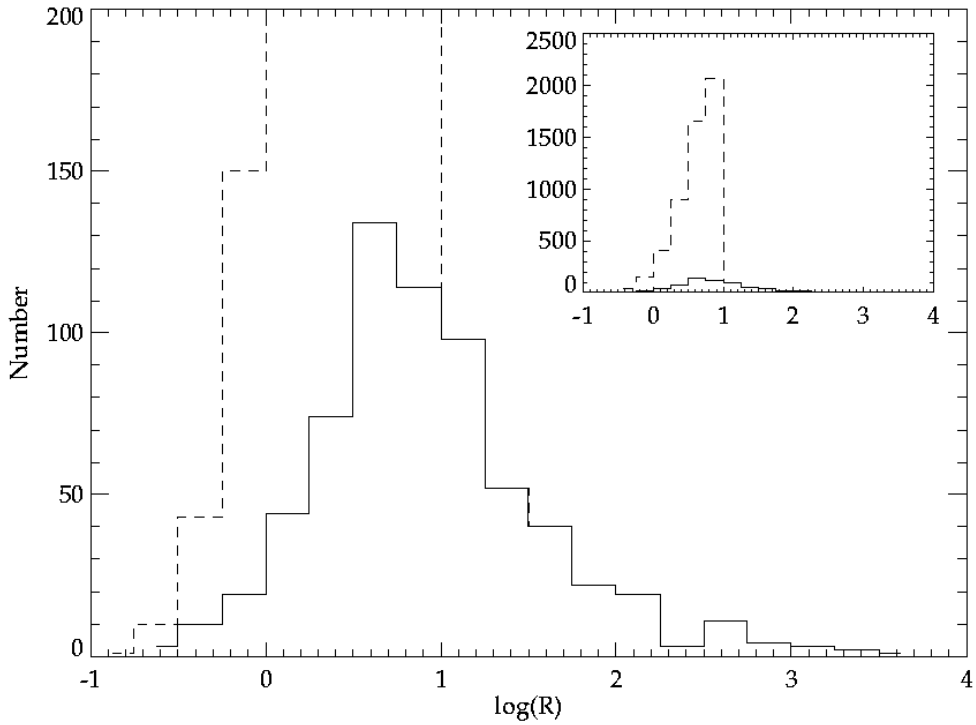


FIGURE 4.2: Flux limited Radio Loudness ($\mathcal{R}$) histogram: the solid line is for the AGN in the detected subsample after the optical flux limit is imposed and the dashed line is an upper limit for all AGN with the optical flux limit imposed. The insert shows the peak of the upper limit histogram.

The same plot is shown in Figure 4.3 for the stringently flux limited sample, with the insert showing the peak of the total sample. The cutoffs at $\log(\mathcal{R}) = 0$ and 2 are due to the limits imposed following Ivezić et al. (2002). The peak for the stringently flux limited sample is again at $\log(\mathcal{R}) \approx 0.75$. Including objects at higher and lower $\mathcal{R}$ values outside the flux cut prescription followed here does not shift the location of the peak or introduce a bimodal distribution with another peak at higher $\mathcal{R}$ values.

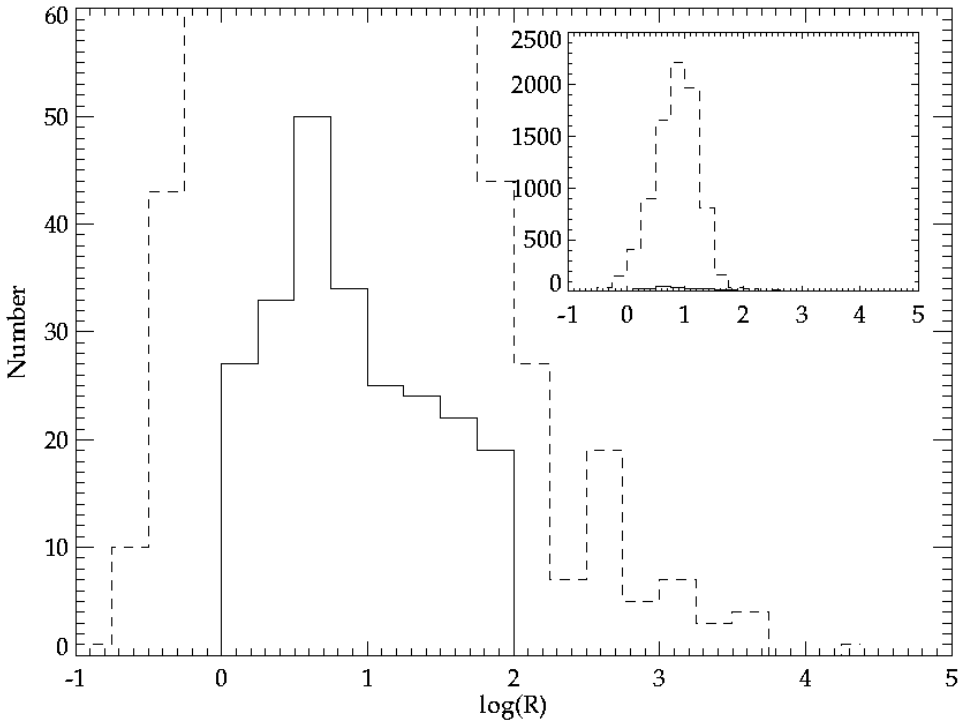


FIGURE 4.3: Stringently flux limited $\mathcal{R}$ histogram: the solid line is for the AGN in the stringently flux limited subsample and the dashed line is the upper limit from the total sample (same as in Figure 4.1). The insert shows the peak of the upper limit histogram.

## 4.2 Radio Loudness and Radio Luminosity Versus Black Hole Mass and Eddington Ratio

Figure 4.4 shows a plot of $\mathcal{R}$ as a function of $L_{bol}/L_{Edd}$ for the detected sample. There are no AGN with $\log(L_{bol}/L_{Edd}) < -2.8$ due to the SDSS limiting magnitude. Although there are broad distributions in both properties, there is a scarcity of AGN in the high accretion rate, high $\mathcal{R}$ regime, and also in the low accretion rate, low $\mathcal{R}$ regime, which is consistent with previous studies that find a global trend of decreasing radio-loudness with increasing Eddington ratio (Ho 2002; Nagar et al. 2005; Sikora et al. 2007). We do note however that we do not cover nearly as much parameter space as Sikora et al. (2007) who get up to an $\mathcal{R}$ of $\sim 10^7$ and down to an $L_{bol}/L_{Edd}$ of $\sim 10^{-7}$. Our sample does not go down to the very low $L_{bol}/L_{Edd}$ values due to the SDSS flux limit. However, Figure 4.4 does not show two distinct populations of AGN at a given Eddington ratio as found in Sikora et al. (2007). The two distinct populations in that paper at intermediate Eddington ratio values (0.01 – 0.1) likely represent the upper radio-loudness limits of two separate populations, with the upper population consisting of BLRGs hosted by giant elliptical galaxies with $M_{BH} > 10^8$ $M_\odot$, and the lower mostly being the most radio-loud Seyferts, hosted by spiral galaxies, and with $M_{BH} < 10^8$ $M_\odot$. Instead we find a continuous distribution from RQ to RL where the radio intermediate (RI) objects ($\log(\mathcal{R}) \approx 1$) are the most numerous.

Figure 4.5 shows a plot of the 1.4 GHz radio luminosity as a function of $L_{bol}/L_{Edd}$. The crosses are objects that are RL (defined by $\mathcal{R} > 10$) and the diamonds are objects that are RQ ($\mathcal{R} < 10$). There is significant overlap in the RL/RQ populations around

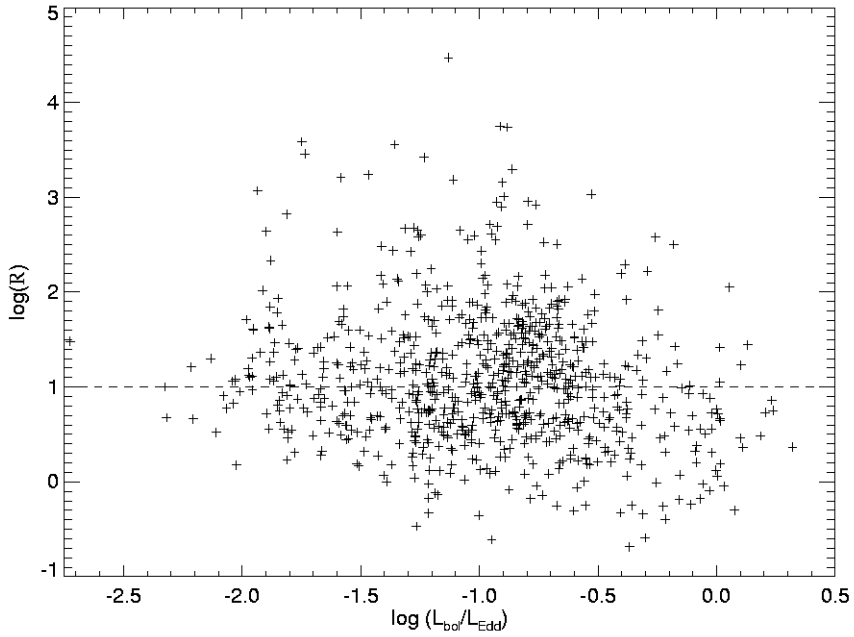


FIGURE 4.4: $\mathcal{R}$ vs $L_{bol}/L_{Edd}$. The dashed line shows the division between RL and RQ. There are clearly a lack of points in both the lower left and upper right of this plot, indicating the paucity of RL AGN that have high accretion rates and of RQ AGN that have low accretion rates.

$L_\nu(1.4\ \mathrm{GHz}) = 10^{23}$ Watts $\mathrm{Hz}^{-1}$, which has previously been used as an alternative division line between RL and RQ sources (e.g., Best et al. 2005). We find that 20% of the objects that have $L_\nu(1.4\ \mathrm{GHz}) > 10^{23}$ Watts $\mathrm{Hz}^{-1}$ are classified as RQ by $\mathcal{R}$, and that 13% of those that have $L_\nu(1.4\ \mathrm{GHz}) < 10^{23}$ Watts $\mathrm{Hz}^{-1}$ are classified as RL by $\mathcal{R}$. No obvious trends exist in Figure 4.5, but it clearly shows the ambiguity that can be involved when these two different definitions of RL and RQ are used.

In Figure 4.6, we show the radio-loud fraction (RLF) as a function of $\log(L_{bol}/L_{Edd})$ for the optically flux limited sample with assumed upper limits. The RLF is the ratio of the number of RL objects to the total number of AGN and is plotted in bins of 0.25 dex. Although the trend is mostly flat over a range of Eddington ratio, the global

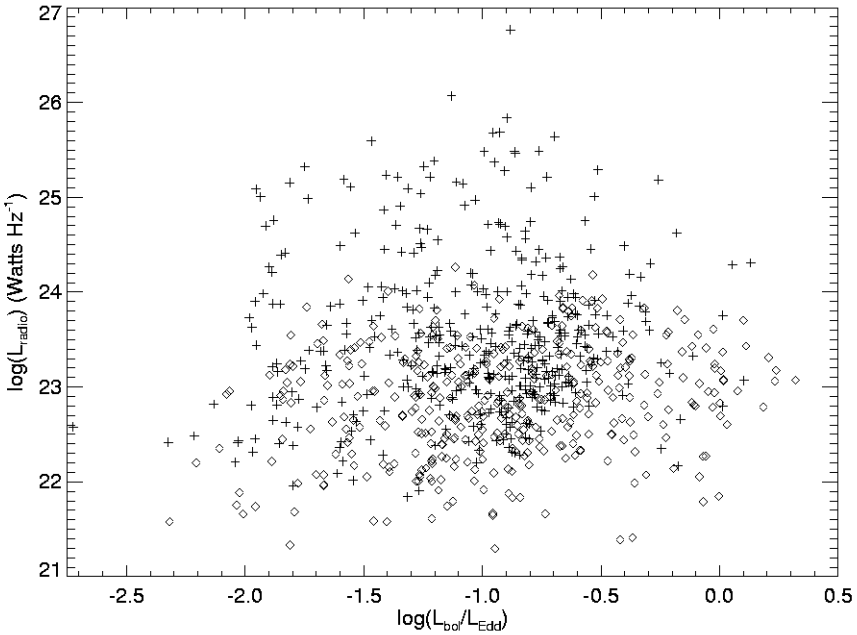


FIGURE 4.5: $L_{1.4GHz}$ vs $L_{bol}/L_{Edd}$. The crosses have $\mathcal{R} > 10$ and the diamonds have $\mathcal{R} < 10$.

trend is that the RLF decreases from ∼13% to ∼2% with increasing Eddington ratio in a manner similar to that found in the previous studies mentioned above. The stringently flux limited sample shows a similar trend, but with a much higher overall RLF in each bin due to the flux limits cutting out all of the RQ objects with upper limits on $\mathcal{R}$.

In some studies of AGN at higher luminosities, the degree of radio-loudness was suggested to be dependent on $M_{BH}$, where RL quasars are typically found to have $M_{BH} > 10^8$ $M_\odot$ (Laor 2000; McLure & Jarvis 2004). Figure 4.7 shows a plot of $\mathcal{R}$ vs $M_{BH}$ for our detected subsample. We find a significant number of RL AGN with $M_{BH} < 10^8$ $M_\odot$, showing that this is not always the case. We find that 367 (53%) of the objects with $M_{BH} < 10^8$ $M_\odot$ are RL, compared to 55 (40%) of the objects with

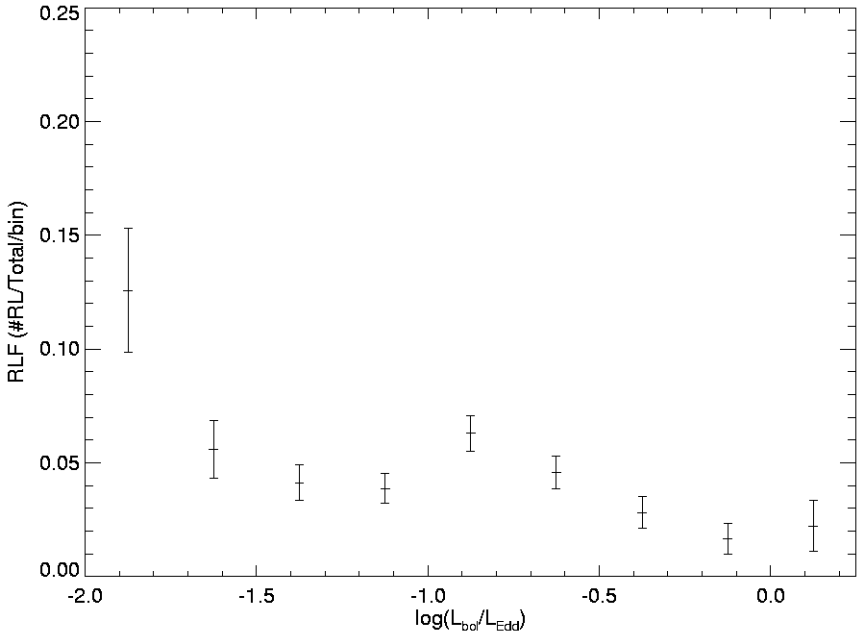


FIGURE 4.6: Radio-loud fraction (RLF) for the optically flux limited sample as a function of $L_{bol}/L_{Edd}$ in bins of 0.25 dex. Error bars are found from a Poisson distribution reduced $\chi^2$ procedure.

$M_{BH} > 10^8$ $M_\odot$ that are RL. Figure 4.7 shows that 11 AGN with $M_{BH} < 10^8$ $M_\odot$ are extremely RL ($\log(\mathcal{R}) > 3$). These outliers do not result from underestimating their H$\alpha$ (and hence continuum) fluxes. Their radio fluxes are truly high, in the range 136 mJy to 1213 mJy, whereas their H$\alpha$ fluxes have a distribution similar to that of the entire sample.

Figures 4.8 & 4.9 show the $\mathcal{R}$ distribution for the high and low mass populations for the detected and flux limited subsamples, respectively. In these figures the solid lines are for the higher mass population and the dashed lines are for the lower mass population. Both distributions cover the same range and peak in about the same place. A K-S test shows that two samples drawn from the same population would

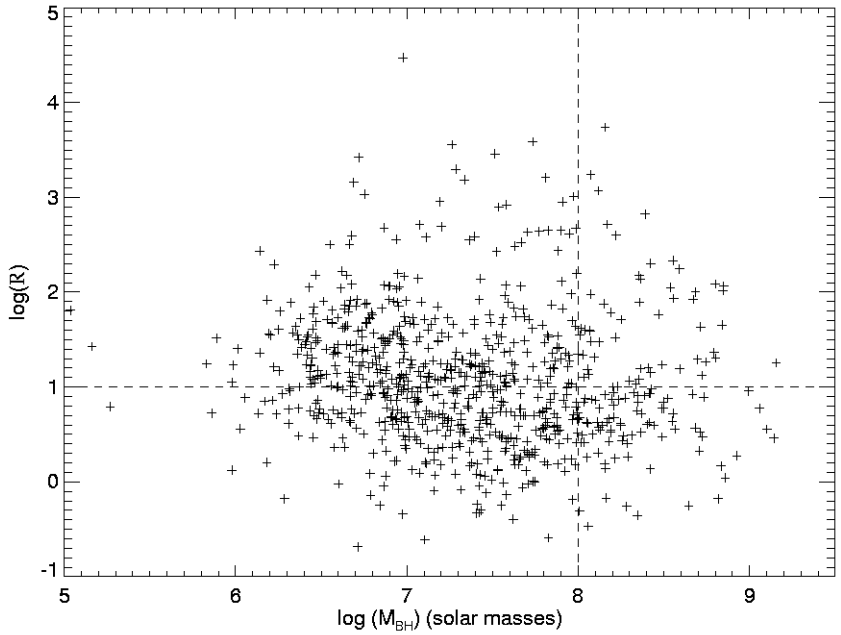


FIGURE 4.7: $\mathcal{R}$ vs $M_{BH}$: The horizontal dashed line is the division between RL and RQ. The vertical line is the 'conventional' separation line between more massive ($M_{BH} > 10^8$ $M_\odot$) and less massive ($M_{BH} < 10^8$ $M_\odot$) black holes. We find 367 AGN with $M_{BH} < 10^8$ $M_\odot$.

differ this much 56% of the time for the detected sample and 84% of the time for the flux limited sample, indicating that the two distributions are not statistically different. This is consistent with the findings of Woo & Urry (2002) and Ho (2002) that radio-loudness is not intrinsically dependent on $M_{BH}$.

Figure 4.10 shows the RLF as a function of $M_{BH}$, for the optically flux limited subsample. The RLF here is the ratio of the number of RL AGN to the total number of AGN in mass bins of $\log(M_{BH}) = 0.5$. The distribution is essentially flat at the low mass end although there is evidence for an increase in the highest mass bin.

In Figure 4.11 we show $L_\nu$(1.4 GHz) as a function of $M_{BH}$ with the symbols the same as those in Figure 8. As in Figure 8 we see a lot of overlap between the RL and

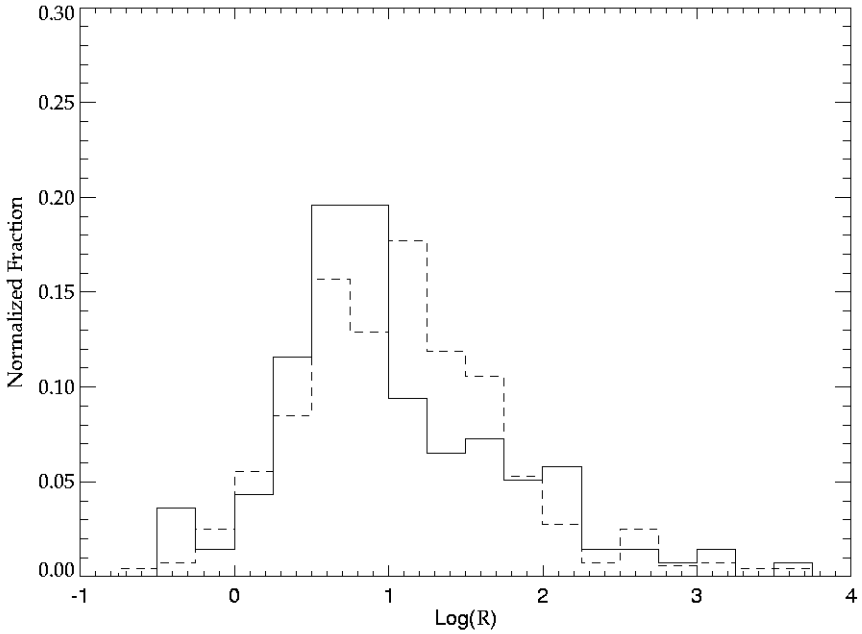


FIGURE 4.8: Histogram of the $\mathcal{R}$ distribution of the high mass ($M_{BH} > 10^8 M_\odot$, solid line) and the low mass ($M_{BH} < 10^8 M_\odot$, dashed line) AGN for the detected sample. The two populations have a K-S value of 0.555.

RQ AGN, as defined by $\mathcal{R}$ around $L_\nu(1.4\ \mathrm{GHz}) = 10^{23}$ Watts $\mathrm{Hz}^{-1}$. This figure is more ordered than Figure 4.9 in that there are a paucity of points in the low (high) $L_{1.4\mathrm{GHz}}$, high (low) $M_{BH}$ range. Thus, the most powerful radio-core sources tend to have higher black hole masses, but we find little evidence that the radio-loudness depends strongly on mass.

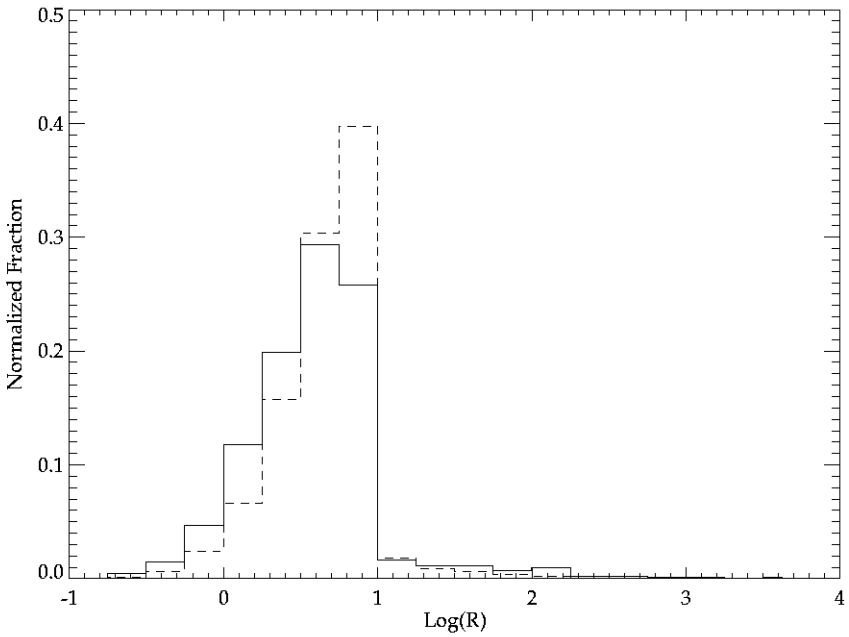


FIGURE 4.9: Histogram of the $\mathcal{R}$ distribution of the high mass ($M_{BH} > 10^8$ $M_\odot$, solid line) and the low mass ($M_{BH} < 10^8$ $M_\odot$, dashed line) AGN for the flux limited sample. The two populations have a K-S value of 0.841.

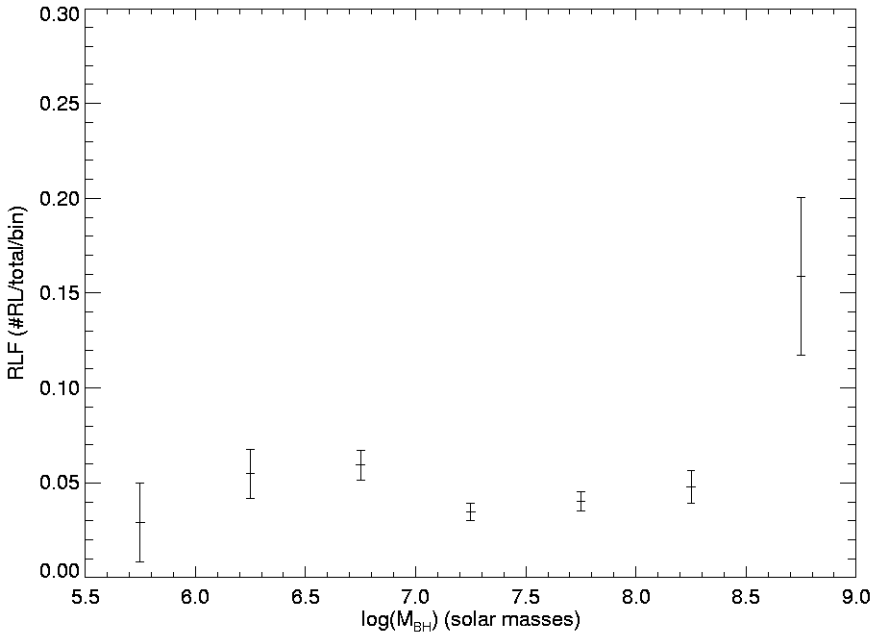


FIGURE 4.10: Radio-loud fraction (RLF) for the flux limited sample as a function of $M_{BH}$ in bins of 0.5 dex.

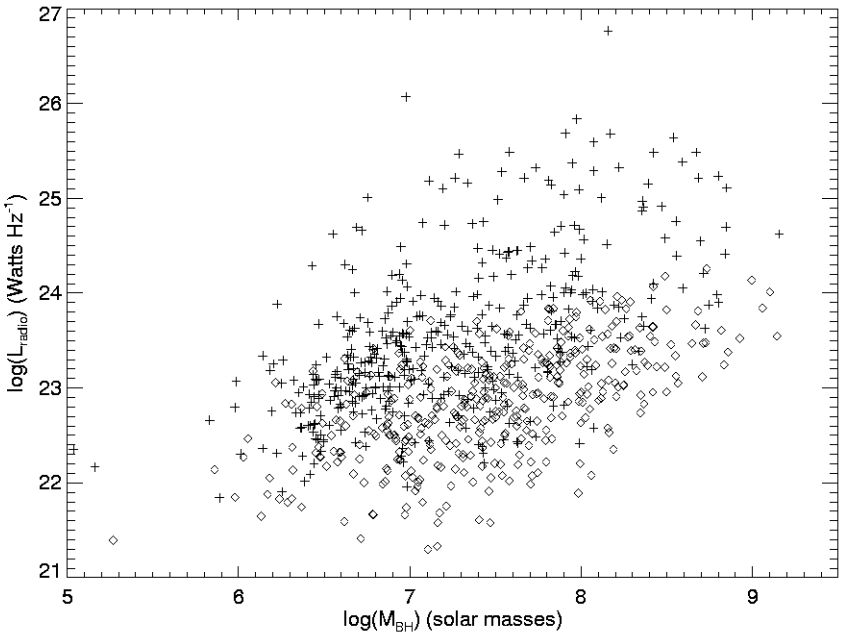


FIGURE 4.11: $L_{1.4GHz}$ vs. $M_{BH}$. The crosses have $\mathcal{R} > 10$ and the diamonds have $\mathcal{R} < 10$.

– 5 –

# Analysis of the Extended Sample

## 5.1 Radio Loudness and Radio Luminosity

In order to determine how the extended sources differ from the rest of the sample we first compare the optical properties of the different subsets, namely the core-only sources, the extended sources and the total flux limited sample. In Figure 5.1 we show the FWHM distributions of the broad component of the H$\alpha$ line ($\mathrm{FWHM_{H\alpha}}$) for the extended, core-only, and non-radio detected sources in the flux limited sample, where all are normalized by the number in each group. The extended source distribution has an average FWHM of 5010 km $\mathrm{s^{-1}}$, the core-only sources have an average FWHM of 3550 km $\mathrm{s^{-1}}$, and the undetected sources in the flux limited sample have an average FWHM of 3242 km $\mathrm{s^{-1}}$. The peak of the distribution for the extended sources is at $\sim$ 4500 km $\mathrm{s^{-1}}$ and is shifted to higher FWHM values by about 2000 km $\mathrm{s^{-1}}$ when compared to the core-only sources and undetected flux limited sources, which peak at $\sim$ 2500 km $\mathrm{s^{-1}}$. Both histograms have long tails that fall off at about the same rate toward higher FWHMs. A K-S test between the core-only source distribution and the extended source distribution yields a probability value of 1.2 $\times 10^{-5}$ and a maximum difference of 0.35, showing that it is extremely likely these two distributions are from different parent populations. A K-S test between the core-only sources and the non-radio detected sources yields a probability value of 0.077 and a maximum difference of 0.05, meaning that the two have similar enough cumulative distribution

functions that they may well be from the same parent population. Many (22/63 = 35%) of the extended AGN have the broadest H$\alpha$ profiles (FWHM $>$ 5000 km s$^{-1}$). This is consistent with the claim that most high redshift BLRGs have intrinsically large $M_{BH}$ (Laor 2003; Dunlop et al. 2003; Chiaberge et al. 2005). This result for high redshift AGN may be linked to a Malmquist bias of selecting the most luminous sources, as this result is favored when calculating $M_{BH}$ based on single epoch $M_{BH}$ relations, where $M_{BH} \propto FWHM^2$; however a large $M_{BH}$ determination is not always guaranteed, since this relation also depends on the optical luminosity of the central source ($M_{BH} \propto FWHM^2 L^{0.5}$).

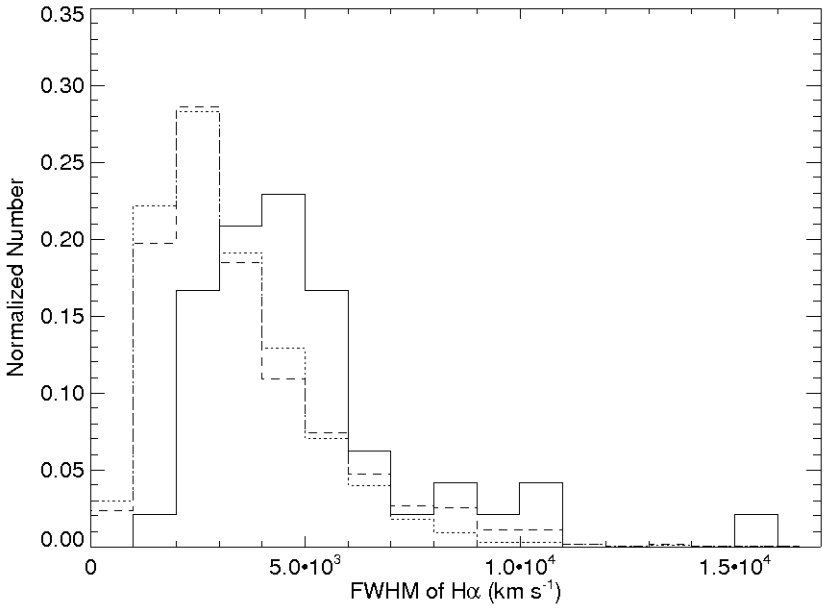


FIGURE 5.1: $FWHM_{H\alpha}$ histogram: the solid line is for the extended sources, the dashed line is for the core-only sources, and the dotted line is for the non-radio detected sources in the flux limited sample. The extended source distribution is shifted to higher values by $\sim$ 2000 km s$^{-1}$ compared to the core-only and flux limited samples.

The next optical property we compare between the radio types is the H$\alpha$ luminosity ($\propto$ $L_{5100}$). The histogram in Figure 5.2 shows the normalized distributions for the extended, core-only, and non-radio detected sources in the flux limited sample. We find that the extended source distribution is slightly shifted to higher $L_{H\alpha}$ by about 0.5 dex when compared to the core-only distribution, but overall the full distributions have similar peak values and show significant overlap. More precisely, the extended sources have an average $L_{H\alpha} = 10^{42.7}$ ergs $s^{-1}$ with a standard deviation of 0.60 dex, and the core-only sources have an average $L_{H\alpha} = 10^{42.3}$ ergs $s^{-1}$ with a standard deviation of 0.68 dex. A K-S test comparing the extended sources and the core-only sources yields a probability value of 1.4 $\times 10^{-4}$ and a maximum difference of 0.32 indicating that these two distributions may well be from different parent populations. In the context of $M_{BH}$ determinations, somewhat similar $L_{H\alpha}$ distributions but systematically higher FWHM distributions should give larger $M_{BH}$ estimates for the extended AGN when compared to the core-only sources. This turns out not to always be the case, since our extended sample has 36 sources with $M_{BH} < 10^8$ $M_\odot$ and 27 sources have $M_{BH} > 10^8$ $M_\odot$.

The normalized distribution of 1.4 GHz radio luminosity ($L_{1.4GHz}$) is shown in Figure 5.3 for the flux limited sample. The peak of the extended sources is shifted to higher luminosities by a factor of 100 when compared to the core-only sources. This is not surprising given the high luminosities of FR II lobes. Looking at the region of overlap we find that there are few sources in these normalized distributions

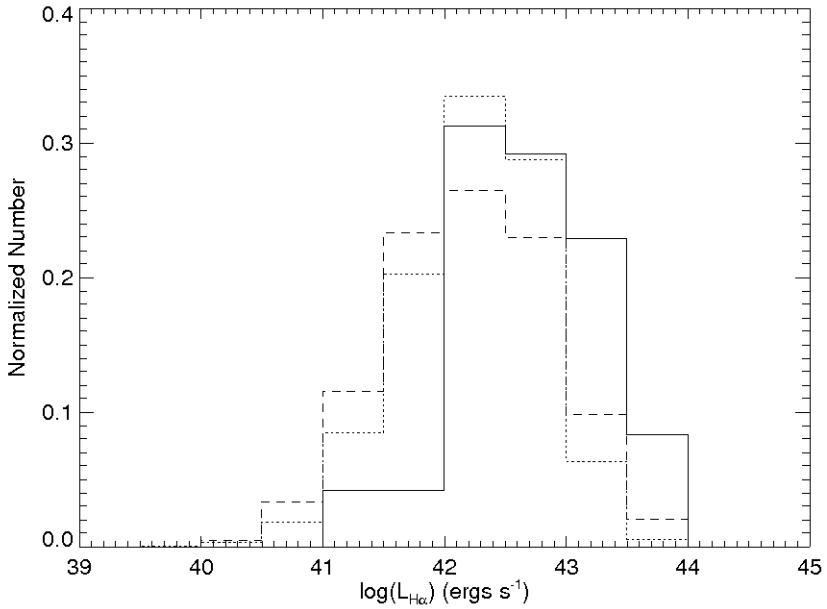


FIGURE 5.2: $L_{H\alpha}$ histogram: the solid line is for the extended sources, the dashed line is for the core-only sources, and the dotted line is for the non-radio detected sources in the flux limited sample. The distributions have similar shapes, peak values, and show significant overlap at luminosities greater than $10^{42}$ ergs $s^{-1}$.

in the $10^{24.5}$ Watts $Hz^{-1}$ region, where the deficit of sources is at the FR I/FR II transition luminosity originally found by Fanaroff & Riley (1974); see also Kawakatu et al. (2009). This is important for the $\log(\mathcal{R})$ histogram shown in Figure 5.4. In the top plot we show the core-only and extended source histograms normalized by the number in each group. The normalization is useful since there are many fewer extended radio sources, making this trend in the unnormalized histogram not as obvious. Here we find what looks like two separate populations, or an apparent bimodality, in that the extended sources peak at $\log(\mathcal{R}) \approx 2.5$ whereas the core-only sources peak at about $\log(\mathcal{R}) \approx 0.75$. This can be explained by the fact that most of the extended sources have much higher radio luminosities compared to the core-only

sources, but not much higher H$\alpha$ luminosities, causing the shift of extended sources to higher log($\mathcal{R}$) values. This produces a bimodal distribution where the upper mode is comprised of RL objects ($\mathcal{R} > 10$) populated by only the extended sources whose distribution drops below log($\mathcal{R}$) = 1 only for the one RQ source mentioned above. The core-only distribution, however, goes well above and below the log($\mathcal{R}$) = 1, RL/RQ dividing line.

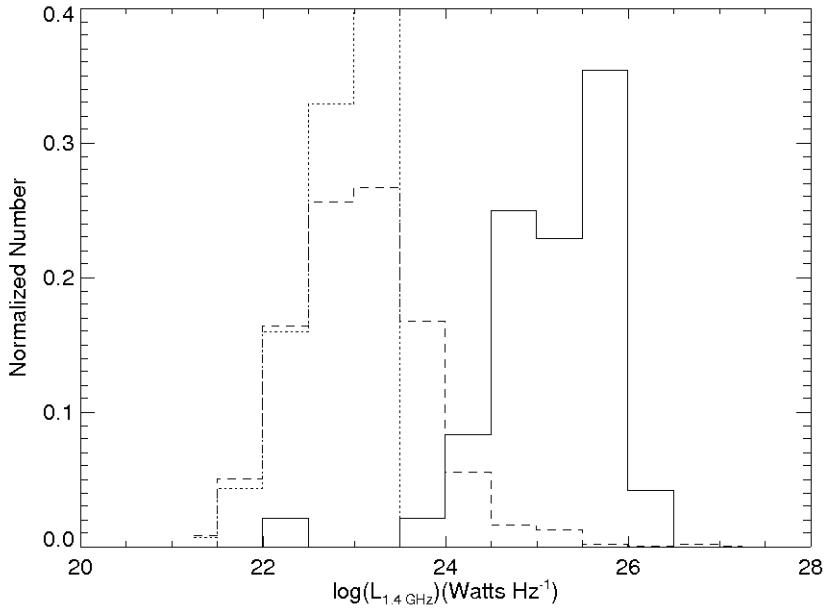


FIGURE 5.3: $L_{1.4\ \mathrm{GHz}}$ histogram: the solid line is for the extended sources, the dashed line is for the core-only sources, and the dotted line is for the full optical sample. The sharp drop off of the dotted line at $10^{23.5}$ Watts Hz$^{-1}$ is due to normalization and it does not actually go to zero. The relative lack of sources at $10^{24.5}$ Watts Hz$^{-1}$ is a manifestation the FR I/FR II dividing line.

The bottom plot in Figure 5.4 shows the histogram of two different populations from the detected sample (core-only and extended sources) based on a radio luminosity dividing line. The value of the radio luminosity dividing line was found by

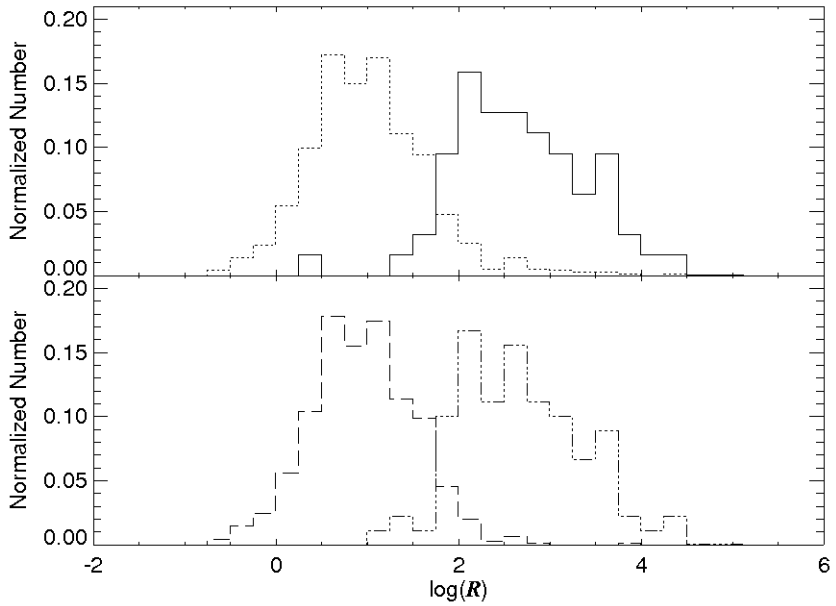


FIGURE 5.4: log($\mathcal{R}$) histogram: Top, the solid line is for the extended sources and the dotted line is for the core-only sources. Bottom, for the combined sample of core-only and extended sources the dashed line is for objects with $L_{1.4\ GHz} < 10^{24.4}$ Watts $Hz^{-1}$ and represents a FR I-like population and the dot-dashed line is for objects with $L_{1.4\ GHz} > 10^{24.4}$ Watts $Hz^{-1}$ and represents a FR II-like population.

adjusting the break luminosity value until the lower histograms best matched the original core-only versus extended source histograms shown in the upper plot (based on K-S statistics given below), and was found to be $10^{24.4}$ Watts $Hz^{-1}$. It is interesting that the two sets of histograms are most similar when the break radio luminosity is nearly equal to that of the FR I/FR II transition luminosity. It is clear that the AGN with $L_r < 10^{24.4}$ Watts $Hz^{-1}$ have a log($\mathcal{R}$) distribution nearly identical to that of the core-only sources and the AGN with $L_r > 10^{24.4}$ Watts $Hz^{-1}$ have a log($\mathcal{R}$) distribution nearly identical to that of the extended sources. A K-S test comparing the extended sources in the top plot and the FR II-like distribution in the bottom

plot yield a probability value of 1.0 and a maximum difference of 0.04, showing that it is extremely unlikely that these two are from different parent populations. This is also found for the core-only and FR I-like distributions, which have a K-S probability value of 0.82 and a maximum difference of 0.03.

Therefore, in order to move away from the 'by eye' morphological classification schemes used to describe individual sources, we can in general use our extended sources as a proxy for the classic FR II objects, and the core-only sources as a proxy for the FR I sources based on a break radio luminosity that is consistent with the previous FR I/FR II dividing line. From this plot we also find that a $\log(\mathcal{R})$ value of $\approx 1.75$ is well suited to separate the FR Is from the FR IIs. The peak values of the $\mathcal{R}$ histogram are consistent with the bimodal distributions found by the previous studies of Ivezić et al. (2004) and Cirasuolo et al. (2004) who find peaks at $\log(\mathcal{R}) << 1$, and $\log(\mathcal{R}) \approx$ 2-3 using only the radio core sources out to higher redshifts, which may possess complex (extended) structure, but which would be unresolvable at the higher redshifts probed in these samples. Here we show that our two populations basically consist of the lower radio power FR Is (which could be young, unresolved or well aligned with the line-of-sight jets and/or lobes) and the higher radio power FR IIs, and that the $\mathcal{R}$ bimodality seen here is likely a manifestation of the FR I/FR II break originally found by Fanaroff & Riley (1974).

## 5.2 Radio Loudness Versus Black Hole Mass and Eddington Ratio

We plot $\log(\mathcal{R})$ vs $\log(L_{bol}/L_{Edd})$ in Figure 5.5 and see that while both the extended and core-only sources span a large range in Eddington ratio, we find a paucity of points in the high accretion rate, high $\log(\mathcal{R})$ regime, as well as the very low accretion rate, low $\log(\mathcal{R})$ regime, as was already seen in Chapter 4.2 and Sikora et al. (2007). We note again as in Chapter 4.2 that we do not cover nearly as much parameter space as did Sikora et al. (2007). Assuming the extended sources represent the FR II class, this would again be congruous with Sikora et al. (2007), who find giant ellipticals hosting FR II's to be a separate upper population, but we still find significant overlap between the lower and upper populations in this sample in the classic RL regime.

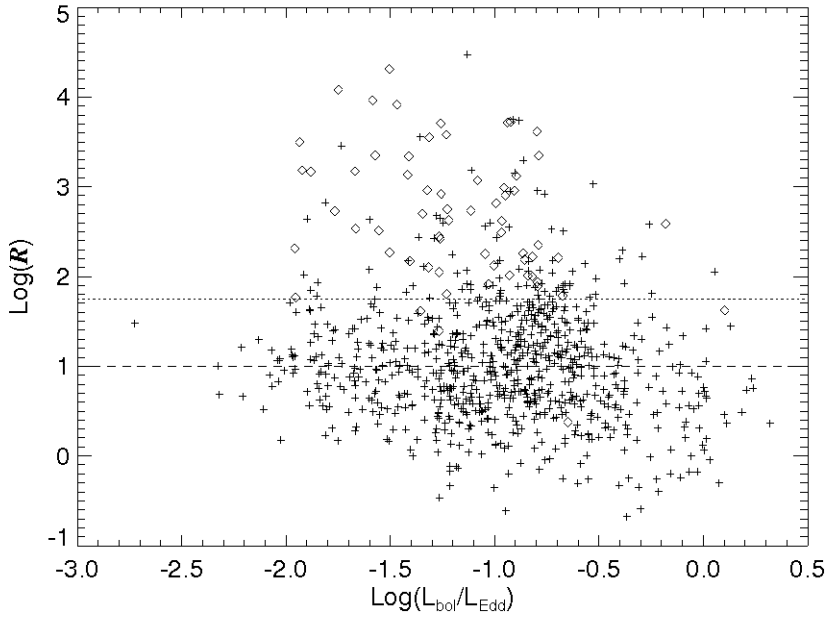


FIGURE 5.5: $\mathcal{R}$ vs $L_{bol}/L_{Edd}$: the diamonds are for the extended sources and the crosses are the core-only sources. The horizontal dashed line represents the conventional RL/RQ dividing line at $\log(\mathcal{R}) = 1$, and the dotted horizontal line shows our suggested division at $\log(\mathcal{R}) = 1.75$.

The radio-loud fraction (RLF) as a function of $\log(L_{bol}/L_{Edd})$ is shown in Figure 5.6 for the flux limited subsample. The error bars are found from a reduced $\chi^2$ procedure, assuming Poisson errors, and thus depend on the number of objects in each bin. When we compare this new plot to the one in Chapter 4.2 we find a slight increase of the RLF in the lowest Eddington ratio bin, although this increase is within the original error bars of Figure 4.6. We also find a modest trend of decreasing RLF with increasing $\log(L_{bol}/L_{Edd})$ that is not much different from Figure 4.6 and consistent with the studies of Ho (2002) and Sikora et al. (2007).

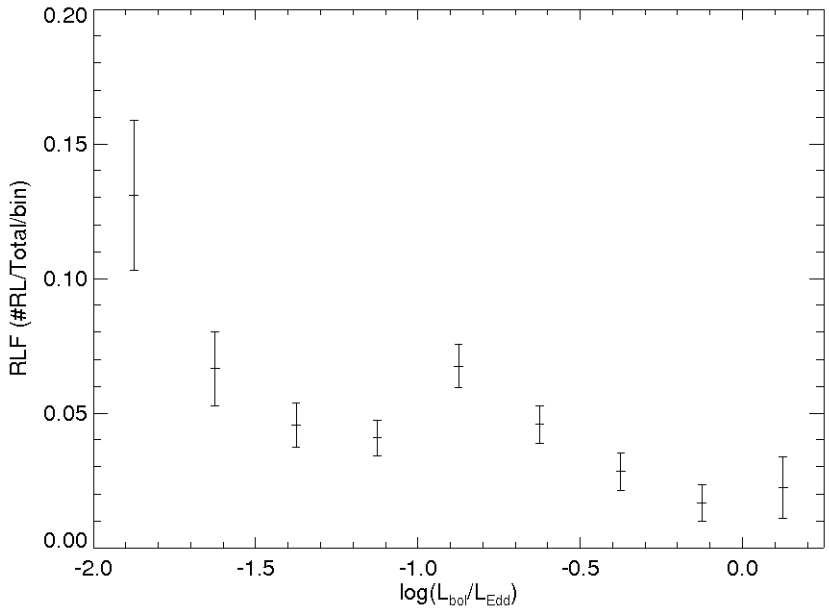


FIGURE 5.6: Radio-loud Fraction vs $L_{bol}/L_{Edd}$ for the flux limited sample where the error bars are from Poisson statistics. There is a modest trend of a decreasing RLF with increasing $L_{bol}/L_{Edd}$.

As noted in section 3, there are 27 extended sources with $M_{BH} > 10^8$ $M_\odot$ and 36 with $M_{BH} < 10^8$ $M_\odot$. The $\log(\mathcal{R})$ vs $M_{BH}$ plot in Figure 5.7 shows that we find

35 extended objects with $M_{BH} < 10^8$ $M_\odot$ that are RL and only one that is RQ (mentioned above). Again the extended sources populate the top of this plot but with some contribution from the core-only sources. The addition of extended sources has significantly raised the number of RL sources in this sample with $M_{BH} > 10^8$ $M_\odot$ from 55 as discussed in Chapter 4 to 63 in this analysis (it is only coincidence that this number matches the total number of extended sources).

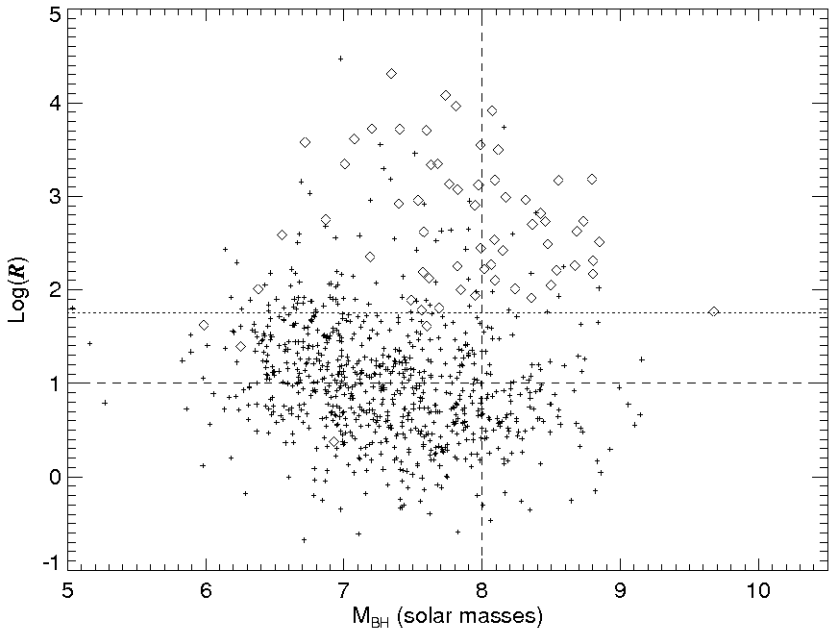


FIGURE 5.7: $\mathcal{R}$ vs $M_{BH}$: the diamonds are for the extended sources and the crosses are the core-only sources. The horizontal dashed line represents the conventional RL/RQ dividing line at $\log\mathcal{R} = 1$, while the dotted horizontal line our higher value. The vertical dashed line is separates the AGN with more massive ($M_{BH} > 10^8$ $M_\odot$) and less massive ($M_{BH} < 10^8$ $M_\odot$) BHs. For the extended sources, there are 36 with $M_{BH} < 10^8$ $M_\odot$ and 27 with $M_{BH} > 10^8$ $M_\odot$.

The RLF as a function of $M_{BH}$ is shown in Figure 5.8. It is mostly flat over 3 decades and hovers around 5% but rises sharply in the highest $M_{BH}$ bin. When we compare this to Figure 4.10 in Chapter 4.2 for the RLF of $M_{BH}$, we find that it is

largely unchanged. The RLF at low $M_{BH}$ is flat but nonzero ($\sim 5\%$ average), showing that RL AGN can be produced by less massive BHs. The sharp rise in the highest mass bin shows that AGN with the most massive BHs ($M_{BH} \geq 2 \times 10^8$ $M_\odot$) are 3 times more likely to be RL than those at lower masses (Laor 2003; Dunlop et al. 2003; Gopal-Krishna et al. 2008). In other words, while having a more massive BH is helpful, it is not the only requirement for producing strong radio emission.

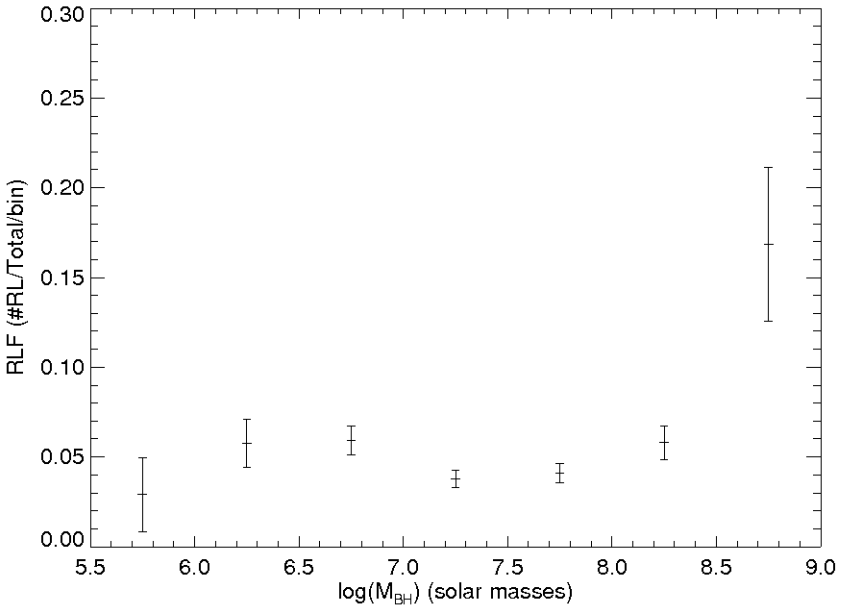


FIGURE 5.8: Radio-loud Fraction vs $M_{BH}$ for the flux limited sample where the error bars are from Poisson statistics. The RLF is mostly flat from $10^{5.5}$ $M_\odot$ up to $10^{8.5}$ $M_\odot$. The sharp rise in the highest $M_{BH}$ bin shows that it is 3 times more likely to produce strong radio emission for the most massive BHs, but it is not a requirement as the RLF elsewhere is never goes to zero.

# – 6 –

# Conclusion

## 6.1 Comparison of the Core-only and Extended Samples

We have taken 8434 optically selected BL AGN from the SDSS and estimated $M_{BH}$ and $L_{bol}/L_{Edd}$ for them. Using fluxes taken from the FIRST survey we compute $\mathcal{R}$, the radio-loudness parameter. Our original search, as described in Chapter 3.2, was for radio emission thought to be mostly from the core. We note that because of the resolution of the FIRST survey and our small search radius ($4''$), we missed AGN with extended radio structures that have very weak core emission. We note that ∼90% of all SDSS/FIRST matched AGN have only core radio emission (Ivezić et al. 2002), although because of the resolution limit of FIRST, many of these 'core' sources will include compact jets and lobes. Furthermore, the higher redshift samples with which we are comparing our results (White et al. 2000; Ivezić et al. 2002; Cirasuolo et al. 2004) are also based on core radio emission from FIRST.

The extended search, as described in Chapter 3.3, has a much larger search radius ($60''$) that allows us to identify associated radio emission that can reveal large scale, resolvable structure such as jets and lobes. At the sample redshift limit (z = 0.35) this corresponds to $\sim$ 1 Mpc, or roughly the size of the largest known radio galaxies. Of the 846 (10% of the total optical sample) objects that have core emission, 63 of those (0.8% of the total sample) have extended emission that must be taken into account when calculating the total radio luminosity. After morphological classification

of each individual source (see Table 2 or Appendix B) we find among them 6 giant radio galaxies, 2 HYMORs candidates, and 1 X-shaped radio galaxy. Since the overall optical properties of the sample do not change, when extended radio emission is taken in to account, they will not be discussed in detail here (see Chapter 2).

When extended emission is not taken into account we find that 4.7% of the sources are RL in the flux limited sample. Adding in the extended emission raises this to 4.9%, but it is not a significant increase since extended sources only account for 0.8% of the total sample. However both values are at the lower limit of the previously quoted values, i.e., that 5% – 10% of all AGN are RL (Kellermann et al. 1989; Urry & Padovani 1995; Ivezić et al. 2002; White et al. 2007). These results are at the lower limit of the expected values and this may be due to the fact that this is a low redshift sample, indicating that the radio luminosity function has a stronger evolution than the optical luminosity function to the current epoch, as suggested by Jiang et al. (2007).

When extended emission is not taken into account, the $\mathcal{R}$ distribution shows no evidence for a bimodal distribution for any of the sample subsets (Figures 4.1, 4.2, 4.3). We do note that the upper limit (dashed-line) histograms could be pushed farther to the left to reveal a bimodal distribution, but at much lower $\mathcal{R}$ values than previously found by Ivezić et al. (2004) and Cirasuolo et al. (2004), who find peaks at $\log(\mathcal{R}) \ll 1$, and $\log(\mathcal{R}) \approx 2$–3. In fact, based on Figure 4.1, there would have to be a large population of radio core-only AGNs with fluxes much less than 1 mJy,

since both distributions peak in the same place, at $\log(\mathcal{R}) \approx 0.75$. After we apply various flux limits to our total sample, we still cannot reproduce a local minimum at $\log(\mathcal{R}) \approx 1$. In all our subsamples we fill in a substantial number of radio-intermediate (RI) objects. The minimum in the $\mathcal{R}$ histogram could be shifted to lower values or could just not be present at all at these low redshifts. Nevertheless, we still see a RL tail. Compared to higher redshift samples, the $\mathcal{R}$ distribution in the local universe for detected sources is narrower and shifted to lower values (Ivezić et al. 2004; White et al. 2007). Again this result and the lack of bimodality may indicate a stronger evolution of the radio luminosity function than the optical luminosity function to the current epoch.

With extended emission taken into account, we find evidence for a distinct population of RL AGN that is separate from the RL core-only sources. We find that most of the extended AGNs in this low redshift sample are FR IIs based on radio morphology and luminosity, using the same FR I/FR II break luminosity defined by Fanaroff & Riley (1974). We find a bimodal distribution in the $\mathcal{R}$ parameter, but at a value above the classic RL/RQ dividing line and propose that this is a manifestation of the FR I/FR II break. In the previous high redshift studies mentioned above, where only the 'core' radio emission is used, the bimodality in $\mathcal{R}$ may again be a manifestation of the FR I/FR II transition, although what is being considered core emission may in fact include jets and/or lobes (or relatively young sources) whose true radio structure is unresolved. We do note that for the sources with just two components where one

is the core source and the other is not at a large angular distance, the morphology is not easy to determine based on the resolution of the FIRST survey, as the emission may be either young and/or projected in our direction.

The distributions of optical luminosity for the H$\alpha$ emission line are more similar for both the core-only and extended sources, as well as the total sample, than are the distributions of radio luminosities. This difference gives rise to the radio dichotomy seen when evaluating radio-loudness based on the $\mathcal{R}$ parameter in this sample. From our sample we propose that a more interesting dividing line is at a $\log(\mathcal{R})$ value of $\sim$ 1.75 instead of the classical $\log(\mathcal{R}) = 1$. This higher break value for $\log(\mathcal{R})$ enforces the requirement that the radio luminosity be more than 50 times the optical luminosity, ensuring that these sources are indeed RL and usually representative of an FR II-like population, whose BH/accretion disk system may have different or extreme physical properties when compared to the much more numerous RQ AGN with detected radio emission. This choice, however, would not account for the fact that FR Is with extremely bright jets can be considered RL based on any of the standard definitions used. Still these sources would have to be at relatively low redshifts, where the jets can be resolved and the surface brightness is high.

The RLF as a function of $L_{bol}/L_{Edd}$ and $M_{BH}$ are largely unchanged in the extended sample, and we find a modest trend of decreasing RLF with increasing $\log(L_{bol}/L_{Edd})$, along with an increase of the RLF as $M_{BH}$ increases above $\sim 2 \times 10^8$ $M_\odot$. We do note that nearly half of the extended RL AGNs do have the most massive BHs, but

many do not, indicating that radio-loudness is not based solely on $M_{BH}$, but must also be closely tied to other fundamental parameters such as black hole spin or accretion mode.

## 6.2 Future Work: TBD

While there is a large amount of data given here on each AGN in the sample, many of the extended sources lack in depth observations in the radio. Using the VLA radio telescope for deep, high resolution follow up observations of the 63 extended objects, in particular objects not in the older radio catalogues (3C, 4C, PKS, etc.), would be useful to determine the true morphologies, as well as to study in depth some of the more exotic (DDRGs, HYMORs, X-shaped galaxies) morphologies found in this sample. Further analysis could be done by measuring more of the features in the SDSS optical spectra and comparing them to other studies for the entire sample. For example measuring the integrated [O III] line flux and comparing it to the radio luminosity as was done by Xu et al. (1999). This would require a complicated yet flexible automated routine for line fitting since the optical sample is so large.

Another way to expand on this project would be to find data in various wavebands such as the IR or X-ray regimes. Because this is a BL AGN sample, and we can presumable see deeper into the central engine without obscuration, many of these objects should have detections in X-ray catalogues like ROSAT or CHANDRA. Many of these sources may be faint in the IR, such that they are below the flux limits of ground based surveys like 2MASS. However, space based observations from Spitzer

could go deep enough to find useful data. Having a few measurements in each of these wavebands would be useful to constrain the SED of these AGN, thereby getting a true measure of the bolometric luminosity, and hence the accretion rate. This could again be used to determine the way in which physical parameters relate to the generation of radio emission.

## References

Adelman-McCarthy, J. K., et al. 2006, ApJS, 162, 38

Antonucci, R. R. J. 1984, ApJ, 278, 499

Becker, R. H., White, R. L., & Helfand, D. J. 1995, ApJ, 450, 559

Bentz, M. C., Peterson, B. M., Netzer, H., Pogge, R. W., & Vestergaard, M. 2009, ApJ, 697, 160

Best, P. N., Kauffmann, G., Heckman, T. M., & Ivezić, Ž. 2005, MNRAS, 362, 9

Blandford, R. D., & Payne, D. G. 1982, MNRAS, 199, 883

Blandford, R. D., & Znajek, R. L. 1977, MNRAS, 179, 433

Bolton, J. G., Stanley, G. J., & Slee, O. B. 1949, Nature, 164, 101

Burbidge, G. R. 1956, ApJ, 124, 416

Capetti, A., Zamfir, S., Rossi, P., Bodo, G., Zanni, C., & Massaglia, S. 2002, A&A, 394, 39

Chiaberge, M., Capetti, A., & Macchetto, F. D. 2005, ApJ, 625, 716

Cirasuolo, M., Celotti, A., Magliocchetti, M., & Danese, L. 2003, MNRAS, 346, 447

Cirasuolo, M., Celotti, A., Magliocchetti, M., & Danese, L. 2004, in Astronomical Society of the Pacific Conference Series, Vol. 311, AGN Physics with the Sloan Digital Sky Survey, ed. G. T. Richards & P. B. Hall, p. 343 (San Francisco: ASP)

Condon, J. J., Broderick, J. J., Seielstad, G. A., Douglas, K., & Gregory, P. C. 1994, AJ, 107, 1829

Dennett-Thorpe, J., Scheuer, P. A. G., Laing, R. A., Bridle, A. H., Pooley, G. G., & Reich, W. 2002, MNRAS, 330, 609

Dunlop, J. S., McLure, R. J., Kukula, M. J., Baum, S. A., O'Dea, C. P., & Hughes, D. H. 2003, MNRAS, 340, 1095

Elder, F. R., Gurewitsch, A. M., Langmuir, R. V., & Pollock, H. C. 1947, Physical Review, 71, 829

Elvis, M., Risaliti, G., & Zamorani, G. 2002, ApJ, 565, L75

Elvis, M., et al. 1994, ApJS, 95, 1

Fanaroff, B. L., & Riley, J. M. 1974, MNRAS, 167, 31P

Fath, E. A. 1909, Lick Observatory Bulletin, 5, 71

Ferland, G. J., Peterson, B. M., Horne, K., Welsh, W. F., & Nahar, S. N. 1992, ApJ, 387, 95

Gopal-Krishna, Biermann, P. L., & Wiita, P. J. 2003, ApJ, 594, L103

Gopal-Krishna, Mangalam, A., & Wiita, P. J. 2008, ApJ, 680, L13

Gopal-Krishna, & Wiita, P. J. 2000, A&A, 363, 507

Gower, J. F. R., Scott, P. F., & Wills, D. 1967, MmRAS, 71, 49

Green, R. F., Schmidt, M., & Liebert, J. 1986, ApJS, 61, 305

Greene, J. E., & Ho, L. C. 2004, ApJ, 610, 722

—. 2005, ApJ, 630, 122

—. 2007, ApJ, 667, 131

Gregory, P. C., & Condon, J. J. 1991, ApJS, 75, 1011

Gregory, P. C., Scott, W. K., Douglas, K., & Condon, J. J. 1996, ApJS, 103, 427

Ho, L. C. 2002, ApJ, 564, 120

Ivezić, Ž., et al. 2002, AJ, 124, 2364

Ivezić, Z., et al. 2004, in Astronomical Society of the Pacific Conference Series, Vol. 311, AGN Physics with the Sloan Digital Sky Survey, ed. G. T. Richards & P. B. Hall, p. 347 (San Francisco: ASP)

Jamrozy, M., Konar, C., Saikia, D. J., & Machalski, J. 2009, in Astronomical Society of the Pacific Conference Series, Vol. 407, Astronomical Society of the Pacific Conference Series, ed. D. J. Saikia, D. A. Green, Y. Gupta, & T. Venturi, p. 137 (San Francisco: ASP)

Jiang, L., Fan, X., Ivezić, Ž., Richards, G. T., Schneider, D. P., Strauss, M. A., & Kelly, B. C. 2007, ApJ, 656, 680

Kaspi, S., Maoz, D., Netzer, H., Peterson, B. M., Vestergaard, M., & Jannuzi, B. T. 2005, ApJ, 629, 61

Kaspi, S., Smith, P. S., Netzer, H., Maoz, D., Jannuzi, B. T., & Giveon, U. 2000, ApJ, 533, 631

Kawakatu, N., Kino, M., & Nagai, H. 2009, ApJ, 697, L173

Kellermann, K. I., Sramek, R., Schmidt, M., Shaffer, D. B., & Green, R. 1989, AJ, 98, 1195

Kewley, L. J., Groves, B., Kauffmann, G., & Heckman, T. 2006, MNRAS, 372, 961

Khachikian, E. Y., & Weedman, D. W. 1974, ApJ, 192, 581

Laor, A. 2000, ApJ, 543, L111

—. 2003, ArXiv Astrophysics e-prints 0312417

McLure, R. J., & Dunlop, J. S. 2004, MNRAS, 352, 1390

McLure, R. J., & Jarvis, M. J. 2004, MNRAS, 353, L45

Merritt, D., & Ekers, R. D. 2002, Science, 297, 1310

Nagar, N. M., Falcke, H., & Wilson, A. S. 2005, A&A, 435, 521

Osterbrock, D. E., & Ferland, G. J. 2006, Astrophysics of gaseous nebulae and active galactic nuclei, ed. (Sausalito, CA: University Science Books)

Osterbrock, D. E., & Pogge, R. W. 1985, ApJ, 297, 166

Paczyński, B., & Wiita, P. J. 1980, A&A, 88, 23

Peterson, B. M. 1997, An Introduction to Active Galactic Nuclei, ed. Peterson, B. M.

Peterson, B. M., et al. 2004, ApJ, 613, 682

Rees, N. 1990, MNRAS, 244, 233

Saikia, D. J., Konar, C., & Kulkarni, V. K. 2006, MNRAS, 366, 1391

Saripalli, L., & Subrahmanyan, R. 2009, ApJ, 695, 156

Schmidt, M., & Green, R. F. 1983, ApJ, 269, 352

Schoenmakers, A. P., de Bruyn, A. G., Röttgering, H. J. A., van der Laan, H., & Kaiser, C. R. 2000, MNRAS, 315, 371

Seyfert, C. K. 1943, ApJ, 97, 28

Sikora, M., Stawarz, Ł., & Lasota, J. 2007, ApJ, 658, 815

Spergel, D. N., et al. 2003, ApJS, 148, 175

Urry, C. M., & Padovani, P. 1995, PASP, 107, 803

Vestergaard, M., & Peterson, B. M. 2006, ApJ, 641, 689

Vigotti, M., Grueff, G., Perley, R., Clark, B. G., & Bridle, A. H. 1989, AJ, 98, 419

White, R. L., & Becker, R. H. 1992, ApJS, 79, 331

White, R. L., Helfand, D. J., Becker, R. H., Glikman, E., & de Vries, W. 2007, ApJ, 654, 99

White, R. L., et al. 2000, ApJS, 126, 133

Woo, J., & Urry, C. M. 2002, ApJ, 581, L5

Wright, A., & Otrupcek, R. 1990, in PKS Catalog (1990), Parkes Radio Sources Catalog (Epping: ATNF)

Xu, C., Livio, M., & Baum, S. 1999, AJ, 118, 1169

# Appendices

# – A –

# Tables of Detected Sources

## A.1 Table of Core-only Sources

Table A.1: The Core-only SDSS and FIRST Sample

| SDSS Name (1) | FIRST field (2) | Flag (3) | $F_{int}$ (mJy) (4) | Log($\mathcal{R}$) (5) |
|---|---|---|---|---|
| J000202.95−103037.9 | 00015−10405G | 0 | 2.21 | 0.86 |
| J000710.01+005329.0 | 00075+01050E | 0 | 1.44 | 0.27 |
| J000813.22−005753.3 | 00075−01050E | 1 | 2.74 | 0.94 |
| J002141.01+003841.8 | 00225+00390E | 0 | 1.38 | 1.17 |
| J002155.10−104315.6 | 00225−10405G | 1 | 1.79 | 1.12 |
| J002608.38−000546.9 | 00255−00130E | 0 | 0.94 | 0.98 |
| J002831.71−000413.1 | 00285−00130E | 0 | 2.41 | 0.78 |
| J003443.51−000226.6 | 00345−00130E | 0 | 56.68 | 2.44 |
| J003659.82−011332.5 | 00375−01050E | 0 | 0.82 | 0.82 |
| J003847.96+003457.4 | 00375+00390E | 0 | 2.03 | 0.44 |
| J004319.74+005115.3 | 00435+00390E | 0 | 1.60 | 0.46 |
| J004653.39+003654.7 | 00465+00390E | 0 | 1.22 | 0.63 |
| J004741.46+004129.5 | 00465+00390E | 0 | 4.00 | 1.64 |
| J005550.75−101905.6 | 00555−10142G | 0 | 3.03 | 0.84 |
| **J010939.01+005950.3** | **01105+01050E** | **0** | **1.19** | **0.35** |
| J011031.30+003636.5 | 01105+00390E | 0 | 5.39 | 1.87 |
| J011110.03−101631.7 | 01105−10142G | 0 | 9.64 | 0.87 |
| J011448.67−002946.0 | 01135−00390E | 0 | 9.75 | 1.09 |
| J011703.58+000027.3 | 01165+00130E | 0 | 1.02 | −0.14 |
| J011935.63−102613.1 | 01195−10142G | 0 | 2.00 | 1.11 |
| J012159.82−010224.3 | 01225−01050E | 0 | 4.01 | 0.13 |
| J013023.43−102512.8 | 01315−10405G | 0 | 1.27 | 0.70 |
| **J013352.65+011345.3** | **01345+01050E** | **0** | **16.69** | **1.62** |
| J013517.54−001939.1 | 01345−00130E | 0 | 1.51 | 1.01 |
| J013521.67−004402.1 | 01345−00390E | 0 | 1.99 | 0.76 |
| J013706.94−090857.5 | 01375−09216G | 0 | 21.22 | 1.78 |
| J014019.05−092110.5 | 01405−09216G | 0 | 2.12 | 1.02 |
| J014045.14−090506.1 | 01405−08553G | 0 | 3.58 | 0.97 |
| J014124.92−094516.3 | 01405−09479G | 0 | 4.55 | 1.39 |
| J014640.81−082117.3 | 01465−08290G | 0 | 1.99 | 0.53 |
| J014644.82−004043.2 | 01465−00390E | 0 | 4.28 | 0.70 |
| J014816.25+001945.0 | 01495+00130E | 0 | 519.53 | 3.46 |
| J015105.80−003426.3 | 01525−00390E | 0 | 4.15 | 1.34 |
| J020615.99−001729.1 | 02075−00130E | 0 | 4.15 | −0.02 |
| J020713.32−011223.1 | 02075−01050E | 0 | 5.91 | 1.60 |

Continued on Next Page...

TABLE A.1 – Continued

| SDSS Name (1) | FIRST field (2) | Flag (3) | $F_{int}$ (mJy) (4) | Log($\mathcal{R}$) (5) |
|---|---|---|---|---|
| J021011.49−090335.5 | 02105−08553G | 0 | 6.92 | 1.06 |
| J021359.77+004226.7 | 02135+00390E | 0 | 3.52 | 0.55 |
| J021433.56−004600.2 | 02135−00390E | 0 | 9.95 | 0.35 |
| J022014.57−072859.1 | 02195−07364G | 0 | 1.42 | 0.44 |
| J022347.48−083655.5 | 02225−08290G | 0 | 1.04 | 0.52 |
| J023411.77−074538.4 | 02345−07364G | 0 | 2.47 | 1.92 |
| J024620.63−080006.2 | 02465−08027G | 0 | 1.95 | 1.40 |
| J024835.63−005503.5 | 02495−01050E | 0 | 1.28 | 0.63 |
| J024940.18−082804.6 | 02495−08290G | 0 | 4.41 | 1.48 |
| J025105.28−070230.1 | 02525−07102G | 0 | 5.80 | 1.34 |
| J025150.37−083706.1 | 02525−08290G | 0 | 2.37 | 1.44 |
| J025451.13+005309.0 | 02555+01050E | 0 | 0.78 | 1.24 |
| J030639.56+000343.1 | 03075+00130E | 0 | 3.65 | 0.66 |
| J030915.55+002508.2 | 03105+00130E | 0 | 2.82 | 0.92 |
| J030959.84+001758.3 | 03105+00130E | 0 | 0.96 | 1.21 |
| J031238.42+005834.4 | 03135+01050E | 0 | 3.84 | 1.37 |
| **J072406.79+380348.6** | **07240+38071F** | **0** | **76.14** | **3.07** |
| J072929.72+391731.5 | 07300+39084F | 0 | 1.29 | 1.06 |
| J073142.37+392623.7 | 07330+39393F | 0 | 4.58 | 1.69 |
| J073521.19+264744.7 | 07360+27003F | 0 | 1.20 | 0.88 |
| J073623.12+392617.8 | 07360+39393F | 0 | 3.63 | −0.01 |
| J073638.86+435316.5 | 07360+43547F | 0 | 4.26 | 1.61 |
| J073648.64+321437.2 | 07360+32118G | 0 | 2.83 | 1.26 |
| J073703.29+424414.6 | 07360+42493F | 0 | 1.01 | 0.41 |
| J073735.59+430851.1 | 07360+43219F | 0 | 1.08 | 0.29 |
| J073933.84+335014.9 | 07390+33389G | 0 | 12.25 | 2.11 |
| J074018.62+291915.1 | 07390+29203E | 0 | 12.69 | 1.89 |
| J074231.95+215804.7 | 07420+21592G | 0 | 3.66 | 1.83 |
| J074251.09+333403.8 | 07420+33389G | 0 | 3.18 | 1.61 |
| J074529.50+231602.5 | 07450+23206E | 0 | 1.71 | 1.04 |
| J074548.27+284838.0 | 07450+28521F | 0 | 1.15 | 0.18 |
| J074630.60+440433.5 | 07480+43547F | 0 | 1.53 | 1.07 |
| J074738.38+245637.3 | 07480+25099E | 0 | 2.45 | 0.32 |
| **J074906.50+451033.9** | **07480+45013F** | **0** | **112.55** | **1.89** |
| J074920.00+234104.4 | 07480+23478E | 0 | 1.48 | 0.48 |
| J074948.26+345444.0 | 07510+35071E | 0 | 0.82 | −0.25 |
| J074948.33+264734.1 | 07510+27003E | 0 | 4.53 | 1.78 |
| J075101.42+291419.2 | 07510+29203E | 0 | 1.52 | 0.06 |
| J075217.84+193542.2 | 07510+19446H | 0 | 22.95 | 0.77 |
| **J075244.19+455657.3** | **07540+46093F** | **0** | **50.15** | **2.07** |
| J075244.63+434105.3 | 07510+43547F | 0 | 11.02 | 1.90 |
| J075245.60+261735.7 | 07540+26050E | 0 | 1.27 | −0.02 |
| J075352.73+264900.5 | 07540+27003E | 0 | 2.07 | 1.21 |
| J075403.62+481428.0 | 07540+48304F | 0 | 7.94 | 0.96 |

Continued on Next Page...

TABLE A.1 – Continued

| **SDSS Name (1)** | **FIRST field (2)** | **Flag (3)** | **$F_{int}$ (mJy) (4)** | **Log($\mathcal{R}$) (5)** |
|---|---|---|---|---|
| J075407.95+431610.5 | 07540+43219F | 0 | 14.89 | 1.25 |
| J075444.08+354712.8 | 07540+35367E | 0 | 35.59 | 2.55 |
| **J075643.09+310248.7** | **07570+31143E** | **0** | **4.83** | **1.60** |
| J075652.81+291942.2 | 07570+29203E | 0 | 1.59 | 0.66 |
| J075751.20+345921.7 | 07570+35071E | 0 | 1.77 | 1.00 |
| J075819.68+421935.1 | 07570+42170F | 0 | 1.81 | 0.21 |
| J075838.14+414512.4 | 08000+41450E | 0 | 2.14 | 0.68 |
| J075902.28+282756.3 | 08000+28240E | 0 | 1.62 | 1.22 |
| J080020.98+263648.7 | 08000+26326E | 0 | 3.13 | 0.55 |
| J080037.63+461257.9 | 08000+46093F | 0 | 1.44 | 0.84 |
| **J080129.57+462622.8** | **08030+46439F** | **0** | **1.41** | **1.15** |
| J080131.96+473616.0 | 08030+47544F | 0 | 64.28 | 1.29 |
| J080322.48+433307.1 | 08030+43219F | 0 | 5.82 | 1.21 |
| J080403.40+404809.3 | 08030+40417E | 0 | 9.87 | 1.91 |
| J080408.02+394728.4 | 08060+39393E | 0 | 0.72 | 0.52 |
| J080409.23+385348.7 | 08030+39084E | 0 | 2.68 | 0.36 |
| J080424.02+491656.2 | 08030+49069F | 0 | 1.25 | 0.80 |
| J080523.29+281815.8 | 08060+28240E | 0 | 5.49 | 1.10 |
| J080540.56+481046.4 | 08060+48304F | 0 | 1.15 | 0.61 |
| J080752.27+383210.9 | 08090+38377E | 0 | 1.18 | 0.56 |
| J081025.89+271010.5 | 08090+27003E | 0 | 2.53 | 1.59 |
| J081026.07+234156.1 | 08090+23478E | 0 | 0.90 | 0.87 |
| J081116.70+320935.4 | 08120+32118E | 0 | 1.31 | 0.43 |
| J081246.86+492643.6 | 08120+49440F | 0 | 1.35 | 1.49 |
| J081307.46+361441.7 | 08120+36065E | 0 | 1.19 | 0.26 |
| J081420.81+303050.5 | 08150+30170E | 0 | 5.64 | 1.67 |
| J081454.96+333401.7 | 08150+33389E | 0 | 2.74 | 1.33 |
| J081516.87+460430.9 | 08150+46093F | 0 | 5.86 | 0.61 |
| J081700.40+343556.3 | 08180+34376E | 0 | 22.77 | 1.25 |
| J081738.33+242330.0 | 08180+24151E | 0 | 4.45 | 0.63 |
| J081739.58+435420.2 | 08180+43547F | 0 | 2.80 | 1.90 |
| J081842.35+360409.6 | 08180+36065E | 0 | 2.32 | 1.08 |
| J081849.27+383416.1 | 08180+38377E | 0 | 2.08 | 0.64 |
| J081855.50+291527.8 | 08180+29203E | 0 | 4.11 | 1.86 |
| J082007.80+372839.6 | 08210+37367E | 0 | 1.64 | 0.83 |
| J082102.58+275035.9 | 08210+27560E | 0 | 1.22 | 1.41 |
| J082308.28+421521.0 | 08240+42170F | 0 | 1.87 | −0.08 |
| J082342.37+482754.5 | 08240+48304F | 0 | 1.79 | 1.10 |
| **J082355.36+244830.4** | **08240+24425E** | **0** | **0.94** | **1.23** |
| J082405.19+445246.0 | 08240+45013F | 0 | 1.16 | 0.98 |
| J082406.23+334244.9 | 08240+33389E | 0 | 1.08 | 0.49 |
| J082443.28+295923.5 | 08240+29486E | 0 | 1.77 | 0.79 |
| J082452.14+055418.6 | 08240+06047I | 0 | 1.88 | 0.69 |
| J082510.23+375919.7 | 08240+38071E | 0 | 4.55 | 0.72 |

Continued on Next Page...

TABLE A.1 – Continued

| SDSS Name (1) | FIRST field (2) | Flag (3) | $F_{int}$ (mJy) (4) | Log($\mathcal{R}$) (5) |
|---|---|---|---|---|
| J082733.93+043617.3 | 08270+04464I | 0 | 2.08 | 0.46 |
| J082753.70+521758.3 | 08270+52196F | 0 | 181.30 | 2.95 |
| J082853.50+274833.2 | 08300+27560E | 0 | 6.62 | 1.70 |
| J082930.58+081238.0 | 08300+08158I | 0 | 2.32 | 0.42 |
| J083045.21+370946.7 | 08300+37065E | 0 | 17.59 | 2.15 |
| J083049.65+304829.3 | 08300+30456E | 0 | 1.28 | 0.96 |
| J083107.63+052105.9 | 08300+05125I | 0 | 1.73 | 0.69 |
| J083116.14+351707.4 | 08300+35071E | 0 | 0.63 | 0.74 |
| J083207.80+403452.6 | 08330+40417E | 0 | 1.87 | 0.46 |
| J083225.34+370736.1 | 08330+37065E | 0 | 11.73 | 0.64 |
| J083246.92+285312.0 | 08330+28521E | 0 | 1.73 | 0.70 |
| J083552.35+295716.0 | 08360+29486E | 0 | 3.39 | 1.18 |
| J083633.97+530049.3 | 08360+53003F | 0 | 0.83 | 0.52 |
| J083658.91+442602.4 | 08360+44278F | 0 | 10.25 | 0.48 |
| J083726.95+312104.8 | 08360+31143E | 0 | 1.57 | 0.56 |
| J083849.36+083510.4 | 08390+08421I | 0 | 6.31 | 1.78 |
| J083939.91+353915.0 | 08390+35367E | 0 | 4.82 | 1.60 |
| J084028.60+332052.2 | 08390+33097E | 0 | 2.55 | 1.20 |
| J084041.04+383819.8 | 08420+38377E | 0 | 1.16 | 1.09 |
| J084116.26+384409.4 | 08420+38377E | 0 | 17.07 | 2.63 |
| J084203.73+401831.3 | 08420+40104E | 0 | 21.89 | 1.19 |
| J084243.15+283940.2 | 08420+28521E | 0 | 1.39 | 0.75 |
| J084503.43+361735.7 | 08450+36065E | 0 | 3.93 | 0.78 |
| J084529.16+385500.3 | 08450+39084E | 0 | 1.92 | 1.76 |
| **J084600.36+070424.6** | **08450+06571I** | **0** | **111.57** | **1.92** |
| J084917.29+531755.8 | 08480+53003F | 0 | 1.59 | 0.61 |
| J084928.05+054629.6 | 08480+05386I | 0 | 2.75 | 1.73 |
| J085010.42+074758.5 | 08510+07495I | 0 | 223.70 | 3.55 |
| J085115.67+545910.1 | 08510+55098G | 0 | 1.72 | 0.96 |
| J085300.39+353829.3 | 08540+35367E | 0 | 1.47 | 1.01 |
| J085338.26+033246.1 | 08540+03281G | 0 | 4.04 | 1.28 |
| **J085348.18+065447.1** | **08540+06571I** | **0** | **135.70** | **3.21** |
| J085422.91+470553.7 | 08540+47189F | 0 | 0.72 | 0.64 |
| J085457.22+544820.5 | 08540+55098G | 0 | 1.31 | 0.72 |
| J085554.27+005110.9 | 08570+00520G | 0 | 1.04 | 0.09 |
| J085602.65+060400.7 | 08570+06047I | 0 | 10.37 | 1.83 |
| **J085627.91+360315.6** | **08570+36065E** | **0** | **16.80** | **2.19** |
| J085809.40+492547.0 | 09000+49440F | 0 | 1.16 | 0.42 |
| J085835.98+013149.5 | 09000+01180G | 0 | 1.84 | 0.69 |
| J085956.53+380234.8 | 09000+38071E | 0 | 51.45 | 2.65 |
| J090018.97+075014.5 | 09000+07495I | 0 | 2.32 | 1.24 |
| J090100.87+353808.8 | 09000+35367E | 0 | 1.35 | 0.88 |
| J090215.45+521248.1 | 09030+52196F | 0 | 4.16 | 1.64 |
| J090307.84+021152.2 | 09030+02100G | 0 | 22.50 | 2.14 |

Continued on Next Page...

TABLE A.1 – Continued

| SDSS Name (1) | FIRST field (2) | Flag (3) | $F_{int}$ (mJy) (4) | Log($\mathcal{R}$) (5) |
|---|---|---|---|---|
| J090359.91+363054.6 | 09030+36364E | 0 | 2.05 | 1.08 |
| J090436.95+553602.7 | 09060+55553G | 0 | 1.36 | −0.33 |
| J090445.44+470601.5 | 09060+47189F | 0 | 2.61 | 0.91 |
| J090613.76+561015.2 | 09060+55553G | 0 | 4.72 | 1.81 |
| J090615.53+463619.0 | 09060+46439F | 0 | 313.57 | 3.16 |
| J090624.60+005756.0 | 09060+00520G | 0 | 7.23 | 1.85 |
| J090743.49+013327.9 | 09090+01440G | 0 | 3.34 | 0.89 |
| J090810.33+500923.1 | 09090+50218F | 0 | 0.96 | 0.08 |
| J090816.57+355131.7 | 09090+35367E | 0 | 0.80 | 0.08 |
| J090838.78+324620.2 | 09090+32407E | 0 | 0.87 | 0.62 |
| J090935.49+105210.5 | 09090+10536I | 0 | 7.99 | 1.88 |
| J091110.83+501608.4 | 09120+50218F | 0 | 2.22 | 0.58 |
| **J091133.85+442250.1** | **09120+44278F** | **0** | **334.60** | **3.01** |
| J091146.42+564112.1 | 09120+56415G | 0 | 1.81 | 0.73 |
| J091222.30+065829.0 | 09120+06571I | 0 | 2.10 | 1.11 |
| J091313.72+365817.2 | 09120+37065E | 0 | 0.84 | 0.22 |
| **J091401.76+050750.6** | **09150+05125I** | **0** | **77.81** | **2.00** |
| J091449.05+085321.1 | 09150+08421I | 0 | 1.43 | 1.05 |
| J091551.66+044732.3 | 09150+04464I | 0 | 1.15 | 0.75 |
| J091614.73+393405.2 | 09150+39393E | 0 | 2.82 | 1.84 |
| J091635.45+541426.9 | 09180+54251G | 0 | 11.86 | 1.71 |
| J091652.79+392714.7 | 09180+39393E | 0 | 2.55 | 0.89 |
| J092019.08+395219.6 | 09210+39393E | 0 | 9.77 | 1.59 |
| J092252.99+395711.9 | 09240+40104E | 0 | 5.01 | 1.66 |
| **J092308.16+561455.3** | **09240+55553G** | **0** | **19.91** | **2.48** |
| J092414.71+030900.7 | 09240+03020G | 0 | 20.57 | 2.06 |
| J092533.68+021342.5 | 09270+02100G | 0 | 6.28 | 1.51 |
| J092555.59+421347.4 | 09270+42170F | 0 | 7.06 | 1.79 |
| J092613.80+065056.4 | 09270+06571I | 0 | 3.83 | 0.90 |
| J092856.27+013246.0 | 09300+01440G | 0 | 0.70 | 0.67 |
| J092913.31+092414.2 | 09300+09084I | 0 | 0.93 | 1.15 |
| J092936.73+571149.8 | 09300+57282I | 0 | 3.05 | 2.04 |
| J093023.16+435047.0 | 09300+43547F | 0 | 2.57 | 0.95 |
| J093044.16+084929.8 | 09300+08421I | 0 | 3.18 | 1.89 |
| J093055.82−001959.8 | 09300−00260G | 0 | 0.82 | 1.12 |
| J093123.85+051345.2 | 09300+05125I | 0 | 0.74 | 0.28 |
| **J093200.08+553347.4** | **09330+55553G** | **0** | **5.23** | **0.87** |
| J093239.70+410610.2 | 09330+41132E | 0 | 5.87 | 1.85 |
| J093342.55+032538.2 | 09330+03281G | 0 | 1.26 | 1.04 |
| J093439.56+002752.1 | 09360+00260G | 0 | 3.03 | 1.33 |
| J093509.47+481910.2 | 09360+48304F | 0 | 1.54 | 0.17 |
| J093518.74+104504.7 | 09360+10536I | 0 | 1.16 | 1.62 |
| J093532.35+073128.5 | 09360+07233I | 0 | 4.27 | 1.57 |
| J093609.13−002639.7 | 09360−00260G | 0 | 0.70 | 0.30 |

Continued on Next Page...

TABLE A.1 – Continued

| SDSS Name (1) | FIRST field (2) | Flag (3) | $F_{int}$ (mJy) (4) | Log($\mathcal{R}$) (5) |
|---|---|---|---|---|
| J093621.50+392131.9 | 09360+39084E | 0 | 28.51 | 1.76 |
| J093641.06+101415.8 | 09360+10273I | 0 | 11.63 | 1.09 |
| J093703.02+361537.1 | 09360+36065E | 0 | 3.21 | 0.98 |
| J093712.33+500852.1 | 09390+50218F | 0 | 167.58 | 3.29 |
| J093811.94+045356.5 | 09390+04464I | 0 | 4.54 | 1.68 |
| J093917.25+363343.9 | 09390+36364E | 0 | 4.50 | 0.68 |
| J094003.77+510421.8 | 09420+51003F | 0 | 16.27 | 2.56 |
| J094021.04+525929.7 | 09420+53003F | 0 | 1.15 | 1.24 |
| J094111.13+492414.5 | 09420+49440F | 0 | 1.28 | 1.14 |
| J094153.11+000918.5 | 09420+00000G | 0 | 1.63 | 1.55 |
| J094200.19+025958.2 | 09420+03020G | 0 | 0.97 | 1.12 |
| J094322.29+401556.3 | 09420+40104E | 0 | 2.12 | 1.24 |
| J094411.95+502656.6 | 09450+50218F | 0 | 2.13 | 1.08 |
| J094451.57+562037.8 | 09450+56415G | 0 | 5.00 | 1.01 |
| J094525.90+352103.6 | 09450+35071E | 0 | 147.55 | 3.18 |
| J094603.94+013923.7 | 09450+01440G | 0 | 7.68 | 0.62 |
| J094725.81+390833.7 | 09480+39084E | 0 | 4.18 | 1.86 |
| J094733.21+100508.7 | 09480+10010I | 0 | 1.80 | 0.06 |
| J094842.67+502931.4 | 09480+50218F | 0 | 5.83 | 0.46 |
| J095033.15+441851.7 | 09510+44278F | 0 | 8.65 | 0.95 |
| J095156.71+023601.9 | 09510+02360G | 0 | 1.07 | 0.72 |
| J095227.79+014121.4 | 09510+01440G | 0 | 6.22 | 1.40 |
| **J095456.89+092955.8** | **09540+09347I** | **0** | **233.87** | **2.72** |
| J095536.69+103752.3 | 09570+10273I | 0 | 1.98 | 0.92 |
| J095539.81+453217.0 | 09570+45351F | 0 | 53.18 | 1.77 |
| J095631.13+084616.7 | 09570+08421I | 0 | 3.02 | 1.40 |
| J095833.95+560224.4 | 10000+55553G | 0 | 0.83 | 0.72 |
| J095851.33+483228.8 | 10000+48304F | 0 | 2.04 | 1.29 |
| J095858.53+021459.0 | 10000+02100G | 0 | 0.96 | 0.85 |
| J095941.36+491529.5 | 10000+49069F | 0 | 7.28 | 0.77 |
| J100013.14+124226.2 | 10000+12392I | 0 | 31.75 | 1.92 |
| J100033.88+104723.7 | 10000+10536I | 0 | 2.17 | 0.24 |
| J100155.79+055413.3 | 10030+06047I | 0 | 1.50 | 0.70 |
| J100202.08+055145.6 | 10030+06047I | 0 | 2.43 | 1.10 |
| J100253.51+513709.4 | 10030+51396F | 0 | 1.04 | 1.17 |
| J100405.00−003253.4 | 10030−00260G | 0 | 2.55 | 1.07 |
| J100410.85+523025.1 | 10030+52196F | 0 | 6.64 | 2.06 |
| J100506.15+562429.1 | 10060+56415G | 0 | 1.60 | 0.52 |
| J100522.95+405834.6 | 10060+41132E | 0 | 1.07 | 0.27 |
| J100541.86+433240.4 | 10060+43219F | 0 | 2.81 | 0.35 |
| J100625.39+091554.3 | 10060+09084I | 0 | 1.13 | 1.18 |
| J100630.42+422943.6 | 10060+42170F | 0 | 0.87 | 1.11 |
| J100642.59+412201.8 | 10060+41132E | 0 | 3.06 | 0.59 |
| **J100726.10+124856.2** | **10060+12392I** | **0** | **13.79** | **0.89** |

Continued on Next Page...

TABLE A.1 – Continued

| SDSS Name (1) | FIRST field (2) | Flag (3) | $F_{int}$ (mJy) (4) | Log($\mathcal{R}$) (5) |
|---|---|---|---|---|
| **J100819.11+372903.4** | **10090+37367E** | **0** | **1.35** | **1.17** |
| J101010.73+462000.5 | 10090+46093F | 0 | 0.89 | 0.67 |
| J101043.36+061201.4 | 10120+06047I | 0 | 99.26 | 1.92 |
| J101044.50+004331.3 | 10120+00520G | 0 | 0.77 | −0.35 |
| J101200.78+515701.8 | 10120+52196F | 0 | 0.95 | 1.36 |
| J101238.52+101719.2 | 10120+10273I | 0 | 3.73 | 0.73 |
| J101238.68+524223.0 | 10120+53003F | 0 | 7.28 | 1.73 |
| J101246.59+061604.7 | 10120+06047I | 0 | 1.03 | 0.72 |
| J101502.24+023128.1 | 10150+02360G | 0 | 9.60 | 1.66 |
| J101527.26+625911.4 | 10180+63011J | 0 | 1.18 | 0.84 |
| J101645.11+421025.4 | 10180+42170F | 0 | 1.47 | −0.25 |
| J101733.20−000145.2 | 10180+00000G | 0 | 2.19 | 0.94 |
| J101738.72+420103.4 | 10180+42170F | 0 | 2.02 | 0.95 |
| J101843.13+413516.1 | 10180+41450E | 0 | 1.04 | 1.06 |
| J101900.45+375240.4 | 10180+38071E | 0 | 2.24 | 0.78 |
| J101912.57+635802.7 | 10180+63562J | 0 | 2.18 | −0.12 |
| J101959.37+064721.1 | 10210+06571I | 0 | 1.27 | 1.35 |
| J102000.45+623944.7 | 10180+62339J | 0 | 1.36 | 1.06 |
| J102056.91+384405.4 | 10210+38377E | 0 | 1.91 | 0.78 |
| J102147.86+131228.1 | 10210+13056I | 0 | 1.41 | 0.52 |
| J102148.90+030732.2 | 10210+03020G | 0 | 1.24 | 0.44 |
| J102256.61+540717.9 | 10240+54251G | 0 | 0.87 | 0.67 |
| J102350.62+411021.3 | 10240+41132E | 0 | 1.04 | 0.71 |
| J102424.59+571511.0 | 10240+57282I | 0 | 1.20 | 0.24 |
| J102452.28+562819.2 | 10240+56415G | 0 | 1.48 | 1.68 |
| J102531.28+514034.8 | 10270+51396F | 0 | 0.60 | −0.68 |
| J102629.13+042915.2 | 10270+04203I | 0 | 0.85 | 0.72 |
| J102724.98+121919.7 | 10270+12128I | 0 | 7.86 | 1.07 |
| J102841.98+490418.7 | 10300+49069F | 0 | 1.17 | 0.09 |
| J102925.73+140823.2 | 10300+13585I | 0 | 1.40 | 0.32 |
| J103020.12+414128.6 | 10300+41450E | 0 | 2.81 | 1.53 |
| J103110.56+115317.7 | 10300+11464I | 0 | 0.80 | 0.61 |
| J103125.26+074415.7 | 10300+07495I | 0 | 2.20 | 1.46 |
| **J103143.51+522535.1** | **10330+52196F** | **0** | **83.67** | **2.69** |
| J103252.60+492612.9 | 10330+49440F | 0 | 2.28 | 1.15 |
| J103311.64+013754.5 | 10330+01440G | 1 | 1.47 | 0.99 |
| J103330.65+070407.3 | 10330+06571I | 0 | 22.78 | 2.60 |
| J103352.59+004403.3 | 10330+00520G | 0 | 18.23 | 1.55 |
| **J103458.35+055231.8** | **10360+06047I** | **0** | **21.16** | **1.87** |
| J103604.66+412517.8 | 10360+41132E | 0 | 1.19 | 0.63 |
| J103606.01+412602.1 | 10360+41132E | 0 | 4.83 | 1.92 |
| J103751.05+510152.8 | 10390+51003F | 0 | 1.08 | 0.57 |
| J103853.29+392151.1 | 10390+39084E | 0 | 1.43 | 0.65 |
| J103859.58+422742.2 | 10390+42170F | 0 | 2.44 | 0.54 |

Continued on Next Page...

TABLE A.1 – Continued

| SDSS Name (1) | FIRST field (2) | Flag (3) | $F_{int}$ (mJy) (4) | Log($\mathcal{R}$) (5) |
|---|---|---|---|---|
| J103915.69−003916.9 | 10390−00520G | 0 | 30.92 | 2.18 |
| J103936.77+443346.9 | 10390+44278F | 0 | 1.05 | 1.16 |
| J104029.16+105318.2 | 10390+10536I | 0 | 8.55 | 2.03 |
| J104058.79+581703.3 | 10420+58155J | 0 | 1.49 | 0.36 |
| J104108.19+562000.3 | 10420+56415G | 0 | 0.90 | 0.59 |
| J104119.23+574500.0 | 10420+57282I | 0 | 6.79 | 0.97 |
| J104134.24+464410.1 | 10420+46439F | 0 | 0.95 | 1.24 |
| J104148.04+401721.5 | 10420+40104E | 0 | 1.92 | 1.40 |
| J104448.88+470935.6 | 10450+47189F | 0 | 1.21 | 1.51 |
| J104500.40−001553.9 | 10450−00260G | 0 | 4.17 | 1.15 |
| J104504.23+114508.8 | 10450+11464I | 0 | 1.04 | 0.72 |
| J104643.94+623816.1 | 10480+62339J | 0 | 0.82 | 0.86 |
| J104837.50+032719.0 | 10480+03281G | 0 | 2.57 | 1.73 |
| J104850.17+062625.3 | 10480+06309I | 0 | 1.27 | 0.46 |
| J104928.28+553927.1 | 10510+55553G | 0 | 0.99 | 0.29 |
| J105007.76+113228.6 | 10510+11200I | 0 | 1.50 | −0.06 |
| J105012.62+625303.3 | 10480+63011J | 0 | 1.50 | 0.73 |
| J105021.57+483410.4 | 10510+48304F | 0 | 1.41 | 1.45 |
| J105057.29+593214.3 | 10480+59294J | 0 | 1.73 | 0.66 |
| J105232.98+103620.0 | 10540+10273I | 0 | 3.60 | 1.36 |
| J105302.66+055631.7 | 10540+06047I | 1 | 2.06 | 0.90 |
| J105444.69+483139.0 | 10540+48304F | 0 | 1.56 | −0.25 |
| **J105500.33+520200.9** | **10570+52196F** | **0** | **174.58** | **2.65** |
| J105518.43+392905.2 | 10540+39393E | 0 | 3.15 | 0.92 |
| J105606.93−004655.5 | 10570−00520G | 0 | 2.59 | 1.36 |
| J105609.80+551604.1 | 10570+55098G | 0 | 2.57 | 0.74 |
| **J105632.01+430055.9** | **10570+42493F** | **0** | **11.60** | **1.97** |
| J105635.05+414602.5 | 10570+41450E | 0 | 13.57 | 1.15 |
| J105713.10+022945.0 | 10570+02360G | 0 | 2.72 | 0.94 |
| J105821.79+442634.2 | 11000+44278F | 0 | 1.13 | 0.87 |
| J110131.04+025504.2 | 11030+03020G | 0 | 0.92 | 0.78 |
| J110145.36+460236.1 | 11030+46093F | 0 | 1.96 | 0.41 |
| J110157.90+101739.2 | 11030+10273I | 0 | 1.52 | 0.07 |
| J110158.16+120531.1 | 11030+12128I | 0 | 1.75 | 1.30 |
| J110205.57+503319.0 | 11030+50218F | 0 | 0.99 | 1.30 |
| J110333.01+083449.0 | 11030+08421I | 0 | 1.71 | 1.04 |
| J110501.97+594103.6 | 11060+59294J | 0 | 5.96 | 1.43 |
| J110504.21+505949.8 | 11060+51003F | 0 | 2.59 | 0.87 |
| J110538.99+020257.4 | 11060+02100G | 0 | 212.83 | 1.98 |
| J110544.94+053738.1 | 11060+05386I | 0 | 0.93 | 0.54 |
| J110639.56+433620.6 | 11060+43219F | 0 | 4.24 | 1.47 |
| J110717.77+080438.1 | 11060+08158I | 0 | 7.36 | 0.60 |
| **J110845.48+020240.8** | **11090+02100G** | **0** | **98.40** | **2.71** |
| J110926.70+422558.0 | 11090+42170F | 0 | 1.73 | 0.92 |

Continued on Next Page...

TABLE A.1 – Continued

| SDSS Name (1) | FIRST field (2) | Flag (3) | $F_{int}$ (mJy) (4) | Log($\mathcal{R}$) (5) |
|---|---|---|---|---|
| J111121.70+482045.9 | 11120+48304F | 0 | 14.31 | 1.65 |
| J111148.31+111542.8 | 11120+11200I | 0 | 2.02 | 1.06 |
| J111206.05+013524.4 | 11120+01440G | 0 | 1.69 | 0.58 |
| J111237.43+120729.4 | 11120+12128I | 0 | 1.92 | 1.03 |
| J111239.58+454141.3 | 11120+45351F | 0 | 1.49 | 0.48 |
| J111349.73+093510.6 | 11150+09347I | 0 | 37.60 | 1.69 |
| J111409.90−000808.6 | 11150+00000G | 0 | 2.88 | 1.37 |
| **J111432.79+105034.7** | **11150+10536I** | **0** | **249.15** | **3.59** |
| J111455.75+423212.3 | 11150+42170F | 0 | 1.95 | 0.52 |
| J111518.31+051037.7 | 11150+05125I | 0 | 1.21 | 0.55 |
| J111525.61+013406.8 | 11150+01440G | 0 | 1.52 | 0.84 |
| J111528.04+534659.5 | 11150+53420G | 0 | 1.72 | 1.02 |
| J111553.88+004734.3 | 11150+00520G | 0 | 1.89 | 1.37 |
| J111603.13+020852.2 | 11150+02100G | 0 | 0.57 | −0.39 |
| J111607.65+412353.1 | 11150+41132E | 0 | 2.27 | 0.23 |
| J111803.22+450646.8 | 11180+45013F | 0 | 14.25 | 1.74 |
| J111807.47+002734.9 | 11180+00260G | 0 | 6.63 | 2.08 |
| J111830.28+402554.0 | 11180+40104E | 0 | 2.32 | 0.07 |
| J111837.90+435105.2 | 11180+43547F | 0 | 1.74 | 1.30 |
| J111907.06+413014.6 | 11180+41450E | 0 | 2.39 | 0.50 |
| J111938.02+513315.5 | 11180+51396F | 0 | 1.33 | −0.17 |
| J112014.85+063341.1 | 11210+06309I | 0 | 1.75 | 0.88 |
| J112019.62+130320.1 | 11210+13056I | 0 | 1.65 | 0.89 |
| J112042.74+084131.2 | 11210+08421I | 0 | 0.85 | 0.72 |
| J112108.58+535121.0 | 11210+53420G | 0 | 2.60 | −0.09 |
| J112114.21+032546.8 | 11210+03281G | 0 | 2.20 | 0.43 |
| J112151.22+405147.0 | 11210+40417E | 0 | 0.97 | 0.18 |
| J112242.74+414355.4 | 11240+41450E | 0 | 2.37 | 1.42 |
| J112324.58+503226.6 | 11240+50218F | 0 | 2.04 | 1.73 |
| J112409.71+104201.9 | 11240+10536I | 0 | 1.38 | 1.44 |
| J112439.43+113117.2 | 11240+11200I | 0 | 8.03 | 1.48 |
| J112455.86+080615.3 | 11240+07495I | 0 | 1.53 | 1.09 |
| J112500.63+001441.2 | 11240+00260G | 0 | 3.66 | 1.75 |
| J112509.57+033955.1 | 11240+03281G | 0 | 16.54 | 2.43 |
| J112611.63+425246.4 | 11270+42493F | 0 | 1.10 | 0.26 |
| J112813.02+102308.3 | 11270+10273I | 0 | 1.13 | −0.18 |
| J112841.00+575006.5 | 11300+57282I | 0 | 1.44 | 0.13 |
| J112941.93+512050.6 | 11300+51396F | 0 | 1.26 | 0.31 |
| J113029.13+493457.8 | 11300+49440F | 0 | 1.88 | 0.19 |
| J113127.78+565524.5 | 11300+56415G | 0 | 1.34 | 1.45 |
| J113240.24+525701.3 | 11330+53003F | 0 | 25.81 | 1.45 |
| J113320.90+043255.1 | 11330+04203I | 0 | 5.02 | 1.18 |
| J113326.34+032654.3 | 11330+03281G | 0 | 2.00 | 0.68 |
| J113426.39+125215.3 | 11330+12392I | 0 | 4.07 | 1.67 |

Continued on Next Page...

TABLE A.1 – Continued

| SDSS Name (1) | FIRST field (2) | Flag (3) | $F_{int}$ (mJy) (4) | Log($\mathcal{R}$) (5) |
|---|---|---|---|---|
| J113447.35+100736.5 | 11360+10010I | 0 | 5.27 | 1.20 |
| J113450.99+491208.9 | 11360+49069F | 0 | 1.10 | 0.68 |
| J113651.66+445016.4 | 11360+45013F | 0 | 3.37 | 1.15 |
| J113704.18+482659.0 | 11390+48304F | 0 | 2.71 | 0.66 |
| J113738.04+103930.1 | 11390+10273I | 0 | 1.65 | 0.28 |
| J113808.12+525705.8 | 11390+53003F | 0 | 1.48 | 1.09 |
| J113925.55+451346.7 | 11390+45351F | 0 | 2.12 | 1.01 |
| J113936.62+035311.5 | 11390+03542I | 0 | 2.24 | 0.57 |
| J114003.39+411503.5 | 11390+41132E | 0 | 2.43 | 0.47 |
| **J114004.35−010527.4** | **11390−01180G** | **0** | **9.73** | **2.07** |
| **J114047.90+462204.8** | **11420+46439F** | **0** | **81.57** | **1.73** |
| J114347.71+112847.9 | 11450+11200I | 0 | 0.90 | 0.18 |
| J114411.74+102202.5 | 11450+10273I | 0 | 1.26 | 0.40 |
| J114420.31+113500.8 | 11450+11464I | 0 | 2.62 | 0.14 |
| J114425.56+514732.3 | 11450+51396F | 0 | 1.14 | 1.22 |
| J114450.20+502609.3 | 11450+50218F | 0 | 1.15 | 0.19 |
| J114719.94+075243.1 | 11480+07495I | 0 | 2.54 | 1.50 |
| J114755.06+090229.0 | 11480+09084I | 0 | 1.15 | −0.47 |
| J114836.39+051608.5 | 11480+05125I | 0 | 1.33 | 0.02 |
| J114845.73+513705.1 | 11480+51396F | 0 | 2.00 | 1.38 |
| J114921.52+532013.4 | 11510+53420G | 0 | 3.60 | 0.79 |
| J114954.99+044812.9 | 11510+04464I | 0 | 1.76 | 0.43 |
| J115018.40+034602.7 | 11510+03542I | 0 | 1.92 | 1.05 |
| J115034.03+474930.3 | 11510+47544F | 0 | 1.55 | 1.44 |
| J115106.69+471157.8 | 11510+47189F | 0 | 2.94 | 0.48 |
| J115111.21+104710.1 | 11510+10536I | 0 | 1.38 | 1.13 |
| J115158.90+122128.9 | 11510+12128I | 0 | 2.63 | 0.73 |
| J115205.96+521114.2 | 11540+52196F | 0 | 1.82 | 0.61 |
| J115232.21+422759.8 | 11540+42170F | 0 | 3.07 | 0.93 |
| J115255.23+610604.8 | 11540+61137J | 0 | 2.03 | 1.11 |
| J115323.95+583138.4 | 11540+58396J | 0 | 79.42 | 2.18 |
| J115341.16+101753.9 | 11540+10273I | 0 | 1.51 | 0.01 |
| **J115409.27+023815.0** | **11540+02360G** | **0** | **29.56** | **2.58** |
| J115431.49+121427.4 | 11540+12128I | 0 | 0.80 | 0.72 |
| J115437.43+114858.9 | 11540+11464I | 0 | 50.04 | 2.95 |
| J115507.60+520129.6 | 11570+52196F | 0 | 2.05 | 0.38 |
| J115537.98−004614.2 | 11570−00520G | 0 | 2.78 | 1.11 |
| J115540.66+434840.3 | 11570+43547F | 0 | 1.22 | 1.10 |
| J115544.40+040631.6 | 11570+03542I | 0 | 0.50 | 0.33 |
| J115727.60+431806.3 | 11570+43219F | 0 | 255.92 | 2.92 |
| J120100.12+133127.7 | 12000+13320I | 0 | 2.29 | 1.36 |
| J120113.76−024241.3 | 12000−02360G | 0 | 0.80 | 0.56 |
| J120149.74−015327.4 | 12030−01440G | 0 | 2.65 | 0.74 |
| J120226.76−012915.2 | 12030−01180G | 0 | 12.40 | 1.48 |

Continued on Next Page...

TABLE A.1 – Continued

| SDSS Name (1) | FIRST field (2) | Flag (3) | $F_{int}$ (mJy) (4) | Log($\mathcal{R}$) (5) |
|---|---|---|---|---|
| J120256.26+102917.4 | 12030+10273I | 0 | 1.35 | 1.22 |
| J120332.94+022934.6 | 12030+02360G | 0 | 1.80 | −0.04 |
| J120346.06+494650.7 | 12030+49440F | 0 | 0.83 | 1.08 |
| J120347.70+520749.7 | 12030+52196F | 0 | 0.68 | −0.59 |
| J120516.26+013508.3 | 12060+01440G | 0 | 4.99 | 1.17 |
| J120550.73+505455.4 | 12060+51003F | 0 | 1.39 | 1.12 |
| J120556.01+495956.1 | 12060+50218F | 0 | 1.79 | 0.18 |
| **J120612.67+490226.2** | **12060+49069F** | **0** | **3.27** | **1.72** |
| J120620.50+565948.0 | 12060+56415G | 0 | 7.09 | 1.68 |
| J120628.97+503001.4 | 12060+50218F | 0 | 1.15 | 0.69 |
| J120700.30−021927.0 | 12060−02100G | 0 | 0.79 | 0.48 |
| J121113.97+464711.9 | 12120+46439F | 0 | 2.21 | 0.75 |
| J121122.44+130937.2 | 12120+13056I | 0 | 3.99 | 1.55 |
| J121151.67+105233.0 | 12120+10536I | 0 | 1.58 | 0.72 |
| J121220.09+440320.9 | 12120+43547F | 0 | 1.22 | 0.58 |
| J121236.39+015803.0 | 12120+02100G | 0 | 0.62 | 0.39 |
| J121303.36+513854.9 | 12150+51396F | 0 | 8.20 | 1.67 |
| J121334.53+591923.2 | 12120+59294J | 0 | 1.29 | 1.00 |
| J121342.81+422743.0 | 12150+42170F | 0 | 2.43 | 0.49 |
| J121426.58+081259.8 | 12150+08158I | 1 | 1.68 | 1.10 |
| J121549.44+544224.0 | 12150+54251G | 0 | 2.35 | 0.37 |
| J121600.04+124114.3 | 12150+12392I | 0 | 3.98 | 1.28 |
| J121607.09+504930.0 | 12180+51003F | 0 | 7.94 | 0.56 |
| J121609.60+415928.3 | 12150+41450E | 0 | 18.42 | 1.93 |
| J121629.91+084253.2 | 12180+08421I | 0 | 1.68 | 0.38 |
| J121637.06−002239.9 | 12180−00260G | 0 | 0.89 | 0.89 |
| J121839.40+470627.6 | 12180+47189F | 0 | 2.36 | 1.24 |
| J121842.08+131639.6 | 12180+13056I | 0 | 1.06 | 0.94 |
| J121855.80+020002.1 | 12180+02100G | 0 | 0.96 | 0.04 |
| J121945.03+082117.9 | 12210+08158I | 0 | 3.08 | 1.05 |
| J121953.10+554506.5 | 12210+55553G | 0 | 1.69 | 0.52 |
| **J122011.89+020342.2** | **12210+02100G** | **0** | **333.07** | **2.05** |
| J122013.55+520206.2 | 12210+52196F | 0 | 1.01 | 0.45 |
| J122209.29+581421.5 | 12240+58155J | 0 | 47.51 | 2.68 |
| J122217.85−000743.7 | 12210+00000G | 0 | 4.24 | 1.21 |
| J122313.21+540906.5 | 12240+54251G | 0 | 387.19 | 2.60 |
| J122320.18+115931.6 | 12240+11464I | 0 | 1.11 | 1.15 |
| J122550.31+510846.3 | 12270+51003F | 0 | 2.59 | 1.62 |
| J122811.89+514622.7 | 12270+51396F | 0 | 4.25 | 1.29 |
| J123152.05+450443.1 | 12330+45013F | 0 | 5.56 | 1.02 |
| J123246.62−013639.8 | 12330−01440G | 0 | 4.82 | 0.94 |
| J123431.08+515629.2 | 12360+52196F | 0 | 1.72 | 1.04 |
| J123503.49+045530.5 | 12360+04464I | 0 | 1.38 | 0.45 |
| J123524.34+500814.3 | 12360+50218F | 0 | 1.87 | 1.29 |

Continued on Next Page...

TABLE A.1 – Continued

| **SDSS Name (1)** | **FIRST field (2)** | **Flag (3)** | **$F_{int}$ (mJy) (4)** | **Log($\mathcal{R}$) (5)** |
|---|---|---|---|---|
| J123628.30+444123.1 | 12360+45013F | 0 | 3.75 | 1.46 |
| J123651.18+453904.1 | 12360+45351F | 0 | 3.43 | 0.61 |
| **J123807.77+532555.9** | **12390+53420G** | **0** | **43.24** | **1.61** |
| J123835.53+032541.4 | 12390+03281G | 0 | 1.62 | 1.47 |
| J123922.18+115759.8 | 12390+11464I | 0 | 1.69 | 1.00 |
| J124035.81−002919.4 | 12420−00260G | 0 | 1.29 | 0.56 |
| J124238.37+045616.5 | 12420+04464I | 0 | 2.13 | 0.72 |
| J124321.76+001537.1 | 12420+00260G | 0 | 1.87 | 1.25 |
| J124323.83+051446.3 | 12420+05125I | 0 | 14.85 | 1.11 |
| J124407.46+010633.5 | 12450+01180G | 0 | 4.57 | 0.78 |
| J124412.05+504201.9 | 12450+51003F | 0 | 2.11 | 0.93 |
| J124428.68+435628.4 | 12450+43547F | 0 | 2.54 | 1.82 |
| J124446.01+602548.7 | 12420+60210J | 0 | 2.67 | 0.93 |
| J124506.89−032156.9 | 12450−03281G | 0 | 3.62 | 0.74 |
| J124612.10+410811.9 | 12450+41132E | 0 | 4.76 | 0.76 |
| J124622.99+002839.9 | 12450+00260G | 0 | 2.60 | 0.99 |
| J124635.24+022208.7 | 12480+02100G | 0 | 2.23 | 0.20 |
| J124651.26+150914.3 | 12480+15180I | 0 | 42.15 | 3.03 |
| J124707.32+490017.8 | 12480+49069F | 0 | 1212.69 | 4.47 |
| J124715.45+622852.6 | 12480+62339J | 0 | 2.78 | 0.60 |
| J124750.24+052200.1 | 12480+05125I | 0 | 5.07 | 1.24 |
| J125016.21+045745.0 | 12510+04464I | 0 | 1.50 | 0.57 |
| J125039.08+141241.0 | 12510+14250I | 0 | 5.96 | 1.44 |
| J125042.44+001957.4 | 12510+00260G | 0 | 1.64 | 1.56 |
| J125051.04+060909.9 | 12510+06047I | 0 | 2.52 | 0.58 |
| J125226.34+563419.7 | 12540+56415G | 0 | 2442.12 | 3.74 |
| J125334.49−034158.1 | 12540−03542I | 0 | 2.68 | 1.19 |
| J125505.24+430355.3 | 12540+42493F | 0 | 1.25 | 1.28 |
| J125519.69+014412.3 | 12540+01440G | 0 | 1.47 | −0.18 |
| J125622.58−015959.5 | 12570−02100G | 0 | 1.24 | 0.84 |
| J125717.57+534555.3 | 12570+53420G | 0 | 1.57 | 0.84 |
| J125858.05+575022.2 | 13000+57282I | 0 | 2.25 | 0.99 |
| J125904.33+504852.5 | 13000+51003F | 0 | 0.71 | 0.66 |
| J130007.99+035556.5 | 13000+03542I | 0 | 21.26 | 1.63 |
| J130317.49+513541.9 | 13030+51396F | 0 | 4.43 | 1.52 |
| **J130359.47+033932.1** | **13030+03281G** | **0** | **6.20** | **1.82** |
| J130633.04+002248.4 | 13060+00260G | 0 | 7.90 | 2.07 |
| J130702.89+563158.4 | 13090+56415G | 0 | 1.38 | 0.45 |
| J130801.17+530751.2 | 13090+53003F | 0 | 9.58 | 1.35 |
| J130842.23+021924.4 | 13090+02100G | 0 | 4.18 | 0.86 |
| J131015.97+541620.5 | 13120+54251G | 0 | 1.22 | 1.13 |
| J131130.21+555849.3 | 13120+55553G | 0 | 1.23 | 0.86 |
| J131140.26−020422.2 | 13120−02100G | 0 | 1.56 | 1.36 |
| J131156.20+602022.1 | 13120+60210J | 0 | 1.43 | 0.93 |

Continued on Next Page...

TABLE A.1 – Continued

| SDSS Name (1) | FIRST field (2) | Flag (3) | $F_{int}$ (mJy) (4) | Log($\mathcal{R}$) (5) |
|---|---|---|---|---|
| J131327.47−023232.9 | 13120−02360G | 0 | 1.67 | 0.87 |
| J131510.07+432547.0 | 13150+43219F | 0 | 1.95 | 0.66 |
| J131549.17+124936.2 | 13150+13056I | 1 | 1.49 | 1.18 |
| J131639.74+445235.0 | 13180+45013F | 0 | 4.53 | 1.01 |
| J131659.37+035319.8 | 13180+03542I | 0 | 1.55 | 1.52 |
| J131750.32+601041.0 | 13180+60210J | 0 | 1.81 | 0.65 |
| **J131827.00+620036.2** | **13180+62070J** | **0** | **36.79** | **2.14** |
| J132022.86+434807.8 | 13210+43547F | 0 | 2.34 | 1.19 |
| J132045.25−002449.6 | 13210−00260G | 0 | 4.84 | 1.71 |
| J132135.33−001305.7 | 13210−00260G | 0 | 2.15 | 0.69 |
| J132249.21+545528.2 | 13240+55098G | 0 | 8.87 | 0.77 |
| J132314.91+463122.2 | 13240+46439F | 0 | 3.03 | 1.09 |
| J132340.92+425417.7 | 13240+42493F | 0 | 2.39 | 1.10 |
| **J132404.20+433407.1** | **13240+43219F** | **0** | **3.62** | **1.36** |
| J132418.25+584911.6 | 13240+58396J | 0 | 6.06 | 0.94 |
| J132420.12+634059.9 | 13240+63285J | 0 | 1.74 | 1.41 |
| J132552.16+113709.7 | 13270+11464I | 0 | 2.98 | 0.93 |
| J132655.41+124658.6 | 13270+12392I | 0 | 1.80 | 0.81 |
| J132832.58−023321.4 | 13300−02360G | 0 | 0.97 | 0.86 |
| **J132834.14−012917.6** | **13300−01180G** | **0** | **15.59** | **1.30** |
| J132834.37−030744.7 | 13300−03020G | 0 | 8.81 | 1.81 |
| J133138.03+013151.6 | 13330+01180G | 0 | 2.99 | 0.64 |
| J133231.17+035928.0 | 13330+03542I | 0 | 1.28 | 0.32 |
| J133237.94+593053.7 | 13300+59294J | 0 | 0.93 | 0.26 |
| J133248.70+415218.6 | 13330+41450E | 0 | 7.63 | 1.53 |
| **J133253.27+020045.6** | **13330+02100G** | **0** | **371.12** | **3.24** |
| J133312.42+013023.7 | 13330+01180G | 0 | 2.27 | 1.03 |
| J133316.83+040826.1 | 13330+04203I | 0 | 5.71 | 1.41 |
| J133345.47+414127.7 | 13330+41450E | 0 | 1.95 | 0.68 |
| J133409.37+455754.8 | 13330+46093F | 0 | 1.13 | 1.12 |
| J133436.04+560639.8 | 13360+55553G | 0 | 1.64 | 1.03 |
| **J133437.48+563147.9** | **13360+56415G** | **0** | **85.15** | **2.62** |
| J133440.74+040513.4 | 13360+03542I | 0 | 0.96 | 1.19 |
| J133450.43+010219.0 | 13360+00520G | 0 | 1.70 | 1.13 |
| J133505.14+564354.7 | 13360+56415G | 0 | 3.37 | 1.88 |
| J133636.65+420934.1 | 13360+42170E | 0 | 3.55 | 0.54 |
| J133706.93+051803.3 | 13360+05125I | 0 | 6.30 | 1.64 |
| J133724.34+600541.7 | 13360+59550J | 0 | 4.56 | 1.42 |
| J133848.18+602643.9 | 13360+60210J | 0 | 1.31 | 0.54 |
| J133912.38+535527.4 | 13390+53420G | 0 | 2.83 | 0.65 |
| J133933.98+554614.1 | 13390+55553G | 0 | 3.88 | 1.23 |
| J134113.93−005315.1 | 13420−00520G | 0 | 5.35 | 0.60 |
| J134206.56+050523.8 | 13420+05125I | 0 | 3.85 | 0.71 |
| J134243.57+464224.0 | 13420+46439F | 0 | 1.26 | 0.47 |

Continued on Next Page...

TABLE A.1 – Continued

| SDSS Name (1) | FIRST field (2) | Flag (3) | $F_{int}$ (mJy) (4) | Log($\mathcal{R}$) (5) |
|---|---|---|---|---|
| J134302.65+445018.6 | 13420+45013F | 0 | 1.20 | 0.48 |
| J134405.69+435358.1 | 13450+43547F | 0 | 1.14 | 1.34 |
| **J134545.35+533252.3** | **13450+53420G** | **0** | **79.60** | **1.88** |
| J134615.89+580008.1 | 13480+58155J | 0 | 1.71 | 0.74 |
| **J134617.54+622045.4** | **13480+62339J** | **0** | **23.24** | **1.31** |
| J134642.90+555038.4 | 13480+55553G | 0 | 4.48 | 1.67 |
| J134703.00+110519.1 | 13480+10536I | 0 | 1.30 | 1.51 |
| J134826.85−005943.9 | 13480−00520G | 0 | 0.91 | 0.50 |
| J134916.60+631351.9 | 13480+63011J | 0 | 9.46 | 1.65 |
| J134934.42+582805.2 | 13480+58396J | 0 | 1.21 | 1.23 |
| J134952.84+020445.1 | 13510+02100G | 0 | 0.85 | −0.61 |
| J135516.54+561244.7 | 13540+55553G | 0 | 6.29 | 0.73 |
| J135558.09+001530.5 | 13570+00260G | 0 | 4.99 | 1.80 |
| J135616.88+482236.4 | 13570+48304F | 0 | 2.40 | 0.94 |
| J135617.79−023101.4 | 13570−02360G | 0 | 1.84 | 0.98 |
| J135621.85+013223.6 | 13570+01440G | 0 | 1.52 | 1.03 |
| J135646.10+102609.0 | 13570+10273I | 0 | 59.58 | 2.22 |
| J135857.34+455630.3 | 14000+46093F | 0 | 1.54 | 0.88 |
| J135934.04+553606.2 | 14000+55553G | 0 | 1.52 | 0.92 |
| J140018.42+050242.2 | 14000+05125I | 0 | 10.00 | 0.75 |
| J140119.02−021126.7 | 14000−02100G | 0 | 3.86 | 1.72 |
| J140127.69+025606.1 | 14000+03020G | 0 | 1.54 | 0.70 |
| J140200.55+420441.5 | 14000+42170F | 0 | 1.23 | 0.30 |
| J140404.18+464209.7 | 14030+46439F | 0 | 1.42 | 0.66 |
| J140438.80+432707.4 | 14060+43219F | 0 | 1.46 | −0.26 |
| J140519.23+034533.9 | 14060+03542I | 0 | 4.51 | 1.52 |
| J140638.22+010254.6 | 14060+00520G | 0 | 9.19 | 2.17 |
| J140829.26+562823.5 | 14090+56415G | 1 | 1.91 | 1.34 |
| J140914.35+565625.6 | 14090+56415G | 0 | 2.81 | 1.10 |
| J141049.55+015134.9 | 14120+01440G | 0 | 2.09 | 1.30 |
| J141117.98+045730.1 | 14120+04464I | 0 | 1.00 | 0.80 |
| J141144.22+052615.0 | 14120+05386I | 0 | 1.92 | 1.35 |
| J141403.15+352311.3 | 14150+35367E | 0 | 25.01 | 1.54 |
| J141556.84+052029.5 | 14150+05125I | 0 | 1.12 | 0.23 |
| **J141613.36+021907.8** | **14150+02100G** | **0** | **21.08** | **1.54** |
| J141630.81+013708.0 | 14180+01440G | 0 | 1.72 | 0.45 |
| J141700.81+445606.3 | 14180+45013F | 0 | 0.96 | −0.33 |
| J141710.52+050911.1 | 14180+05125I | 0 | 1.25 | 0.91 |
| J141920.65+043623.3 | 14180+04464I | 0 | 2.90 | 1.00 |
| J142004.29+470716.8 | 14210+47189F | 0 | 2.52 | 0.64 |
| J142237.91+044848.5 | 14240+04464I | 0 | 1.65 | 3.75 |
| J142314.19+505537.3 | 14240+51003F | 0 | 139.13 | 2.25 |
| J142410.21+512508.6 | 14240+51396F | 0 | 1.49 | 1.53 |
| J142424.22+595300.5 | 14240+59550J | 0 | 2.51 | 0.25 |

Continued on Next Page...

TABLE A.1 – Continued

| SDSS Name (1) | FIRST field (2) | Flag (3) | $F_{int}$ (mJy) (4) | Log($\mathcal{R}$) (5) |
|---|---|---|---|---|
| J142545.90+002242.7 | 14270+00260G | 0 | 66.53 | 2.53 |
| J142646.86−003033.4 | 14270−00260G | 0 | 1.27 | 1.59 |
| J142704.55+355409.5 | 14270+36065E | 0 | 3.03 | 0.97 |
| J142817.98+571018.4 | 14300+57282I | 1 | 4.80 | 0.96 |
| J142936.23+454626.5 | 14300+46093F | 0 | 3.28 | 0.98 |
| J143237.25+012050.8 | 14330+01180G | 0 | 3.09 | 1.24 |
| J143248.13+492139.9 | 14330+49440F | 0 | 2.42 | 1.56 |
| J143411.18+501640.7 | 14360+50218F | 0 | 3.22 | 1.49 |
| J143510.30+494819.3 | 14360+49440F | 0 | 3.00 | 0.72 |
| J143515.65+023221.5 | 14360+02360G | 0 | 1.09 | −0.19 |
| J143714.18+612728.9 | 14360+61403J | 0 | 1.17 | 0.85 |
| J143727.80−002343.5 | 14360−00260G | 0 | 10.08 | 1.71 |
| J143807.17+483331.3 | 14390+48304F | 0 | 4.12 | 0.58 |
| J143818.58+360222.4 | 14390+36065E | 0 | 1.27 | 1.17 |
| J143830.23+353916.1 | 14390+35367E | 0 | 3.59 | 1.08 |
| J143918.60−011824.8 | 14390−01180G | 0 | 0.63 | 1.05 |
| J143952.91+392358.9 | 14390+39393E | 0 | 1.11 | 0.35 |
| J144012.76+615633.0 | 14420+62070J | 0 | 2.88 | 0.46 |
| J144205.82−024803.1 | 14420−02360G | 0 | 2.45 | 1.48 |
| J144239.82+421141.1 | 14420+42170F | 0 | 3.44 | 1.53 |
| J144250.45+545308.5 | 14420+55098G | 0 | 2.21 | 0.49 |
| **J144302.76+520137.2** | **14450+52196F** | **0** | **279.24** | **2.67** |
| J144331.27+492335.2 | 14450+49440F | 0 | 2.88 | 0.83 |
| J144341.53+383521.8 | 14450+38377E | 0 | 12.95 | 2.29 |
| J144739.32+610656.0 | 14480+61137J | 0 | 3.12 | 0.77 |
| J144819.36+443232.7 | 14480+44278F | 0 | 4.55 | 0.55 |
| J144825.10+355946.6 | 14480+36065E | 0 | 1.48 | 0.21 |
| J144930.49−004746.3 | 14510−00520G | 0 | 2.36 | 0.88 |
| J145054.16+350837.8 | 14510+35071E | 0 | 5.26 | 1.54 |
| J145110.06+490813.6 | 14510+49069F | 0 | 0.89 | 0.49 |
| J145116.54−023627.8 | 14510−02360G | 0 | 38.55 | 2.64 |
| J145305.80+015501.4 | 14540+01440G | 0 | 2.58 | 1.57 |
| J145310.45+580955.5 | 14540+58155J | 0 | 2.47 | 0.93 |
| J145549.42+485436.3 | 14570+49069F | 0 | 6.35 | 1.66 |
| J145706.80+494008.4 | 14570+49440F | 0 | 14.33 | 0.77 |
| J145732.32+341746.6 | 14570+34082E | 0 | 1.61 | 1.53 |
| J145826.24+015646.2 | 14570+01440G | 0 | 5.50 | 1.89 |
| J145836.45+011939.1 | 15000+01180G | 0 | 3.71 | 1.27 |
| J145911.57+455731.3 | 15000+46093F | 0 | 1.26 | 1.25 |
| J150026.19−005428.3 | 15000−00520G | 0 | 1.43 | 1.00 |
| J150122.30+502228.4 | 15030+50218F | 0 | 3.77 | 1.72 |
| J150150.51+493338.4 | 15030+49440F | 0 | 3.09 | 1.72 |
| J150225.26+490220.6 | 15030+49069F | 0 | 1.91 | 1.00 |
| J150420.90+015159.4 | 15030+01440G | 0 | 2.98 | 1.15 |

Continued on Next Page...

TABLE A.1 – Continued

| SDSS Name (1) | FIRST field (2) | Flag (3) | $F_{int}$ (mJy) (4) | Log($\mathcal{R}$) (5) |
|---|---|---|---|---|
| J150513.94+030143.5 | 15060+03020G | 0 | 1.91 | 0.63 |
| J150521.92+014149.8 | 15060+01440G | 0 | 1.52 | 0.76 |
| J150556.40+011641.5 | 15060+01180G | 0 | 5.48 | 1.90 |
| J150556.55+034226.3 | 15060+03542I | 0 | 8.83 | 0.11 |
| J150719.94+002905.0 | 15060+00260G | 0 | 4.55 | 1.11 |
| J150740.93+445331.6 | 15090+45013F | 0 | 2.25 | 0.99 |
| J150745.00+512710.2 | 15090+51396F | 0 | 3.04 | 0.37 |
| J150803.17+485728.1 | 15090+49069F | 0 | 5.41 | 1.27 |
| J150853.95−001148.9 | 15090+00000G | 0 | 22.95 | 1.23 |
| J150904.21+043441.7 | 15090+04464I | 0 | 20.77 | 1.66 |
| J151000.87+422857.5 | 15090+42170E | 0 | 1.79 | 0.96 |
| J151021.25−020402.7 | 15090−02100G | 0 | 1.06 | 0.50 |
| J151129.01+561317.5 | 15120+55553G | 0 | 2.61 | 0.91 |
| J151131.32+502218.9 | 15120+50218F | 0 | 2.44 | 1.12 |
| J151144.93+400951.2 | 15120+40104E | 0 | 1.00 | 1.22 |
| J151325.90+465408.0 | 15120+46439F | 0 | 0.79 | −0.30 |
| J151335.51+324141.8 | 15150+32407E | 0 | 2.26 | 1.23 |
| J151420.52+424445.4 | 15150+42493F | 0 | 0.98 | 0.47 |
| J151513.58+552504.2 | 15150+55098G | 0 | 9.25 | 2.50 |
| J151600.40+572415.7 | 15180+57282I | 0 | 3.77 | 1.25 |
| J151600.58+342119.1 | 15150+34082E | 0 | 2.46 | 1.37 |
| **J151640.22+001501.8** | **15180+00260G** | **0** | **755.72** | **3.42** |
| **J151913.35+362343.4** | **15180+36364E** | **0** | **30.30** | **2.33** |
| J151919.20+385829.8 | 15180+39084E | 0 | 1.39 | 1.42 |
| J152019.74−013611.2 | 15210−01440G | 0 | 1.40 | 1.55 |
| J152036.04+312225.8 | 15210+31143E | 0 | 1.68 | 1.13 |
| J152205.40+393441.2 | 15210+39393E | 0 | 2.52 | 1.18 |
| J152333.07+573949.6 | 15240+57282I | 0 | 2.52 | 1.36 |
| J152515.18+601409.0 | 15240+60210J | 0 | 1.28 | 0.76 |
| J152620.63+480317.2 | 15270+47544F | 0 | 2.27 | 0.62 |
| **J152942.20+350851.2** | **15300+35071E** | **0** | **89.99** | **2.09** |
| J153015.54+531035.1 | 15300+53003F | 0 | 1.64 | 0.85 |
| J153031.17+424656.2 | 15300+42493F | 0 | 2.15 | 1.21 |
| J153043.08−002259.1 | 15300−00260G | 0 | 0.92 | 0.73 |
| J153502.27+345538.3 | 15360+35071E | 0 | 0.86 | 0.91 |
| J153529.12+532138.6 | 15360+53420G | 0 | 9.43 | 1.49 |
| J153552.40+575409.4 | 15360+58155J | 0 | 5.32 | −0.14 |
| J153619.28+334627.6 | 15360+33389E | 0 | 1.12 | 0.96 |
| J153732.62+494247.7 | 15390+49440F | 0 | 1.43 | 0.93 |
| J153911.16+002600.7 | 15390+00260G | 0 | 0.93 | 0.75 |
| J153950.96+564333.6 | 15390+56415G | 0 | 1.34 | 1.13 |
| J153952.21+334930.7 | 15390+33389E | 0 | 2.12 | 0.99 |
| J154019.57−020505.4 | 15390−02100G | 0 | 4.31 | 0.55 |
| J154348.62+401324.9 | 15450+40104E | 0 | 2.75 | 0.57 |

Continued on Next Page...

TABLE A.1 – Continued

| SDSS Name (1) | FIRST field (2) | Flag (3) | $F_{int}$ (mJy) (4) | Log($\mathcal{R}$) (5) |
|---|---|---|---|---|
| J154512.92+300508.1 | 15450+30170E | 0 | 6.26 | 1.64 |
| J154518.05+463838.0 | 15450+46439F | 0 | 3.67 | 0.79 |
| J154617.76+500824.4 | 15480+50218F | 0 | 26.98 | 2.44 |
| J154724.34+513747.0 | 15480+51396F | 0 | 2.19 | 0.77 |
| J154751.93+025550.8 | 15480+03020G | 0 | 2.40 | 0.40 |
| J154833.03+442226.0 | 15480+44278F | 0 | 3.84 | 0.68 |
| J155021.40+295027.8 | 15510+29486E | 0 | 16.29 | 1.83 |
| J155141.42+351315.0 | 15510+35071E | 0 | 2.21 | 1.41 |
| **J155206.58−005339.3** | **15510−00520G** | **0** | **92.17** | **2.90** |
| J155315.94+440749.3 | 15540+43547F | 0 | 3.18 | 1.57 |
| J155329.56+353150.0 | 15540+35367E | 0 | 0.93 | 0.93 |
| J155417.43+323837.8 | 15540+32407E | 0 | 2.52 | −0.00 |
| J155451.13+461917.4 | 15540+46093F | 0 | 0.91 | 0.60 |
| J155501.44+540326.9 | 15570+54251G | 0 | 1.46 | 0.62 |
| J155522.04+281323.1 | 15540+28240E | 0 | 14.83 | 2.06 |
| J155539.28+523000.4 | 15570+52196F | 0 | 1.09 | 0.97 |
| J155609.80+030922.3 | 15570+03020G | 0 | 1.05 | −0.04 |
| J155620.24+521520.0 | 15570+52196F | 0 | 1.60 | 0.19 |
| J155625.90+090318.6 | 15570+09084I | 0 | 3.47 | 0.54 |
| J155707.13+450700.0 | 15570+45013F | 0 | 3.75 | 1.20 |
| J155909.62+350147.4 | 16000+35071E | 0 | 3.39 | 0.12 |
| J155930.39+380838.7 | 16000+38071E | 0 | 2.41 | 1.41 |
| J155936.13+544203.7 | 16000+54251G | 0 | 4.20 | 1.21 |
| J160006.09+395402.9 | 16000+39393E | 0 | 2.02 | 1.62 |
| J160508.87+323921.5 | 16060+32407E | 0 | 1.03 | 0.66 |
| J160558.12+440319.5 | 16060+43547F | 1 | 2.34 | 0.78 |
| J160713.91+483326.2 | 16090+48304F | 0 | 2.47 | 0.41 |
| J160732.86+484619.9 | 16090+49069F | 0 | 1.50 | 0.11 |
| J161035.44+480022.5 | 16120+47544F | 0 | 7.34 | 1.47 |
| J161047.72+330337.5 | 16120+33097E | 0 | 6.21 | 0.54 |
| J161141.95+495847.9 | 16120+50218F | 0 | 1.50 | 0.33 |
| J161143.57+494644.0 | 16120+49440F | 0 | 0.82 | 0.14 |
| J161156.31+521116.8 | 16120+52196F | 0 | 3.67 | 0.62 |
| J161159.54+311041.5 | 16120+31143E | 0 | 7.45 | 1.12 |
| J161241.28+003751.7 | 16120+00260G | 0 | 2.54 | 0.84 |
| J161259.83+421940.3 | 16120+42170E | 0 | 3.60 | 1.15 |
| J161413.20+260416.2 | 16150+26050E | 0 | 17.75 | 0.78 |
| J161436.82+283906.0 | 16150+28521E | 0 | 1.31 | 0.53 |
| J161454.55+261930.1 | 16150+26326E | 0 | 1.17 | 1.20 |
| J161456.18+413055.8 | 16150+41450E | 0 | 5.00 | 1.36 |
| J161849.25+442517.2 | 16180+44278F | 0 | 3.09 | 0.41 |
| J162021.14+301020.5 | 16210+30170E | 0 | 1.43 | 0.89 |
| J162209.41+352107.4 | 16210+35071E | 0 | 2.06 | 1.51 |
| J162453.96+420700.1 | 16240+42170E | 0 | 1.41 | 1.64 |

Continued on Next Page...

TABLE A.1 – Continued

| SDSS Name (1) | FIRST field (2) | Flag (3) | $F_{int}$ (mJy) (4) | Log($\mathcal{R}$) (5) |
|---|---|---|---|---|
| J162607.24+335915.2 | 16270+34082E | 0 | 3.74 | 0.24 |
| J162633.93+480230.1 | 16270+47544F | 0 | 1.31 | 0.66 |
| J162726.67+350815.6 | 16270+35071E | 0 | 0.80 | 0.52 |
| J162750.55+473623.5 | 16270+47544F | 0 | 4.07 | 0.58 |
| J162755.42+464248.7 | 16270+46439F | 0 | 1.83 | 0.72 |
| J162824.49+452810.9 | 16300+45351F | 0 | 0.68 | 1.14 |
| J162833.05+330853.9 | 16300+33097E | 0 | 7.47 | 1.57 |
| J162901.31+400759.9 | 16300+40104E | 0 | 11.94 | 1.45 |
| J163115.52+235257.4 | 16300+23478E | 0 | 4.47 | 1.60 |
| J163124.24+253054.6 | 16300+25374E | 0 | 2.68 | 1.19 |
| J163306.82+415740.1 | 16330+41450E | 0 | 1.18 | 0.78 |
| J163323.58+471858.9 | 16330+47189F | 0 | 65.02 | 2.05 |
| J163344.99+372335.1 | 16330+37367E | 0 | 1.04 | 1.15 |
| J163348.87+355318.5 | 16330+36065E | 0 | 1.24 | 0.68 |
| J163453.66+231242.6 | 16360+23206E | 0 | 2.83 | 0.84 |
| J163516.93+371228.3 | 16360+37065E | 0 | 3.28 | 1.66 |
| J163545.58+372243.7 | 16360+37367E | 1 | 1.81 | 0.74 |
| J163605.98+441357.9 | 16360+44278F | 0 | 5.17 | 1.91 |
| J163631.28+420242.4 | 16360+42170E | 0 | 1.18 | 0.31 |
| J163700.22+222114.0 | 16360+22263G | 0 | 1.39 | 1.01 |
| **J163856.53+433512.5** | **16390+43219F** | **0** | **47.73** | **2.07** |
| J163859.48+390808.8 | 16390+39084E | 0 | 1.42 | 1.31 |
| J163931.78+390845.3 | 16390+39084E | 0 | 0.72 | 0.49 |
| J164054.94+211030.8 | 16420+21052G | 0 | 5.02 | 1.30 |
| J164100.10+345452.6 | 16420+35071E | 0 | 2.69 | 0.95 |
| J164126.91+432121.6 | 16420+43219F | 0 | 27.73 | 2.19 |
| J164211.95+302713.2 | 16420+30170E | 0 | 3.78 | 1.46 |
| J164232.17+431417.4 | 16420+43219F | 0 | 3.86 | 1.53 |
| J164329.09+442351.6 | 16450+44278F | 0 | 1.53 | 0.86 |
| J164331.91+304835.5 | 16450+30456E | 0 | 65.48 | 2.02 |
| J164430.26+245728.3 | 16450+25099E | 0 | 2.65 | 1.22 |
| **J164442.53+261913.2** | **16450+26326E** | **0** | **90.80** | **2.50** |
| J164819.02+302210.8 | 16480+30170E | 0 | 10.42 | 1.42 |
| J165028.00+291052.9 | 16510+29203E | 0 | 4.52 | 1.26 |
| J165252.60+360057.4 | 16540+36065E | 0 | 2.22 | 1.04 |
| J165551.37+214601.8 | 16570+21592G | 0 | 7.22 | 0.31 |
| J165601.60+211241.1 | 16570+21052G | 0 | 2.27 | 0.49 |
| J165627.31+623226.6 | 16540+62339J | 0 | 1.15 | 0.34 |
| J165642.07+363049.2 | 16570+36364E | 0 | 1.46 | 0.91 |
| J165641.98+632307.7 | 16540+63285J | 0 | 0.92 | 1.22 |
| J165824.16+344042.7 | 16570+34376E | 1 | 1.53 | 1.18 |
| J165939.77+183436.8 | 17000+18243I | 0 | 2.56 | 0.60 |
| **J170013.70+400855.6** | **17000+40104E** | **0** | **11.90** | **1.37** |
| J170033.27+355256.5 | 17000+36065E | 0 | 1.64 | 0.45 |

Continued on Next Page...

TABLE A.1 – Continued

| SDSS Name (1) | FIRST field (2) | Flag (3) | $F_{int}$ (mJy) (4) | Log($\mathcal{R}$) (5) |
|---|---|---|---|---|
| J170226.20+341117.3 | 17030+34082E | 0 | 1.10 | 0.24 |
| J170231.06+324719.6 | 17030+32407E | 0 | 1.52 | −0.30 |
| **J170425.11+333145.9** | **17030+33389E** | **0** | **7.87** | **1.28** |
| J171013.42+334402.6 | 17090+33389E | 0 | 4.60 | 0.43 |
| J171024.04+314818.4 | 17090+31430E | 0 | 2.59 | 1.26 |
| **J171322.58+325628.0** | **17120+33097E** | **0** | **38.62** | **1.74** |
| J171601.93+311213.8 | 17150+31143E | 0 | 2.42 | −0.24 |
| J171647.40+310403.0 | 17180+31143E | 0 | 81.83 | 2.82 |
| J171807.73+304705.6 | 17180+30456E | 0 | 1.33 | 1.36 |
| J171850.30+304201.6 | 17180+30456E | 0 | 0.64 | 0.19 |
| J171930.57+293412.8 | 17210+29203E | 0 | 1.23 | 0.50 |
| J172711.81+632241.8 | 17300+63285J | 0 | 1.23 | 0.33 |
| J173107.87+620026.1 | 17300+62070J | 0 | 0.98 | 0.17 |
| J210109.58−054747.3 | 21015−05517G | 0 | 2.46 | 1.07 |
| J210358.74−072802.4 | 21045−07364G | 0 | 3.79 | 0.92 |
| J211307.77−055541.6 | 21135−05517G | 0 | 2.27 | 0.89 |
| J211843.24−063618.0 | 21195−06440G | 0 | 77.44 | 1.98 |
| J211852.96−073227.5 | 21195−07364G | 0 | 98.68 | 2.58 |
| J212512.48−071329.8 | 21255−07102G | 0 | 4.24 | 1.48 |
| J213400.60−074942.6 | 21345−08027G | 0 | 4.29 | 1.71 |
| J213814.57−004701.6 | 21375−00390E | 0 | 3.28 | 1.46 |
| J214054.55+002538.2 | 21405+00390E | 0 | 0.77 | −0.34 |
| J214247.88+000156.9 | 21435+00130E | 0 | 1.78 | 1.26 |
| J215226.03−081024.9 | 21525−08027G | 0 | 181.26 | 2.18 |
| J215924.07+011305.4 | 21585+01050E | 0 | 2.10 | 0.20 |
| **J220233.84−073225.0** | **22015−07364G** | **0** | **2.31** | **0.22** |
| J220509.50−004820.6 | 22045−00390E | 0 | 0.74 | 0.12 |
| J221542.29−003609.7 | 22165−00390E | 0 | 1.74 | 0.19 |
| J222246.62−081943.9 | 22225−08290G | 0 | 4.55 | 0.60 |
| J222634.05−090106.2 | 22255−08553G | 0 | 1.72 | 1.48 |
| J222852.76−090452.5 | 22285−08553G | 0 | 4.06 | 0.65 |
| J223438.05−092146.0 | 22345−09216G | 0 | 1.87 | 0.63 |
| J224605.44−091925.1 | 22465−09216G | 0 | 0.82 | 0.56 |
| J224740.28−094012.3 | 22465−09479G | 0 | 1.39 | 1.48 |
| J224817.51−101547.1 | 22495−10142G | 0 | 19.22 | 1.23 |
| J224824.63+000920.7 | 22495+00130E | 0 | 2.38 | 0.72 |
| J225331.39+004825.5 | 22525+00390E | 0 | 4.80 | 1.02 |
| J225810.01−011516.2 | 22585−01050E | 0 | 4.00 | 0.65 |
| J230007.93−082020.0 | 23015−08290G | 0 | 2.71 | 1.50 |
| J230231.14+000147.6 | 23015+00130E | 0 | 3.56 | 1.55 |
| J230306.88−000508.9 | 23045−00130E | 0 | 1.32 | 1.04 |
| J230321.72+011056.3 | 23045+01050E | 0 | 2.11 | 1.13 |
| J230727.37−003313.5 | 23075−00390E | 0 | 0.90 | 0.72 |
| J232300.00−005359.3 | 23225−01050E | 0 | 1.03 | 0.25 |

Continued on Next Page...

TABLE A.1 – Continued

| **SDSS Name (1)** | **FIRST field (2)** | **Flag (3)** | **$F_{int}$ (mJy) (4)** | **Log($\mathcal{R}$) (5)** |
|---|---|---|---|---|
| J232714.52−102317.5 | 23285−10142G | 0 | 2.25 | 0.99 |
| J234736.46−103005.6 | 23465−10405G | 0 | 3.58 | 1.34 |
| **J235156.12−010913.3** | **23525−01050E** | **0** | **444.99** | **2.30** |
| J235240.10+002653.4 | 23525+00390E | 0 | 2.59 | 1.53 |
| J235251.87+003814.9 | 23525+00390E | 0 | 2.38 | 1.19 |

Table 1 Notes: Col.(1): SDSS Name; Col.(2): FIRST Name; Col.(3): Flag (1 = bad flag); Col.(4): Integrated Radio Flux at 1.4 GHz (mJy); Col.(5): Radio Loudness Parameter - Log($\mathcal{R}$). All objects in bold face are extended sources in Table 2. Note that there are only 51 extended sources in this table and not 63, since there are 12 sources not listed here that have no core emission.

## A.2 Table of Extended Sources

TABLE A.2: THE EXTENDED SDSS AND FIRST SAMPLE

| SDSS Name (1) | Radio Catalogue and Source Name (2) | Redshift (3) | Total Integrated Flux (mJy) (4) | Projected Physical Size (Mpc) (5) | Radio Classification (6) |
|---|---|---|---|---|---|
| J005550.75-101905.6 | FBQS J0055-1019 | 0.3091 | 48.58 | 0.94 | GRG/FRII |
| J013352.65+011345.3 | 87GB 013118.8+005811 | 0.3081 | 67.15 | 0.62 | FRII |
| J072406.79+380348.6 | | 0.2413 | 203.46 | 0.58 | FRII |
| J074906.50+451033.9 | B3 0745+453,GB6 J0749+4510 | 0.1921 | 117.74 | 0.12 | Core + weak jet(5%) |
| J075244.19+455657.3 | B30749+460A,6CB074906.2+460422 | 0.0518 | 238.41 | 0.14 | FRI |
| J075643.09+310248.7 | | 0.2715 | 22.59 | 0.14 | Classic Triple FRII |
| J080129.57+462622.8 | | 0.3159 | 13.37 | 0.26 | Classic Triple FRII |
| J082133.60+470237.2 | 3C 197.1, *B3 0818+472A | 0.1280 | 1711.27 | 0.06 | Bright FRII |
| J082355.36+244830.4 | | 0.2339 | 2.32 | 0.06 | Faint FRII? |
| J084600.36+070424.6 | 87GB 084319.4+071534 | 0.3421 | 241.53 | 0.85 | GRG/FRII |
| J085348.18+065447.1 | PMN J0853+0654 | 0.2232 | 769.90 | 0.08 | Core + 1 Bright lobe |
| J085627.91+360315.6 | | 0.3449 | 29.96 | 0.20 | FRII? |
| J091133.85+442250.1 | B3 0908+445,GB6 J0911+4422 | 0.2976 | 433.23 | 0.15 | FRI (unresolved) |
| J091401.76+050750.6 | 4C +05.38 | 0.3014 | 328.72 | 0.46 | Large FRII lobe to S |
| J091519.55+563837.8 | | 0.2631 | 19.98 | 0.56 | FRII |
| J092308.16+561455.3 | | 0.2493 | 143.01 | 0.23 | FRII |
| J092837.97+602521.0 | 8C 0924+606 | 0.2955 | 278.21 | 0.25 | FRII |
| J093200.08+553347.4 | 6C B092828.4+554656 | 0.2657 | 73.43 | 0.94 | GRG/FRII |
| J094144.82+575123.6 | GB6 J0941+5751 | 0.1585 | 90.43 | 0.11 | FRII? |
| J094745.14+072520.5 | 3C 227, PKS 0945+07 | 0.0858 | 3117.09 | 0.40 | FRII |
| J095456.89+092955.8 | 4C +09.35, PKS 0952+097 | 0.2984 | 440.66 | 0.17 | FRII? |
| J100726.10+124856.2 | 4C +13.41, PKS 1004+13 | 0.2406 | 959.14 | 0.52 | FRII |
| J100819.11+372903.4 | | 0.0522 | 2.27 | 0.02 | 2nd source in host galaxy? |
| J103143.51+522535.1 | 4C +52.22, GB6 J1031+5225 | 0.1662 | 904.01 | 0.13 | FRII |
| J103458.35+055231.8 | | 0.3002 | 28.72 | 0.15 | one lobe |
| J105220.30+454322.2 | | 0.2406 | 112.05 | 0.26 | FRI (asymmetric) |

Continued on Next Page...

TABLE A.2 – Continued

| SDSS Name (1) | Radio Catalogue and Source Name (2) | Redshift (3) | Total Integrated Flux (mJy) (4) | Projected Physical Size (Mpc) (5) | Radio Classification (6) |
|---|---|---|---|---|---|
| J105500.33+520200.9 | 6C B105202.4+521804 | 0.1874 | 461.07 | 0.21 | FRII |
| J105632.01+430055.9 | | 0.3177 | 19.37 | 0.22 | FRII |
| J110845.48+020240.8 | PKS 1106+023 | 0.1574 | 784.08 | 0.08 | Core + lobe |
| J111432.79+105034.7 | | 0.1931 | 780.25 | 0.23 | FRII/DDRG |
| J113021.40+005823.0 | 4C +01.30, PKS 1127+012 | 0.1323 | 566.72 | 0.16 | X-shaped |
| J114004.35-010527.4 | [WB92] 1137-0048 | 0.3470 | 34.17 | 1.12 | GRG/HYMORS |
| J114047.90+462204.8 | 87GB 113808.0+463858 | 0.1149 | 91.99 | 0.06 | core + bent jet |
| J114958.70+411209.4 | 6C B114721.6+412848 | 0.2497 | 118.46 | 0.33 | FRI |
| J115409.27+023815.0 | 87GB 115136.0+025423 | 0.2106 | 64.12 | 0.26 | FRI |
| J115420.72+452329.4 | | 0.1912 | 964.77 | 0.29 | FRII |
| J120612.67+490226.2 | | 0.1194 | 6.30 | 0.09 | Possible core-only source |
| J122011.89+020342.2 | PKS 1217+02 | 0.2404 | 482.78 | 0.57 | FRI (asymmetric and bent) |
| J123807.77+532555.9 | 87GB123550.3+534219 | 0.3475 | 61.60 | 1.02 | GRG/FRII |
| J123915.39+531414.6 | 6C B123659.8+533024 | 0.2013 | 23.11 | 0.26 | FRII w/ faint core |
| J130359.47+033932.1 | 4C +03.26 | 0.1837 | 210.85 | 0.45 | FRII |
| J131827.00+620036.2 | 87GB131634.0+621623,8C 1316+622 | 0.3075 | 133.41 | 0.38 | FRII |
| J132404.20+433407.1 | | 0.3377 | 239.62 | 1.10 | GRG/FRII |
| J132834.14-012917.6 | | 0.1514 | 158.85 | 0.98 | GRG/FRII |
| J133253.27+020045.6 | 3C 287.1 | 0.2158 | 1759.16 | 0.57 | FRII |
| J133437.48+563147.9 | 87GB133243.4+564710 | 0.3428 | 164.18 | 0.24 | FRI |
| J134545.35+533252.3 | 87GB 134352.4+534755 | 0.1354 | 278.19 | 0.13 | FRII |
| J134617.54+622045.4 | 6C B134441.6+623604 | 0.1164 | 142.99 | 0.15 | FRI (bent) |
| J141613.36+021907.8 | | 0.1582 | 107.70 | 0.67 | possible DDRG? |
| J144302.76+520137.2 | 3C 303 | 0.1412 | 2119.27 | 0.12 | FRII |
| J151640.22+001501.8 | GB6 J1516+0015, 4C +00.56 | 0.0524 | 1090.21 | 0.28 | FRII |
| J151913.35+362343.4 | 6C B151717.1+363448 | 0.2857 | 207.25 | 0.58 | HYMORS? |
| J152942.20+350851.2 | 7C 1527+3519,6C B152745.2+35192 | 0.2873 | 109.27 | 0.08 | Bright core + 1 lobe |

Continued on Next Page...

TABLE A.2 – Continued

| SDSS Name (1) | Radio Catalogue and Source Name (2) | Redshift (3) | Total Integrated Flux (mJy) (4) | Projected Physical Size (Mpc) (5) | Radio Classification (6) |
|---|---|---|---|---|---|
| J155206.58-005339.3 | | 0.2977 | 105.67 | 0.12 | FRI (partially resolved) |
| J163856.53+433512.5 | B3 1637+436A,6CB163723.1+434051 | 0.3390 | 133.04 | 0.45 | FRII |
| J164442.53+261913.2 | | 0.1442 | 110.36 | 0.06 | Unresolved core structure |
| J170013.70+400855.6 | | 0.0941 | 20.68 | 0.07 | faint lobe in SW? |
| J170425.11+333145.9 | | 0.2902 | 36.07 | 0.37 | FRII |
| J171322.58+325628.0 | FBQS J171322.6+325628 | 0.1013 | 44.80 | 0.15 | FRI? |
| J220233.84-073225.0 | | 0.0594 | 3.33 | 0.02 | 2 sources in host galaxy |
| J230545.66-003608.6 | 4C -01.59, PKS 2303-008 | 0.2689 | 517.76 | 0.15 | FRII? |
| J233313.16+004911.8 | PKS 2330+005 | 0.1700 | 317.86 | 0.17 | FRI |
| J235156.12-010913.3 | 4C -01.61, PKS 2349-01 | 0.1740 | 1460.41 | 0.09 | FRII |

Table 2 Notes: Col.(1): SDSS Name; Col.(2): Radio Catalogue and Source Name: taken from the NASA Extragalactic Database (NED); Col.(3): Redshift: taken from SDSS spectra; Col.(4): Total Integrated Radio Flux at 1.4 GHz (mJy); Col.(5): Projected Physical Size: these approximate values are calculated using the FIRST radio maps (Mpc); Col.(6): Radio Classification: Radio Quiet (RQ), Fanaroff & Riley class 1 & 2 (FR I, FR II respectively), Giant Radio Galaxy (GRG), HYbrid MOrphology Radio Source (HYMORS), Double-Double Radio Galaxy (DDRG), X-shaped (having radio emission that resembles an 'x' pattern, where there are two sets of symmetric emission regions at $\sim 90°$ to each other)

# – B –

## Notes on Individual Sources with Extended Emission

Note that in all the FIRST images north is up and east is to the left. The contrast in each image is different due to the very different flux levels found in this sample. Each image is adjusted to achieve the best contrast between the brightest and most faint parts in the field of view.

## B.1 SDSS J005550.75−101905.6

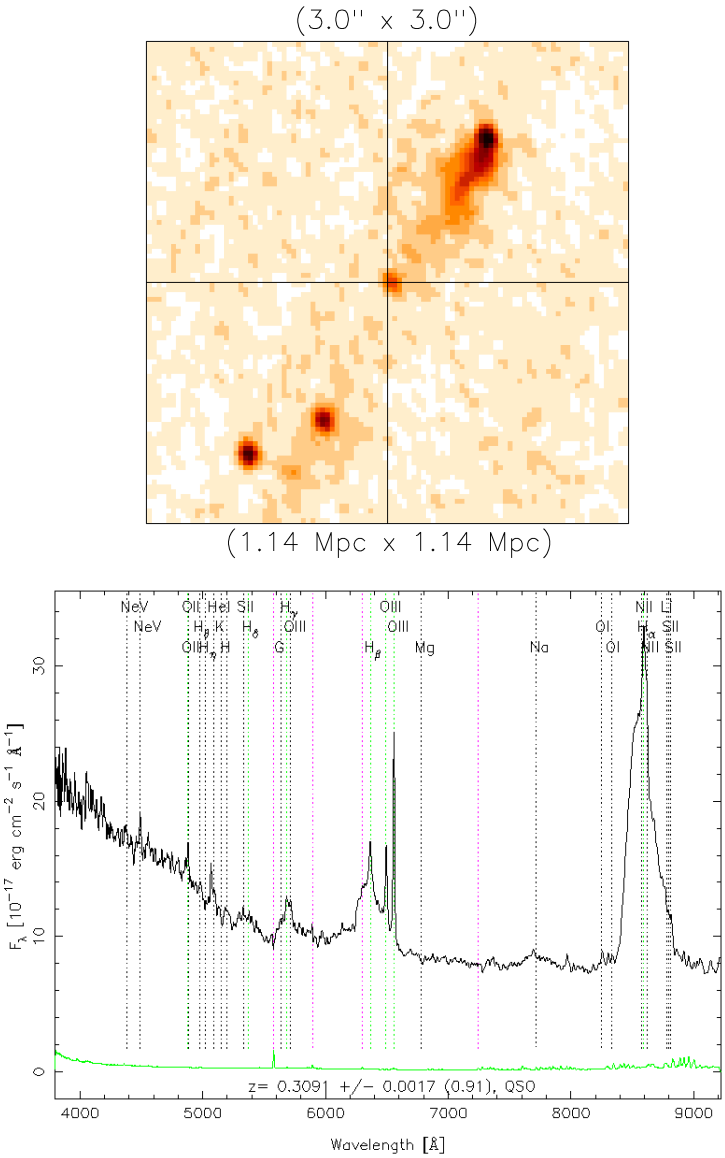


FIGURE B.1: The 3′ x 3′ radio image (top) of SDSS J005550.75−101905.6 shows a core source with extended jets and lobes. This object is a GRG and has a FR II morphology. The total physical extent is ∼ 0.94 Mpc (with z=0.309) and has $F_{1.4\ \mathrm{GHz}} = 48.58$ mJy. The SDSS spectrum (bottom) has very broad Balmer lines ($\mathrm{FWHM}_{\mathrm{H}\alpha} \approx 5850$ km s$^{-1}$). This is an original FIRST source and has the radio designation FBQS J0055−1019 (White et al. 2000).

## B.2 SDSS J013352.65+011345.3

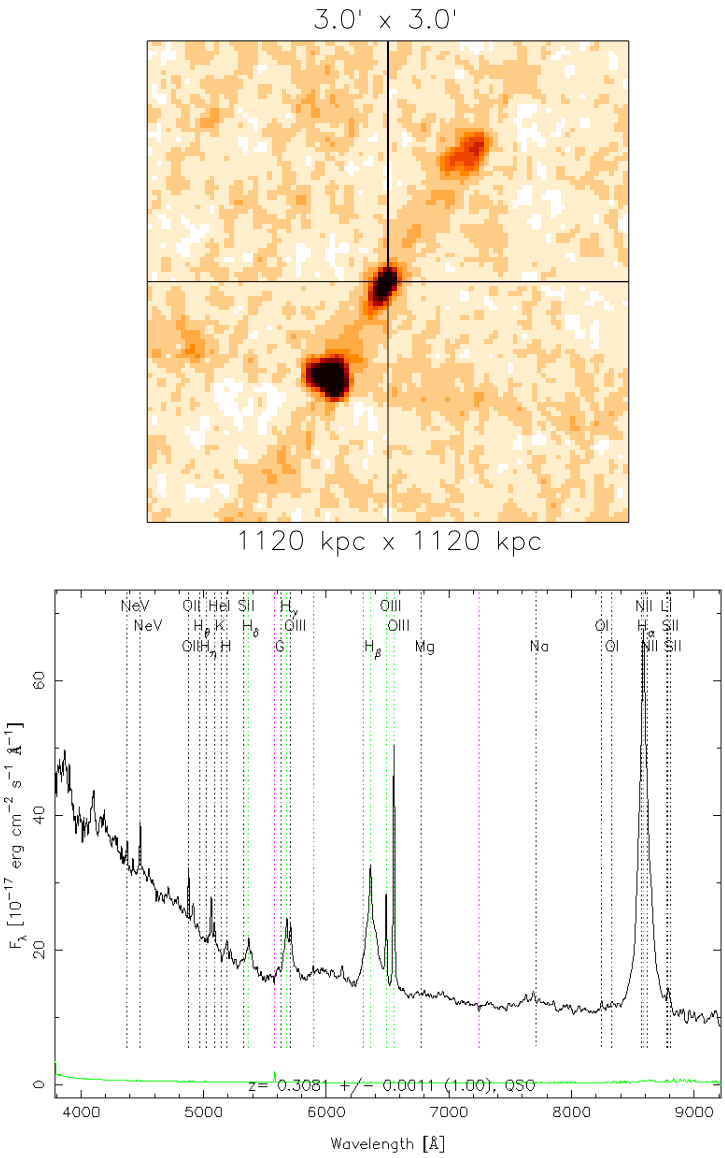


FIGURE B.2: The 3′ x 3′ radio image (top) of SDSS J013352.65+011345.3 shows a bright core source with and two lobes with hot spots. This object has a FR II morphology. The total physical extent is $\sim$ 0.62 Mpc (with z = 0.3081) and has $F_{1.4\ \mathrm{GHz}} = 67.15$ mJy. The SDSS spectrum (bottom) has broad Balmer lines ($FWHM_{H\alpha} \approx 3500$ km s$^{-1}$). This source was identified in the 87 Green Bank (87GB) catalogue as 87GB 013118.8+005811 (Gregory & Condon 1991)

## B.3 SDSS J072406.79+380348.6

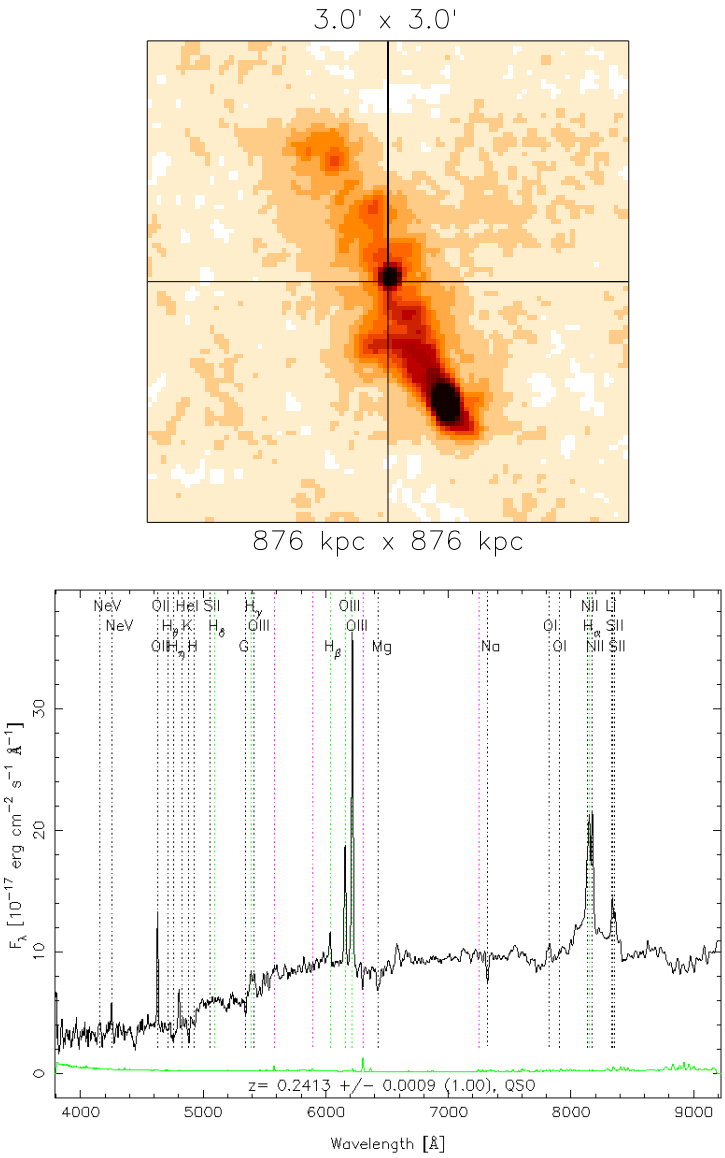


FIGURE B.3: The 3′ x 3′ radio image (top) of SDSS J072406.79+380348.6 shows a bright core source with and two lobes with hot spots. This object has a FR II morphology. The total physical extent is $\sim 0.58$ Mpc (with z = 0.2413) and has $F_{1.4\ \mathrm{GHz}} = 203.46$ mJy. The SDSS spectrum (bottom) has a broad H$\alpha$ base ($\mathrm{FWHM_{H\alpha}} \approx 8100$ km s$^{-1}$). This object has no known designation in any other radio survey.

## B.4 SDSS J074906.50+451033.9

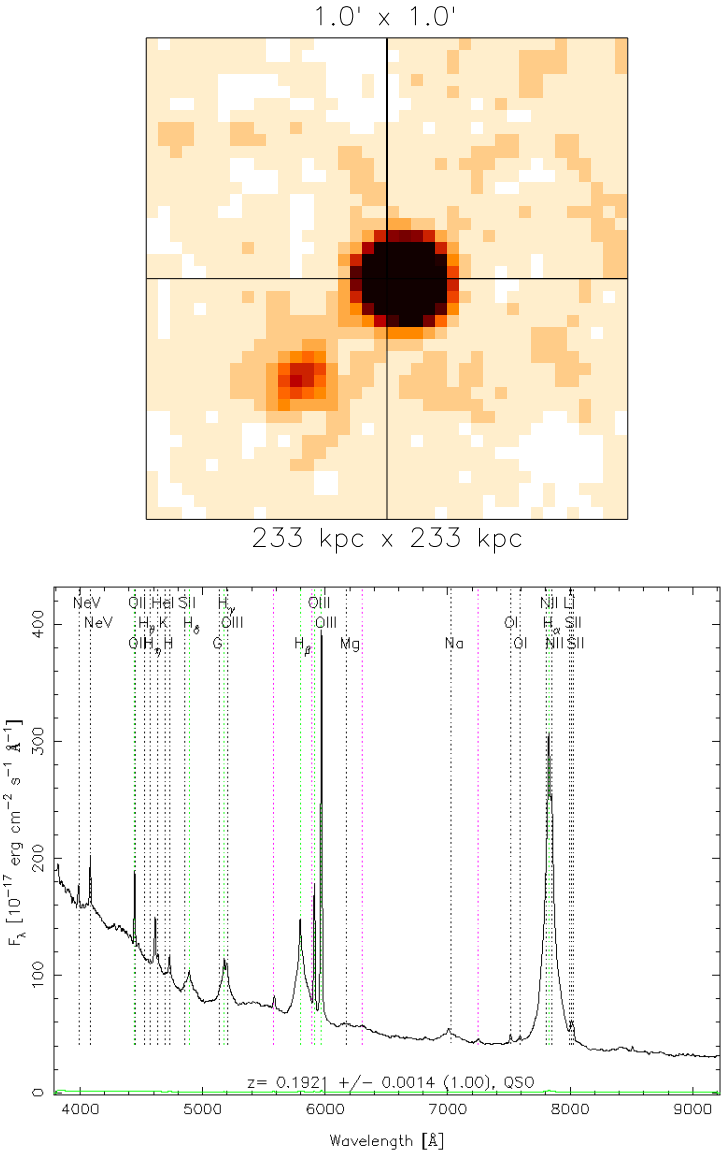


FIGURE B.4: The 1′ x 1′ radio image (top) of SDSS J074906.50+451033.9 shows a core source with a weak jet that is only 5% of the total flux. This object has an unresolved FR I morphology. The total physical extent is $\sim$ 0.12 Mpc (with z = 0.1921) and has $F_{1.4\ \mathrm{GHz}}$ = 117.74 mJy. The SDSS spectrum (bottom) has broad Balmer lines ($FWHM_{H\alpha} \approx 4670$ km $s^{-1}$). This object is found in the B3-VLA (B3) catalogue and is designated B3 0745+453 (Vigotti et al. 1989) and also in the Green Bank 6 (GB6) catalogue and is designated GB6 J0749+4510 (Gregory et al. 1996).

## B.5 SDSS J075244.19+455657.3

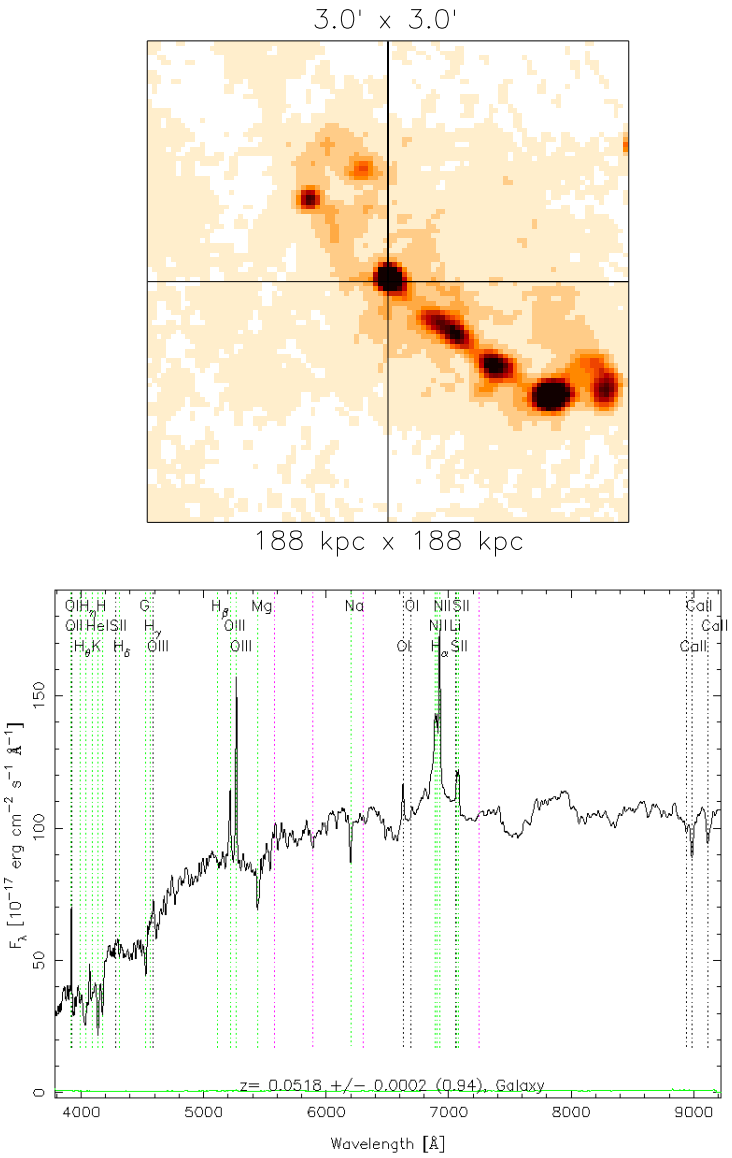


FIGURE B.5: The 3′ x 3′ radio image (top) of SDSS J075244.19+455657.3 shows a bright core source and a strong jet that terminates with a hot spot in the south. This object has a FR I morphology. The total physical extent is $\sim$ 0.14 Mpc (with z = 0.0518) and has $F_{1.4\ \mathrm{GHz}}$ = 238.41 mJy. The SDSS spectrum (bottom) has a broad H$\alpha$ base (FWHM$_{\mathrm{H}\alpha} \approx$ 2950 km s$^{-1}$). This object is designated B30749+460A and 6CB074906.2+460422

## B.6 SDSS J075643.09+310248.7

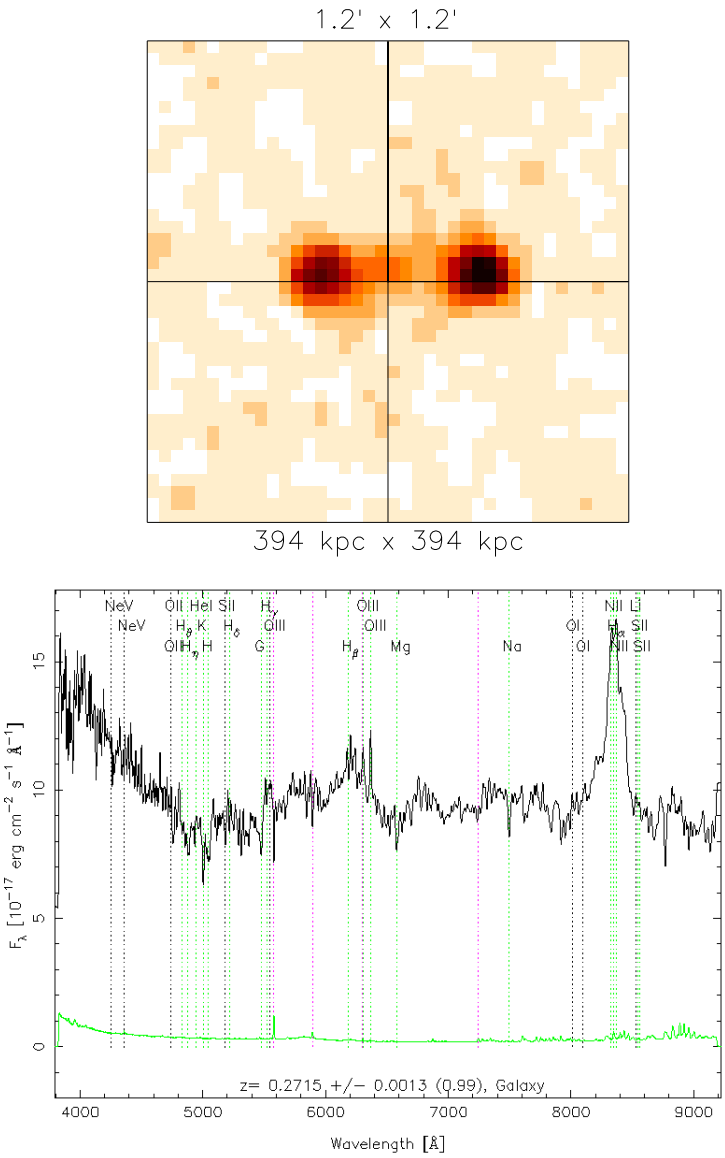


FIGURE B.6: The 1.2′ x 1.2′ radio image (top) of SDSS J075643.09+310248.7 shows two lobes with hot spots on both sides of the core source. This object has a classic triple FR II morphology. The total physical extent is $\sim$ 0.14 Mpc (with z = 0.2715) and has $F_{1.4\ \mathrm{GHz}}$ = 22.59 mJy. The SDSS spectrum (bottom) has broad Balmer lines ($FWHM_{H\alpha} \approx 5830$ km $s^{-1}$). This object has no known designation in any other radio survey.

## B.7 SDSS J080129.57+462622.8

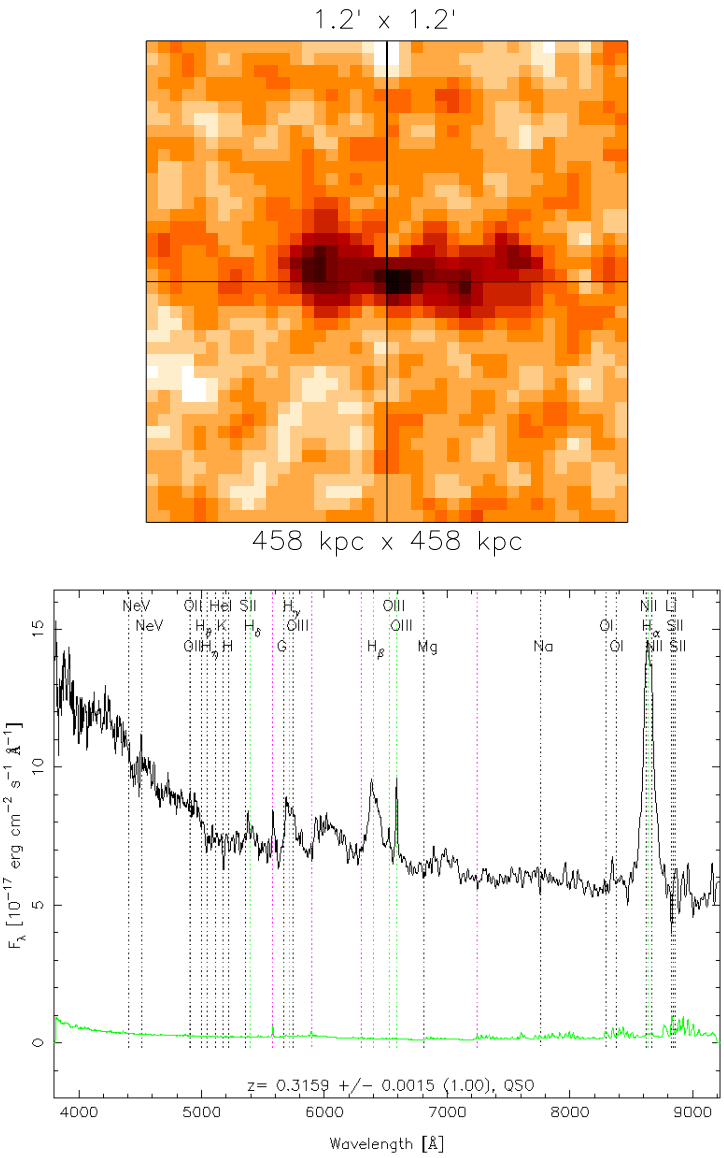


FIGURE B.7: The 3′ x 3′ radio image (top) of SDSS J080129.57+462622.8 shows shows two lobes with hot spots on both sides of the core source. This object has a classic triple FR II morphology. The total physical extent is $\sim 0.26$ Mpc (with z = 0.3159) and has $F_{1.4\ \mathrm{GHz}} = 13.37$ mJy. The SDSS spectrum (bottom) has broad Balmer lines ($\mathrm{FWHM}_{\mathrm{H}\alpha} \approx 3400$ km $\mathrm{s}^{-1}$). This object has no known designation in any other radio survey.

## B.8 SDSS J082133.60+470237.2

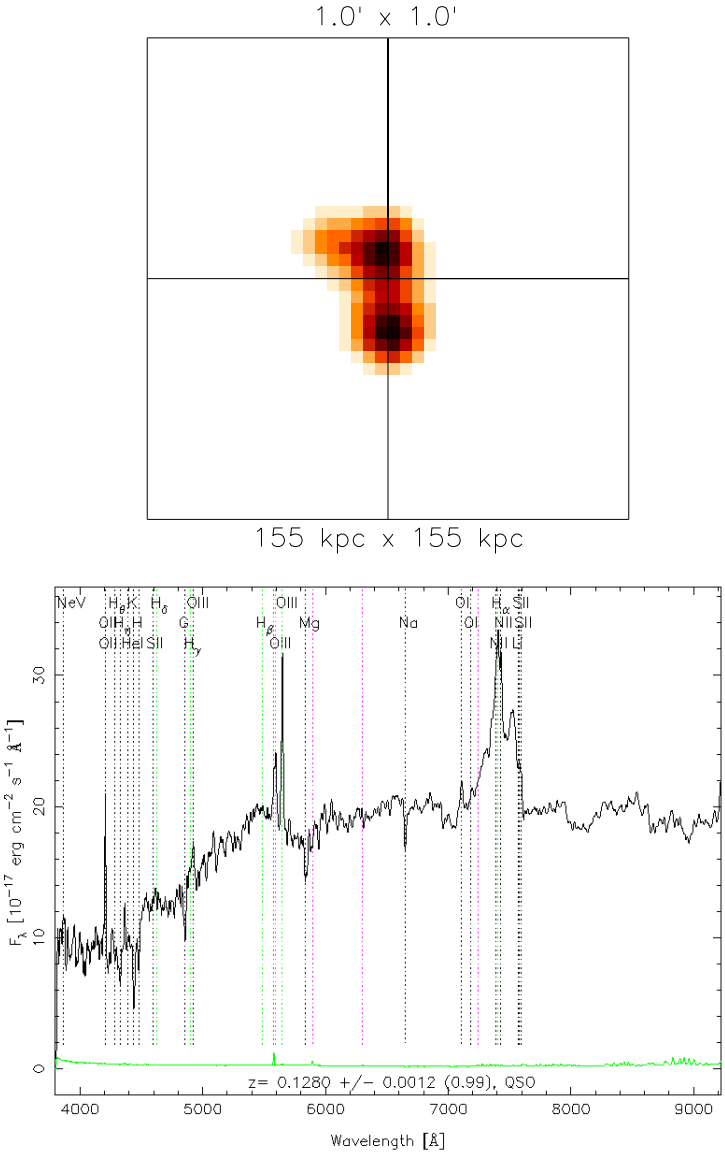


FIGURE B.8: The 1′ x 1′ radio image (top) of SDSS J082133.60+470237.2 shows two bright lobes about the optical center. This object has a FR II morphology. The total physical extent is $\sim$ 0.06 Mpc (with z = 0.1280) and has $F_{1.4\ \mathrm{GHz}}$ = 1711.27 mJy. The SDSS spectrum (bottom) has a broad H$\alpha$ base (FWHM$_{\mathrm{H}\alpha} \approx$ 4050 km s$^{-1}$). This object was an original 3C source designated 3C 197.1.

## B.9 SDSS J082355.36+244830.4

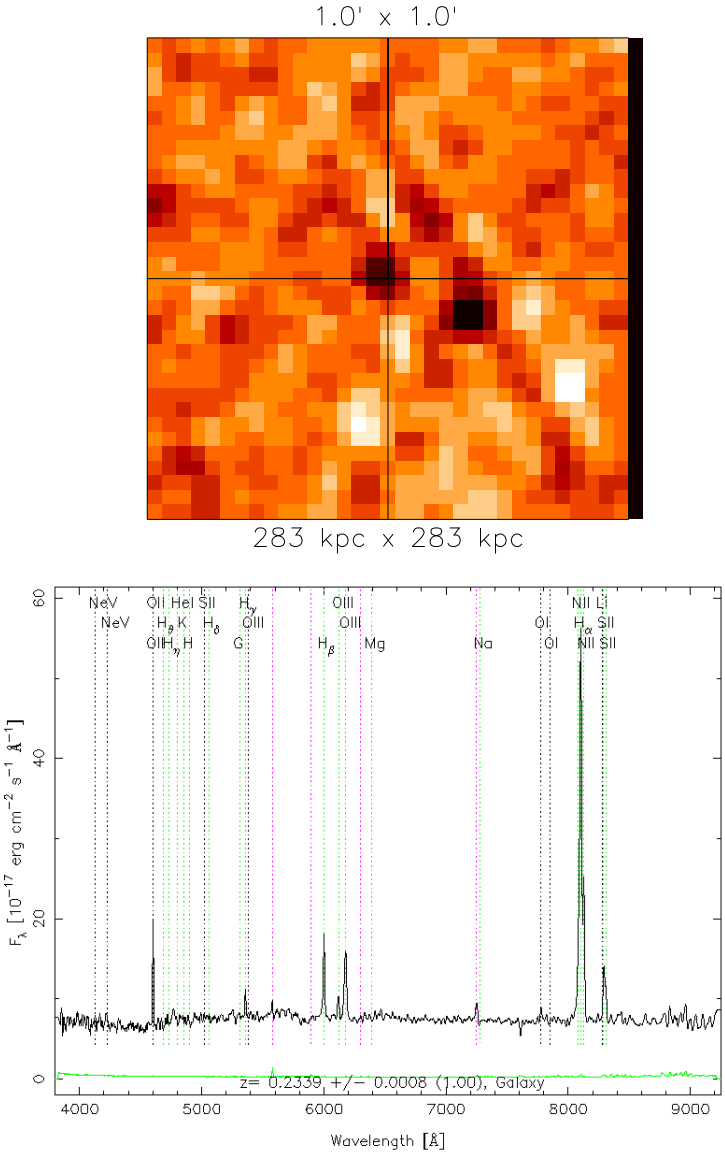


FIGURE B.9: The 1′ x 1′ radio image (top) of SDSS J082355.36+244830.4 shows a two faint hot spots just offset from the optical center. This very weak object may have a FR II morphology. The total physical extent is $\sim$ 0.06 Mpc (with z = 0.2339) and has $F_{1.4\ \mathrm{GHz}}$ = 2.32 mJy. The SDSS spectrum (bottom) has a more narrow H$\alpha$ ($FWHM_{H\alpha} \approx 800$ km $s^{-1}$), similar to a Narrow Line Seyfert 1 (NLS1)(Osterbrock & Pogge 1985). This object has no known designation in any other radio survey.

## B.10 SDSS J084600.36+070424.6

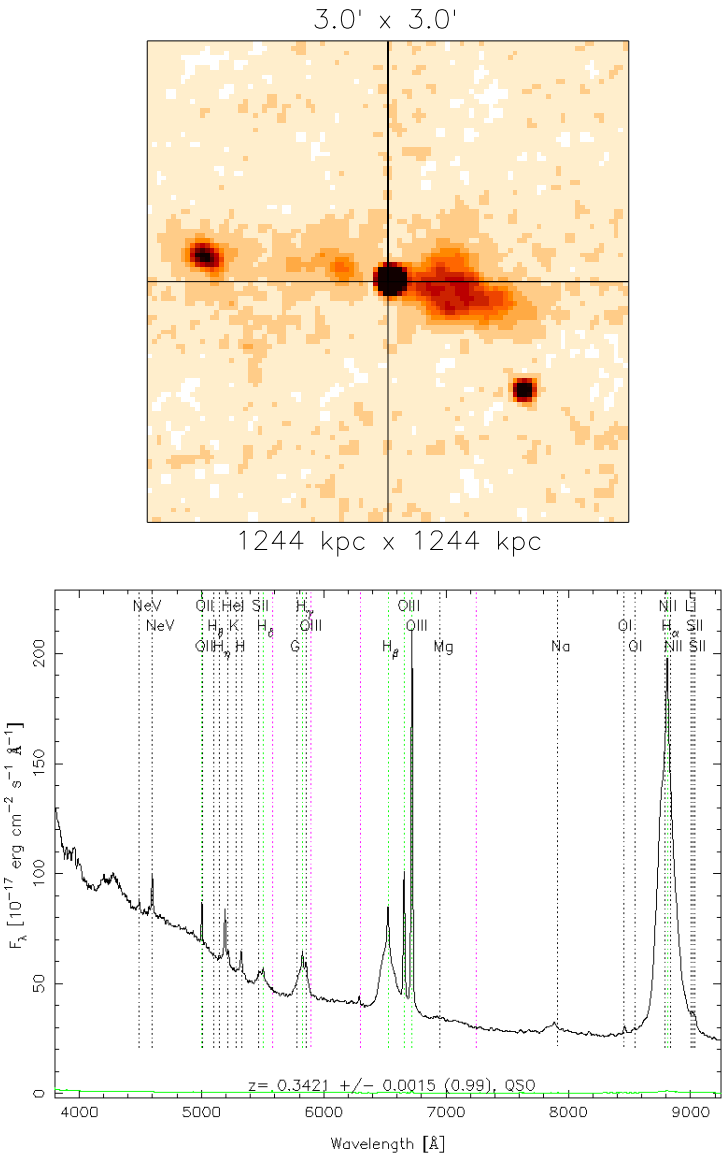


FIGURE B.10: The 3′ x 3′ radio image (top) of SDSS J084600.36+070424.6 shows a bright core source and two lobes. This object has a FR II morphology and is a GRG. The total physical extent is $\sim 0.85$ Mpc (with z = 0.3421) and has $F_{1.4\ \mathrm{GHz}} = 241.53$ mJy. The SDSS spectrum (bottom) has broad Balmer lines ($\mathrm{FWHM}_{\mathrm{H}\alpha} \approx 4710$ km s$^{-1}$). This object is an original 87GB source designated 87GB 084319.4+071534

## B.11 SDSS J085348.18+065447.1

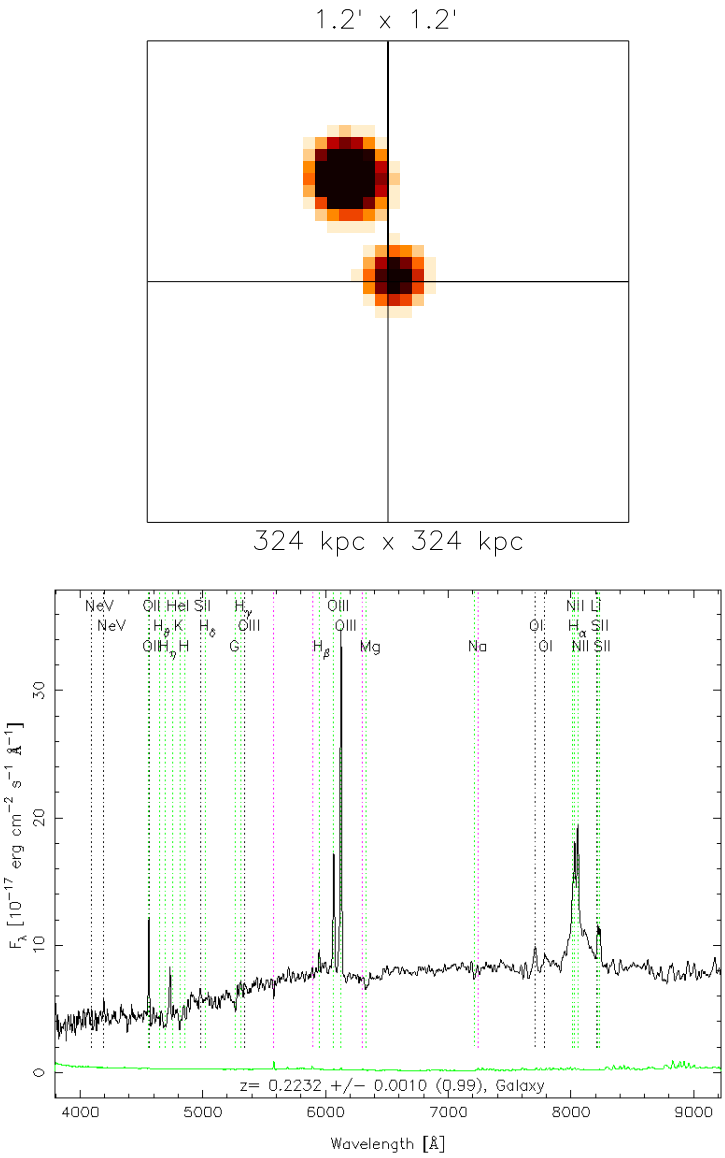


FIGURE B.11: The 1.2′ x 1.2′ radio image (top) of SDSS J085348.18+065447.1 shows a bright core source and one bright lobe. This object has an indeterminate morphology. The total physical extent is $\sim$ 0.08 Mpc (with z = 0.2232) and has $F_{1.4\ \mathrm{GHz}}$ = 769.90 mJy. The SDSS spectrum (bottom) has a broad H$\alpha$ base (FWHM$_{\mathrm{H}\alpha} \approx$ 5570 km s$^{-1}$). This source was an original PMN source designated PMN J0853+0654 (Condon et al. 1994).

## B.12 SDSS J085627.91+360315.6

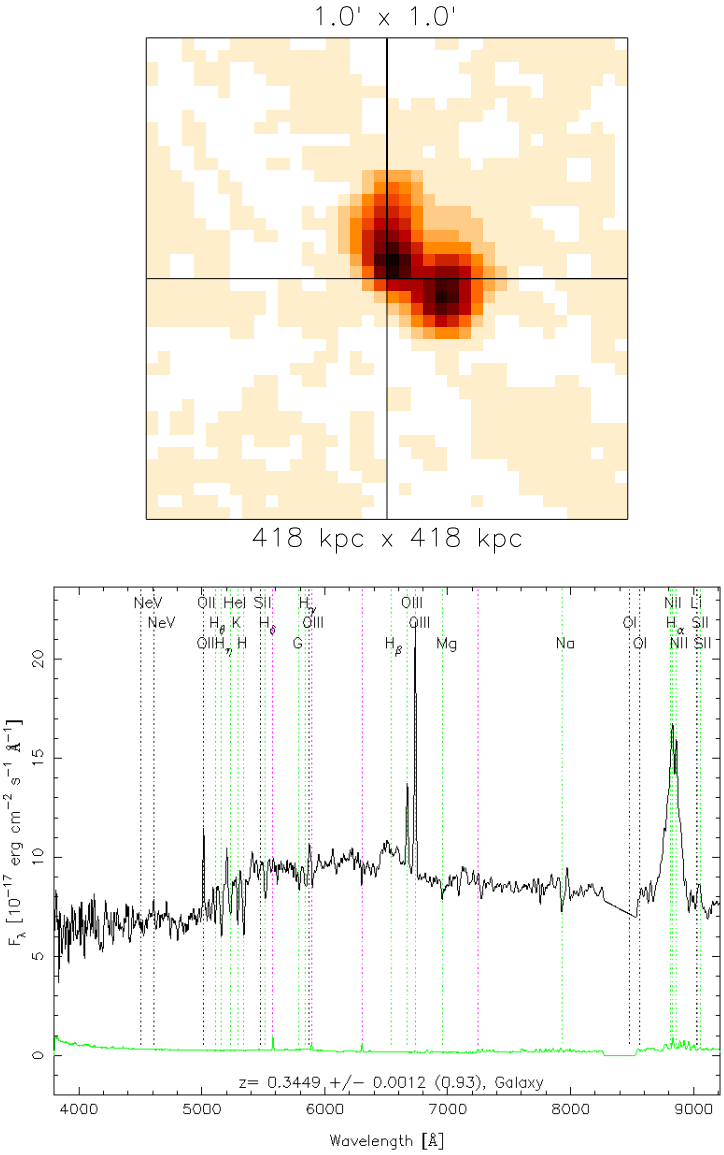


FIGURE B.12: The 1′ x 1′ radio image (top) of SDSS J085627.91+360315.6 shows two lobes, one at the location of the optical center. This object likely has a FR II morphology. The total physical extent is ∼ 0.20 Mpc (with z = 0.3449) and has $F_{1.4\ \mathrm{GHz}} = 29.96$ mJy. The SDSS spectrum (bottom) has a broad H$\alpha$ base (FWHM$_{\mathrm{H}\alpha} \approx 4770$ km s$^{-1}$). This object has no known designation in any other radio survey.

## B.13 SDSS J091133.85+442250.1

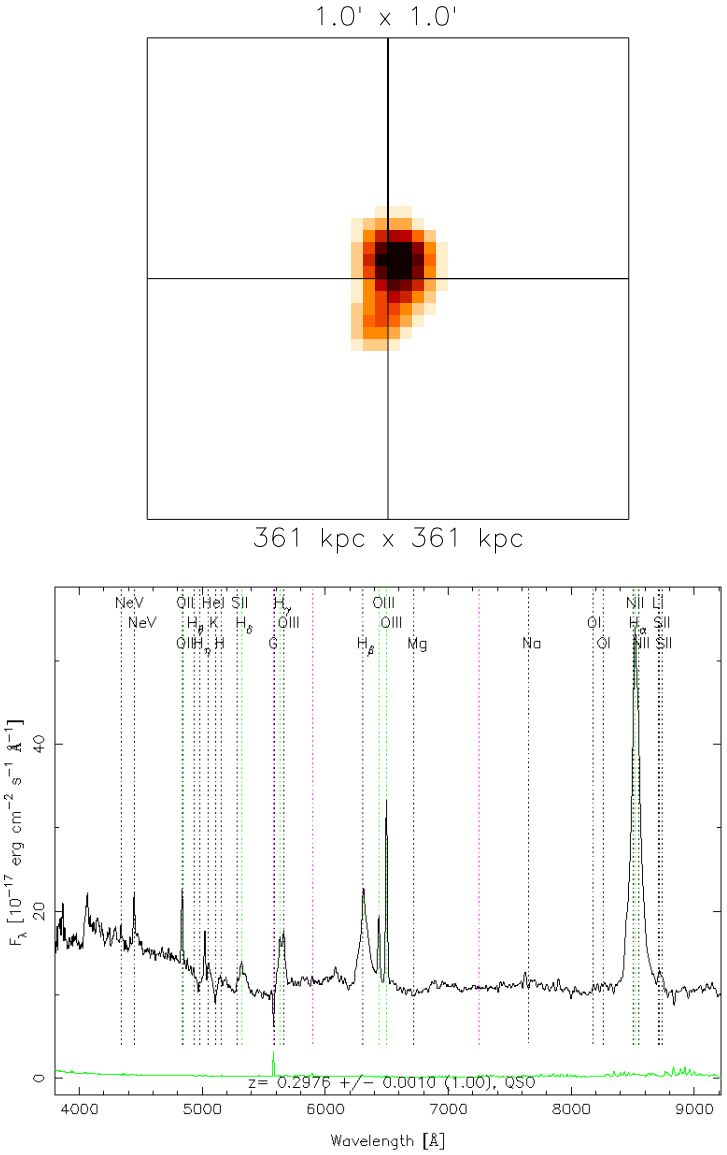


FIGURE B.13: The 1′ x 1′ radio image (top) of SDSS J091133.85+442250.1 shows a bright core source with a small unresolved jet. This object has a FR I morphology. The total physical extent is $\sim 0.15$ Mpc (with z = 0.2976) and has $F_{1.4\ \mathrm{GHz}} = 433.23$ mJy. The SDSS spectrum (bottom) has broad Balmer lines ($\mathrm{FWHM_{H\alpha}} \approx 3640$ km s$^{-1}$). This objects was an original B3 source designated B3 0908+445 and is also in the GB6 catalogue as GB6 J0911+4422

## B.14 SDSS J091401.76+050750.6

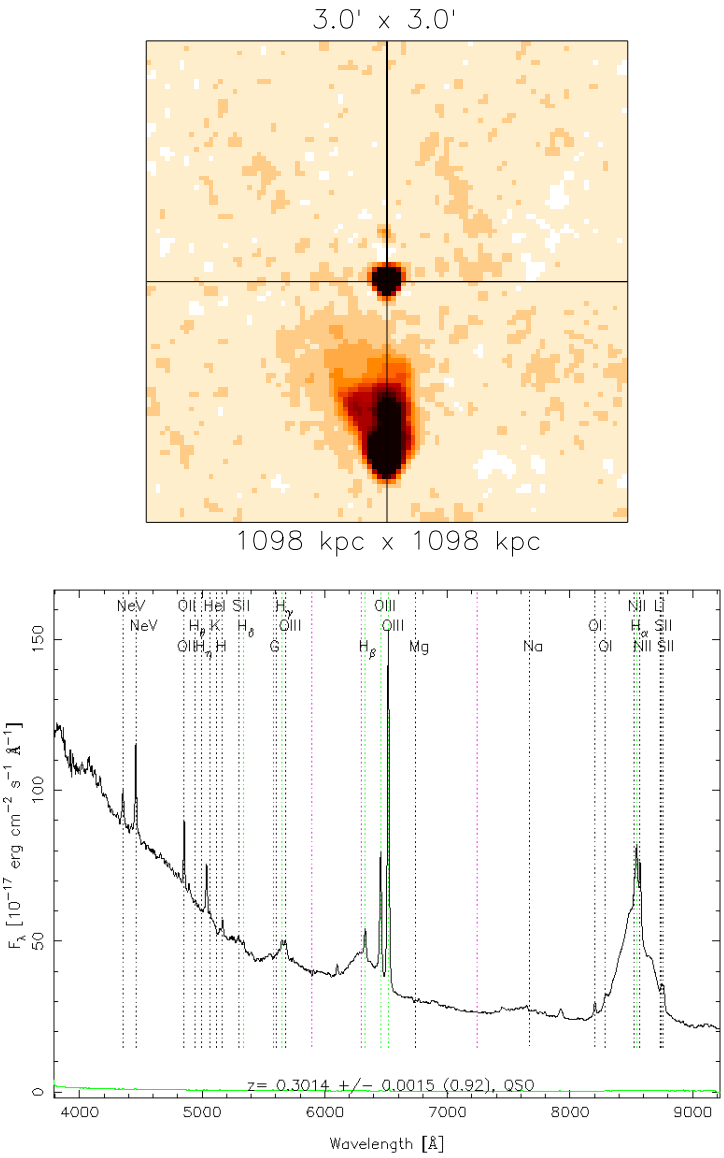


FIGURE B.14: The 3′ x 3′ radio image (top) of SDSS J091401.76+050750.6 shows a bright core source with and one bright lobe to the south. This object has a FR II morphology, although the second lobe is below the flux detection level of FIRST. The total physical extent is $\sim 0.46$ Mpc (with z = 0.3014) and has $F_{1.4\ \mathrm{GHz}} = 328.72$ mJy. The SDSS spectrum (bottom) has broad Balmer lines ($FWHM_{H\alpha} \approx 6110$ km $s^{-1}$).This object was an original 4C source designated 4C +05.38 (Gower et al. 1967).

## B.15 SDSS J091519.56+563837.8

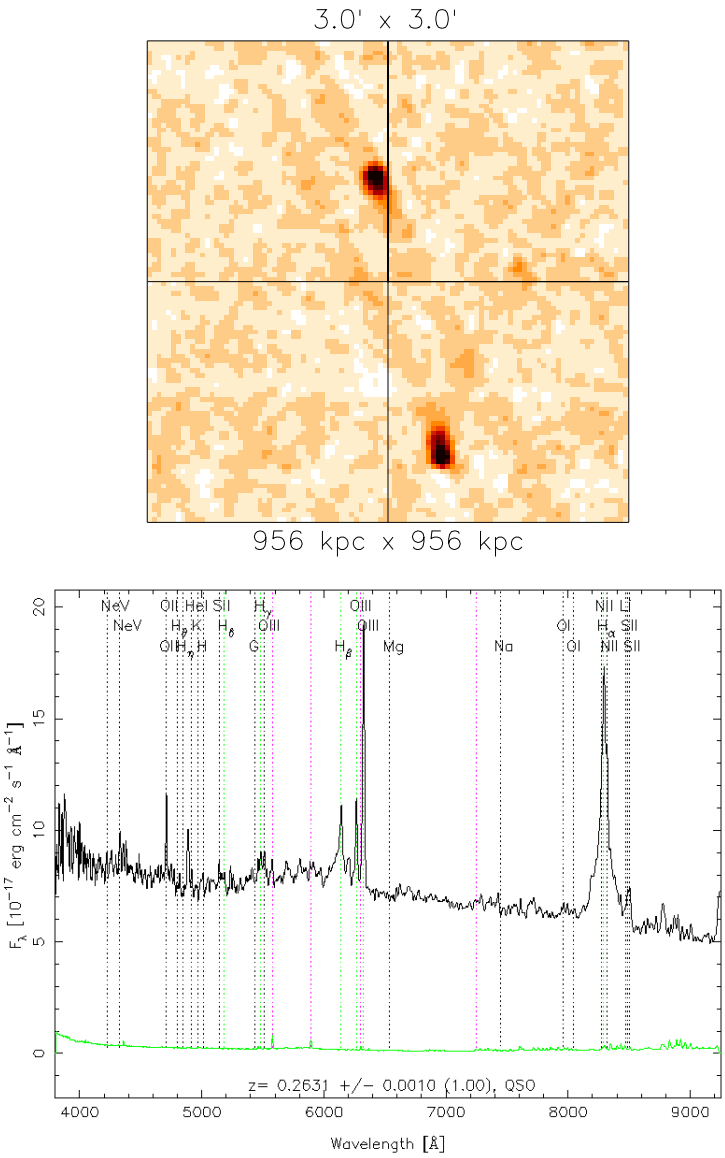


FIGURE B.15: The 3′ x 3′ radio image (top) of SDSS J091519.56+563837.8 shows two lobes with hot spots nearly symmetric about the optical center. This object has a FR II morphology. The total physical extent is $\sim$ 0.56 Mpc (with z = 0.2631) and has $F_{1.4\ \mathrm{GHz}}$ = 19.98 mJy. The SDSS spectrum (bottom) has broad Balmer lines ($FWHM_{H\alpha} \approx 2460$ km $s^{-1}$). This object has no known designation in any other radio survey.

## B.16 SDSS J092308.16+561455.3

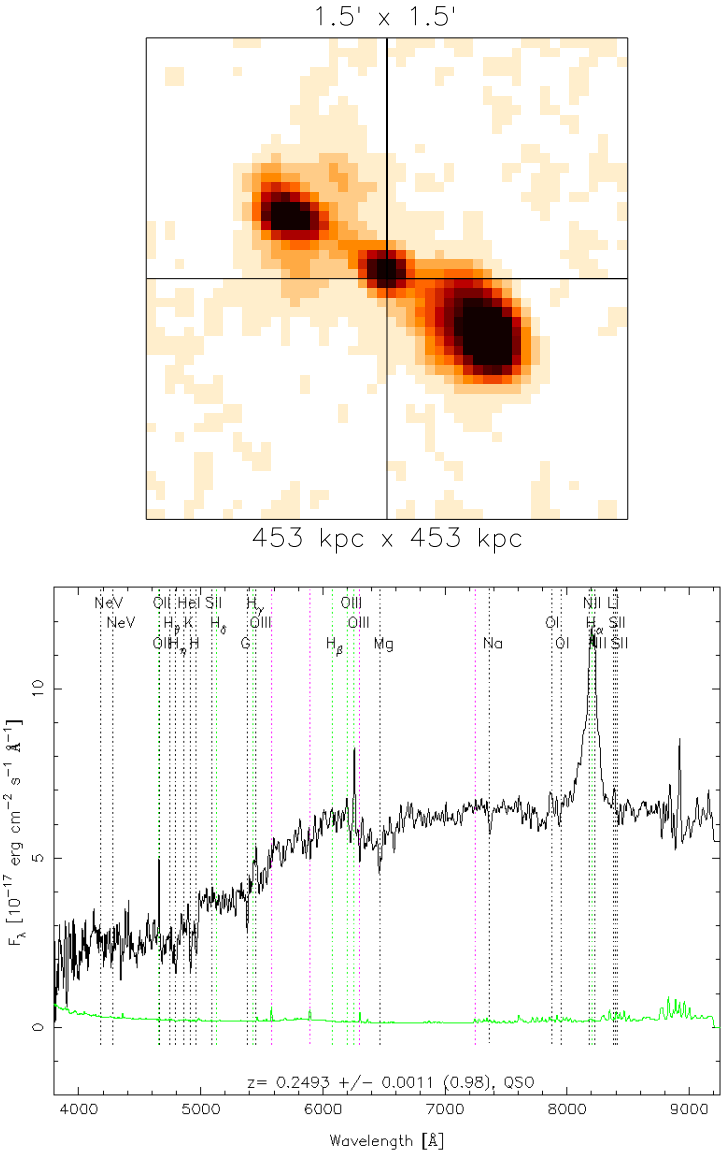


FIGURE B.16: The 1.5′ x 1.5′ radio image (top) of SDSS J092308.16+561455.3 shows a bright core source with two nearly symmetric lobes. This object has a FR II morphology. The total physical extent is $\sim$ 0.23 Mpc (with z = 0.2493) and has $F_{1.4\ \mathrm{GHz}} = 143.01$ mJy. The SDSS spectrum (bottom) has a broad H$\alpha$ base (FWHM$_{\mathrm{H}\alpha} \approx 4580$ km s$^{-1}$). This object has no known designation in any other radio survey.

## B.17 SDSS J092837.97+602521.0

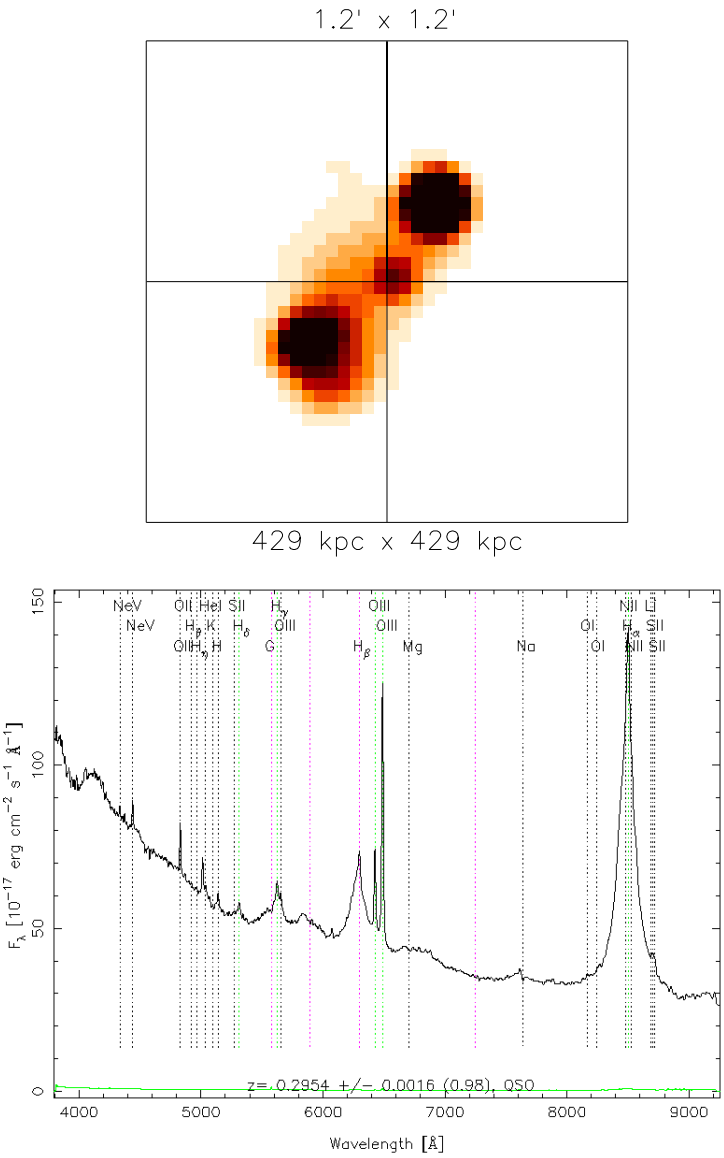


FIGURE B.17: The 1.2′ x 1.2′ radio image (top) of SDSS J092837.97+602521.0 shows a bright core source with two symmetric lobes. This object has a FR II morphology. The total physical extent is $\sim 0.25$ Mpc (with z = 0.2955) and has $F_{1.4\ \mathrm{GHz}} = 278.21$ mJy. The SDSS spectrum (bottom) has broad Balmer lines ($FWHM_{H\alpha} \approx 4690$ km s$^{-1}$). This object is an original 8C source designated 8C 0924+606 (Rees 1990).

## B.18 SDSS J093200.08+553347.4

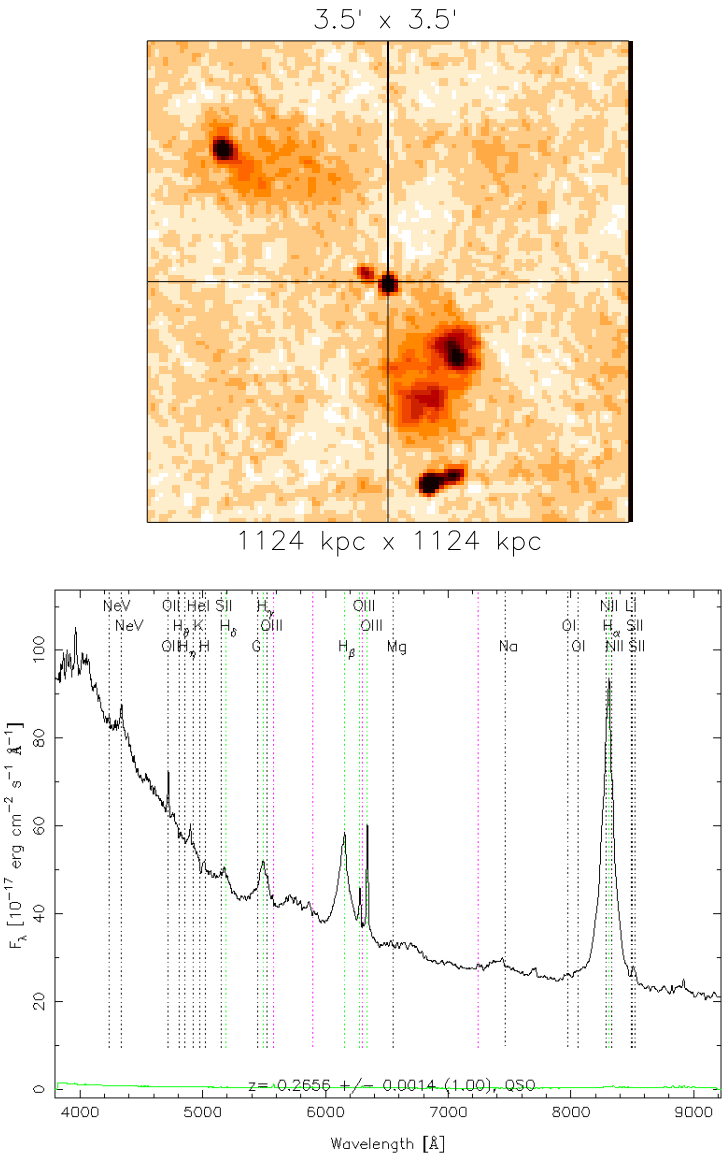


FIGURE B.18: The 3.5′ x 3.5′ radio image (top) of SDSS J093200.08+553347.4 shows a core source with two asymmetric lobes. This object is a GRG and has a FR II morphology. The total physical extent is $\sim$ 0.94 Mpc (with z = 0.2657) and has $F_{1.4\ \mathrm{GHz}} = 73.43$ mJy. The SDSS spectrum (bottom) has broad Balmer lines ($FWHM_{H\alpha} \approx 4140$ km s$^{-1}$). This object is an original 6C source designated 6C B092828.4+554656.

## B.19 SDSS J094144.82+575123.6

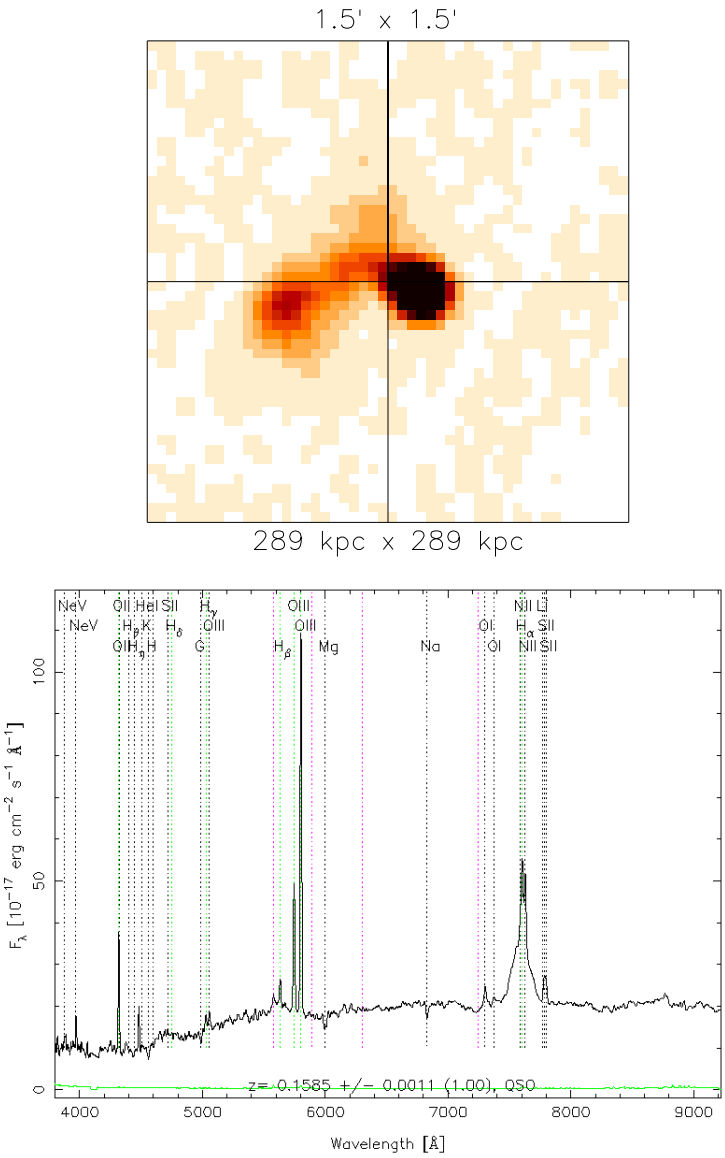


FIGURE B.19: The 1.5′ x 1.5′ radio image (top) of SDSS J094144.82+575123.6 shows a two small lobes that are bent. This object has a distorted, but possible FR II morphology. The total physical extent is $\sim$ 0.11 Mpc (with z = 0.1585) and has $F_{1.4\ \mathrm{GHz}} = 90.43$ mJy. The SDSS spectrum (bottom) has a broad H$\alpha$ base (FWHM$_{\mathrm{H}\alpha} \approx 6610$ km s$^{-1}$). This object is an original GB6 source designated GB6 J0941+5751.

## B.20 SDSS J094745.14+072520.5

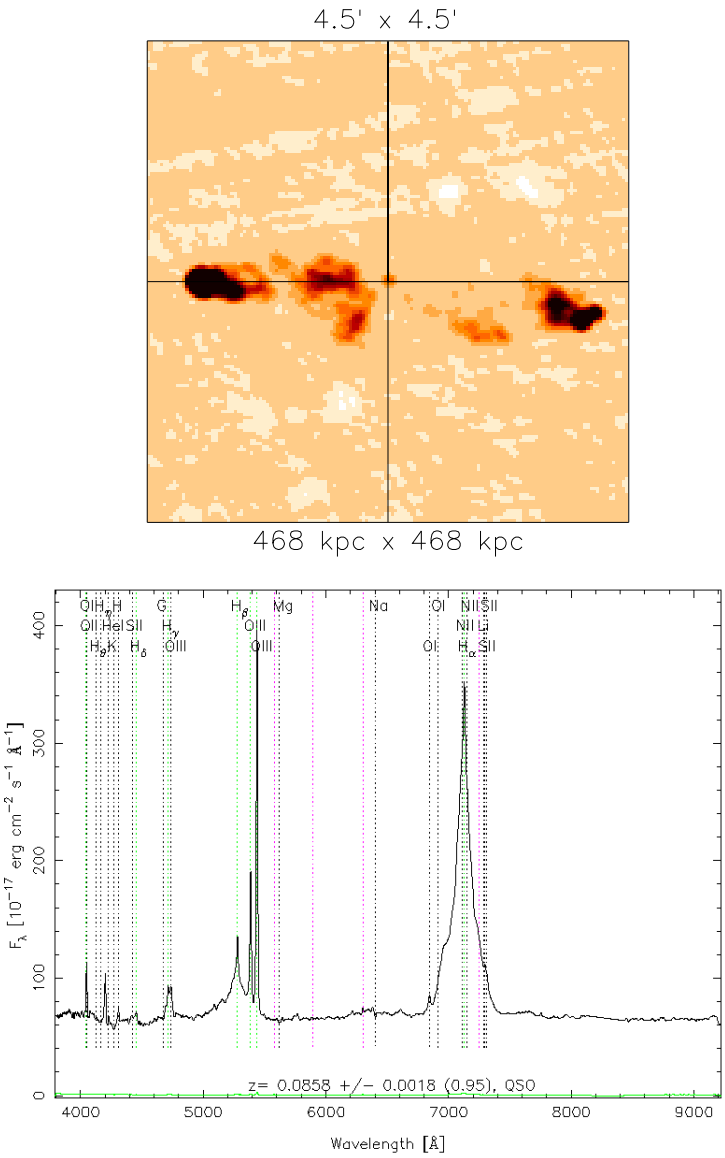


FIGURE B.20: The 4.5′ x 4.5′ radio image (top) of SDSS J094745.14+072520.5 shows a faint core source with two bright lobes with hot spots. This object has a FR II morphology. The total physical extent is $\sim 0.40$ Mpc (with z = 0.0858) and has $F_{1.4\ \mathrm{GHz}} = 3117.09$ mJy. The SDSS spectrum (bottom) has broad Balmer lines ($\mathrm{FWHM_{H\alpha}} \approx 5660$ km s$^{-1}$). This object is an original 3C source designated 3C 227, and later in the Parkes radio survey (PKS) designated PKS 0945+07 (Wright & Otrupcek 1990).

## B.21 SDSS J095456.89+092955.8

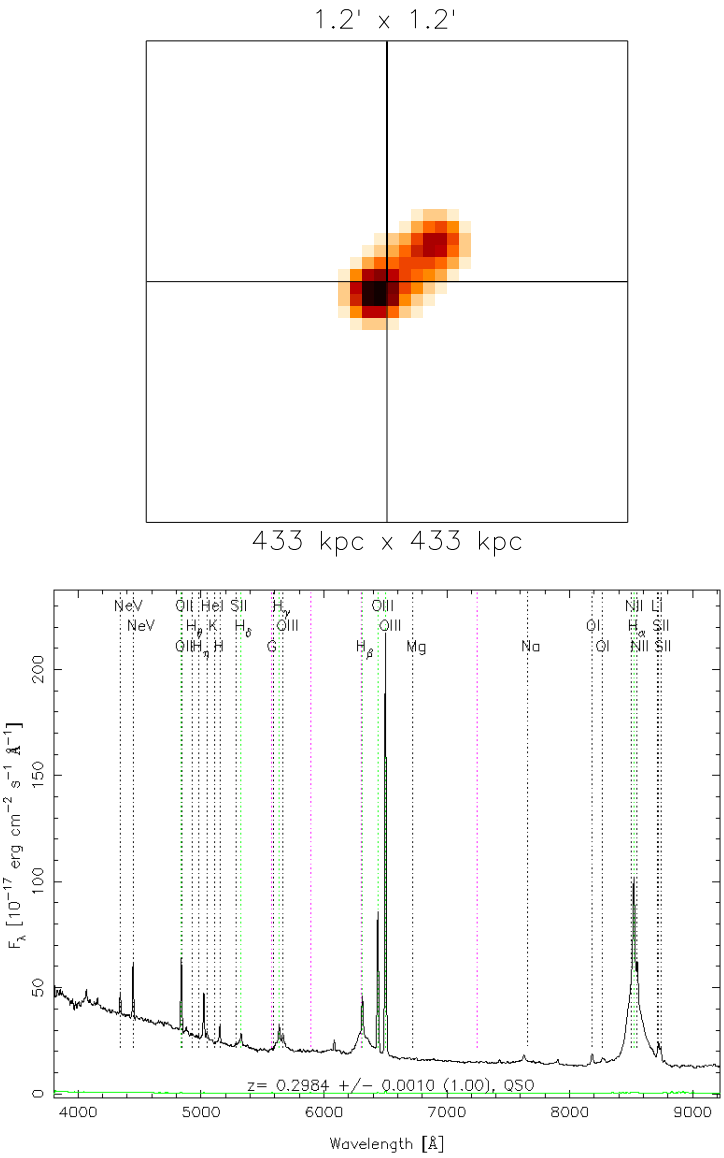


FIGURE B.21: The 1.2′ x 1.2′ radio image (top) of SDSS J095456.89+092955.8 shows two lobes nearly symmetric about the optical center. This object seems to have an asymmetric FR II morphology. The total physical extent is $\sim$ 0.17 Mpc (with z = 0.2984) and has $F_{1.4\ \mathrm{GHz}} = 440.66$ mJy. The SDSS spectrum (bottom) has broad Balmer lines ($FWHM_{H\alpha} \approx$ 4110 km s$^{-1}$). This object is an original 4C source designated 4C +09.35 and is also PKS 0952+097.

## B.22 SDSS J100726.10+124856.2

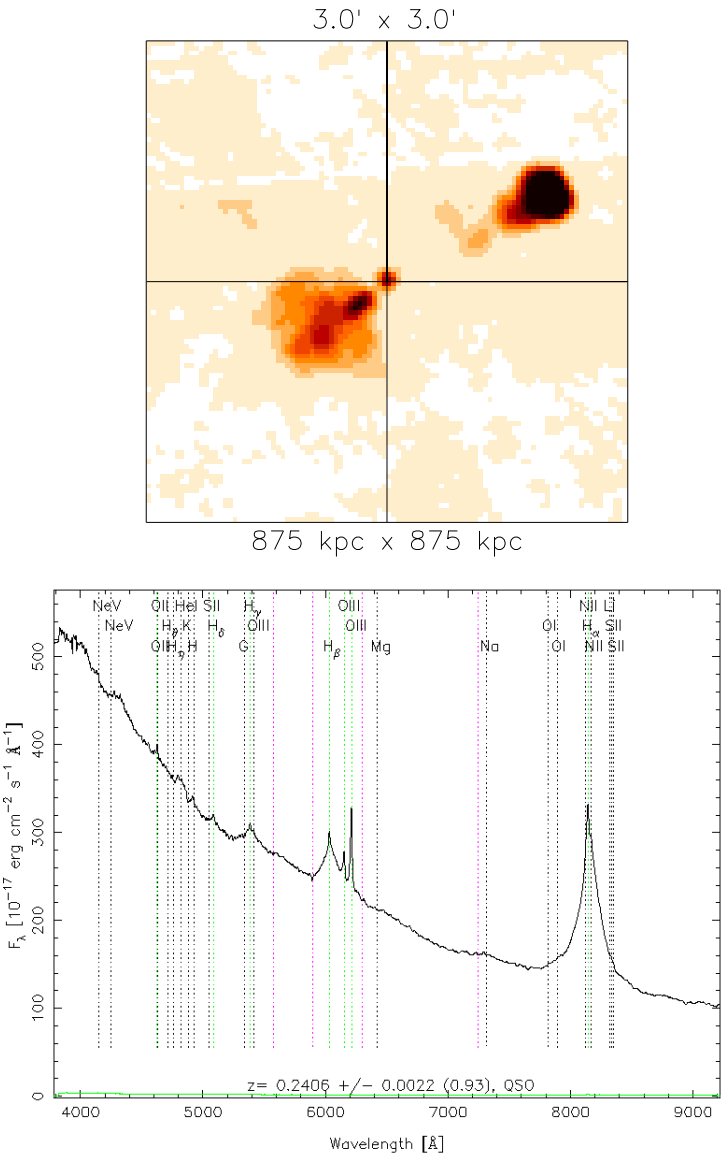


FIGURE B.22: The 3′ x 3′ radio image (top) of SDSS J100726.10+124856.2 shows a faint core source and two large lobes. This object has a FR II morphology. The total physical extent is $\sim 0.52$ Mpc (with z = 0.2406) and has $F_{1.4\ \mathrm{GHz}} = 959.14$ mJy. The SDSS spectrum (bottom) has broad Balmer lines ($FWHM_{H\alpha} \approx 5770$ km s$^{-1}$). This object is an original 4C source designated 4C +13.41 and is also PKS 1004+13.

## B.23 SDSS J100819.11+372903.4

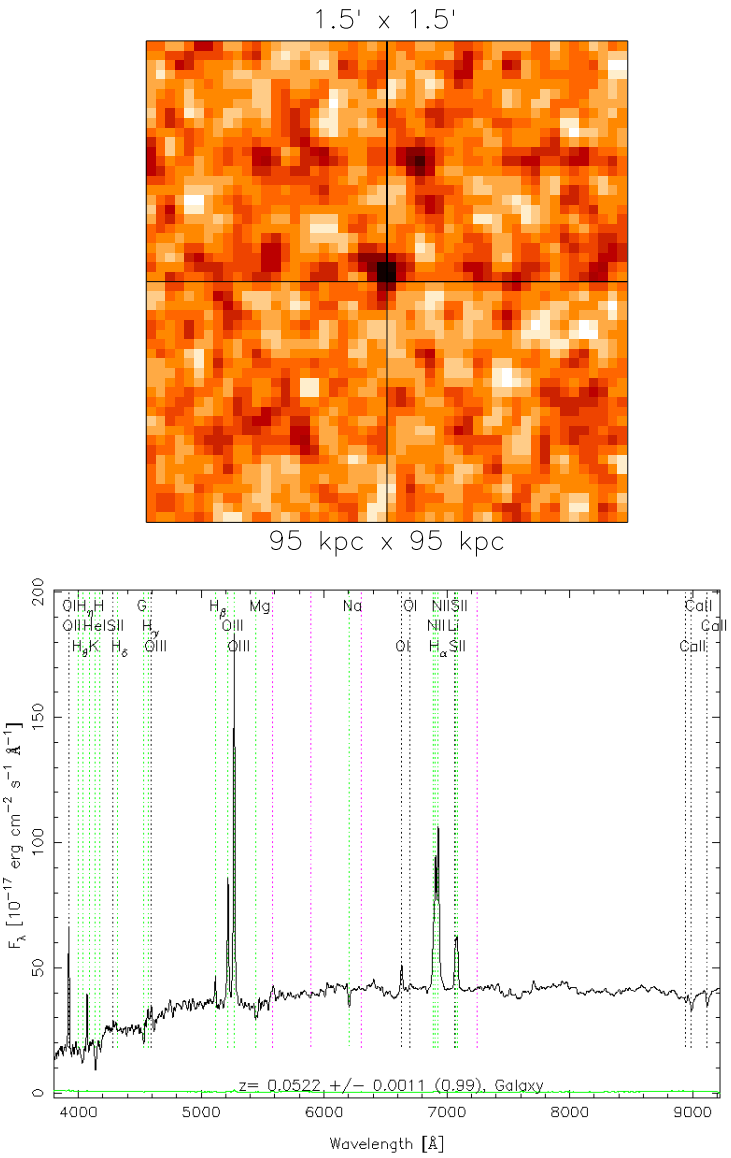


FIGURE B.23: The 1.5′ x 1.5′ radio image (top) of SDSS J100819.11+372903.4 shows a faint core source and one other source to the north that is within the host galaxy. This object has an indeterminate morphology. The total physical extent is $\sim$ 0.02 Mpc (with z = 0.0522) and has $F_{1.4\ \mathrm{GHz}} = 2.27$ mJy. The SDSS spectrum (bottom) has a broad H$\alpha$ base (FWHM$_{\mathrm{H}\alpha} \approx 2370$ km s$^{-1}$). This object has no known designation in any other radio survey.

## B.24 SDSS J103143.51+522535.1

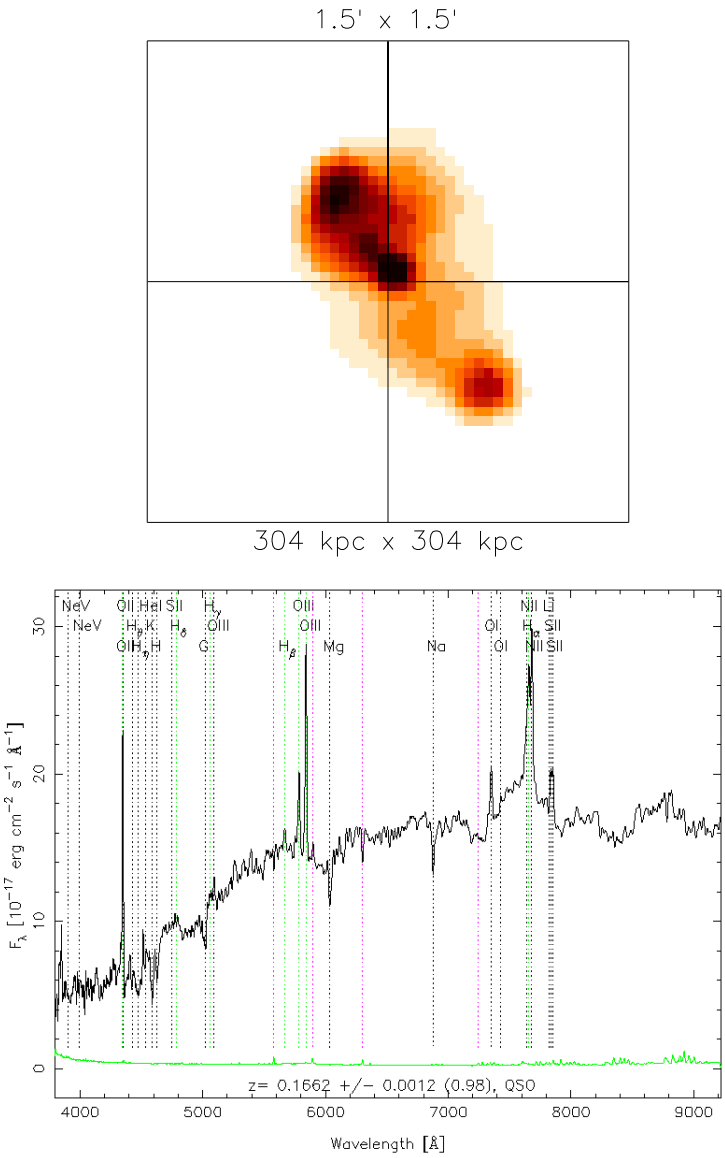


FIGURE B.24: The 1.5′ x 1.5′ radio image (top) of SDSS J103143.51+522535.1 shows a bright core source and two lobes with hot spots. This object has a FR II morphology. The total physical extent is $\sim 0.13$ Mpc (with z = 0.1662) and has $F_{1.4\ \mathrm{GHz}} = 904.01$ mJy. The SDSS spectrum (bottom) has a broad H$\alpha$ base (FWHM$_{\mathrm{H}\alpha} \approx 2720$ km s$^{-1}$). This object is an original 4C source designated 4C +52.22 and is also in the GB6 catalogue as GB6 J1031+5225

## B.25 SDSS J103458.35+055231.8

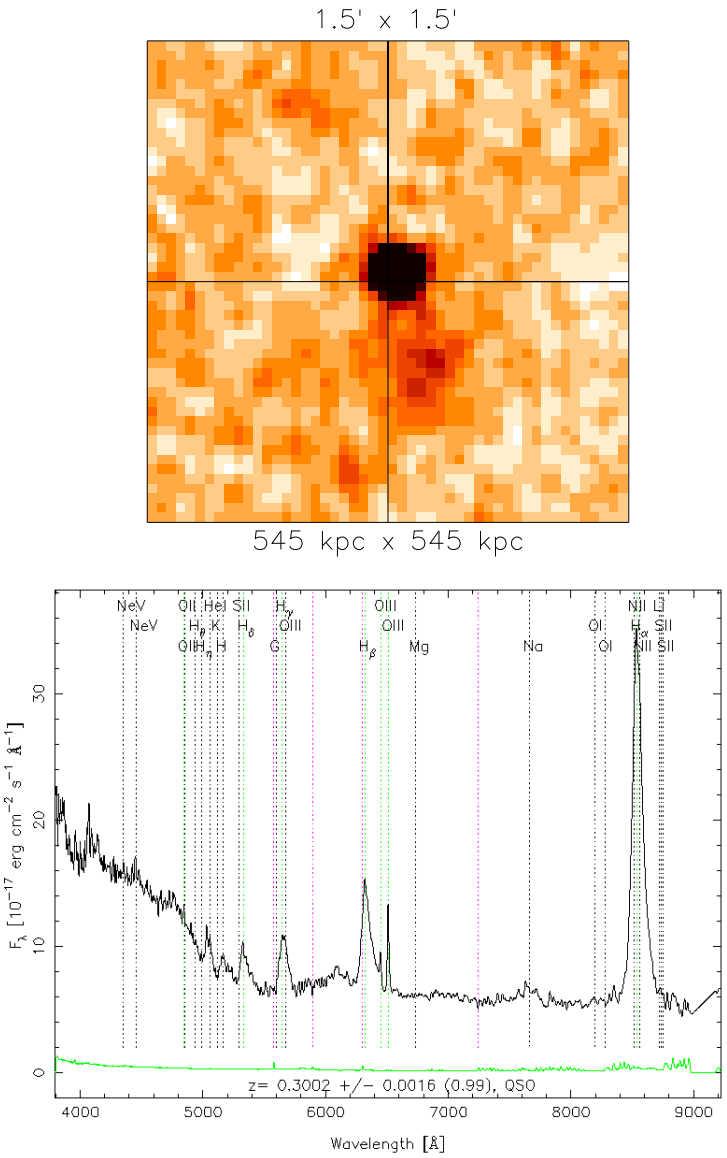


FIGURE B.25: The 1.5′ x 1.5′ radio image (top) of SDSS J103458.35+055231.8 shows a bright core source and one faint lobe to the south. This object has a FR II morphology. The total physical extent is $\sim$ 0.15 Mpc (with z = 0.3002) and has $F_{1.4\ \mathrm{GHz}} = 28.72$ mJy. The SDSS spectrum (bottom) has broad Balmer lines ($\mathrm{FWHM}_{\mathrm{H}\alpha} \approx 3270$ km s$^{-1}$). This object has no known designation in any other radio survey.

## B.26 SDSS J105220.30+454322.2

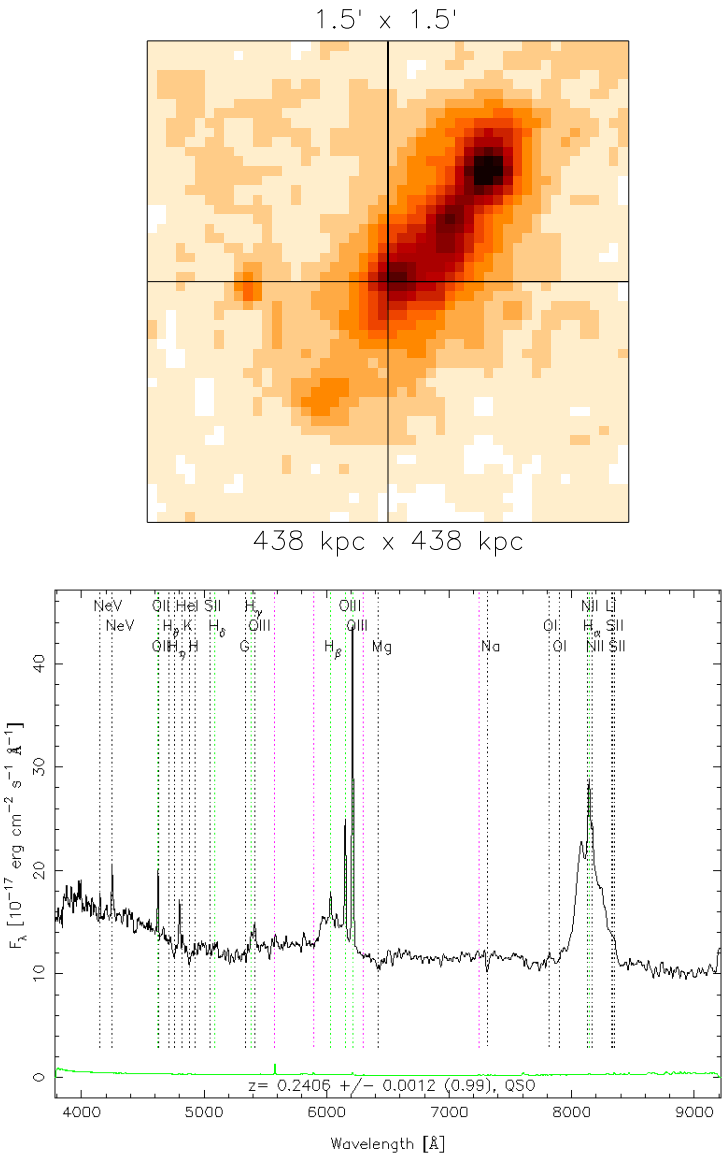


FIGURE B.26: The 1.5′ x 1.5′ radio image (top) of SDSS J105220.30+454322.2 shows a core source and an asymmetric jet. This object has a FR I morphology. The total physical extent is $\sim 0.26$ Mpc (with z = 0.2406) and has $F_{1.4\ \mathrm{GHz}} = 112.05$ mJy. The SDSS spectrum (bottom) has a broad H$\alpha$ base ($\mathrm{FWHM_{H\alpha}} \approx 8230$ km s$^{-1}$). This object has no known designation in any other radio survey.

## B.27 SDSS J105500.33+520200.9

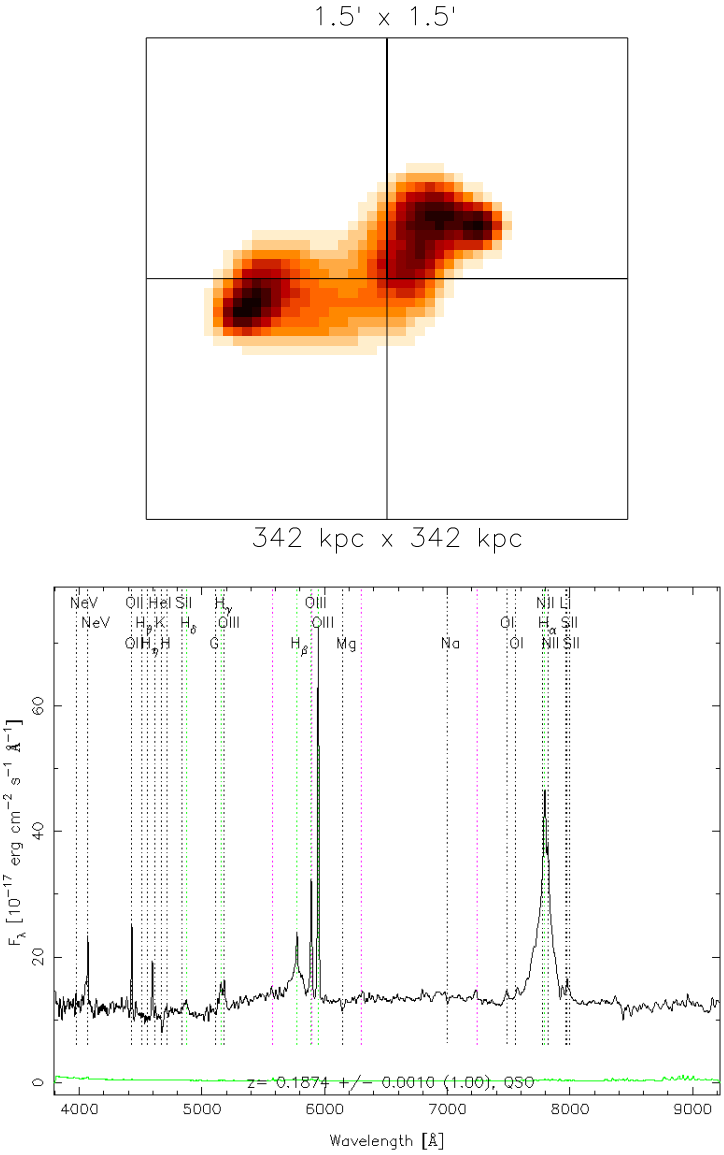


FIGURE B.27: The 1.5′ x 1.5′ radio image (top) of SDSS J105500.33+520200.9 shows two lobes that both bend and terminate with hot spots. This object has a FR II morphology. The total physical extent is $\sim$ 0.21 Mpc (with z = 0.1874) and has $F_{1.4\ \mathrm{GHz}} = 461.07$ mJy. The SDSS spectrum (bottom) has broad Balmer lines ($\mathrm{FWHM}_{\mathrm{H}\alpha} \approx 3910$ km s$^{-1}$). This object is an original 6C source designated 6C B105202.4+521804.

## B.28 SDSS J105632.01+430055.9

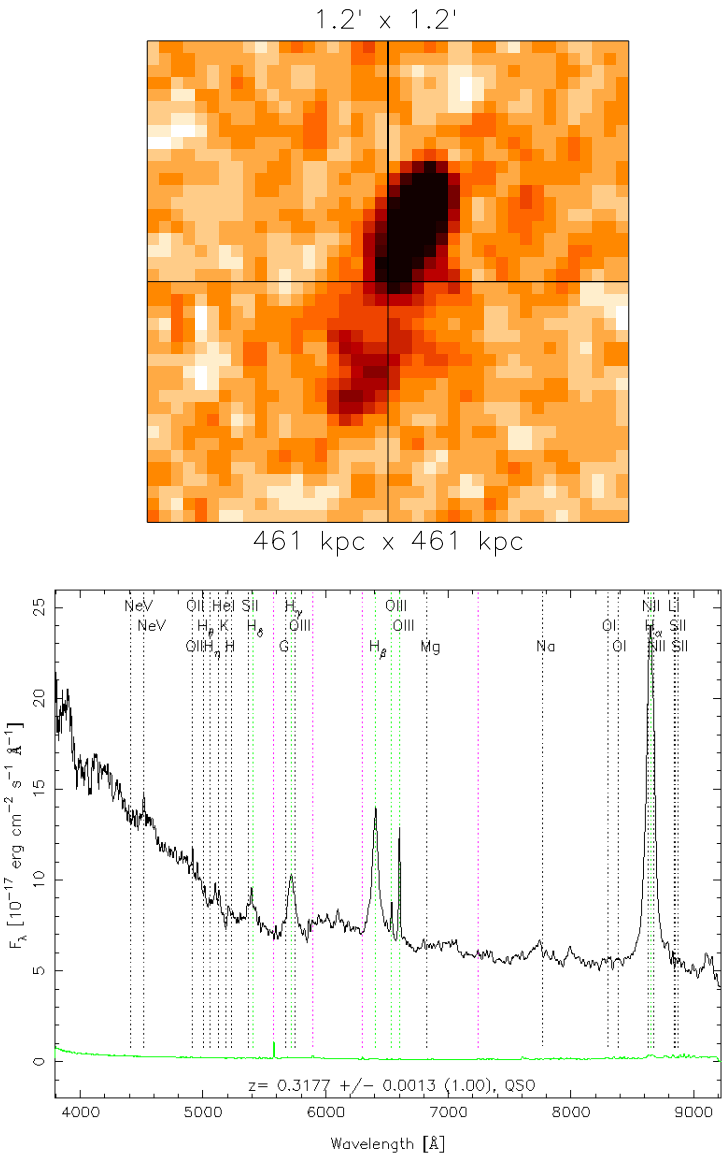


FIGURE B.28: The 1.2′ x 1.2′ radio image (top) of SDSS J105632.01+430055.9 shows a bright core source and two lobes, one much dimmer than the other. This object has a FR II morphology. The total physical extent is $\sim$ 0.22 Mpc (with z = 0.3177) and has $F_{1.4\ \mathrm{GHz}}$ = 19.37 mJy. The SDSS spectrum (bottom) has broad Balmer lines ($FWHM_{H\alpha} \approx 3010$ km $s^{-1}$). This object has no known designation in any other radio survey.

## B.29 SDSS J110845.48+020240.8

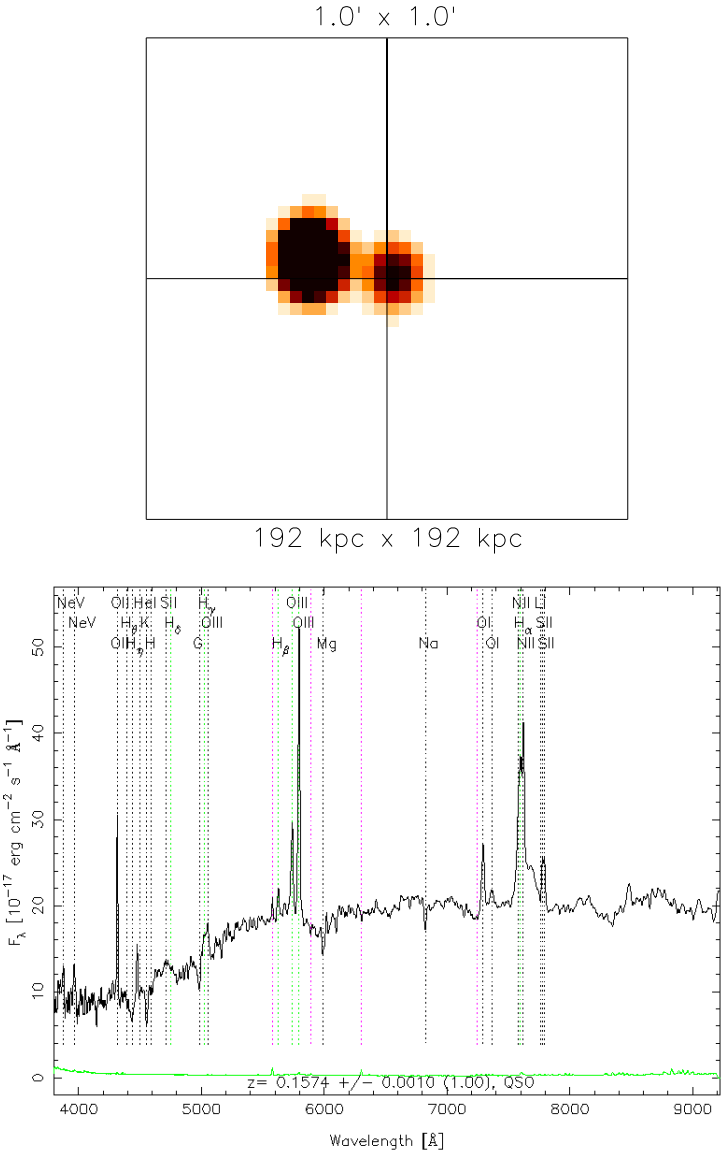


FIGURE B.29: The 1′ x 1′ radio image (top) of SDSS J110845.48+020240.8 shows a bright core source and one lobes that is within the host galaxy. This object has an indeterminate morphology. The total physical extent is $\sim$ 0.08 Mpc (with z = 0.1574) and has $F_{1.4\ \mathrm{GHz}}$ = 784.08 mJy. The SDSS spectrum (bottom) has a broad H$\alpha$ base ($FWHM_{H\alpha} \approx$ 2360 km $s^{-1}$). This object is an original PKS source and is designated PKS 1106+023.

## B.30 SDSS J111432.79+105034.7

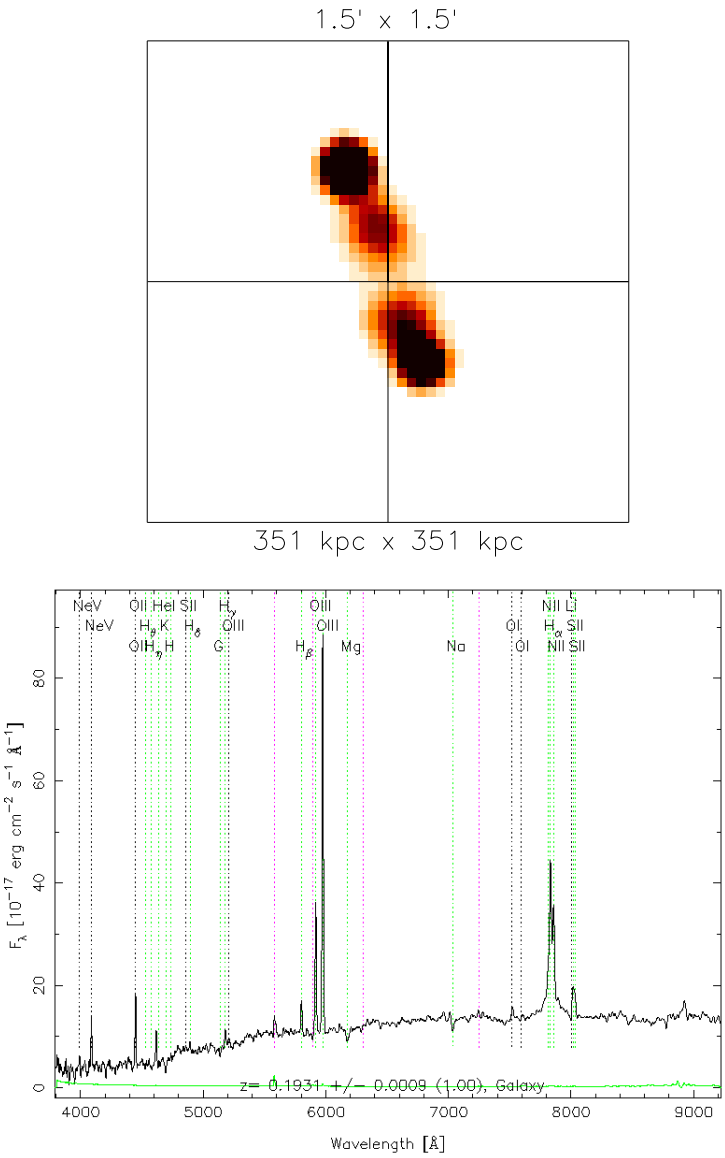


FIGURE B.30: The 1.5′ x 1.5′ radio image (top) of SDSS J111432.79+105034.7 shows a dim core and two sets of symmetric lobes. This object may be a DDRG or have a FR II morphology. The total physical extent is $\sim 0.23$ Mpc (with z = 0.1931) and has $F_{1.4\ \mathrm{GHz}} = 780.25$ mJy. The SDSS spectrum (bottom) has broad Balmer lines ($FWHM_{H\alpha} \approx 6080$ km $s^{-1}$). This object has no known designation in any other radio survey.

## B.31 SDSS J113021.40+005823.0

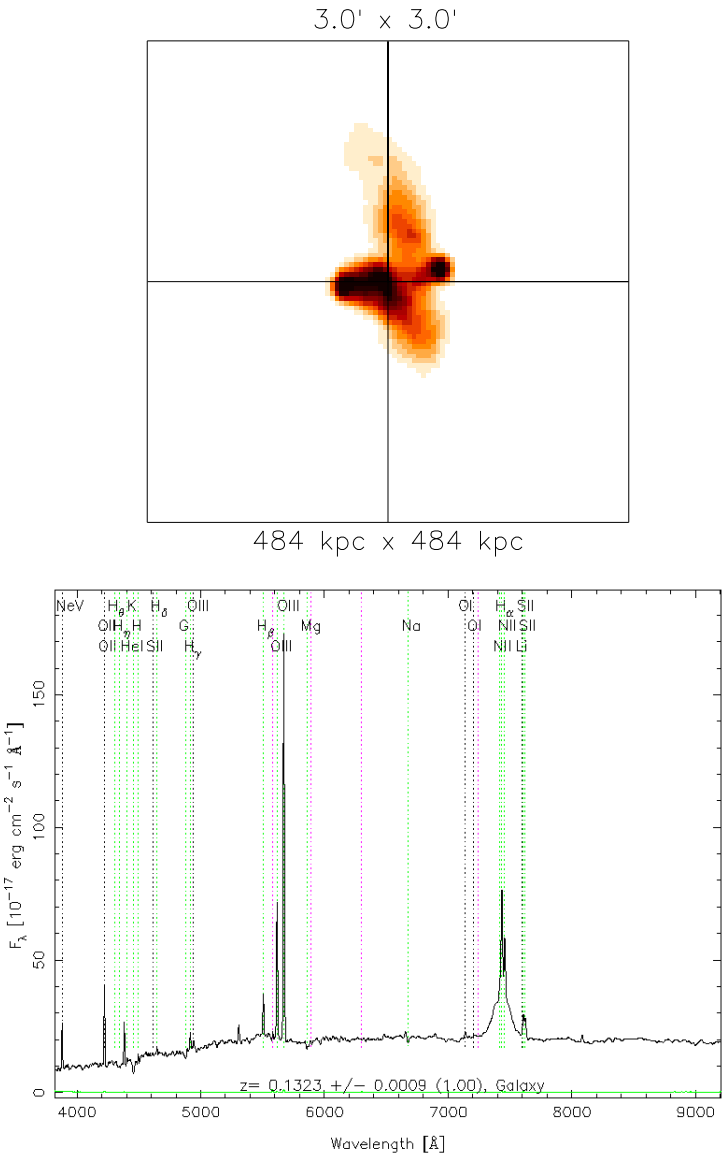


FIGURE B.31: The 3′ x 3′ radio image (top) of SDSS J113021.40+005823.0 shows a bright core source two sets of lobes, one pair orthogonal to the other. This object has an X-shaped morphology. The total physical extent is $\sim$ 0.16 Mpc along the direction with hotspots and $\sim$ 0.26 Mpc along the weaker lobes(with z = 0.1323). This object has $F_{1.4\ \mathrm{GHz}} = 566.72$ mJy. The SDSS spectrum (bottom) has a broad H$\alpha$ base (FWHM$_{\mathrm{H}\alpha} \approx$ km s$^{-1}$). This object is an original 4C source designated 4C +01.30 and is in the PKS catalogue as PKS 1127+012.

## B.32 SDSS J114004.35−010527.4

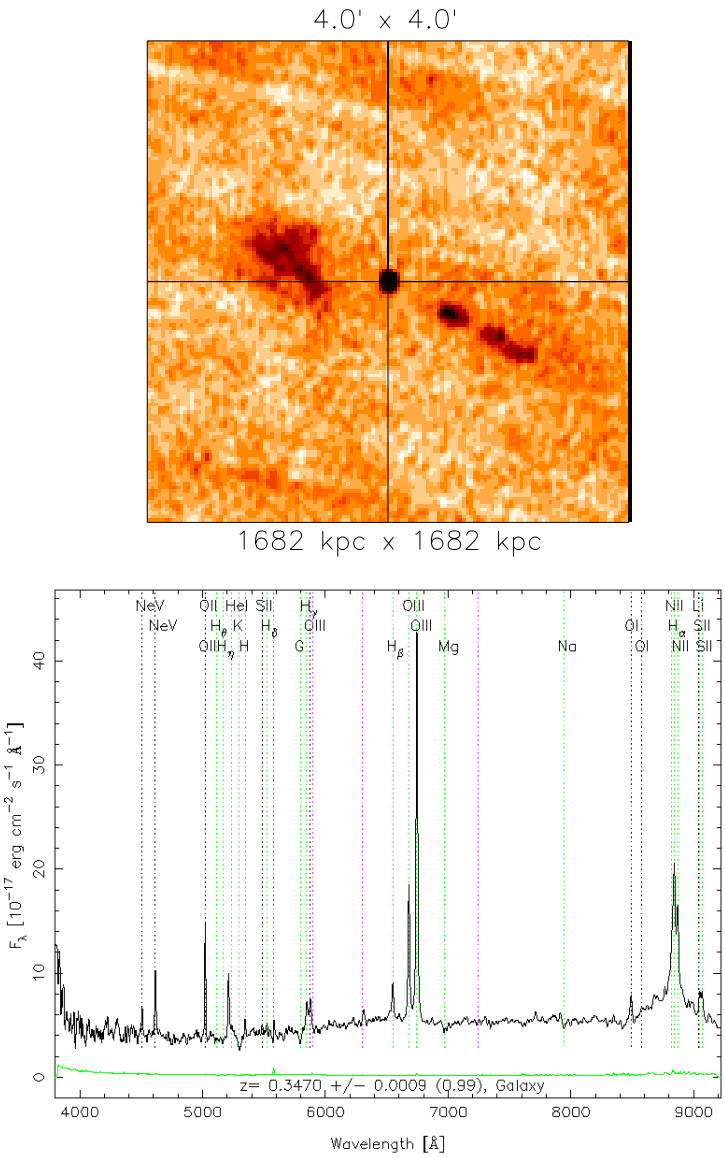


FIGURE B.32: The 4′ x 4′ radio image (top) of SDSS J114004.35−010527.4 shows a bright core source with a lobe in the east and a jet in the west. This object is a GRG and has a HYMORS morphology. The total physical extent is ∼ 1.12 Mpc (with z = 0.3470) and has $F_{1.4\ \mathrm{GHz}} = 34.17$ mJy. The SDSS spectrum (bottom) has broad Balmer lines ($FWHM_{H\alpha} \approx 3260$ km s$^{-1}$). This object is an original source in the White-Becker 1992 (WB92) catalogue and is designated WB92 1137-004 (White & Becker 1992).

## B.33 SDSS J114047.90+462204.8

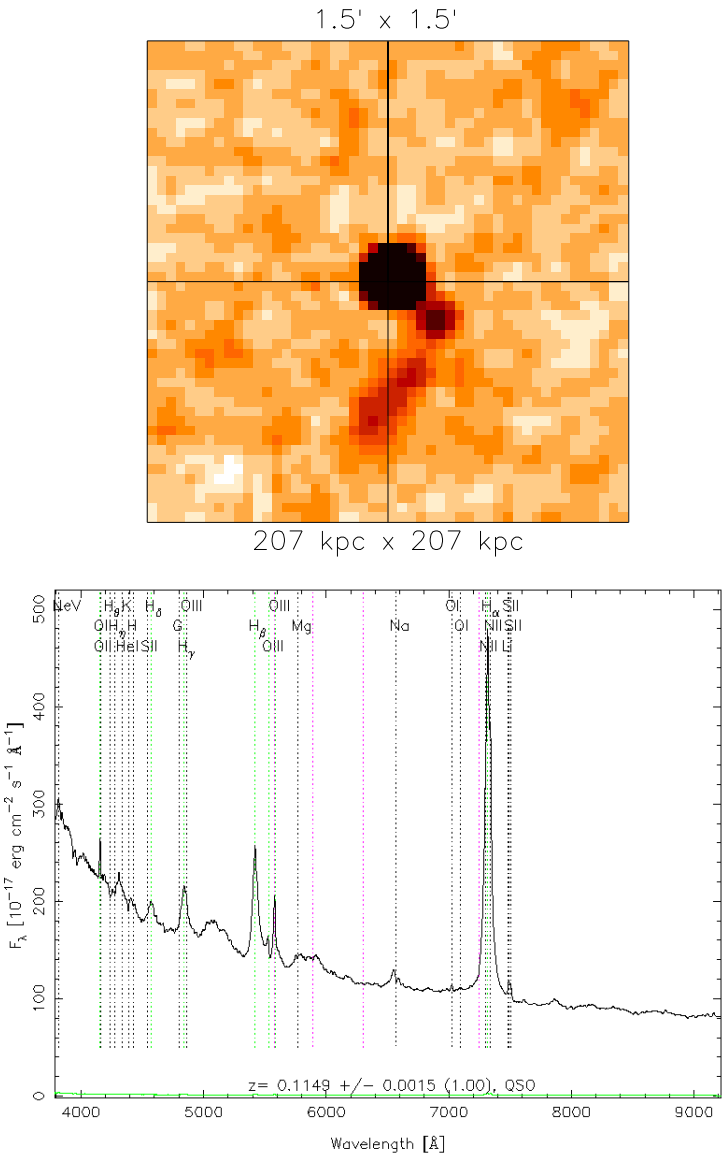


FIGURE B.33: The 1.5′ x 1.5′ radio image (top) of SDSS J114047.90+462204.8 shows a bright core source a bent jet to the south. This object has an indeterminate morphology. The total physical extent is $\sim$ 0.06 Mpc (with z = 0.1149) and has $F_{1.4\ \mathrm{GHz}} = 91.99$ mJy. The SDSS spectrum (bottom) has broad Balmer lines ($\mathrm{FWHM_{H\alpha}} \approx 2630$ km s$^{-1}$). This object is an original 87GB source designated 87GB 113808.0+463858.

## B.34 SDSS J114958.70+411209.4

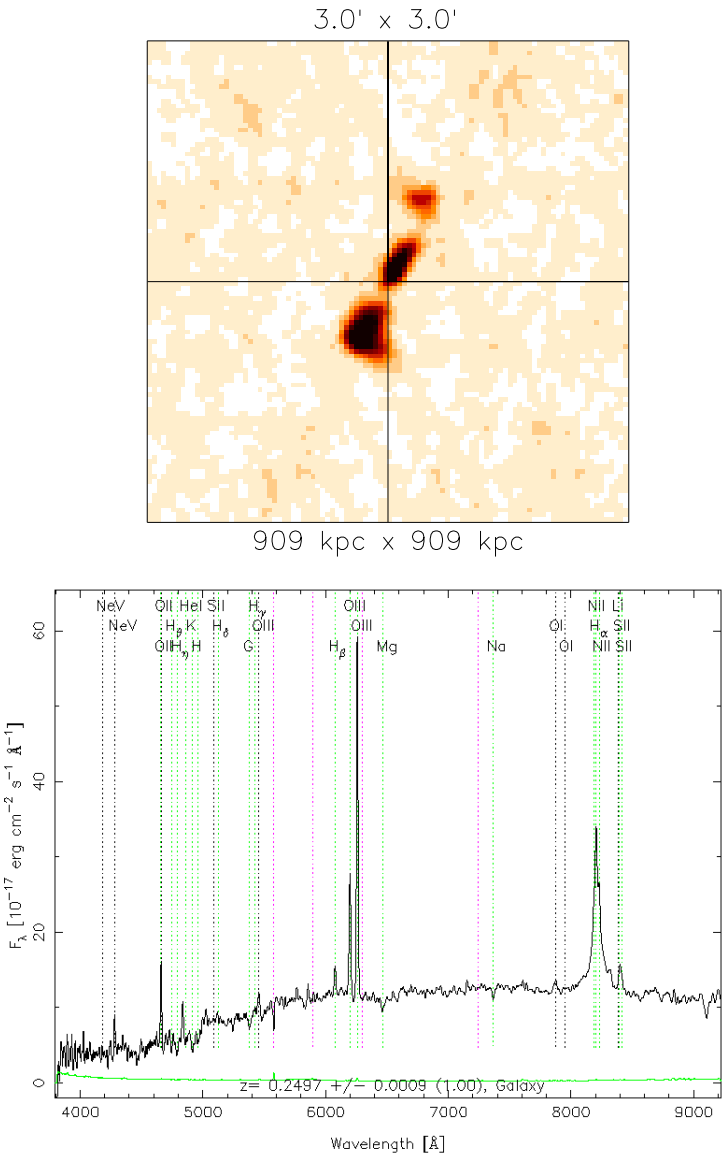


FIGURE B.34: The 3′ x 3′ radio image (top) of SDSS J114958.70+411209.4 shows a bright core source and two lobes, the northern with lower flux. This object has a FR I morphology. The total physical extent is ∼ 0.33 Mpc (with z = 0.2497) and has $F_{1.4\ \mathrm{GHz}} = 118.46$ mJy. The SDSS spectrum (bottom) has a broad H$\alpha$ base ($\mathrm{FWHM}_{\mathrm{H}\alpha} \approx 4850$ km s$^{-1}$). This object is an original 6C source designated 6C B114721.6+412848.

B.35 SDSS J115409.27+023815.0

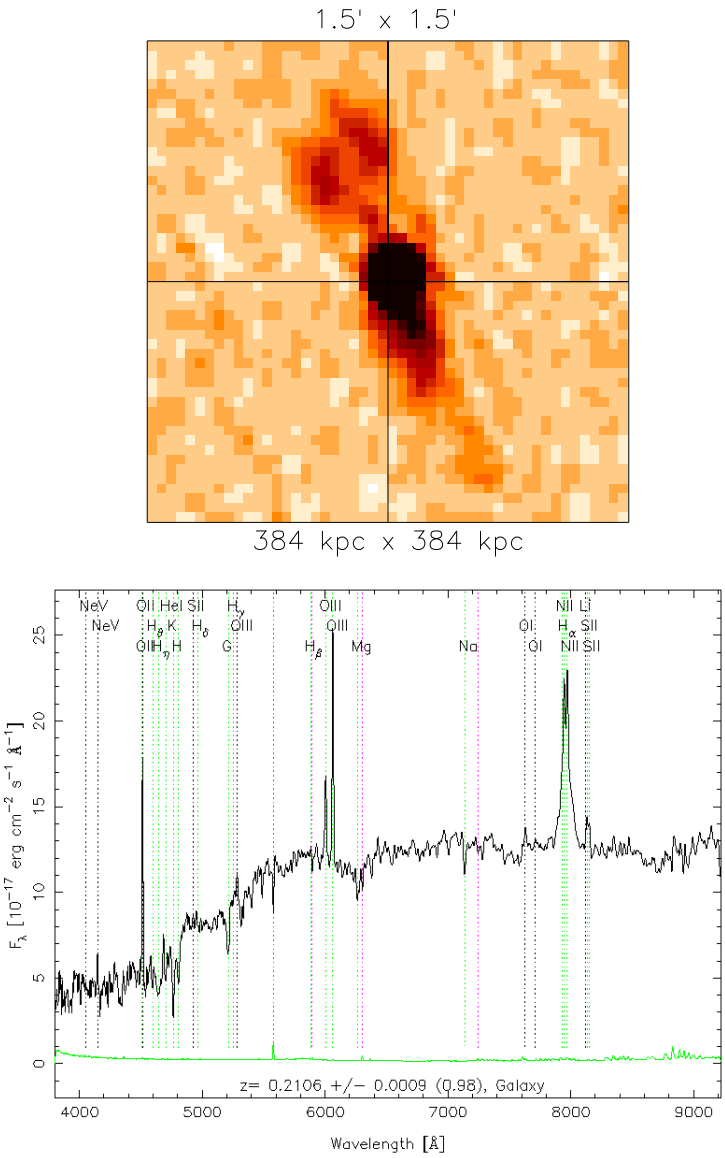


FIGURE B.35: The 1.5′ x 1.5′ radio image (top) of SDSS J115409.27+023815.0 shows a very bright core source with two faint lobes. This object has a FR I morphology. The total physical extent is $\sim$ 0.26 Mpc (with z = 0.2106) and has $F_{1.4\ \mathrm{GHz}} = 64.12$ mJy. The SDSS spectrum (bottom) has a broad H$\alpha$ base ($\mathrm{FWHM}_{\mathrm{H}\alpha} \approx 3730$ km s$^{-1}$). This object is an original 87GB source designated 87GB 115136.0+025423.

## B.36 SDSS J115420.72+452329.4

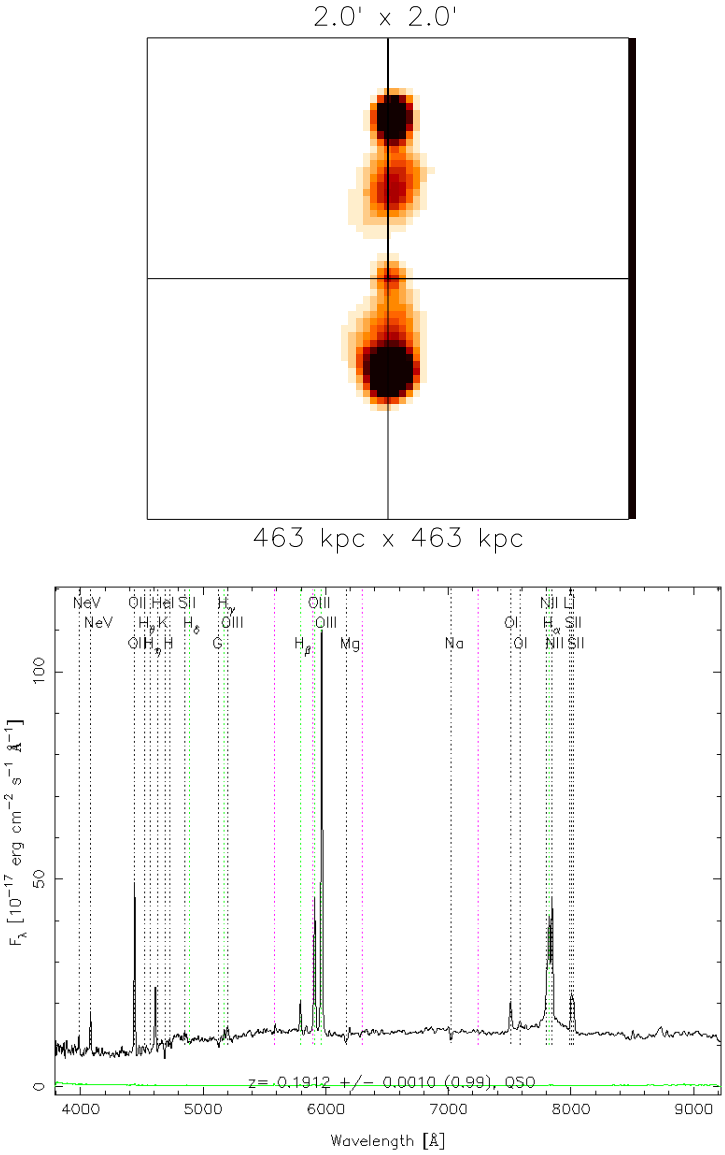


FIGURE B.36: The 2′ x 2′ radio image (top) of SDSS J115420.72+452329.4 shows a dim core source and two lobes that terminate in hot spots . This object has a FR II morphology. The total physical extent is $\sim$ 0.29 Mpc (with z = 0.1912) and has $F_{1.4\ \mathrm{GHz}} = 964.77$ mJy. The SDSS spectrum (bottom) has a broad H$\alpha$ base (FWHM$_{\mathrm{H}\alpha} \approx 4360$ km s$^{-1}$). This object has no known designation in any other radio survey.

## B.37 SDSS J120612.67+490226.2

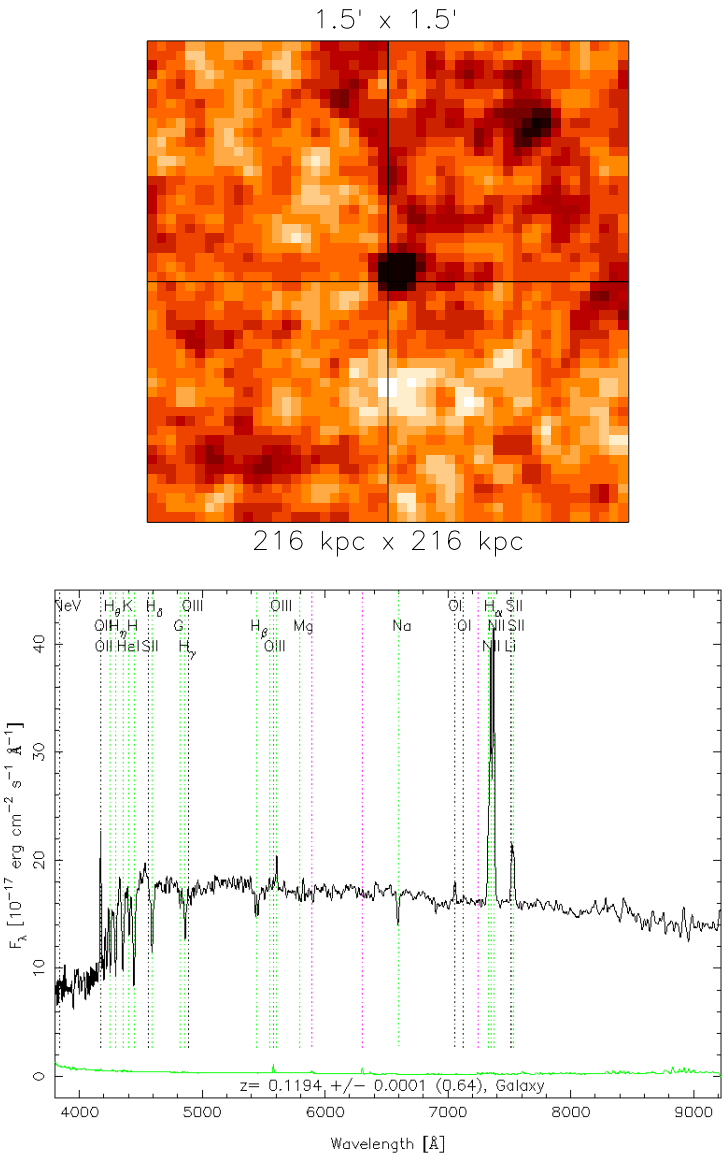


FIGURE B.37: The 1.5′ x 1.5′ radio image (top) of SDSS J120612.67+490226.2 shows a core source and one other faint source in the north-west. This object has an indeterminate morphology. The total physical extent is $\sim$ 0.09 Mpc (with z = 0.1194) and has $F_{1.4\ \mathrm{GHz}}$ = 6.30 mJy. The SDSS spectrum (bottom) has a broad H$\alpha$ base (FWHM$_{\mathrm{H}\alpha} \approx$ 1840 km s$^{-1}$). This object has no known designation in any other radio survey.

## B.38 SDSS J122011.89+020342.2

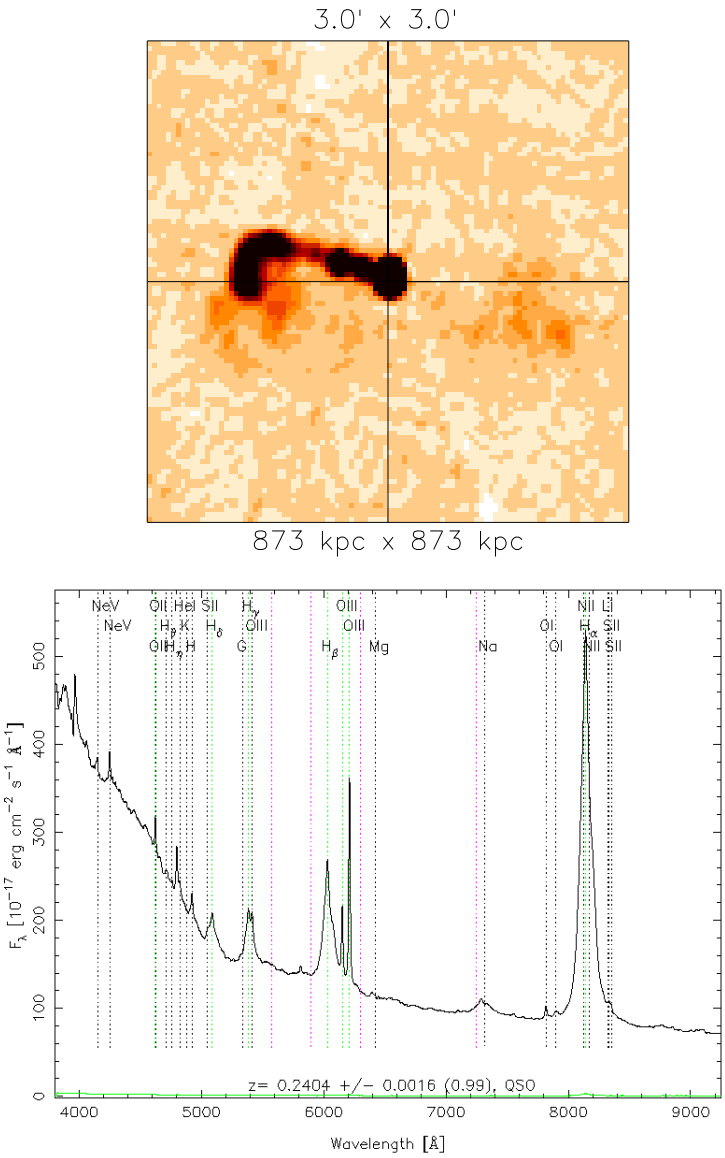


FIGURE B.38: The 3′ x 3′ radio image (top) of SDSS J122011.89+020342.2 shows a bright core source, a bent jet to the east and a faint lobe structure to the west. This object has an asymmetric FR I morphology. The total physical extent is $\sim$ 0.57 Mpc (with z = 0.2404) and has $F_{1.4\ \mathrm{GHz}} = 482.78$ mJy. The SDSS spectrum (bottom) has broad Balmer lines ($\mathrm{FWHM_{H\alpha}} \approx 3960$ km s$^{-1}$). This object is an original PKS source designated PKS 1217+02.

## B.39 SDSS J123807.77+532555.9

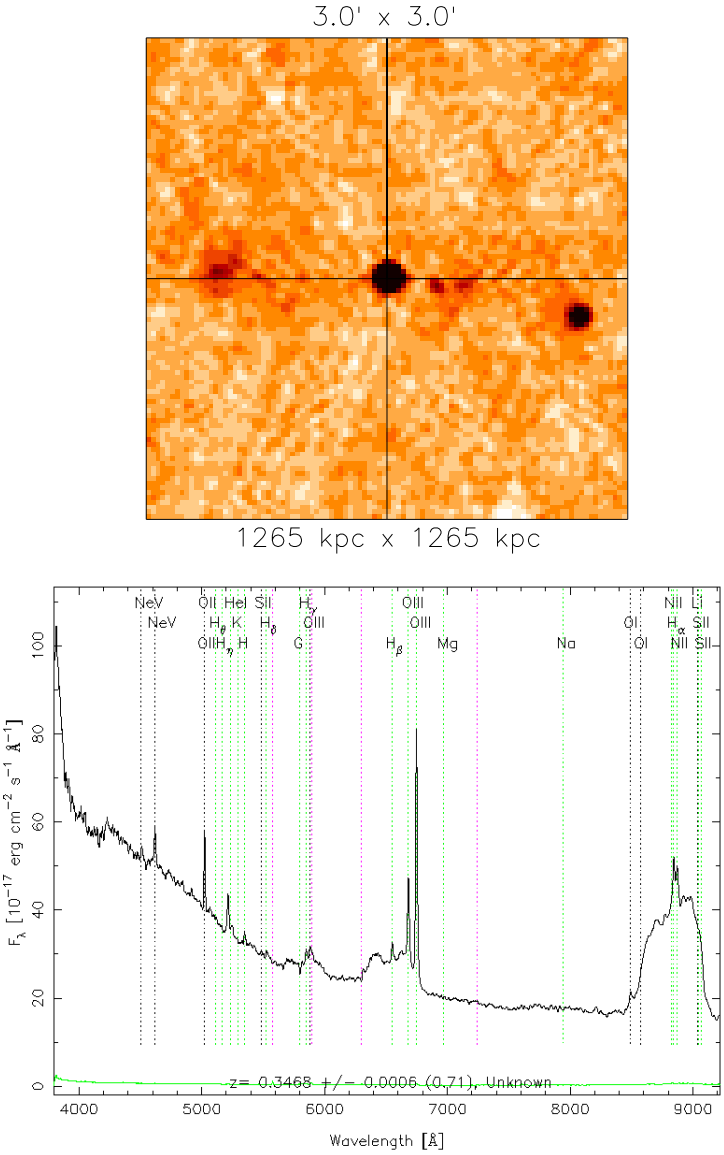


FIGURE B.39: The 3′ x 3′ radio image (top) of SDSS J123807.77+532555.9 shows a bright core source and two hot spots in the distant lobes. This object is a GRG and has a FR II morphology. The total physical extent is $\sim$ 1.02 Mpc (with z = 0.3475) and has $F_{1.4\ \mathrm{GHz}}$ = 61.60 mJy. The SDSS spectrum (bottom) has very broad Balmer lines ($FWHM_{H\alpha} \approx 15390$ km $s^{-1}$). This object is an original 87GB source designated 87GB123550.3+534219.

## B.40 SDSS J123915.39+531414.6

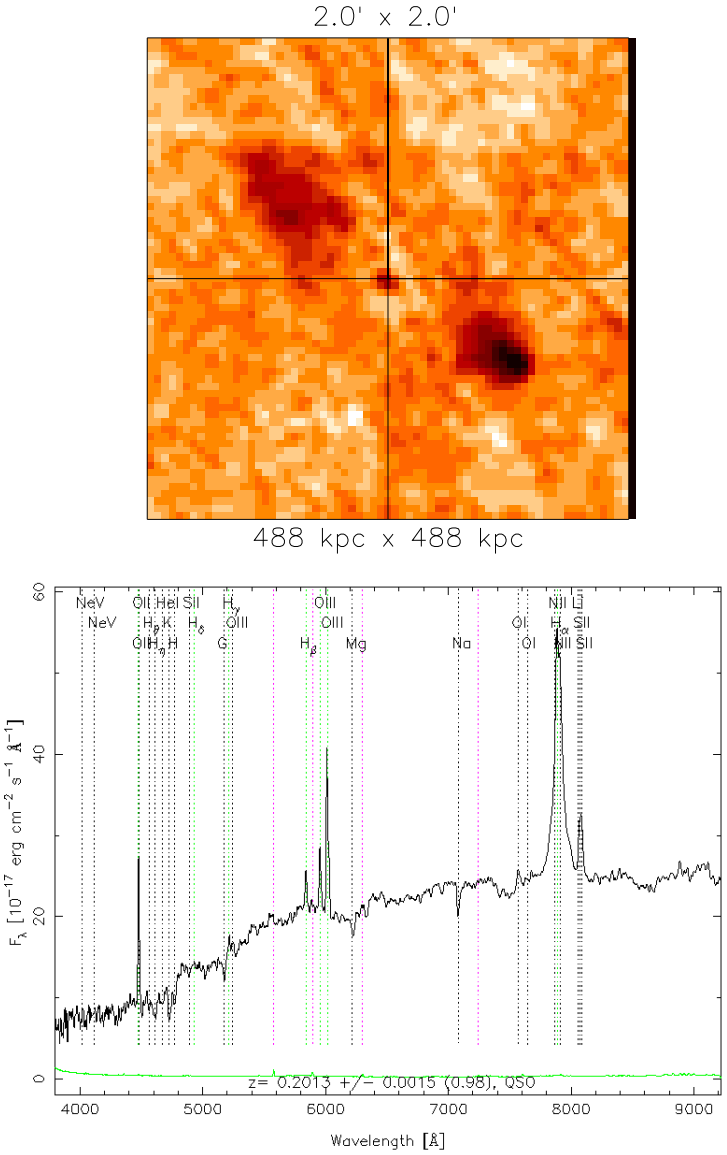


FIGURE B.40: The 2′ x 2′ radio image (top) of SDSS J123915.39+531414.6 shows a dim core source with two symmetric lobes. This object has a FR II morphology. The total physical extent is $\sim$ 0.26 Mpc (with z = 0.2013) and has $F_{1.4\ \mathrm{GHz}} = 23.11$ mJy. The SDSS spectrum (bottom) has a broad H$\alpha$ base ($\mathrm{FWHM}_{\mathrm{H}\alpha} \approx 2780$ km s$^{-1}$). This object is an original 6C source designated 6C B123659.8+533024.

## B.41 SDSS J130359.47+033932.1

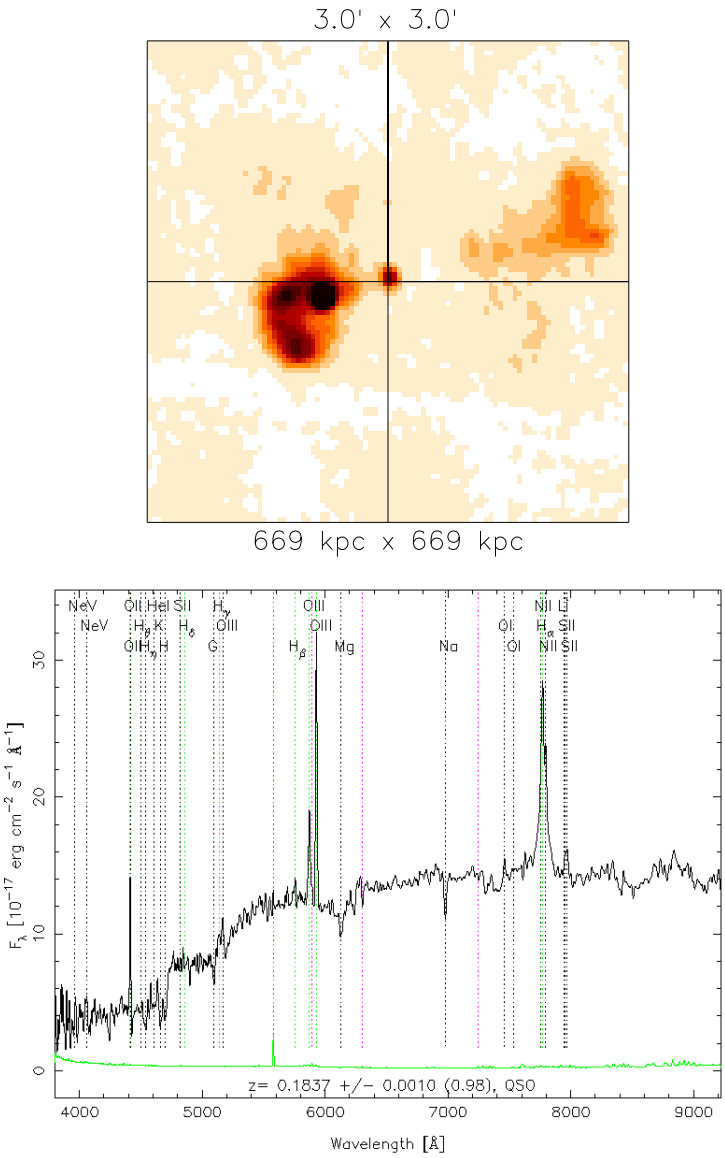


FIGURE B.41: The 3′ x 3′ radio image (top) of SDSS J130359.47+033932.1 shows a faint core source and two lobes of different brightness. This object has a FR II morphology. The total physical extent is ∼ 0.45 Mpc (with z = 0.1837) and has $F_{1.4\ \mathrm{GHz}} = 210.85$ mJy. The SDSS spectrum (bottom) has a broad H$\alpha$ base ($\mathrm{FWHM_{H\alpha}} \approx 5240$ km s$^{-1}$). This object is an original 4C source designated 4C +03.26.

## B.42 SDSS J131827.00+620036.2

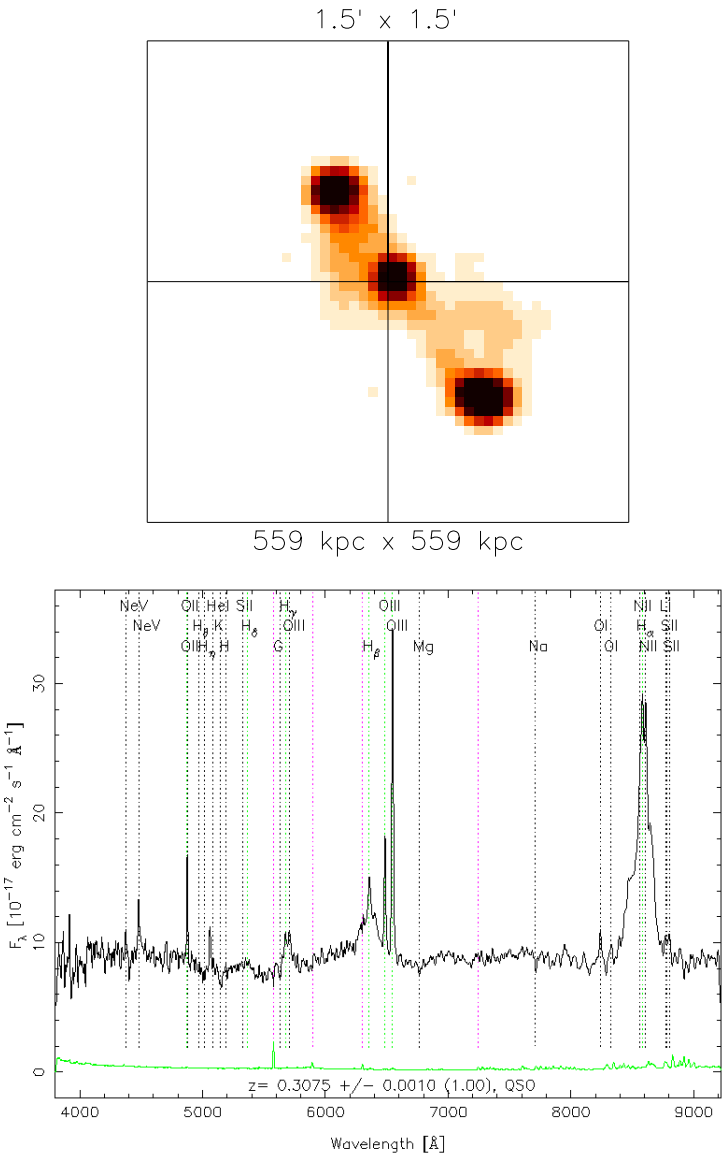


FIGURE B.42: The 1.5′ x 1.5′ radio image (top) of SDSS J131827.00+620036.2 shows a bright core source and two symmetric lobes. This object has a FR II morphology. The total physical extent is $\sim 0.38$ Mpc (with z = 0.3075) and has $F_{1.4\ \mathrm{GHz}} = 133.41$ mJy. The SDSS spectrum (bottom) has broad Balmer lines ($FWHM_{H\alpha} \approx 5870$ km s$^{-1}$). This object is an original 87GB source designated 87GB131634.0+621623, and is also in the 8C catalogue as 8C 1316+622.

## B.43 SDSS J132404.20+433407.1

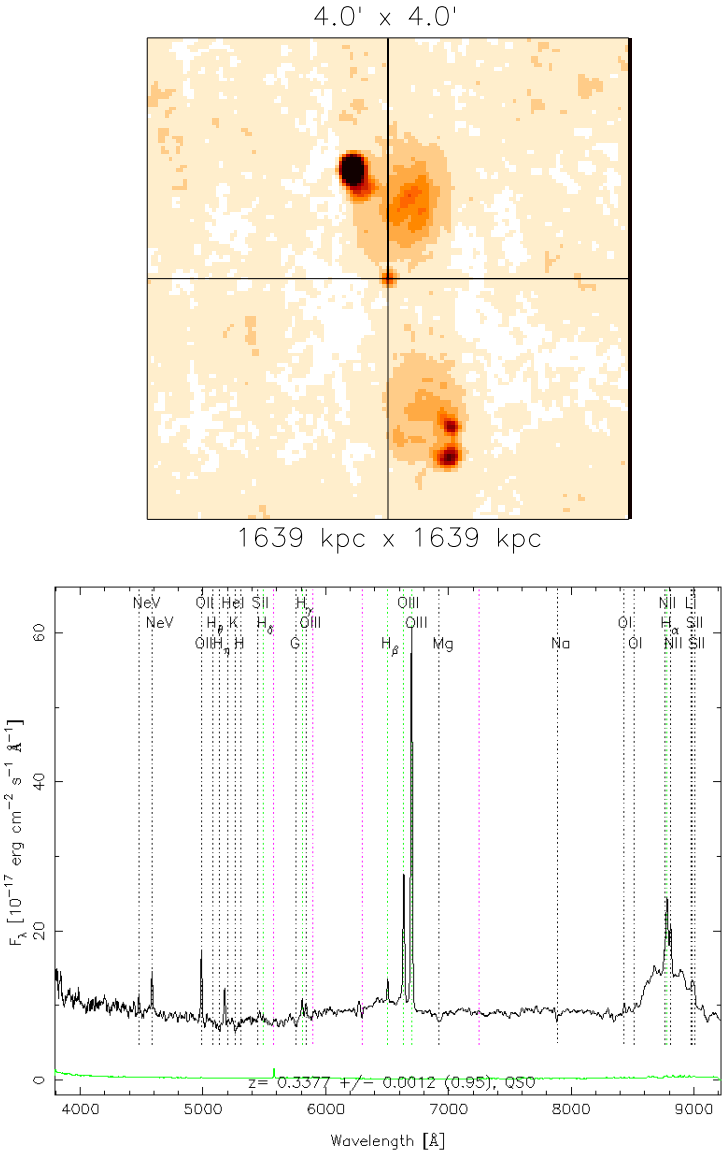


FIGURE B.43: The 4′ x 4′ radio image (top) of SDSS J132404.20+433407.1 shows a core source and two lobes with hot spots. This object is a GRG and has a FR II morphology. The total physical extent is $\sim$ 1.10 Mpc (with z = 0.3377) and has $F_{1.4\ \mathrm{GHz}} = 239.62$ mJy. The SDSS spectrum (bottom) has very broad Balmer lines ($\mathrm{FWHM_{H\alpha}} \approx 10540$ km s$^{-1}$). This object has no known designation in any other radio survey.

## B.44 SDSS J132834.14−012917.6

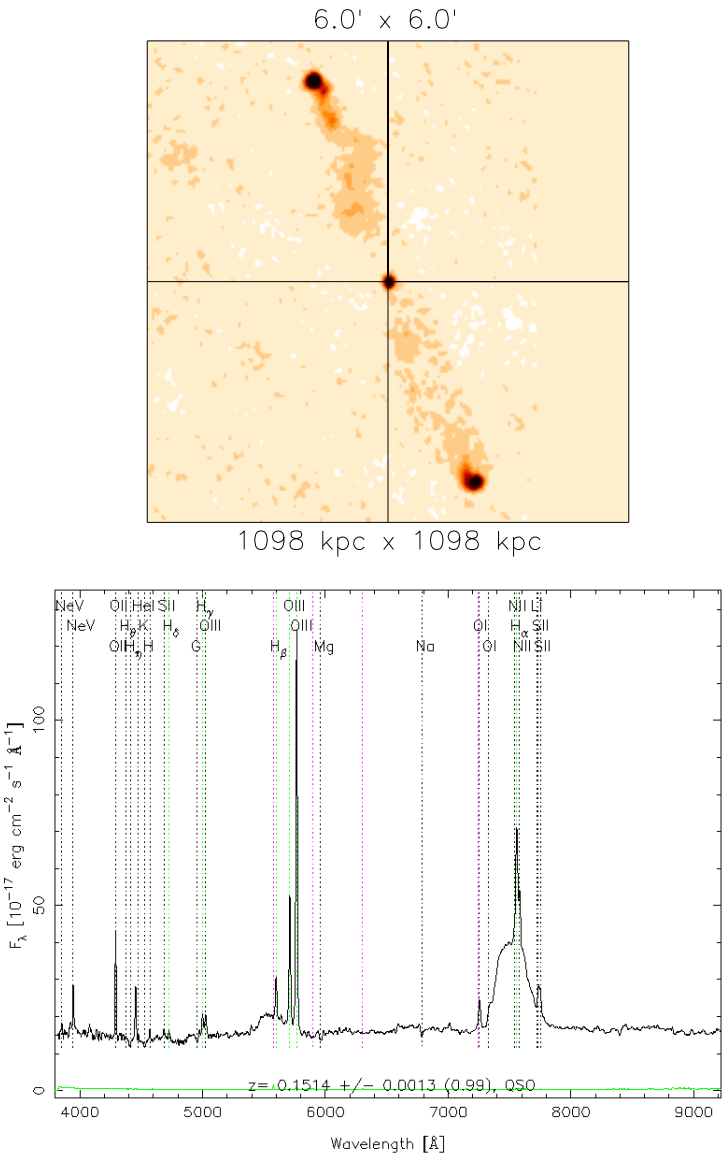


FIGURE B.44: The 6′ x 6′ radio image (top) of SDSS J132834.14−012917.6 shows a bright core source and two very distant and symmetric lobes that terminate in hot spots. This object is a GRG has a FR II morphology. The total physical extent is ∼ 0.98 Mpc (with z = 0.1514) and has $F_{1.4\ \mathrm{GHz}} = 158.85$ mJy. The SDSS spectrum (bottom) has very broad Balmer lines ($\mathrm{FWHM}_{\mathrm{H}\alpha} \approx 10850$ km s$^{-1}$). This object has no known designation in any other radio survey.

## B.45 SDSS J133253.27+020045.6

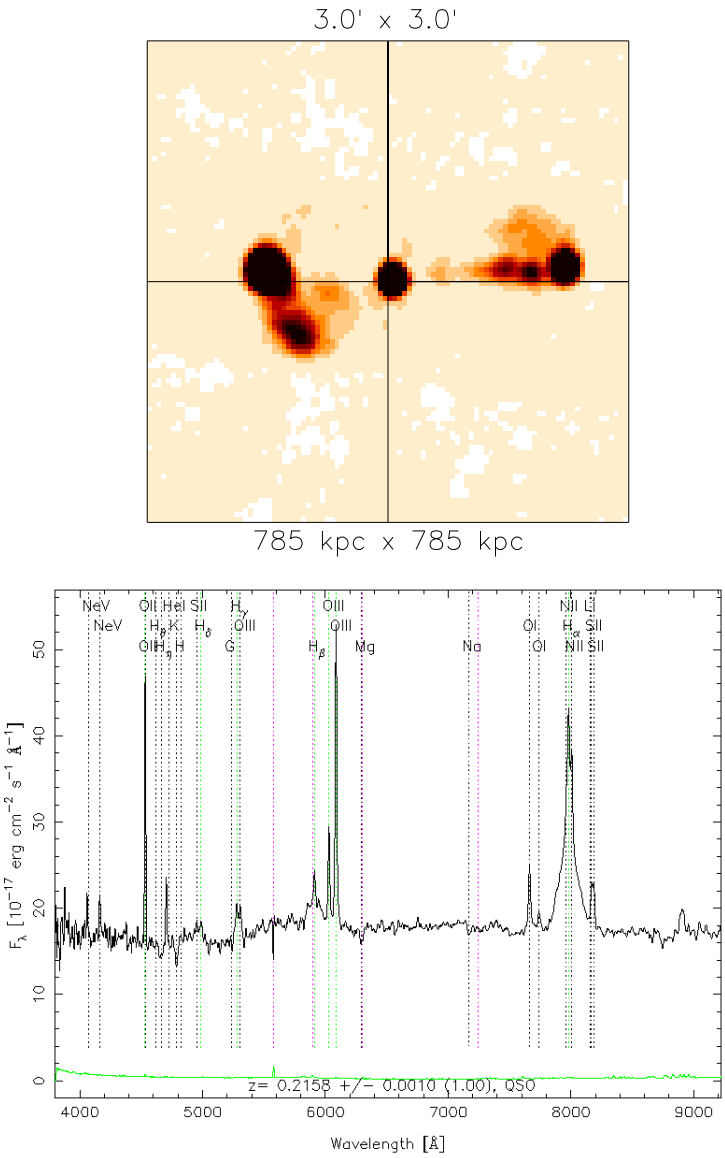


FIGURE B.45: The 3′ x 3′ radio image (top) of SDSS J133253.27+020045.6 shows a bright core and two bright asymmetric lobes. This object has a FR II morphology. The total physical extent is ∼ 0.57 Mpc (with z = 0.2158) and has $F_{1.4\ \mathrm{GHz}} = 1759.16$ mJy. The SDSS spectrum (bottom) has broad Balmer lines ($\mathrm{FWHM_{H\alpha}} \approx 5700$ km s$^{-1}$). This object is is an original 3C source designated 3C 287.1.

## B.46 SDSS J133437.48+563147.9

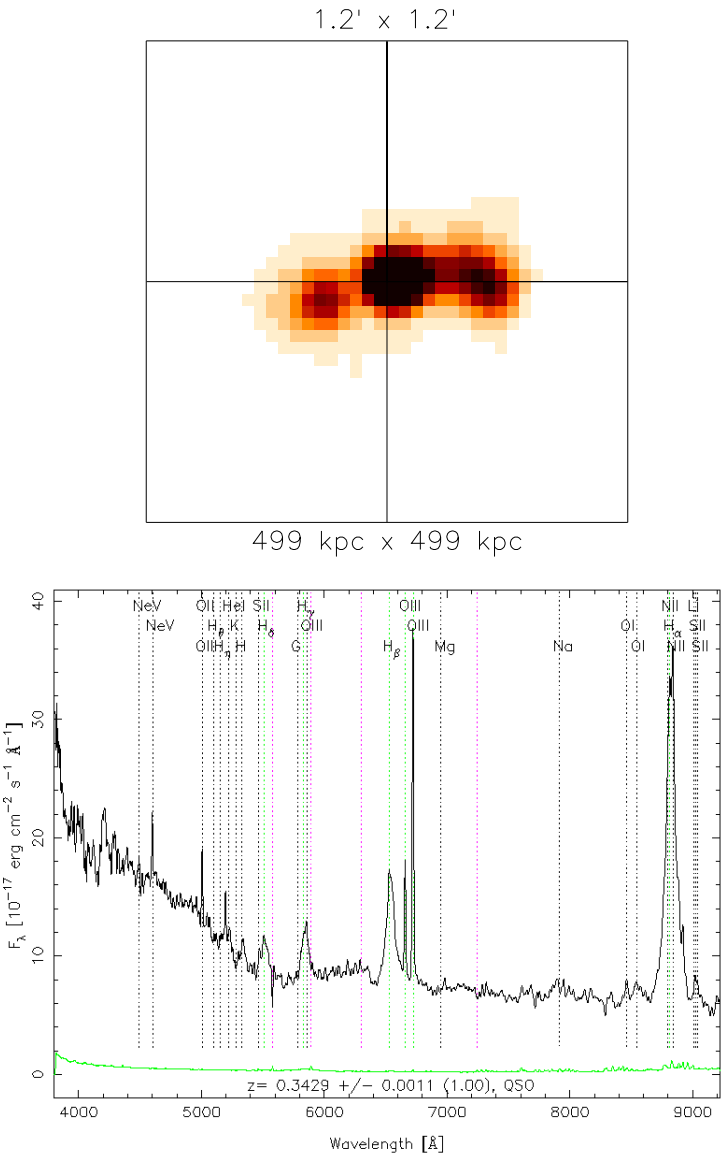


FIGURE B.46: The 1.2′ x 1.2′ radio image (top) of SDSS J133437.48+563147.9 shows a bright core source and two jets, the western one slightly bent. This object has a FR I morphology. The total physical extent is $\sim$ 0.24 Mpc (with z = 0.3428) and has $F_{1.4\ \mathrm{GHz}}$ = 164.18 mJy. The SDSS spectrum (bottom) has broad Balmer lines ($FWHM_{H\alpha} \approx 3740$ km $s^{-1}$). This object is an original 87GB source designated 87GB133243.4+564710.

## B.47 SDSS J134545.35+533252.3

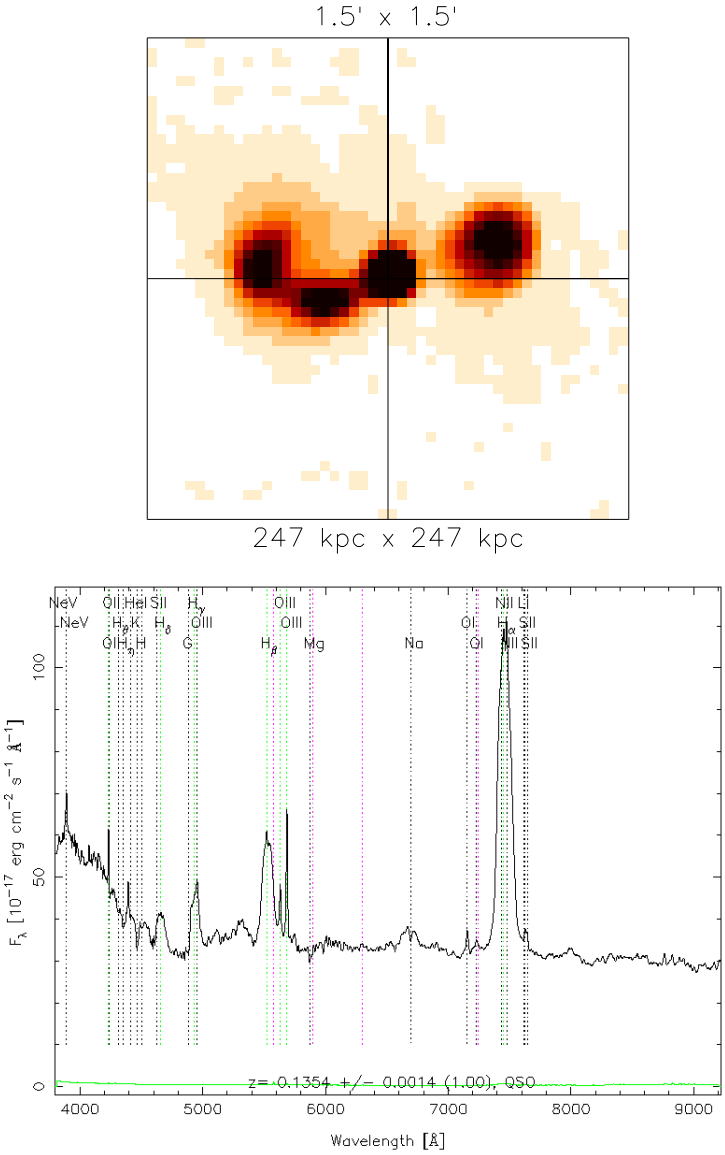


FIGURE B.47: The 1.2′ x 1.2′ radio image (top) of SDSS J134545.35+533252.3 shows a bright core source with one bent jets to the east and a hot spot in the west. This object has a FR II morphology. The total physical extent is $\sim$ 0.13 Mpc (with z = 0.1354) and has $F_{1.4\ \mathrm{GHz}} = 278.19$ mJy. The SDSS spectrum (bottom) has broad Balmer lines ($FWHM_{H\alpha} \approx$ 5070 km s$^{-1}$). This object is an original 87GB source designated 87GB 134352.4+534755.

## B.48 SDSS J134617.54+622045.4

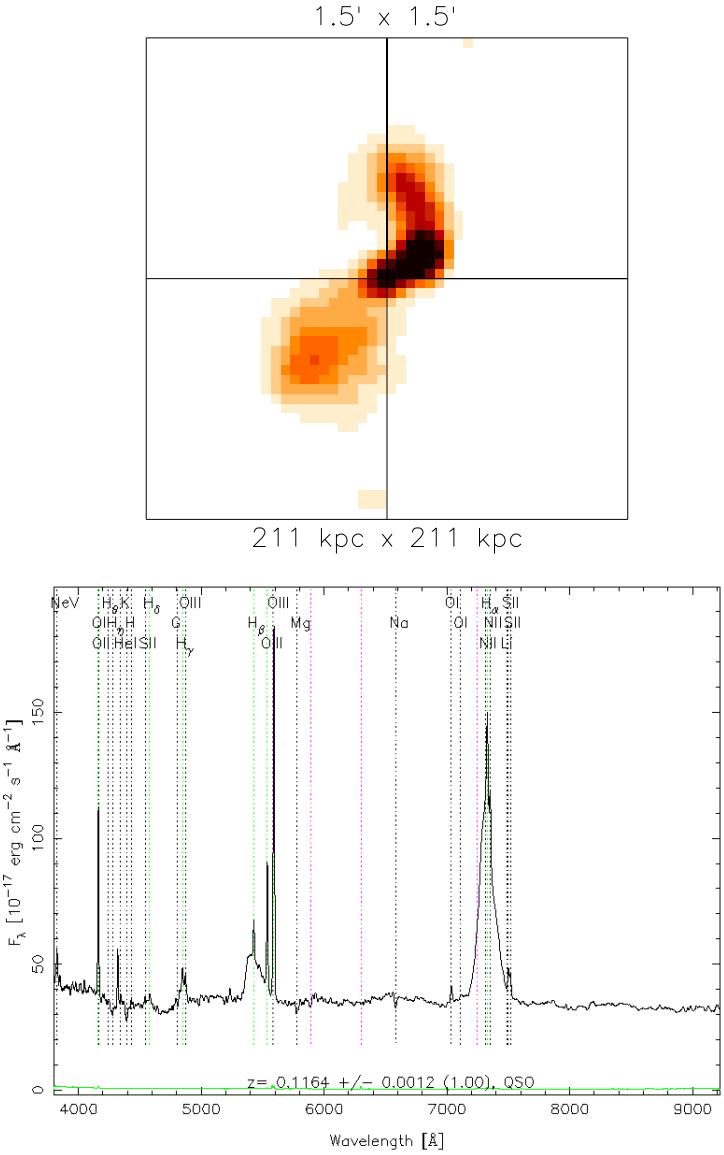


FIGURE B.48: The 1.5′ x 1.5′ radio image (top) of SDSS J134617.54+622045.4 shows a bright core source and a bent jets to both the north and south. This object has a FR I morphology. The total physical extent is $\sim 0.15$ Mpc (with z = 0.1164) and has $F_{1.4\ \mathrm{GHz}} = 142.99$ mJy. The SDSS spectrum (bottom) has broad Balmer lines ($\mathrm{FWHM}_{\mathrm{H}\alpha} \approx 5160$ km $\mathrm{s}^{-1}$). This object is an original 6C source designated 6C B134441.6+623604.

## B.49 SDSS J141613.36+021907.8

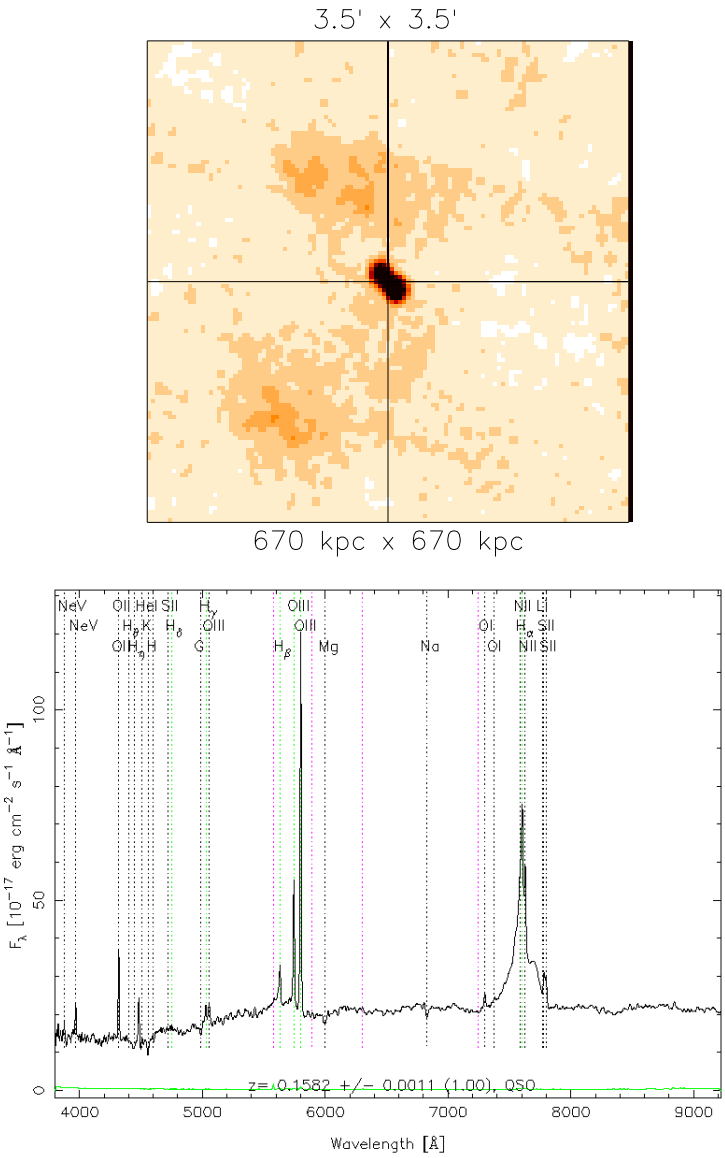


FIGURE B.49: The 3.5′ x 3.5′ radio image (top) of SDSS J141613.36+021907.8 shows a bright core, possibly a double unresolved source and two faint lobes. This object has a possible FR II morphology although most of the flux is from the central pixels. This is a possible DDRG. The total physical extent is $\sim 0.67$ Mpc (with z = 0.1582) and has $F_{1.4\ \mathrm{GHz}}$ = 107.70 mJy. The SDSS spectrum (bottom) has broad Balmer lines ($FWHM_{H\alpha} \approx 3810$ km $s^{-1}$). This object has no known designation in any other radio survey.

## B.50 SDSS J144302.76+520137.2

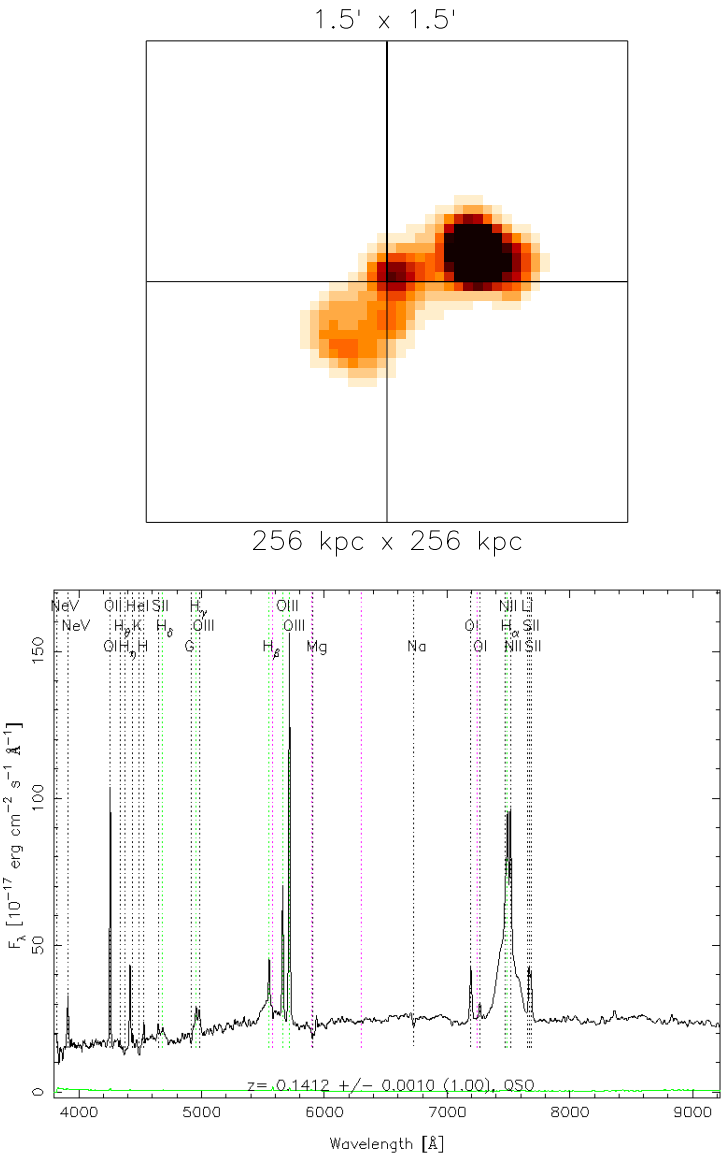


FIGURE B.50: The 1.5′ x 1.5′ radio image (top) of SDSS J144302.76+520137.2 shows a core source and two lobes, the southern one dimmer. This object has a FR II morphology. The total physical extent is $\sim 0.12$ Mpc (with z = 0.1412) and has $F_{1.4\ \mathrm{GHz}} = 2119.27$ mJy. The SDSS spectrum (bottom) has a broad H$\alpha$ base ($\mathrm{FWHM_{H\alpha}} \approx 4930$ km s$^{-1}$). This object is an original 3C source designated 3C 303.

## B.51 SDSS J151640.22+001501.8

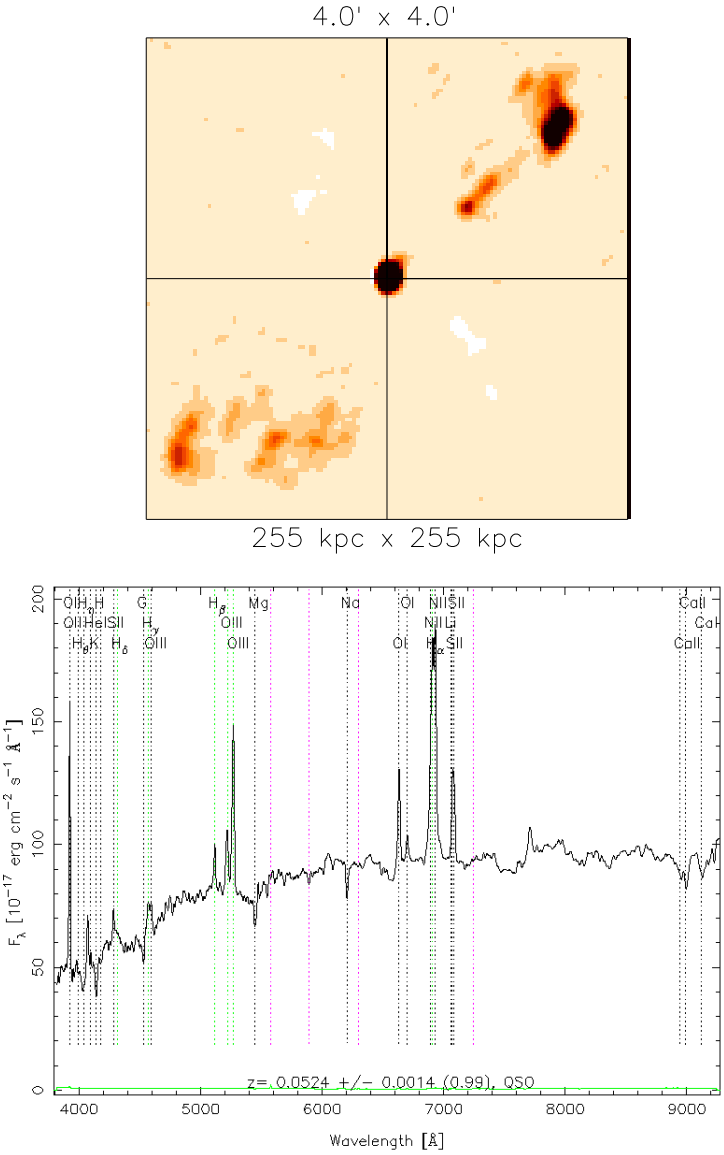


FIGURE B.51: The 4′ x 4′ radio image (top) of SDSS J151640.22+001501.8 shows a bright core source and two diffuse lobes with various hot spots. This object has a FR II morphology. The total physical extent is $\sim 0.28$ Mpc (with z = 0.0524) and has $F_{1.4\ \mathrm{GHz}} = 1090.21$ mJy. The SDSS spectrum (bottom) has broad Balmer lines ($\mathrm{FWHM}_{\mathrm{H}\alpha} \approx 2790$ km s$^{-1}$). This object is a GB6 source designated GB6 J1516+0015 and the 4C source C +00.56.

## B.52 SDSS J151913.35+362343.4

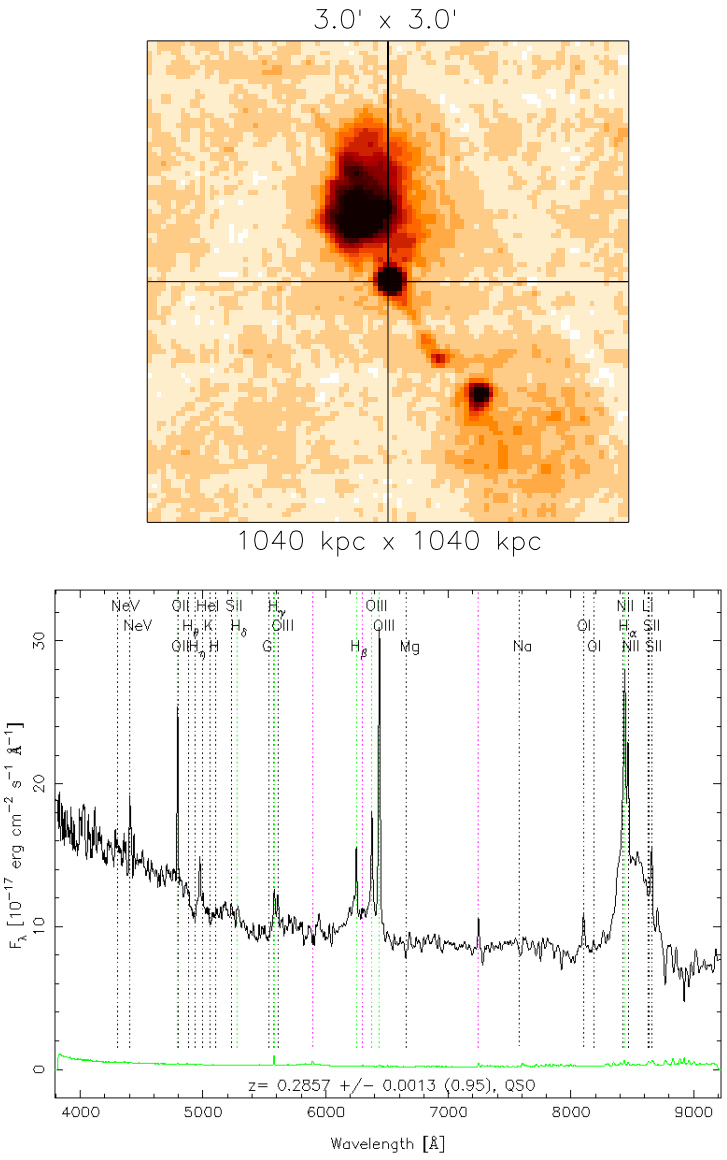


FIGURE B.52: The 3′ x 3′ radio image (top) of SDSS J151913.35+362343.4 shows a bright core source a with a lobe in the north and a jet to the south. This object is a possible HYMORS candidate. The total physical extent is ∼ 0.58 Mpc (with z = 0.2857) and has $F_{1.4\ \mathrm{GHz}} = 207.25$ mJy. The SDSS spectrum (bottom) has broad Balmer lines ($FWHM_{H\alpha} \approx$ 9280 km $s^{-1}$). This object is an original 6C source designated 6C B151717.1+363448.

## B.53 SDSS J152942.20+350851.2

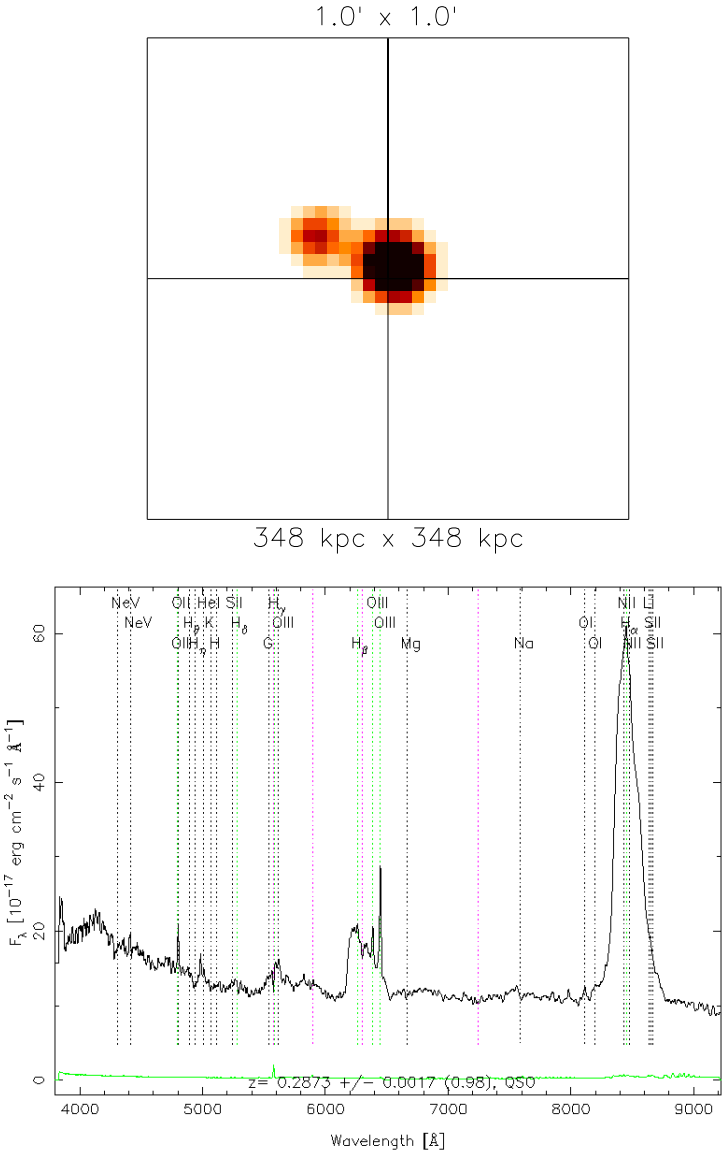


FIGURE B.53: The 1′ x 1′ radio image (top) of SDSS J152942.20+350851.2 shows a bright core source and a weak jet to the east. This object has a FR I morphology. The total physical extent is ∼ 0.08 Mpc (with z = 0.2873) and has $F_{1.4\ \mathrm{GHz}} = 109.27$ mJy. The SDSS spectrum (bottom) has broad Balmer lines ($\mathrm{FWHM}_{\mathrm{H}\alpha} \approx 7310$ km s$^{-1}$). This object is a 7C source designated 7C 1527+3519.

## B.54 SDSS J155206.58−005339.3

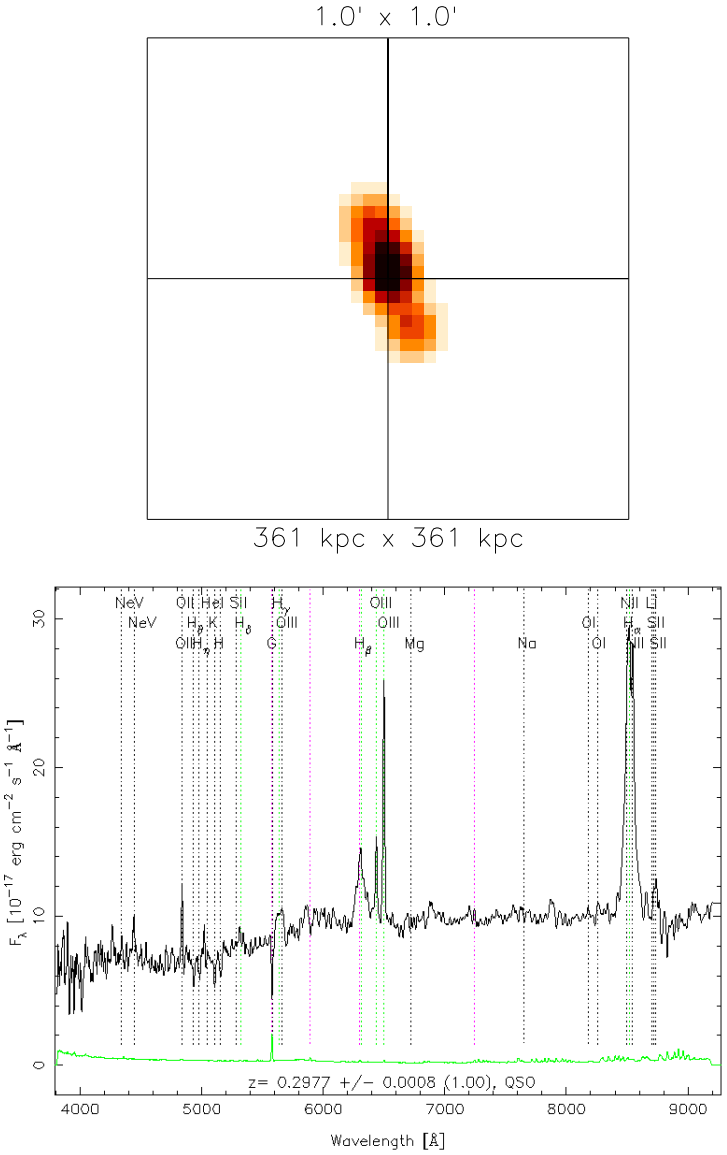


FIGURE B.54: The 1′ x 1′ radio image (top) of SDSS J155206.58−005339.3 shows a bright core source a two jets. This object has a FR I morphology. The total physical extent is ∼ 0.12 Mpc (with z = 0.2977) and has $F_{1.4\ \mathrm{GHz}} = 105.67$ mJy. The SDSS spectrum (bottom) has broad Balmer lines ($FWHM_{H\alpha} \approx 3070$ km s$^{-1}$). This object has no known designation in any other radio survey.

## B.55 SDSS J163856.53+433512.5

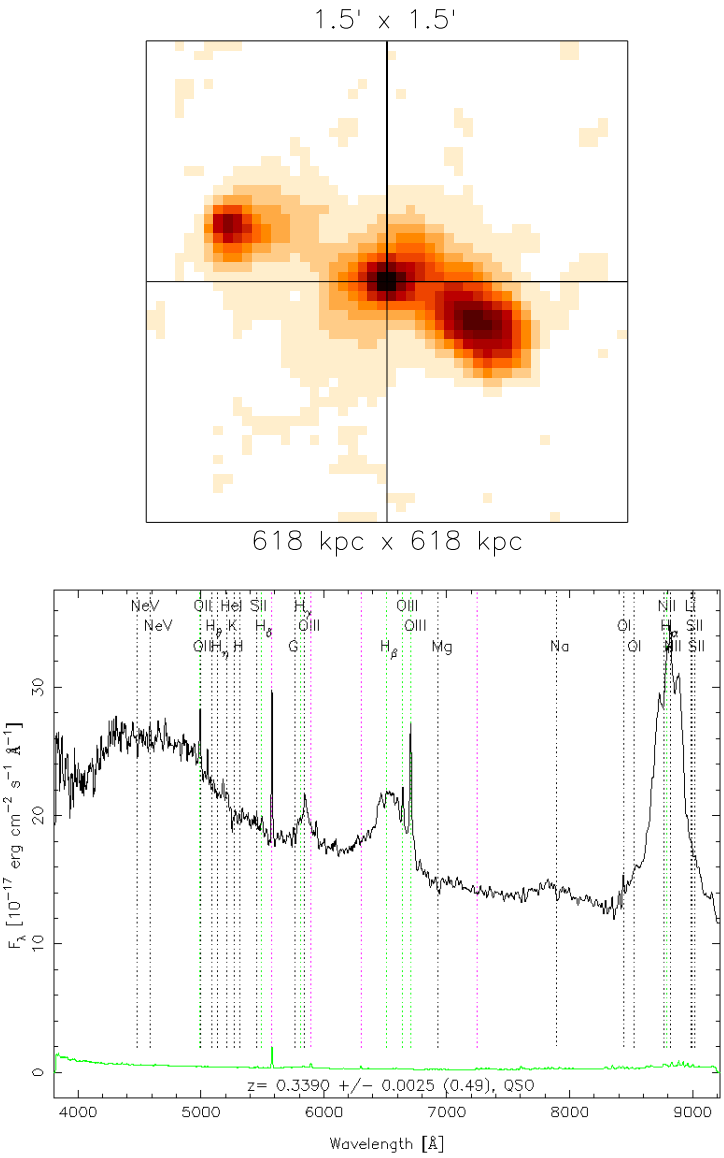


FIGURE B.55: The 1.5′ x 1.5′ radio image (top) of SDSS J163856.53+433512.5 shows a bright core source and two lobes. This object has a FR II morphology. The total physical extent is $\sim 0.45$ Mpc (with z = 0.3390) and has $F_{1.4\ \mathrm{GHz}} = 133.04$ mJy. The SDSS spectrum (bottom) has very broad Balmer lines ($\mathrm{FWHM}_{\mathrm{H}\alpha} \approx 8290$ km s$^{-1}$). This object is a B3 source designated B3 1637+436 and the 6C source 6CB163723.1+434051.

B.56 SDSS J164442.53+261913.2

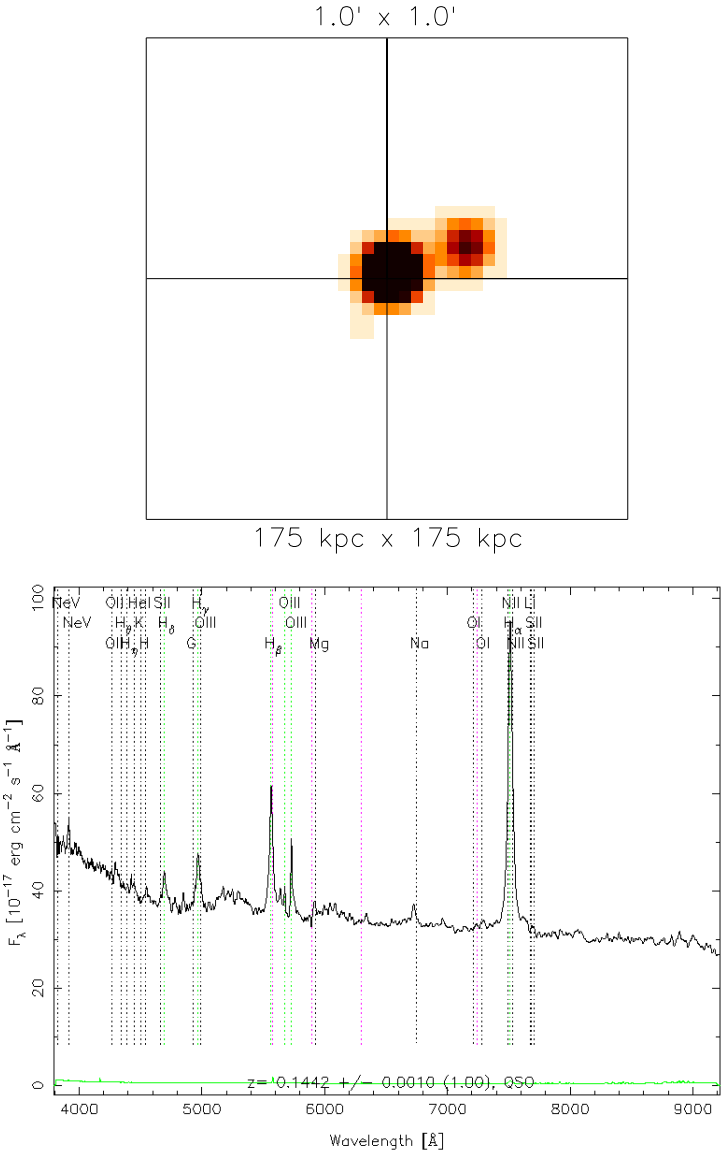


FIGURE B.56: The 1′ x 1′ radio image (top) of SDSS J164442.53+261913.2 shows a bright core source and one hot spot to the west. This object has an indeterminate morphology. The total physical extent is ∼ 0.06 Mpc (with z = 0.1442) and has $F_{1.4\ \mathrm{GHz}} = 110.36$ mJy. The SDSS spectrum (bottom) has broad Balmer lines ($\mathrm{FWHM}_{\mathrm{H}\alpha} \approx 1230$ km s$^{-1}$). This object has no known designation in any other radio survey.

B.57 SDSS J170013.70+400855.6

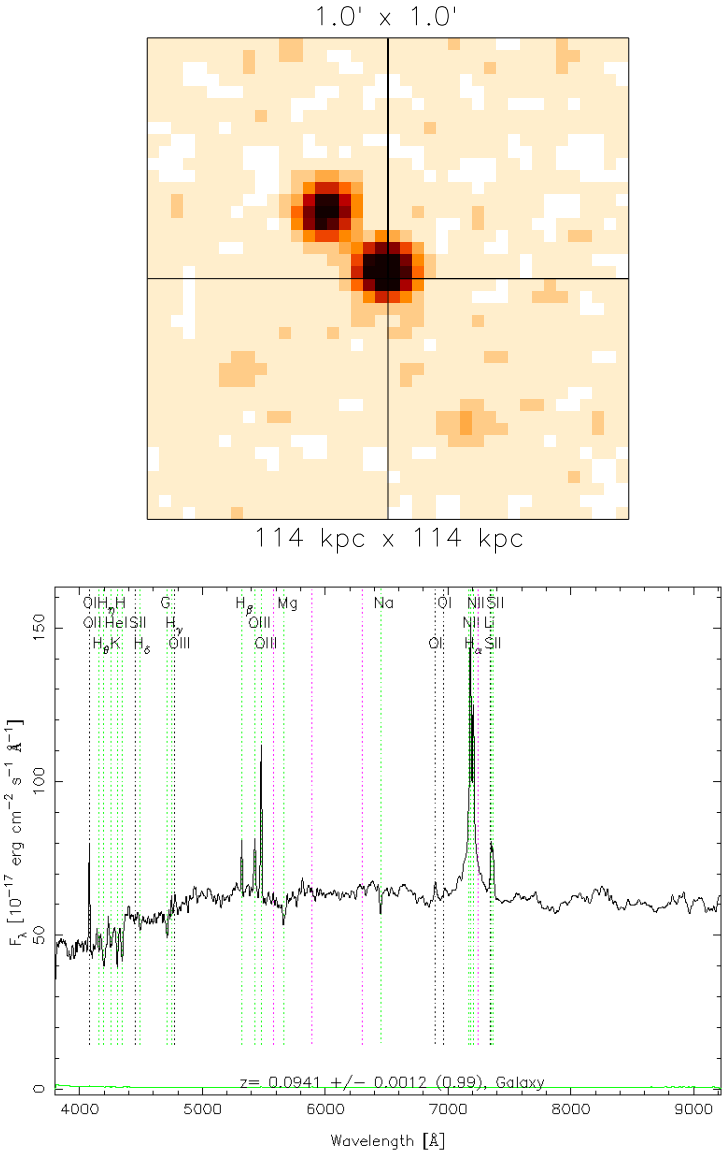


FIGURE B.57: The 1′ x 1′ radio image (top) of SDSS J170013.70+400855.6 shows a bright core source and a hot spot in the north east within the host galaxy. There is a possible lobe to the SW which if present could make this a FR II. The total physical extent is $\sim 0.07$ Mpc (with z = 0.0941) and has $F_{1.4\ \mathrm{GHz}} = 20.68$ mJy. The SDSS spectrum (bottom) has broad Balmer lines ($\mathrm{FWHM_{H\alpha}} \approx 4350$ km s$^{-1}$). This object has no known designation in any other radio survey.

B.58 SDSS J170425.11+333145.9

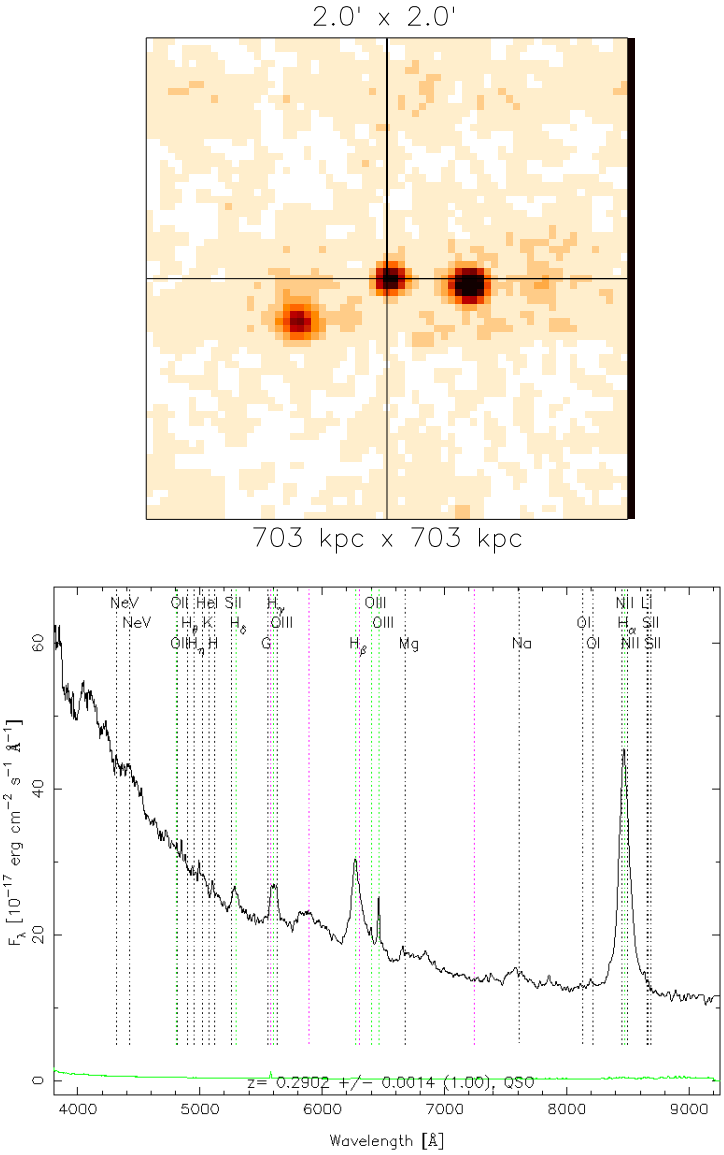


FIGURE B.58: The 2′ x 2′ radio image (top) of SDSS J170425.11+333145.9 shows a bright core source with two asymmetric lobes. This object has a FR II morphology. The total physical extent is $\sim$ 0.37 Mpc (with z = 0.2902) and has $F_{1.4\ \mathrm{GHz}} = 36.07$ mJy. The SDSS spectrum (bottom) has broad Balmer lines ($\mathrm{FWHM_{H\alpha}} \approx 3350$ km s$^{-1}$). This object has no known designation in any other radio survey.

## B.59 SDSS J171322.58+325628.0

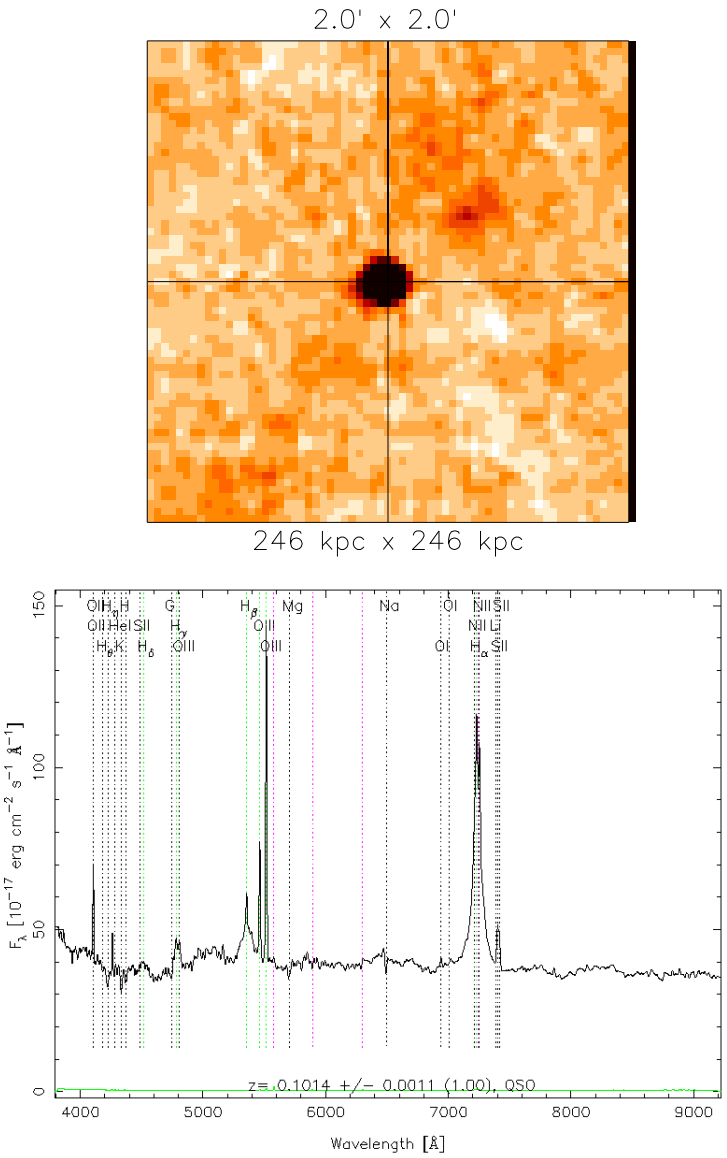


FIGURE B.59: The 2′ x 2′ radio image (top) of SDSS J171322.58+325628.0 shows a bright core source and one weak hot spot to the north-west. This object may have a FR I morphology. The total physical extent is $\sim$ 0.15 Mpc (with z = 0.1013) and has $F_{1.4\ \mathrm{GHz}}$ = 44.80 mJy. The SDSS spectrum (bottom) has broad Balmer lines ($\mathrm{FWHM}_{\mathrm{H}\alpha} \approx 4120$ km $\mathrm{s}^{-1}$). This object is an original FBQS source designated FBQS J171322.6+325628.

B.60 SDSS J220233.84−073225.0

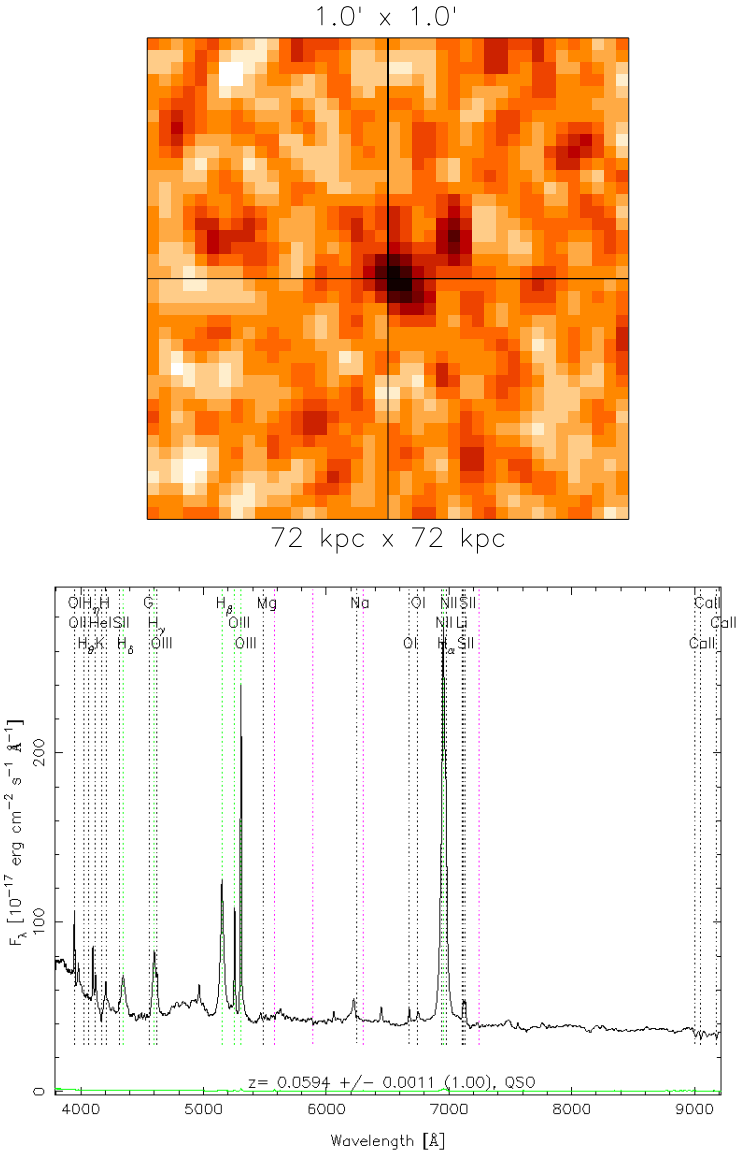


FIGURE B.60: The 1′ x 1′ radio image (top) of SDSS J220233.84−073225.0 shows a core source and a nearby hot spot within the host galaxy. This object has an indeterminate morphology. The total physical extent is ∼ 0.02 Mpc (with z = 0.0594) and has $F_{1.4\ \mathrm{GHz}}$ = 3.33 mJy. The SDSS spectrum (bottom) has broad Balmer lines ($FWHM_{H\alpha} \approx 2000$ km $s^{-1}$). This object has no known designation in any other radio survey.

## B.61 SDSS J230545.66−003608.6

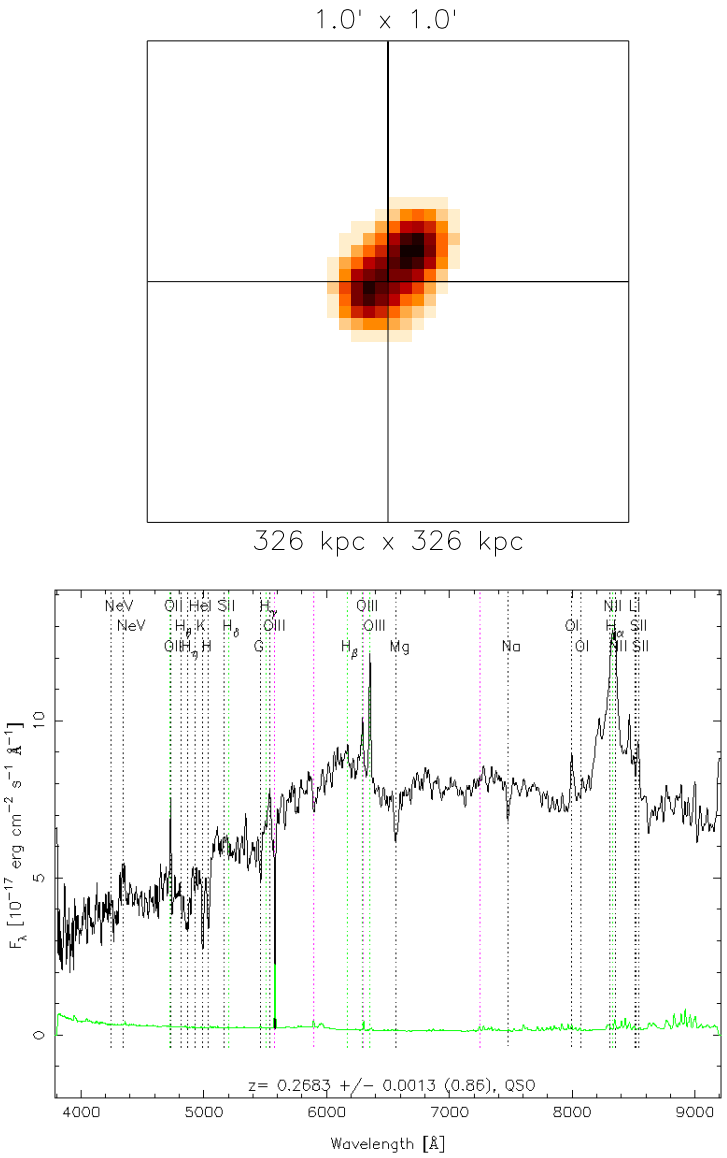


FIGURE B.61: The 1′ x 1′ radio image (top) of SDSS J230545.66−003608.6 shows a bright core source with unresolved, nearby lobes. This object may have either a FR I or FR II morphology. The total physical extent is ∼ 0.15 Mpc (with z = 0.2689) and has $F_{1.4\ \mathrm{GHz}}$ = 517.76 mJy. The SDSS spectrum (bottom) has broad Balmer lines ($\mathrm{FWHM}_{\mathrm{H}\alpha} \approx 2980$ km $\mathrm{s}^{-1}$). This object is a 4C source designated 4C -01.59 and the PKS source PKS 2303-008.

## B.62 SDSS J233313.16+004911.8

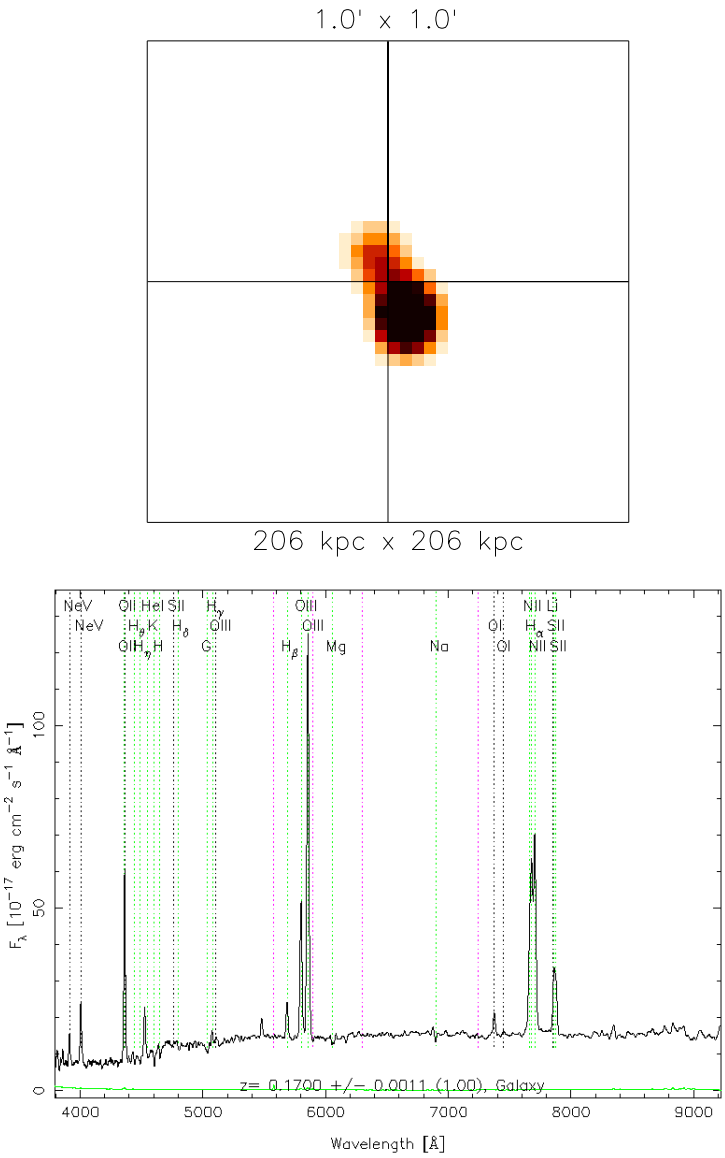


FIGURE B.62: The 1′ x 1′ radio image (top) of SDSS J233313.16+004911.8 shows a bright core source and an unresolved small scale jet. This object has a FR I morphology. The total physical extent is ∼ 0.17 Mpc (with z = 0.1700) and has $F_{1.4\ \mathrm{GHz}}$ = mJy. The SDSS spectrum (bottom) has broad Balmer lines ($\mathrm{FWHM_{H\alpha}} \approx 317.86$ km s$^{-1}$). This object is an original PKS source designated PKS 2330+005.

## B.63 SDSS J235156.12−010913.3

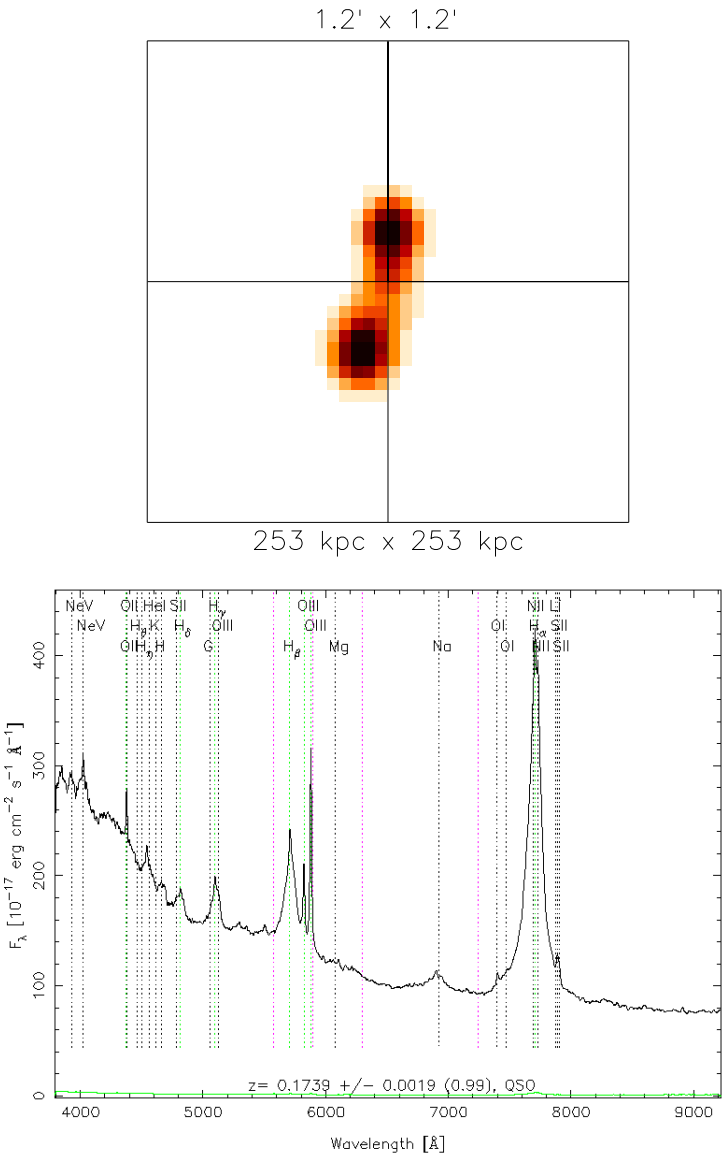


FIGURE B.63: The 1.2′ x 1.2′ radio image (top) of SDSS J235156.12−010913.3 shows two lobes symmetric about the optical core. This object has a FR II morphology. The total physical extent is ∼ 0.09 Mpc (with z = 0.1740) and has $F_{1.4\ \mathrm{GHz}} = 1460.41$ mJy. The SDSS spectrum (bottom) has broad Balmer lines ($\mathrm{FWHM_{H\alpha}} \approx 4670$ km s$^{-1}$). This object is a 4C source designated 4C −01.61 and the PKS source PKS 2349−01.